

A Study of the Mechanism for Vortex Breakdown and Some Measures for its Control

This thesis is submitted in fulfillment of
the requirements for the degree of Doctor of Philosophy,
Department of Mechanical Engineering
Monash University
August 2002

By Michael Jones B.Sc.(Hons)

Abstract

This computational study begins by detailing an existing theory for the onset of vortex breakdown in an open pipe. This theory states that a necessary condition for breakdown onset is the generation of negative azimuthal vorticity upstream of breakdown. The theory is interpreted here for breakdown produced in the torsionally driven cylinder. It is shown that the azimuthal vorticity generation mechanisms which lead to breakdown in the pipe are also applicable to the cylinder breakdown flow. However, in the cylinder azimuthal vorticity production in the breakdown region is augmented by generation at the rotating lid.

The theory for breakdown in the pipe states that much of the generation of azimuthal vorticity occurs through stretching. We modify this generation mechanism directly by introducing a slip aerofoil upstream of breakdown. The aerofoil reduces the radial outflow and hence suppresses the generation of negative azimuthal vorticity via stretching. By varying the aerofoil location it has been possible to completely remove the breakdown bubble.

A comparison is drawn between the types of breakdown observed in the cylinder and in the more open flows (in pipes and over delta wings). The different manifestations of breakdown in these geometries is attributed to the different Reynolds number regimes in which they operate (the Reynolds number here is based on quantities associated with the vortex core, and hence enables a more consistent comparison between geometries.) The claim that the cylinder flow is not an example of vortex breakdown is then refuted based on this and other arguments. The generation of a cylinder type axisymmetric breakdown in an open pipe at low Re confirms the analysis.

Finally a method is examined by which breakdown can be promoted or suppressed within the parameter range in which hysteresis is observed. Transient pulses in the inlet swirl are applied with varying magnitude and duration, and the response of the flow observed to the point where the final state has evolved. It proves possible to switch the pipe flow between breakdown and no-breakdown states by this method.

Statement of originality

This thesis contains no material which has been accepted for the award of any other degree or diploma in any university or other institution.

To the best of my knowledge, this thesis contains no material previously published or written by another person, except where due reference is made in the text of the thesis.

Michael Jones

August 2002

Acknowledgements

There are many people who have supported this work. I'd first like to thank my supervisors Professor Kerry Hourigan and Associate Professor Mark Thompson, who have provided excellent guidance throughout this project.

The active postgraduate group at Monash Mechanical Engineering has been a great source of help during my candidature. I have enjoyed being a part of this group, and appreciated the assistance I've received over the years.

I make special mention of colleagues Dr Paul Reichl and Dr Tan Boon Thong, for their technical assistance, especially with regard to computing, and also for the frequent diversions from work which helped make postgrad life more enjoyable.

Thanks also to the members of the department who contribute to keeping the responsions and disputations alive and interesting.

I acknowledge the financial support of the University in the form of a Monash Graduate Scholarship.

Finally thanks to family and friends for their patience and support, having heard the excuse 'I have to work on my thesis' too many times.

Publications

Michael Jones, Kerry Hourigan, and Mark Thompson, “**An Investigation of Wave Trapping as a Cause of Vortex Breakdown in the Torsionally Driven Cylinder**”, *Proceedings of the 13th Australasian Fluid Mechanics Conference*, Monash University, Melbourne, Australia, 13-18 December 1998.

Michael Jones, Paul Morris, Kerry Hourigan, and Mark Thompson, “**Some Observations of the Flow in a Centrifugal Separator**”, *Proceedings of the 13th Australasian Fluid Mechanics Conference*, Monash University, Melbourne, Australia, 13-18 December 1998.

Michael Jones, Kerry Hourigan, and Mark Thompson, “**Azimuthal Vorticity Dynamics in the Torsionally Driven Cylinder**”, *Proceedings of the 30th AIAA Fluid Dynamics Conference, AIAA Paper 99-3807*, Richmond, Virginia, USA, 1999.

Brendon Adams, Michael Jones, Kerry Hourigan, and Mark Thompson, “**Hysteresis in the Open Pipe Flow with Vortex Breakdown**”, *Proceedings of the Second International Conference on Computational Fluid Dynamics in the Minerals and Process Industries*, Melbourne, Australia, December, 1999.

M. C. Jones, K. Hourigan, and M. C. Thompson, “**The Generation and Suppression of Vortex Breakdown by Upstream Swirl Perturbations**”, *Proceedings of the 14th Australasian Fluid Mechanics Conference*, Adelaide University, Adelaide, Australia, 10-14 December 2001.

M. C. Jones, K. Hourigan, and M. C. Thompson, “**Toward a Geometry Independent Criterion for Vortex Breakdown**”, *Proceedings of the 14th Australasian Fluid Mechanics Conference*, Adelaide University, Adelaide, Australia, 10-14 December 2001.

Nomenclature

Re	Reynolds number
ρ	density
\mathbf{u}	velocity
u	axial velocity
v	radial velocity
w	azimuthal velocity
ν	kinematic viscosity
Θ	angular velocity
AR	aspect ratio of the torsionally driven cylinder
Ω	swirl ratio $\left(\frac{\Gamma_\infty}{\delta u_\infty}\right)$
Γ_∞	freestream circulation
δ	vortex core radius
u_∞	freestream velocity
x	x coordinate
y	y coordinate
z	z coordinate
r	radial coordinate
ϕ	azimuthal coordinate
u_1, u_2, α, k	Garg and Leibovich [20] velocity profile constants
r_t	pipe radius at the inlet
C_+	velocity of wave travelling with the flow
C_-	velocity of wave travelling against the flow
N	Benjamin's [3] criticality variable
ϕ	delta wing sweep angle (Chapter 2 only)
$J(r)$	Howard and Gupta's [33] Richardson number criticality criterion
AOA	Angle Of Attack
Ro	Rosby number
ω	vorticity
ω_x	x component of vorticity

ω_y	y component of vorticity
ω_r	radial component of vorticity
ω_ϕ	azimuthal component of vorticity
\mathbf{i}	unit vector in the x direction
\mathbf{j}	unit vector in the y direction
\mathbf{k}	unit vector in the z direction
\mathbf{e}_x	unit vector in the axial direction
\mathbf{e}_r	unit vector in the radial direction
\mathbf{e}_ϕ	unit vector in the azimuthal direction
t	time ordinate
Γ	circulation $\int \boldsymbol{\omega} \cdot \mathbf{n} \cdot d\mathbf{s}$
ψ	streamfunction
k	circulation
Ψ	base flow streamfunction
$F(r, x)$	perturbation coefficient function
ϵ	perturbation coefficient
R	pipe radius
γ^2	eigenvalue of Sturm-Liouville system
H	total pressure
I	$\frac{1}{2}k^2$
S	source term in the momentum equation
S_x	source term x component
S_y	source term y component
S_z	source term z component
τ_{ij}	viscous stress components
p	pressure
μ	dynamic viscosity
V	volume element in divergence theorem
A	surface area of volume element in divergence theorem
\mathbf{n}	unit normal to surface element dA
C	central control volume node
E	east control volume node

W	west control volume node
EE	second east control volume node
WW	second west control volume node
F	ρu
δx	node spacing
D	$\frac{\mu}{\delta x}$
p^*	pressure field guess
p'	pressure field correction
$g(z, \delta z)$	pipe wall function
u_0	inlet axial velocity profile
v_0	inlet radial velocity profile
w_0	inlet azimuthal velocity profile
n	number of timesteps
dt	normalised timestep
B	azimuthal vorticity generation by stretching and tilting
S	azimuthal vorticity generation by stretching
T	azimuthal vorticity generation by tilting (turning)
A	total azimuthal vorticity generation
R	azimuthal vorticity generation by diffusion
$\delta\omega$	perturbation vorticity
$\delta\omega_x$	perturbation axial vorticity
$\delta\omega_r$	perturbation radial vorticity
$\delta\omega_\phi$	perturbation azimuthal vorticity
γ	helix angle
Q	flow rate
L	characteristic length scale
a	characteristic radial length scale
S	swirl $\left(\frac{2\pi a}{Q}\right)$
C_B	Billant's [5] breakdown criterion
α	sloped cylinder wall ratio
Re_c	cylinder Reynolds number
Re_p	pipe Reynolds number

Ω_p	pipe swirl
Ω_i	initial condition swirl
Ω_P	perturbation swirl $\left(\frac{\Omega}{\Omega_i}\right)$
δt	pulse duration
dt	normalised pulse duration

Contents

1	Vortex breakdown	1
2	Current knowledge	5
2.1	Observations of vortex breakdown	5
2.1.1	Flows over delta wings	5
2.1.2	Torsionally driven cylinder flows	6
2.1.3	Diverging pipe flows	8
2.1.4	The various breakdown types	12
2.2	Theoretical aspects of vortex breakdown	14
2.2.1	Analogy to boundary layer separation	15
2.2.2	Hydrodynamic instabilities	16
2.2.3	Concept of conjugate critical states	17
2.3	Control of vortex breakdown over delta wings	19
2.3.1	Changes to wing geometry	20
2.3.2	Flow modification by nett mass flow	21
2.3.3	Leading edge suction	23
2.3.4	Trailing edge flow modifiers	24
2.4	Discussion	25
3	Vorticity dynamics	26

3.1	The vorticity dynamics approach	26
3.2	The vorticity equation	28
3.3	Vorticity generation in an axisymmetric geometry	28
3.4	Stretching	29
3.5	Tilting	30
3.6	Diffusion	32
3.7	Feedback mechanism	32
3.8	Critical state and wave trapping	33
4	Method and Validation	39
4.1	Introduction	39
4.2	Numerical method	40
4.3	Discretisation	42
4.4	Pressure-velocity coupling	43
4.5	The open pipe geometry	44
4.6	Grid resolution and verification of numerical results	47
4.6.1	Grid resolution	47
4.6.2	Comparison with other numerical results	49
4.6.3	Timestep tests	52
4.6.4	Validation against experimental results	52
4.7	Azimuthal vorticity generation	55
4.7.1	Validation of vorticity calculations	56
4.7.1.1	Components of vorticity	56
4.7.1.2	Azimuthal vorticity generation terms	57
4.7.2	Tilting of axial and radial vorticity	61
4.7.2.1	Tilting of axial vorticity	62

4.7.2.2	Tilting of radial vorticity	62
5	Vortex breakdown in the driven cylinder	65
5.1	The cylinder geometry	67
5.2	Grid resolution and convergence considerations	67
5.3	Comparison of computational with experimental results	70
5.3.1	Time dependence validation	71
5.4	The wave trapping hypothesis: present study	72
5.5	Method	73
5.6	Vorticity propagation	79
5.6.1	Velocity change propagation	86
5.6.2	Vorticity generation	86
5.6.3	Stretching and turning	91
5.6.4	Dependence of generation term on Reynolds number	93
5.7	Conclusions and further work	94
6	Breakdown control by a slip aerofoil	97
6.1	Mesh study	98
6.2	The effect of varying angle of attack	101
6.3	The effect of varying aerofoil radial location	103
6.4	The effect of varying aerofoil axial location	104
6.5	Discussion	105
7	Geometry dependence of breakdown	108
7.1	Cylinder and pipe velocity profiles	110
7.1.1	Axial velocity	112
7.1.2	Radial velocity	112

7.1.3	Azimuthal velocity	112
7.1.4	Other derived quantities	112
7.2	Streampipe	115
7.3	Equivalence of Ω and Re in different geometries	122
7.3.1	Billant <i>et al.</i> 's [5] criterion	124
7.3.2	Some definitions	127
7.3.3	Effect of sloping cylinder walls	132
7.3.4	Some conclusions	141
7.4	Absence of hysteresis in the cylinder	141
7.5	Is the cylinder 'breakdown' really breakdown?	143
7.6	Three-dimensional simulation of the pipe flow	147
7.6.1	Method	148
7.6.2	Varying Re_p	149
7.7	Summary	151
8	Breakdown promotion by an upstream pulse	152
8.1	Hysteresis and delta wing vortex breakdown	152
8.2	Hysteresis and pipe vortex breakdown	154
8.3	This study	155
8.4	Problem formulation	156
8.5	Steady initial condition	157
8.6	Flow behaviour for $\Omega_P > 1$	160
8.7	Results for varying Ω_P	165
8.7.1	$\Omega_P = 1.10, 1.125$	165
8.7.2	$\Omega_P = 1.20, 1.25, 1.30$	167
8.7.3	$\Omega_P = 1.375$	169

8.7.4	$\Omega_P = 1.50$	170
8.7.5	$\Omega_P = 1.75, 2.00$	170
8.8	Observed trends	172
8.9	Ramped pulse	173
8.10	Onset of three-dimensionality	175
8.11	Note on bubble evolution	176
8.12	Flow state at Ω_P	177
8.13	$dt \gg 4$	179
8.14	Discussion	180
9	Breakdown suppression by an upstream pulse	182
9.1	Introduction	182
9.2	Results for varying Ω_P	183
9.2.1	$\Omega_P = 0.0$	183
9.2.2	$\Omega_P = 0.50, 0.75$	186
9.2.3	$\Omega_P = 0.85, 0.875$	186
9.2.4	$\Omega_P = 0.90$	188
9.2.5	$\Omega_P = 0.925, 0.95, 0.975$	188
9.3	$dt \gg 32$	191
9.4	Conclusions	192
9.5	Relevance and further work	193
10	Conclusions	194

Chapter 1

Vortex breakdown

In the 1950s, experiments were conducted to determine the optimum planform, or geometry, for new aircraft designed to travel faster than sound. As a result of these investigations, the delta wing began to dominate as the preferred configuration for these types of aircraft. Since the delta wing planform was mainly for military applications, manoeuvrability was of major concern, and this drove studies onto the range of angles of attack at which the delta wing could perform. The results of one such study were reported by Werle in 1954 (in [10]). Werle's water tunnel investigation of a delta wing was the first to document over a wing the occurrence of what is now termed vortex breakdown. It amounted to a destruction of the strong vortical core which forms above the leading edge of a delta wing. A contemporary visualisation of vortex breakdown over the wing of an aircraft in flight is presented in figure 1.1. A vortex trailing from the leading edge extension is visualised in this experiment. It undergoes a rapid expansion and transition to turbulence just upstream of the twin tails; it is this transition which is termed vortex breakdown.

The effect of vortex breakdown is to destroy the vortex core. Since the vortex contributes up to half the total lift generated by the wing [38], its destruction can result in a dramatic reduction in the performance of the wing. Successive investigations have revealed further characteristics of breakdown which have significant effects on the wing in flight, the major ones being transient roll and pitch moments, and buffeting of downstream control surfaces.

Initial studies concentrated on discerning the mechanism for vortex breakdown, to the extent that a number of theories now provide some understanding of the generation principles. However no consensus has yet been reached as to the mechanism for breakdown.



Figure 1.1: F-18 High Angle-of-Attack (Alpha) Research Vehicle in flight [13]

In recent years vortex breakdown has become of increasing importance to operators of highly manoeuvrable aircraft. The F/A-18 and F-22 have wing planforms which are derived from the delta wing; they also have twin tails. These tails are in the direct path of turbulence resulting from the destruction of leading-edge vortex cores by vortex breakdown - see figure 1.1. The result is excessive vibration of the tails, and reduction of their lifespan. This combined with the other problems mentioned earlier may prohibit the aircraft from operating in this flight regime. Hence the efforts involved in creating the extensive performance envelope of the aircraft are to some extent foiled by the onset of breakdown. Drastic engineering fixes have been implemented in an attempt to offset the effect of breakdown, such as the positioning of fences on the wing to deflect the vortex core [68].

Despite the negative effects breakdown has on aircraft in flight, the phenomenon does have some useful applications. The intense vortices generated by heavy aircraft on landing and takeoff can potentially be destroyed by breakdown, reducing the hazard for following planes. Breakdown also has benefits in the areas of combustion and mixing.

Efforts toward determining a mechanism for breakdown continue. Meanwhile what has been learned so far has been tested in the form of experiments in breakdown control. Changes to wing geometry ([47], [27], [65], [66], [29]), leading- and trailing-edge flaps ([12], [19], [11]), sucking or blowing of fluid ([60], [74], [2], [37], [36], [59], [51]) and a variety of other means ([34], [28]) have been proposed in an attempt to effect some control over breakdown. Complete control of breakdown has still not been realised however. In

order to be able to effect better control over breakdown, more research is required into its generation mechanism, and into its control in practical situations. The work presented in the following chapters aims to make some contribution to the understanding of breakdown, and to its eventual control. The way this thesis is structured is set out as follows:

Chapter 2: We summarise the work previously conducted into vortex breakdown in order to assess the current state of knowledge, and highlight the most important questions yet to be answered.

Chapter 3: Examines the vorticity dynamics associated with swirling flows and how the generation and transport of vorticity can be used to describe the progression toward vortex breakdown. The notion of wave trapping will be introduced, as we will make use of this idea in a subsequent chapter.

Chapter 4: Here the methods used to generate and post-process the results throughout this thesis will be described, and the pipe geometry introduced.

Chapter 5: We apply a vorticity dynamics analysis, previously applied to the pipe, to the torsionally driven cylinder. The aim is to compare mechanisms for breakdown in these two geometries to determine how conclusions drawn for pipe flow can be related to the more confined torsionally driven cylinder flow.

Chapter 6: Previous chapters will have highlighted the role of production of negative azimuthal vorticity (ω_ϕ) in the mechanism for breakdown. In this chapter we show that the placement of a small aerofoil to reduce the radial outflow, and hence inhibit the generation of negative azimuthal vorticity, can eliminate breakdown in the open pipe flow.

Chapter 7: Here we contrast the forms of breakdown which appear in the two geometries introduced in chapter 4 (the open pipe and torsionally driven cylinder), and offer an explanation for why the manifestations of breakdown appear so different in these two geometries. We also add to the discussion regarding the relevance of the cylinder flow to breakdown generally.

Chapter 8: The region in parameter space where hysteresis occurs in the open pipe is determined, and an attempt made to transfer the flow to its conjugate breakdown state within this region by applying upstream perturbations to the flow.

Chapter 9: In the reverse of the study in the previous chapter we attempt a transition from a flow with breakdown to one without, ie. suppression of breakdown by applying a perturbation upstream.

Chapter 10: The results obtained are summarised and discussed in terms of the contribution to vortex breakdown understanding and control. We also indicate potential future directions for research in this area.

Chapter 2

Current knowledge

2.1 Observations of vortex breakdown

Vortex breakdown appears to be a product of swirling flows in general, as it can be found in various geometries which produce a swirling flow. We begin this section by describing three situations in which vortex breakdown is commonly studied, i.e. over delta wings, in torsionally driven cylinders, and in open pipe flows.

In the following section, the prevailing theories which have been proposed to explain breakdown in swirling flows will be described. Here three concepts will be presented: the analogy to boundary layer separation; relevance of hydrodynamic stability; and the conjugate critical state.

In the final section of this chapter a summary of the methods which have been used to control breakdown in experiments will be presented.

2.1.1 Flows over delta wings

Delery [10] provides a precis of one of the first experimental studies of vortex breakdown, conducted by Werle. Werle's experiment involved a 65° sweep angle delta wing placed in a water tunnel with its chord at an angle of 20° to the flow. Werle observed that the nominally straight vortex tubes expanded at a certain chord-wise location to form thick spirals, eventually breaking down into turbulence.

After Werle's experiments, studies of breakdown continued to concentrate on the delta

wing, and the behaviour of breakdown as a function of wing sweep angle (ϕ) and angle of attack (AOA) was mapped out.

One study, by Wentz and Kohlman [75], mapped out the effect of sweep angle ϕ on vortex breakdown for the range $45^\circ < \phi < 85^\circ$, and found that increasing the sweep angle resulted in an increase in the angle of attack required for breakdown to occur. Beyond $\phi = 75^\circ$ the angle of attack at which breakdown occurred was independent of ϕ . Other studies have confirmed the influence of angle of attack and degree of sweep on the occurrence and location of vortex breakdown (Delery [10]), and as a result two general statements regarding the behaviour of vortex breakdown can be made:

- Breakdown location is largely determined by the angle of attack of the wing - for increasing angle of attack the breakdown moves closer to the leading edge of the wing.
- For sweep angle $\phi < 75^\circ$, a decrease in ϕ likewise results in motion of breakdown toward the leading edge of the wing.

2.1.2 Torsionally driven cylinder flows

The first observation of vortex breakdown of which this author is aware was reported by Wilcke in 1785 (in [49]), in a version of the torsionally driven cylinder. Wilcke's apparatus consisted of a fluid-filled closed cylinder with fixed walls, and a small piece of bent wire which was inserted through the centre of the top lid, and rotated. The rotating wire produced a circulating flow, by inducing an outward, rotating flow at the top of the cylinder. This resulted in a circulation which extended to the opposite end of the cylinder via the outside walls, and induced an axial return flow. The induced flow along the axis had the profile of a vortical core. For some wire rotation rate the flow along the axis could be made to stagnate, and a secondary recirculation region develop. The observed phenomenon has many of the hallmark properties of the vortex breakdown observed in other geometries.

The torsionally driven cylinder generally used in modern experiments similarly consists of a volume of fluid enclosed by a cylindrical container - see figure 2.1.

Here the entire floor of the cylinder is rotated. The flow produced is fundamentally

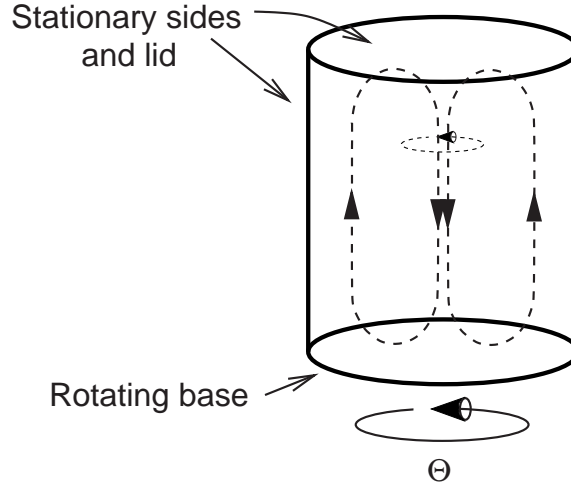


Figure 2.1: Torsionally driven cylinder geometry.

the same as that generated in Wilcke's apparatus. The occurrence of breakdown in a torsionally driven cylinder geometry, with a particular aspect (height to radius) ratio, is controlled by the Reynolds number, where the Reynolds number (Re) is defined:

$$Re = \frac{\rho v r}{\nu} = \frac{\rho \Theta r^2}{\nu}, \quad (2.1)$$

where ρ is the density of the fluid, $v = \Theta r$ is the speed of the rotating lid, r is the radius of the cylinder, Θ is the angular speed of the lid, and ν is the viscosity of the fluid.

In practice, the viscosity is kept constant, and Re is varied using Θ . This geometry has been commonly used to investigate breakdown, due to the large degree of control the experimenter has and the relative ease of construction of the rig.

An observation from an experiment using the torsionally driven cylinder, including part of the rig, is shown in figure 2.2 (from Graham *et al.* [24]).

This cylinder has an aspect ratio of 2.5, which is typical of other studies. There are two breakdown bubbles visible here, and they are both characterised by an abrupt expansion of the vortex core upstream, a region of recirculation in the centre, and a resumption of the original vortex at the rear. By increasing the aspect ratio more bubbles can be generated, and decreasing the aspect ratio results in less bubbles (Graham *et al.* [24]).

For some combinations of Re and aspect ratio, the bubbles begin to oscillate in the axial direction about their mean position, and above a certain Re for a particular aspect ratio

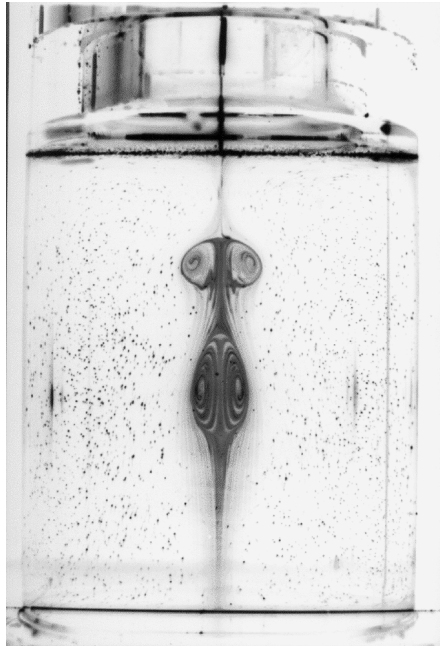


Figure 2.2: Experimental observation for aspect ratio 2.5, $Re = 2252$, from Graham *et al.* [24].

the flow appears to become unstable, with the bubbles moving away from the axis of the cylinder (Gelfgat [21]).

There are many interesting phenomena associated with vortex breakdown in this geometry, which are not necessarily reflected in more real-world flows. It is important to note that some of the characteristics of the other types of breakdown vary significantly from those of the axisymmetric bubble, and it has been suggested by some that the mechanism which produces the axisymmetric bubble is different to that which produces the spiral and other types (Leibovich [42]). We will address this question in Chapter 7, giving justification for use of the term vortex breakdown to describe this secondary recirculating flow generated in the cylinder.

2.1.3 Diverging pipe flows

The geometry which produces the widest range of breakdown forms is the diverging pipe. A typical apparatus is shown in figure 2.3 from Sarpkaya [57], and consists of a diverging cylindrical tube with a flow generator at one end. Swirl vanes at the upstream end of the pipe produce a rotating flow. The other end of the pipe is open or constructed so that the

fluid can recirculate back to the input end.

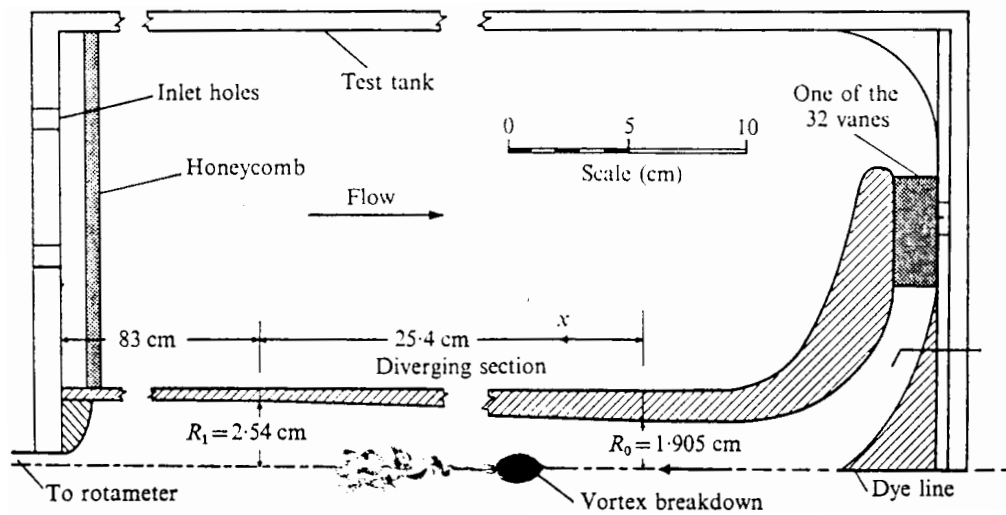


Figure 2.3: Sarpkaya's apparatus (from Sarpkaya [57]).

Every type of breakdown so far observed can be produced in a diverging pipe flow. The geometry of this system is more like the unbounded flow above a delta wing, and so may be more enlightening than the torsionally driven cylinder in efforts to determine the mechanism for breakdown in unbounded flows.

Sarpkaya's work has revealed that in general a particular combination of flow rate (Re) and swirl angle will produce a specific type of breakdown (there are some exceptions to this; they are mentioned later). Faler and Leibovich [17] conducted a comprehensive study of all the forms of low Re vortex breakdown so far observed in an apparatus similar to that of Sarpkaya [57]. They documented six distinct types of breakdown (3 of these 6 types are illustrated in figure 2.4).

1. Type 0: The axisymmetric bubble (figure 2.4(a)). This form was almost identical to the bubble observed in the torsionally driven cylinder, except that as the back of the bubble was not constrained by the proximity of a rotating lid, the flow downstream of the bubble was able to resolve in a number of different ways, depending on both Re and swirl;

- after the flow had resumed its original vortex profile, the bubble sometimes broke down into a second axisymmetric bubble, about one bubble length from

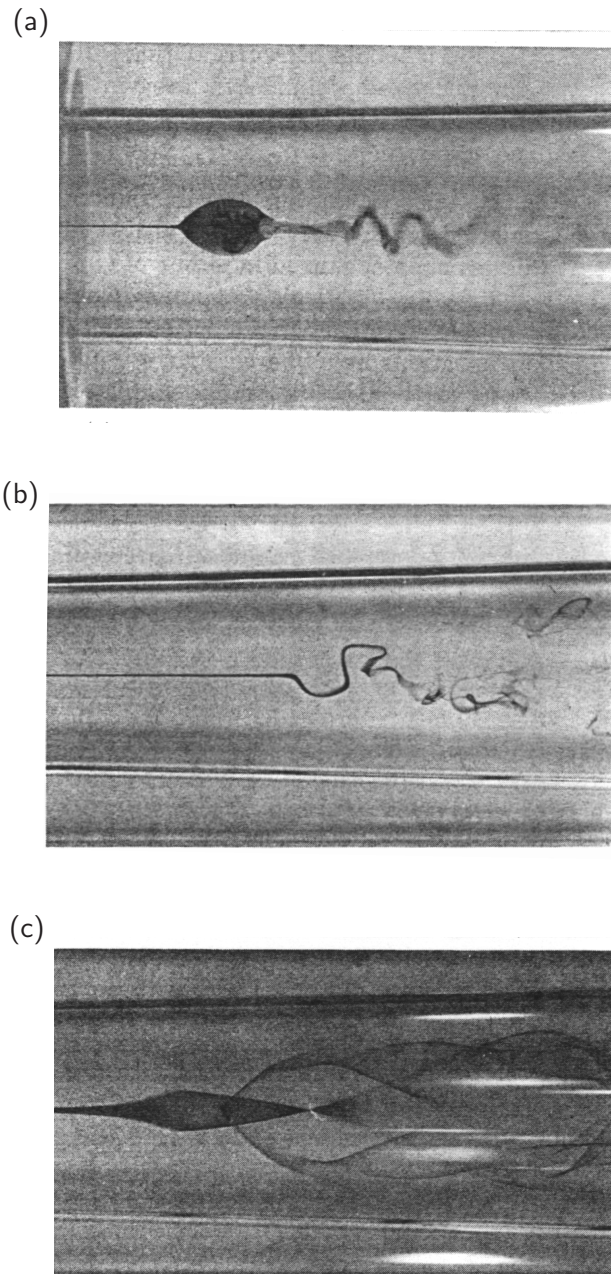


Figure 2.4: Three types of breakdown observed by Faler and Leibovich [17]. From top to bottom: the bubble, the spiral, and the double helix.

the tail of the first breakdown. The second breakdown bubble was often followed by turbulence, but sometimes the vortex structure reappeared, then broke down again;

- the flow momentarily re-assumed the original vortex structure, then progressed into the spiral type, which always degenerated into turbulence;

- the flow downstream of the bubble sometimes directly degenerated into turbulence.
2. Type 1: This form appeared to be very similar to the type 0 bubble, apart from a more open-ended structure - the recirculation zone behind the stagnation point was less well established and the region behind the bubble was dominated by turbulent flow. This mode would also occasionally change to type 0 and back again, as if a potential hill existed between the two modes which was occasionally crossed. It was possible, by introducing a perturbation to the flow, to precipitate the change from type 0 to type 1, but once the type 1 form was produced it was not possible to consistently retrieve the type 0 mode. These findings bring into question the validity of extrapolating conclusions about the torsionally driven cylinder version of breakdown for certain flow regimes to unbounded flows, as this type of behaviour is not observed in the torsionally driven cylinder.
 3. Type 2: The spiral mode (figure 2.4(b)). With this type the dye filament did not spread out, but rapidly decelerated in the axial direction and moved away from the original vortex axis. The filament then assumed a spiral form and after about 1 turn degenerated into turbulence.

It was noted by Faler and Leibovich that the turns of the spiral in their experiment in a tube were in the same sense as the general rotating flow, but in flows over delta wings at high angle of attack the turns of the spiral have been observed to be in the opposite sense to the general rotating flow.

Care must be taken when diagnosing this form of breakdown. Some results show the evolution of a small spiral in the torsionally driven cylinder. However, as asserted by Hourigan *et al.* [32], this observation is most likely due to dye injection which is slightly off-axis. A true spiral form of breakdown has not been definitively seen in the cylinder.

4. Type 5 (figure 2.4(c)). This double helix form was discovered by Sarpkaya [58]. It appeared to be a less abrupt type of breakdown, and some have questioned the use of the term vortex breakdown to describe it as no stagnation point is associated with the onset of this form.

The double helix resulted when the vortex filament sheared into two triangular tapes,

which then rotated about the central axis of the tube. Sarpkaya showed that perturbing this double helix could precipitate the spiral form, suggesting that the spiral form was the more stable flow state for that Re /swirl combination than the double helix, and giving an explanation for the absence of the double helix until that investigation.

5. Other forms of breakdown were observed by Faler and Leibovich, among them the flattened bubble and a combination of the flattened bubble and spiral. These different types appeared to blend into one another, making it difficult to discern at what point one form had changed into another.

2.1.4 The various breakdown types

This multiplicity of forms has resulted in a number of questions:

1. are they all breakdown? (how do we define breakdown?);
2. are they all products of the same mechanism?;
3. is breakdown fundamentally axisymmetric or asymmetric?

The most commonly observed breakdown types are the axisymmetric bubble and the spiral. Sarpkaya [57] catalogued the types of breakdown which occurred for a range of Reynolds numbers Re and swirls Ω in the open pipe. Here $\Omega = \frac{\Gamma}{U_0 D_0}$, where Γ is the freestream circulation, U_0 is the mean axial velocity at the pipe entrance, and D_0 is the diameter of the pipe. The results are represented in figure 2.5, where we plot the breakdown type as a function of Re and Ω .

At low Ω and low Re the spiral form tends to dominate. With increasing Re there is a crossover region, where both bubbles and spirals are possible, then for high Re only bubbles are observed. As Ω is increased the Re at which bubbles appear decreases. For low Re and relatively high Ω another type of breakdown was recorded; the double helix (type 6 from Faler and Leibovich [17]). This type is represented by blue dots in figure 2.5.

Escudier and Zehnder [16] were able to attain even lower Re than those implemented by Sarpkaya [57] and Faler and Leibovich [17]. They found in their apparatus that for $Re = 140$ a bubble-shaped disturbance appeared for high swirl ($\Omega = 11.6$). Downstream

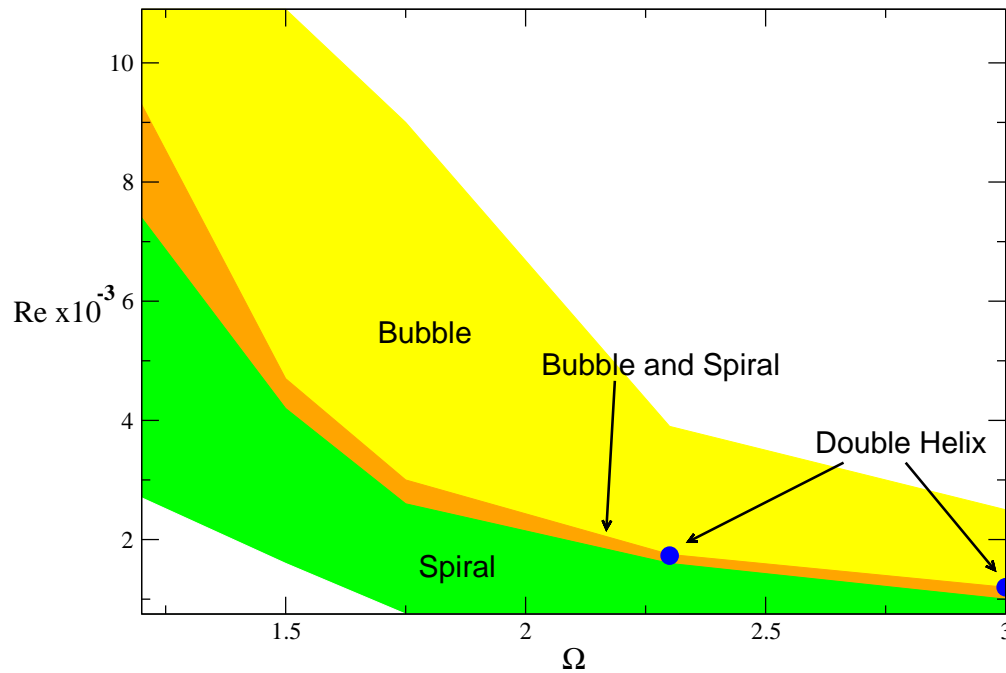


Figure 2.5: Breakdown type with Re and Ω , due to Sarpkaya [57].

of this bubble the flow resolved into a cylindrical, laminar wake, i.e. the vortex core reformed behind the bubble. This observation of an axisymmetric bubble at such a low Re has implications which we address in chapter 7; we argue that this bubble may be more comparable with that observed in the torsionally driven cylinder.

The breakdown type in Escudier and Zehnder's [16] experiments, as in Sarpkaya's [57] was not purely a function of Re and Ω . Occasionally multiple breakdown forms were observed for a single set of parameters, and it was impossible to predict which form would persist. At $\Omega = 2.03$ and $Re = 3800$ the flow alternated between the bubble and spiral forms spontaneously.

A question has arisen from these experiments: is vortex breakdown fundamentally axisymmetric or asymmetric, i.e. is the bubble or the spiral the basic form? Faler and Leibovich and Sarpkaya assert that breakdown is fundamentally asymmetric. Escudier [14] argues that breakdown is fundamentally symmetric; asymmetries are claimed to be the result of asymmetric disturbances inherent in practical swirling pipe flows. One situation which has a high degree of symmetry is the torsionally driven cylinder, and in this geometry only the axisymmetric form is observed. However there is some contention as to whether the

cylinder breakdown should be termed breakdown at all; Hall [30] refers to the phenomenon in the cylinder as an “internal separation” analogous to boundary layer separation. This view is shared by Goldshtik and Hussain [22].

The question of whether the phenomenon in the cylinder is vortex breakdown is of some importance, as much of the theory to explain vortex breakdown has arisen from torsionally driven cylinder studies (see for example Lopez [44] and Brown and Lopez [6]). Part of the problem lies in the definition of breakdown; there is no universally agreed-upon definition. Similarities in appearance and behaviour of a flow are used to determine the presence of breakdown. Faler and Leibovich claim the double helix form is a type of breakdown, but Escudier and Zehnder [16] refer to the double helix as a pre-breakdown state. The fact that the downstream end of the bubble is closed in cylinders compared to the open-ended nature of experimental pipe bubbles is another observation used to distinguish between the cylinder bubble and pipe bubble. But fundamentally are they the result of different generation mechanisms? This question will be addressed in chapters 5 and 7.

2.2 Theoretical aspects of vortex breakdown

A number of mechanisms have been proposed to explain vortex breakdown. Again the situation has been confused by the goal of finding a general theory to explain all forms of breakdown. Faler and Leibovich [17] have documented 6 different types of breakdown, some of which seem similar, but others, like the spiral and bubble forms, are very different in their appearance and defining features.

Most attention in computational studies has been paid to the axisymmetric bubble form (Salas and Kuruvila [56]) due to the ability to assume axisymmetry and hence greatly reduce the size of the problem. The result has been many studies into the form, occurrence, and behaviour of the bubble form.

The other types of breakdown, on the other hand, have scarcely been touched upon computationally. This is at odds with the observation that the dominant type of breakdown over delta wings is the spiral, and the initial motivation for studying vortex breakdown was to understand its occurrence over delta wings. However, the difficulty involved in computationally simulating the non-axisymmetric forms of breakdown, and the assumption that the mechanism underlying both forms of breakdown is the same, explains why

the asymmetric types have not been extensively investigated.

In the following sections the 3 most common theories so far proposed to explain vortex breakdown will be examined. These describe breakdown in terms of:

1. analogy to boundary layer separation;
2. the concept of conjugate critical states;
3. hydrodynamic instabilities.

2.2.1 Analogy to boundary layer separation

The difficulties intrinsic to solving the full Navier-Stokes equations for the swirling flows which produce breakdown led to assumptions which simplify the problem. An assumption which has been commonly used for these flows is the quasi-cylindrical or slender vortex approximation. In this approximation the variations in the vortex in the axial direction are assumed to be small in comparison to the variations in the radial direction.

Mager [48] found that in practice the quasi-cylindrical equations could not be solved at the point where vortex breakdown occurred. This was attributed to failure of the quasi-cylindrical approximation at the onset of breakdown due to the rapid changes along the vortex axis as the breakdown evolved.

This behaviour can be compared with the divergence of the solution which occurs at the onset of boundary layer separation. The flows after solution divergence are also somewhat similar for boundary layer separation and vortex breakdown, as they both involve some streamline divergence and a region of reversed flow.

The fact that the solution diverges at the onset of breakdown does not shed much light on what is occurring physically however. All it implies is that the quasi-cylindrical approximation becomes invalid as the vortex structure varies significantly with axial distance, which is to be expected. However, the quasi-cylindrical approximation can be used to determine the susceptibility of a flow to breakdown and to give an indication of where breakdown is expected.

2.2.2 Hydrodynamic instabilities

The sudden onset of vortex breakdown and its catastrophic effect on the vortex core led to the suspicion that breakdown was the result of an instability of the flow which preceded it. Hence some investigations concentrated on the stability of flows leading to breakdown. Comprehensive summaries and interpretations of the results of these investigations are given in Escudier [14] and Leibovich [42]. In the following section we discuss briefly the stability of the core flow and its relevance to breakdown.

Howard and Gupta [33] showed that an inviscid vortex is stable to infinitesimal axisymmetric disturbances if a Richardson number criterion is satisfied everywhere. This criterion states:

$$J(r) = r^{-3} \frac{d}{dr} \left(r^2 w^2 \right) \left(\frac{du}{dr} \right)^2 > \frac{1}{2}, \quad (2.2)$$

where u and w are the axial and azimuthal velocities respectively, and r is the radial coordinate. Garg and Leibovich [20] determined an equivalent criterion for their experimental pipe flow, which had a measured velocity profile upstream of breakdown that was well approximated by the equations:

$$u(r) = u_1 + u_2 \exp \left[\frac{-\alpha r^2}{r_t^2} \right] \quad (2.3)$$

$$w(r) = \frac{K r_t}{r} \left[1 - \exp \left(\frac{-\alpha r^2}{r_t^2} \right) \right], \quad (2.4)$$

where r_t is the pipe radius at the inlet, and α , K , u_1 , and u_2 are constants. The stability of the flow to infinitesimal axisymmetric disturbances is then guaranteed if $q > 0.402$, where q is defined:

$$q = \frac{K \sqrt{\alpha}}{|u_2|}. \quad (2.5)$$

Also, Lessen *et al.* [43] showed that this flow is also stable to asymmetric disturbances if $q > 1.5$. Garg and Leibovich [20] applied these criteria to the velocity profile upstream of breakdown in their experimental pipe study. The smallest value of q obtained for their experiments was 0.8, and hence all of the flows were stable to axisymmetric perturbations. This left the possibility of instability to asymmetric disturbances; however breakdown

was only observed for $q > 1.5$, where the core is stable to both types of disturbance; this indicates instability does not have a role to play in the mechanism for vortex breakdown. Vortical flows are generally more susceptible to asymmetric instability than axisymmetric instability, so the onset of an axisymmetric bubble rather than some asymmetric structure is another hint that breakdown is not the result of instability.

In the wake of breakdown q was observed to decrease to a value $q < 1.5$ in all those cases studied. Hence the wake flow suffered from asymmetric instability. This is consistent with the observation of a spiral mode downstream of the bubble in the open pipe; the spiral in this case may be due to instability of the wake flow to asymmetric disturbances.

To more accurately model breakdown as it occurs over a wing, Lessen *et al.* [43] examined the stability of a vortical flow superimposed on a shearing flow. Previously it had been shown (Lessen *et al.*) that axisymmetric disturbances had a purely stabilising effect on the vortex, so in this study only nonaxisymmetric disturbances were considered. It was found that the flow was stable for positive modes of the Fourier-type perturbation applied, but unstable for some swirl velocities and negative perturbation modes. Hence flow instability cannot yet be completely ruled out when it comes to vortex breakdown over a delta wing.

Gelfgat *et al.* [21] performed a numerical study of the steady state and oscillatory vortex breakdowns in a torsionally driven cylinder. It was found that the steady state breakdown was not the result of two-dimensional flow instability, but developed as a natural progression of the flow. The onset of oscillatory instability (where for higher Re the breakdown bubble oscillated up and down the cylinder axis) was not connected with the vortex breakdown, as the same oscillation of the flow at the axis occurred for conditions where the breakdown bubble was not present, and hence it probably plays no part in the onset of vortex breakdown.

2.2.3 Concept of conjugate critical states

Squire (in [14]) is credited with the first suggestion that the waveguide nature of vortical flows may have relevance to the onset of vortex breakdown. The importance of travelling waves in the mechanism for breakdown is indicated by the presence of breakdown at the transition from a core incapable of supporting upstream travelling finite amplitude waves to one capable of supporting such waves. The theory states that if a vortex can sustain

standing waves, then a disturbance can propagate upstream along the vortex core to a critical location, and initiate breakdown.

A problem with this theory was highlighted by Benjamin [3]. The group velocities of these waves would be directed downstream, hence energy could not be transferred upstream to initiate breakdown. Instead Benjamin [3] proposed a conjugate state theory. This is based on the existence of 2 conjugate solutions to the equations for inviscid cylindrical flow. One solution corresponds to a supercritical flow, which supports only downstream-travelling waves, and the other to a subcritical flow, which can support waves with group velocities pointing upstream. A simple criterion to determine the supercritical, critical, or subcritical nature of the vortex core is also provided by Benjamin [3]. Define C_+ as the absolute velocity at which waves travel with the flow (relative to a stationary observer), and C_- the absolute velocity at which waves travel against the flow. If the direction of the base flow specifies the positive direction, then C_+ must be positive and C_- may be positive or negative, depending on the flow speed. Benjamin defines a quantity N such that:

$$N = \frac{C_+ + C_-}{C_+ - C_-}. \quad (2.6)$$

If $N > 1$ the flow is supercritical (ie. waves cannot travel upstream), and if $N < 1$ the flow is subcritical (ie. certain waves can travel upstream).

Vortex breakdown, it is proposed, may be interpreted as a marker of the transition between the two flow states. This makes vortex breakdown analogous to the hydraulic jump in channel flows.

Escudier [14] has noted some deficiencies in the conjugate state model. The assumption that a flow force deficit in the supercritical flow could be compensated for by standing waves (for small deficits) or turbulence (for large deficits) does not hold up against experimental evidence, as large flow force change transitions in the case of vortex breakdown can be turbulence-free. It is also noted that while Benjamin's [3] theory implied breakdown should occur any time the flow is supercritical, in practice breakdown is not observed below a critical swirl ratio for supercritical flows.

Another theory, first described in 1973 by Randall and Leibovich [54], and refined in a subsequent paper by Leibovich [42], also makes use of the waveguide nature of vortex

cores. The theory suggests that waves may become trapped at the location of criticality, where amplification of the wave and its dissipation by viscosity are in equilibrium. In Leibovich [42] the loss of stability to three-dimensional perturbations is also suggested as a contributor to fixing the eventual steady location of breakdown.

Darmofal [9] claims however that three-dimensionality is not necessarily observed in these flows, and hence cannot be used as a mechanism to limit the growth of breakdown. Darmofal's analysis consisted of numerical simulations of the onset of the axisymmetric bubble form, and focused on the role of wave trapping in the production of negative azimuthal vorticity, a necessary condition for breakdown (see Lopez [44]). Darmofal's modified version of the theory proposed by Randall and Leibovich [54] describes a trapping and focusing of waves analogous to the formation of a shock wave. Breakdown is said to occur where the group velocity of long waves travelling on the vortical core becomes negative. Waves propagate at speed $u - a$, where u is the flow speed and a is the wave group velocity. Linear theory states that the amplitude of the wave varies as $(u - a)^{-\frac{1}{2}}$, and hence as the wave approaches the critical location, where $u = a$, the amplitude becomes (in the linear limit) infinite. In compressible flows this process results in a shock; in swirling flows it is proposed that vortex breakdown results. We consider in more detail the wave trapping model in Chapter 3.

2.3 Control of vortex breakdown over delta wings

Despite the uncertainty regarding mechanism, enough is known about the causes of breakdown for experiments into its control to be attempted. The observations that vortex breakdown occurrence and location is a strong function of angle of attack, and that sweep angle also plays an important part, leads to two obvious methods of control over wings, i.e. vary these two parameters until breakdown is either downstream of the wing or has disappeared altogether. However angle of attack is fundamental to the lift of the wing and applying limits on the angle of attack further restricts the performance envelope. The wing sweep determines to a large extent the flight characteristics of the wing, and is also not likely to be varied in practice solely to control breakdown, although at least one control experiment has utilised this method.

Profiling of the vortex core has determined that the onset of breakdown is a function of

the core swirl to axial velocity ratio, and the pressure gradient. Hence methods to control breakdown over wings have attempted to modify one or both of these parameters. We give a brief precis of breakdown control experiments for delta wings here, as some of the observations indicate characteristics of breakdown which we make use of in our analysis later.

The methods are grouped into four categories: changes to wing geometry; nett mass flow; leading edge suction; and trailing edge flow modification.

2.3.1 Changes to wing geometry

Gursul *et al.* [27] produced a system which controlled the location of breakdown above a delta wing, by varying the sweep angle in response to detection of the helical mode of breakdown. The helical mode was detected by sensing pressure fluctuations. Increasing sweep angle as breakdown occurred resulted in relocation of breakdown downstream of the wing.

Lowson and Riley [47] showed that wing thickness and details of the leading edge geometry have a significant effect on the location of breakdown. Large discrepancies in the breakdown location in previous studies were shown to be the result of these geometry variations, particularly at the apex of the delta. Given the large impact apex geometry had on the location of breakdown, the next stage in their investigation tested the prospect for controlling breakdown by installing a movable flap at the apex. Adjusting the incidence of this flap had a large effect on the chordwise location of breakdown, moving breakdown by distances of up to the chord length, depending on wing angle of attack.

An interesting observation appeared in the case for the 25% apex flap at a flap angle of $\sim 20^\circ$ for wing angle of attack = 20° . Typically a breakdown bubble forms upstream of either a transition to a helical mode or complete break up of the vortex core. However, at the conditions stated above the vortex re-formed downstream of the breakdown bubble. This behaviour had previously only been seen in closed flows such as the torsionally driven cylinder, so it is of note that the re-forming of the vortex has been observed in at least one unconfined flow.

In a study by Hebbar *et al.* [29] the geometry of the junction between wing sections of a double delta configuration was varied. The double delta is a planform utilised in

a number of modern fighter aircraft (F/A-18, F-16), and is comprised of a main delta shaped wing with a triangular leading edge extension. Hebbar *et al.* [29] modified the vortical flow generated by the wing by adding a fillet to the junction between the leading edge extension and the main wing. It was found that a diamond-shaped fillet resulted in a change in breakdown location, but the change was not as significant as the changes due to the larger-scale geometry modifications of previous studies, as expected.

A recent analysis by Srigrarom and Kurosaka [65], [66] proposed a new mechanism for breakdown, which led to an alteration to the delta wing leading edge in their experiments. The ‘self-induction theory’ states that the conditions for generation of breakdown include a straight vortex core and a spiralling shear layer, which they observe surrounding the core. It is proposed that breakdown may then be suppressed by imposing a wavy structure on the vortex core. This is done for a delta wing by constructing a wavy leading edge. The effect is to move breakdown further down the wing chord. Another experiment [66] involved placing small bulges on the top of a standard delta wing, near the leading edge. The effect again was to move breakdown further downstream.

Deng and Gursul [11] investigated the effect of varying the angle of a leading edge flap. The flap was attached to the entire delta wing leading edge, and the angle between the wing and the flap could be adjusted between 60° and 150° . The angle of attack of the wing and angle of the flap were found to have a large effect on the location of breakdown. This result is not surprising; Traub *et al.* [70] and Lowson and Riley [47] have documented the strong dependence of breakdown on the leading edge geometry. A subsequent study by Deng and Gursul [12] observed the effect of applying an oscillation to the leading edge flap. Hysteresis loops were identified, and it was shown that the oscillation of the flaps did not significantly alter the mean location of breakdown more than a static flap. Gangulee and Ng [19] examined the effect of a flap placed inboard of the leading edge; this flap was found to promote breakdown at high angles of attack.

2.3.2 Flow modification by nett mass flow

The swirl to axial velocity ratio is a major factor in the susceptibility of a vortex core to breakdown. This is reflected in the various propositions for breakdown criteria, which are usually based on this ratio, or the equivalent circulation/axial velocity ratio (eg. Robinson

et al.'s [55] Rossby number criterion, $Ro = \frac{U}{r\Omega} < 0.9$.) Consequently, some attempts to control breakdown over delta wings have concentrated on modifying directly the swirl to axial velocity ratio.

One attempt at control of this ratio by blowing was conducted by Schmücker and Gersten [59]. They mounted a half delta wing on a rotatable turntable in the wall of a water tunnel, so that the wing was joined to the turntable at the wing root. Just above the wing, and between $\frac{x}{c} \sim 0.25$ and $\frac{x}{c} \sim 0.50$ (c is the chord length, and x the distance from the leading edge), six jets were positioned, at angles which produced a flow parallel to the wing leading edge. The aim was to use these jets to increase the axial velocity, reducing the swirl ratio, and hence delay the stagnation associated with breakdown. This was accomplished, as breakdown was moved downstream by activation of the jets. Modification of the vortex core was also attempted by Mitchell *et al.* [51] as part of an ongoing study into the effect of direct injection of axial flow into the vortical structure. A nozzle was positioned on the suction side of the wing, and oriented so that the flow coming from it was parallel to the wing leading edge and in the downstream direction. This arrangement also resulted in displacement of the vortex breakdown, in this case by 20% of the root chord. In addition, asymmetric blowing resulted in the breakdown on the side undergoing blowing moving further down the wing, while the breakdown on the other side tended to move upstream past the location it would occupy without blowing on either side. The disadvantage of this form of flow modification is that a device needs to be placed near the core upstream of breakdown, and will by its presence possibly also result in some unwanted modification of the flow.

Methods which aim to increase the lift by enhancing the roll-up of vortices above the delta wing tend to promote breakdown, as the axial velocity is not similarly increased. An attempt to stabilise the vortex with respect to vortex breakdown using swirl enhancement was conducted by Johari *et al.* [37]. Johari *et al.* examined the effect on vortex breakdown of a flow injection inboard of the leading edge, at an angle equal to that of the leading edge bevel. The advantage of this arrangement is that direct injection of fluid into the vortex is possible without placing a blowing port in the upstream flow, as was done in Mitchell *et al.* [51]. Blowing ports were arranged in a line on each side of the wing at three chordwise locations.

The aim of Johari *et al.*'s study was to increase the stability of the vortex to perturbations

by making use of the Rayleigh criterion, which states that the vortex will be stable if the circulation increases monotonically with radial distance from the vortex centre. But this assumes that breakdown is a result of instability; breakdown can occur in stable flows, and hence the relationship between the stability of the core and breakdown is not so well defined. Instead, by increasing the circulation upstream of breakdown this flow injection method should actually promote the onset of breakdown, and this is what is observed in the experiment; Johari *et al.* acknowledge this, but note that the observation that fluid injection downstream of breakdown moves the breakdown location further downstream cannot be explained on this basis.

Johari and Moreira [36], in an extension of the study described above, tested the effect of pulsed blowing on breakdown location. Pulsed blowing was found to be more effective at displacing breakdown than steady blowing when applied downstream of the breakdown location. Pulsed blowing proved to be effective in both steady and ramped pitching conditions. The nett mass flow for effective pulsed blowing was half that used for steady blowing; Johari and Moreira [36] suggest further work could concentrate on finding the optimum blowing frequency for breakdown control.

2.3.3 Leading edge suction

Suction applied at the leading edge has been used to reduce the circulation of the vortex core resulting from roll-up of the leading edge shear layer, thus reducing the swirl ratio and delaying breakdown. The effect of suction applied at the leading edge was studied by Wood *et al.* [76]. Their delta wing had a rounded leading edge so that suction tangential to the boundary layer could be applied. The effect was to delay the onset of breakdown at higher angles of attack.

Gu *et al.* [26] utilised a similar arrangement for their half-delta mounted in a water channel. Both blowing and suction were applied at the (rounded) leading edge, and it was found that steady blowing, steady suction, and alternating blowing and suction were capable of displacing breakdown to a steady location further downstream. The greatest effect on breakdown occurred just after initiation of the blowing or suction, after which the breakdown moved back upstream, though not to its original location. Alternating blowing and suction with time resulted in the greatest downstream displacement of breakdown.

McCormick and Gursul [50] suggest there is a reliance in these studies on the Coanda effect, via the rounded leading edge. In their study a slit was installed along the sharp leading edge of a delta wing, through which some of the external fluid could be drawn. The result was a decrease in the maximum swirl angle with increasing suction coefficient, and movement of breakdown downstream. McCormick and Gursul [50] tested the effect of moving the suction port slightly inboard, and found that this led to an increase in swirl angle, and movement of breakdown upstream. A subsequent study (Badran *et al.* [2]) investigated the effect of moving the suction port further inboard. Less effective control of breakdown was again observed, for the same suction coefficient, although the promotion of breakdown by inboard suction was not seen in this later study.

2.3.4 Trailing edge flow modifiers

The trailing edge of the delta wing has also been used as a platform for breakdown control experiments. Shih and Ding [60] added vectored trailing edge jets to their delta wing model in a water tank towing apparatus. They showed that blowing fluid through these nozzles after the onset of breakdown would displace breakdown downstream, in both static and dynamic pitching conditions. It was possible to independently vary the angle of the nozzles on each side of the wing; this resulted in an asymmetry in breakdown location, suggesting the possibility of using such an arrangement to apply roll moments. This method of breakdown control relies on a reduction in the adverse pressure gradient over the wing, rather than the more direct modifications of the vortex core described previously.

The best control of breakdown may lie in the implementation of more than one type of control device. Vorobieff and Rockwell [74] implemented both trailing edge blowing and deflection of a leading edge flap on a pitching delta wing model. They found that trailing edge blowing was the more efficient of the methods, and similarly to Johari and Moreira [36], intermittent blowing seemed to give the most efficient breakdown control. Also, the flow rate through the blowing orifices was much lower than that used by Shih and Ding [60].

2.4 Discussion

The search for a cause of breakdown is complicated by the fact that the phenomenon has so many different forms, and is manifest in a number of different situations or geometries. Instability has been ruled out as a cause for the axisymmetric form of breakdown (ie. the bubble), but may play a role in the onset of the three-dimensional forms (ie. the spiral and double helix).

While efforts continue into the search for a mechanism, the knowledge already gained has been put toward finding methods for controlling breakdown. Some control has been demonstrated for various types of flow modifiers, which either work on the swirl/axial velocity ratio in the core, or the adverse pressure gradient. Further research into various combinations of these breakdown control methods may lead to ways of controlling breakdown without adversely affecting other characteristics of the wing.

We return to the issue of breakdown control in chapters 6, 8, and 9. In the next section we concentrate on the analysis of vortex breakdown in terms of vorticity dynamics.

Chapter 3

Vorticity dynamics

3.1 The vorticity dynamics approach

Vorticity is simply the curl of the velocity; it is represented in Cartesian coordinate form in equation 3.1:

$$\boldsymbol{\omega} = \nabla \times \mathbf{u} = \mathbf{i} \left(\frac{\partial w}{\partial y} - \frac{\partial v}{\partial z} \right) - \mathbf{j} \left(\frac{\partial w}{\partial x} - \frac{\partial u}{\partial z} \right) + \mathbf{k} \left(\frac{\partial v}{\partial x} - \frac{\partial u}{\partial y} \right), \quad (3.1)$$

where $\mathbf{u} = (u, v, w)$ is the velocity, $\boldsymbol{\omega} = (\omega_x, \omega_y, \omega_z)$ the vorticity, and $(\mathbf{i}, \mathbf{j}, \mathbf{k})$ unit vectors in the (x, y, z) directions respectively.

Although the vorticity is described by three components of a vector equation, (one expression each for \mathbf{i} , \mathbf{j} , and \mathbf{k}), the three components of vorticity are not independent. This becomes evident after taking the divergence:

$$\nabla \cdot \boldsymbol{\omega} = \frac{\partial \omega_x}{\partial x} + \frac{\partial \omega_y}{\partial y} + \frac{\partial \omega_z}{\partial z} = 0. \quad (3.2)$$

Hence, once two components of vorticity are known, the third may be determined by integrating and applying the boundary conditions. The equivalent relation for the velocity components gives the continuity equation. Later, analysis of the Helmholtz vorticity equation, which governs the dynamics of vorticity in an incompressible homogeneous fluid, will show the well known result that there is no mechanism for the generation of total vorticity in the body of such a fluid, so any change in one component of vorticity must be reflected in a change in one or both of the other components.

Since the geometries considered later have cylindrical symmetry, it is more useful to define the vorticity in a cylindrical polar coordinate system (r, ϕ, x) , and the result of the conversion is shown in equation 3.3:

$$\boldsymbol{\omega} = \mathbf{e}_r \left(\frac{1}{r} \frac{\partial u}{\partial \phi} - \frac{\partial w}{\partial x} \right) - \mathbf{e}_\phi \left(\frac{\partial u}{\partial r} - \frac{\partial v}{\partial x} \right) + \mathbf{e}_x \frac{1}{r} \left(\frac{\partial (rw)}{\partial r} - \frac{\partial v}{\partial \phi} \right). \quad (3.3)$$

Some understanding of the mechanism for breakdown has been gained from a vorticity dynamics approach. The importance of the generation of azimuthal vorticity (the second term on the right in equation 3.3) as a necessary condition for breakdown was recognised by Brown and Lopez [6]. They proposed that breakdown evolves in two stages: the initial generation of azimuthal vorticity, and the amplification of this azimuthal vorticity to the point where breakdown occurs. The second stage was suggested to be the same for the pipe and cylinder, but the process which leads to initial generation of azimuthal vorticity could differ between geometries.

Brown and Lopez suggest that in order for the cylinder flow to transition to breakdown there must be some initial streamline divergence. This divergence will only occur in the event that at some axial location there is an imbalance in the centrifugal force/radial pressure gradient equilibrium. In the torsionally driven cylinder, the turning of the flow at the stationary end of the cylinder into the vortical core flow can result in an overshoot, so that in the vortical core there is some dominance of the centrifugal force over the radial pressure gradient. This results in waviness in the vortical core, and some initial generation of negative azimuthal vorticity.

Brown and Lopez [6] attribute the initial generation of negative azimuthal vorticity in a pipe with swirling inflow to the stretching and tilting of axial vorticity as a result of viscous diffusion. After the initial generation of negative azimuthal vorticity a feedback loop begins, as the streamline divergence caused by the increasingly negative azimuthal vorticity increases turning of the axial and radial vorticity. This feedback mechanism was found to be common to both the pipe and cylinder flows.

We next examine in more detail the process by which negative azimuthal vorticity is generated, since the mechanism described above appears to be fundamental to the onset of vortex breakdown in the geometries we consider. The concept of wave trapping and its relevance to breakdown will also be discussed. In a following chapter (chapter 5) the relationship between these processes and the onset of breakdown in the torsionally driven

cylinder is examined.

3.2 The vorticity equation

The Helmholtz vorticity equation describes the dynamics of vorticity in an incompressible homogeneous fluid, and is shown in equation 3.4 in vector form:

$$\frac{\partial \boldsymbol{\omega}}{\partial t} + (\mathbf{u} \cdot \nabla) \boldsymbol{\omega} = (\boldsymbol{\omega} \cdot \nabla) \mathbf{u} + \nu \nabla^2 \boldsymbol{\omega}. \quad (3.4)$$

\mathbf{u} and $\boldsymbol{\omega}$ represent the velocity and vorticity respectively, where $\boldsymbol{\omega} = \nabla \times \mathbf{u}$. The expression $(\boldsymbol{\omega} \cdot \nabla) \mathbf{u}$ on the right hand side represents the change in vorticity due to vortex filament stretching and turning, and $\nu \nabla^2 \boldsymbol{\omega}$ represents the contribution from diffusion.

The properties of this equation, and vorticity dynamics in general, are described in Morton [52], Wu *et al.* [77], and Green [25]. The equation contains no generation term, hence vorticity cannot spontaneously arise if there is no vorticity initially present (in the body of the fluid). However it is possible to exchange vorticity between components through turning, and to amplify existing vorticity through stretching. Alternatively, vorticity may only be introduced to a flow at the boundary, from where it can then be diffused into the body of the flow. There are two ways in which vorticity may be generated at solid boundaries: wall acceleration, and the presence of a pressure gradient along the wall. The second mechanism is relevant to the generation of azimuthal vorticity at the walls of the torsionally driven cylinder, which we consider later.

3.3 Vorticity generation in an axisymmetric geometry

Both the geometries we consider (the pipe and cylinder) have circular symmetry, so it is advantageous to rewrite the vorticity equation in cylindrical polar coordinates. This transformation results in equations for the three components: axial (equation 3.5), radial (equation 3.6), and azimuthal (equation 3.7):

$$\frac{\partial \omega_x}{\partial t} + \mathbf{u} \cdot \nabla \omega_x = \boldsymbol{\omega} \cdot \nabla u_x + \nu \nabla^2 \omega_x, \quad (3.5)$$

$$\frac{\partial \omega_r}{\partial t} + \mathbf{u} \cdot \nabla \omega_r - \frac{u_\phi \omega_\phi}{r} = \boldsymbol{\omega} \cdot \nabla u_r - \frac{\omega_\phi u_\phi}{r} + \nu \left(\nabla^2 \omega_r - \frac{\omega_r}{r^2} - \frac{2}{r^2} \frac{\partial \omega_\phi}{\partial \phi} \right), \quad (3.6)$$

$$\frac{\partial \omega_\phi}{\partial t} + \mathbf{u} \cdot \nabla \omega_\phi + \frac{u_\phi \omega_r}{r} = \boldsymbol{\omega} \cdot \nabla u_\phi + \frac{\omega_\phi u_r}{r} + \nu \left(\nabla^2 \omega_\phi + \frac{2}{r^2} \frac{\partial \omega_r}{\partial \phi} - \frac{\omega_\phi}{r^2} \right). \quad (3.7)$$

These equations describe the generation and transport of each component of vorticity. Concentrating on the azimuthal vorticity component (eqn. 3.7), each term represents a specific physical mechanism, as was mentioned earlier for the vorticity equation in general. If we disregard the viscous term for the moment, assume axisymmetry, and expand the other terms on the right hand side of equation 3.7, equation 3.8 is obtained:

$$\frac{D\omega_\phi}{Dt} = \omega_r \frac{\partial u_\phi}{\partial r} + \omega_x \frac{\partial u_\phi}{\partial x} - \frac{u_\phi \omega_r}{r} + \frac{u_r \omega_\phi}{r}. \quad (3.8)$$

Darmofal [7] described this equation. The four terms on the right hand side correspond to two mechanisms. The first three terms describe the local generation of azimuthal vorticity by vortex filament turning (or tilting), and the fourth term describes the amplification of azimuthal vorticity by stretching.

3.4 Stretching

Kelvin's Theorem states that, neglecting viscous effects, the total circulation around a vortex tube must be constant at any given instant in time, where the circulation Γ is defined in equation 3.9; dS is an element of a cross-sectional surface element through a vortex tube S , and \mathbf{n} is the unit normal to S :

$$\Gamma = \int_S \boldsymbol{\omega} \cdot \mathbf{n} \, dS. \quad (3.9)$$

The circulation around a vortex tube is constant, so decreasing its radius must result in an increase in $\boldsymbol{\omega}$. Hence if a vortex tube is stretched in the axial direction, ie. its circumference decreased, the vorticity must increase to keep the circulation constant. In the case of a pipe with a constricting section, the radius of the axial vortex tube decreases, and so to conserve circulation the axial vorticity increases.

In the same fashion, the azimuthal vorticity increases in magnitude when moving through an expansion. Consider the pipe half-section shown in figure 3.1.

Here the flow is from left to right. A streamwise divergence results in stretching of the vortex tube, which forms a torus around the pipe axis in the azimuthal direction (orientation out of the page). In order to conserve total circulation, Kelvin's Theorem implies

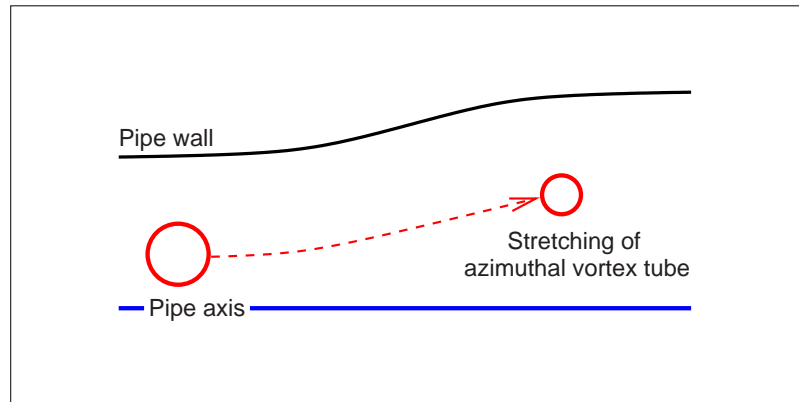


Figure 3.1: Generation of azimuthal vorticity by stretching, due to streamwise divergence.

that the azimuthal vorticity must increase. So as long as the radial velocity is positive, the azimuthal vorticity torus increases in radius, the vortex tube becomes stretched, and the azimuthal vorticity increases.

As noted by Darmofal [8], this process can only begin once some azimuthal vorticity is already present; another mechanism is needed to generate the initial azimuthal vorticity. This process is tilting.

3.5 Tilting

Vortex tilting is the method by which vorticity can be transferred between axial, azimuthal, and radial forms in three-dimensional (or axisymmetric) flows. So although the total vorticity present in the flow is constant, vorticity of a particular orientation can be generated at the expense of another component.

In an axisymmetric geometry two processes can result in the generation of azimuthal vorticity through tilting:

- tilting of axial vorticity by an azimuthal velocity gradient in the axial direction (the second term on the right in equation 3.8);
- tilting of radial vorticity by an azimuthal velocity gradient in the radial direction (the first term on the right in equation 3.8).

The first case is illustrated in figure 3.2.

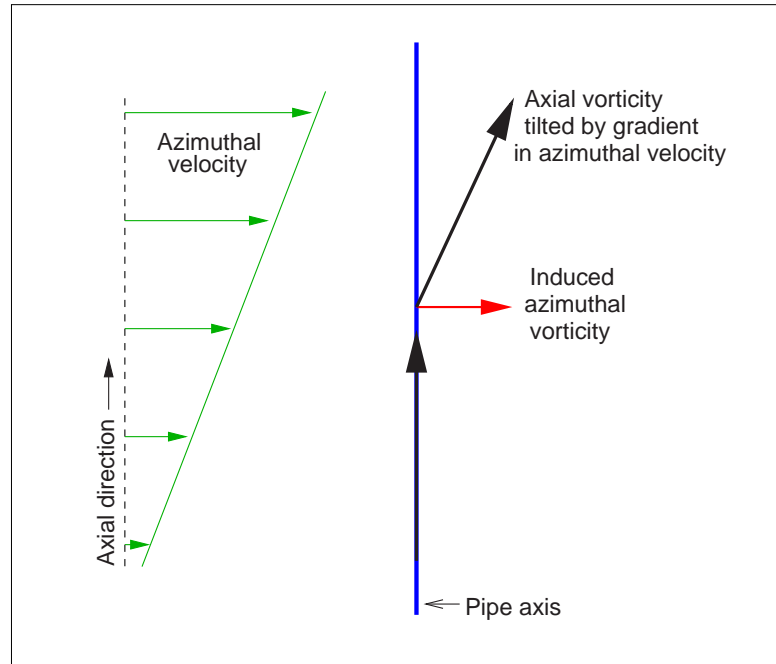


Figure 3.2: Generation of azimuthal vorticity by tilting of axial vorticity, due to a gradient in the axial direction of the azimuthal velocity.

In figure 3.2 the axial vorticity vector is initially oriented parallel to the pipe axis. As this vector is translated in the axial direction a change in the azimuthal velocity results in tilting of the vector. This tilting introduces a component of vorticity in the azimuthal direction (represented by a red arrow).

By a similar process tilting of the radial vorticity vector contributes to the generation of azimuthal vorticity - see figure 3.3.

Here the pipe axis is oriented into the page. A change in the azimuthal velocity with increasing radial distance tilts the radial vorticity vector, again into the azimuthal direction.

Hence in this simple system there are two means of generating azimuthal vorticity where the original flow contained none. Both of these methods require an azimuthal velocity gradient. For turning of radial vorticity, a gradient in the radial direction is required. For turning of axial vorticity, a gradient in the axial direction is required.

Once turning of one or both of the axial and radial components has resulted in the generation of some azimuthal vorticity, the stretching mechanism described earlier can take over if there is some radial outflow.

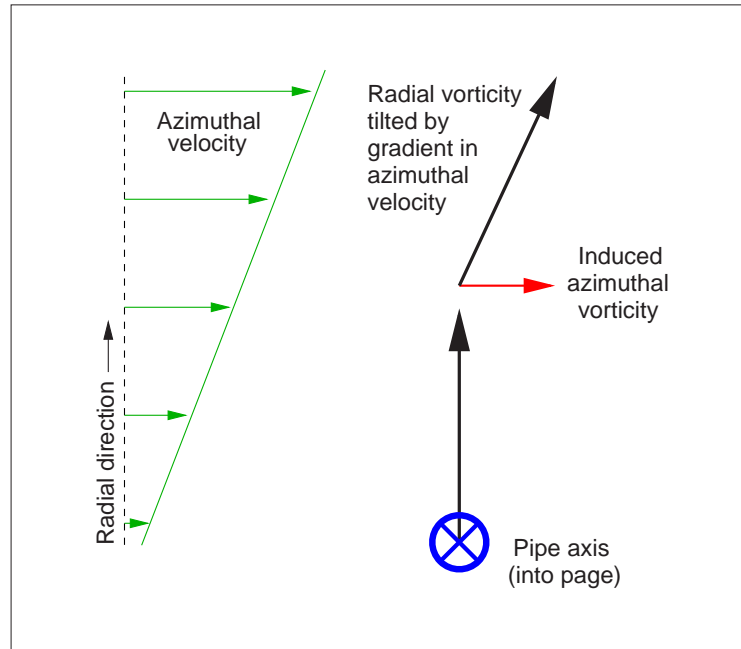


Figure 3.3: Generation of azimuthal vorticity by tilting of radial vorticity, due to a gradient in the radial direction of the azimuthal velocity.

3.6 Diffusion

As mentioned earlier, Brown and Lopez [6] suggested a role for diffusion in the initial production of azimuthal vorticity in the open pipe geometry. However, the observation of vortex breakdown in simulations which assume inviscid flow show that diffusion does not play an important part in the mechanism for breakdown. The mechanism of tilting described above also removes the need for another means of introducing initial azimuthal vorticity into the flow. An exception may be the torsionally driven cylinder, where the Reynolds number is very low compared to that in the pipe and over delta wings (see chapter 7).

3.7 Feedback mechanism

Once negative azimuthal vorticity has been generated, if the radial velocity near the axis is greater than zero, a feedback mechanism which relies on the stretching term in the equation for the azimuthal vorticity above can fuel the further growth of negative azimuthal vorticity. Darmofal [8] described this process, and it is summarised below:

1. $u_r > 0$ and $\omega_\phi < 0$ results in $\frac{u_r \omega_\phi}{r} < 0$ (the stretching term in equation 3.8), and hence $\frac{D\omega_\phi}{Dt} < 0$ (in the absence of turning);
2. Increasingly negative ω_ϕ results in a reduction in the axial flow, ie. u_x decreases near the axis;
3. Continuity dictates that fluid must then acquire some radial component, so u_r increases;
4. $\frac{u_r \omega_\phi}{r}$ decreases until breakdown evolves.

Hence some understanding of breakdown evolution can be understood from a vorticity dynamics standpoint. However, the presence of breakdown at the transition from a supercritical to a subcritical flow state suggests a role for wave trapping in the mechanism for breakdown, at least in the initial stages. In the next section the theory of the critical state and its relation to breakdown onset will be discussed.

3.8 Critical state and wave trapping

Vortical flows have the property that they can support travelling waves. There can arise however a point at which the vortex will be incapable of supporting upstream travelling waves. A region of the core in which both upstream and downstream travelling waves are permitted is termed ‘subcritical’, and where waves can only propagate downstream ‘supercritical’. Hall [30] describes a method first suggested by Benjamin [3] for determining the critical point which marks the transition between these two states.

First the equations of motion in a steady axisymmetric swirling flow are presented in a streamfunction formulation, as in equation 3.10:

$$\frac{\partial^2 \psi}{\partial r^2} - \frac{1}{r} \frac{\partial \psi}{\partial r} + \frac{\partial^2 \psi}{\partial x^2} = -k \frac{dk}{d\psi} + \frac{r^2}{\rho} \frac{dh}{d\psi}. \quad (3.10)$$

where $k = rw$ is the circulation, and h is the total pressure. Here the cylindrical polar coordinate system is used, with axial (x), radial (r) and azimuthal (ϕ) coordinates with corresponding velocities (u, v, w).

If an axisymmetric perturbation $F(r, x)e^{\gamma x}$ is applied to a base quasi-cylindrical solution, $\Psi(r, x)$, then an expression for the streamfunction can be obtained:

$$\psi(r, x) = \Psi(r, x) + \epsilon F(r, x) e^{\gamma x} \quad (3.11)$$

where $\epsilon \ll 1$ for a small perturbation. An equation for the function F can be obtained by substituting 3.11 into equation 3.10 and disregarding higher order terms:

$$\frac{\partial^2 F}{\partial r^2} - \frac{1}{r} \frac{\partial F}{\partial r} + \left[\gamma^2 - \frac{1}{u} \frac{\partial^2 u}{\partial r^2} + \frac{1}{ru} \frac{\partial u}{\partial r} + \frac{1}{r^3 u^2} \frac{\partial k^2}{\partial r} \right] F = 0 \quad (3.12)$$

where u is the axial component of velocity. If we confine the flow to a pipe of radius R , then the boundary conditions are $F(r=0) = F(r=R) = 0$. This is now a Sturm-Liouville equation, which can be solved for the eigenvalues γ^2 .

Now, if there is at least one eigenvalue $\gamma^2 < 0$, then the flow can support an infinitesimal standing wave, and is subcritical. If all $\gamma^2 > 0$, then only solutions with exponentials exist and the flow is supercritical. Hence $\gamma^2 = 0$ represents the transition between supercritical and subcritical states. If the axial velocity and circulation profiles are known for a particular axial location, it is then possible to determine whether a flow is subcritical or supercritical at that point by setting γ^2 to zero, then solving equation 3.12 for F . If F has negative values in the range $(0 < r < R)$ the flow is subcritical. If F is zero only at $r=0$ and $r=R$ then the flow is at that point exactly critical, and if $F > 0$ for all r then the flow is supercritical.

Darmofal [8] makes use of an alternative implementation of equation 3.12, with $\gamma^2 = 0$, as provided by Benjamin [3]:

$$\frac{d^2 F}{dy^2} = \left[H''(\Psi) - \frac{1}{2y} I''(\Psi) \right] F, \quad (3.13)$$

where $y = \frac{1}{2}r^2$, $I = \frac{1}{2}k^2$, H is the total pressure, and Ψ is the base quasi-cylindrical solution.

Benjamin [3] showed that as the coefficient of F in equation 3.13 becomes more negative, an initially supercritical flow tends toward criticality, due to an increase in the oscillatory nature of the solution F . Darmofal used this result to show that streamline divergence results in an increase in the coefficient by considering the H'' and I'' profiles with respect

to Ψ in a q-vortex, which has a profile characteristic of that observed in flows which contain breakdown in experiments (the q-vortex will be described in further chapters, as it will be used to define the inlet velocity profile for the pipes to be implemented later.)

The profiles of H'' and I'' are presented in figures 3.4 and 3.5.

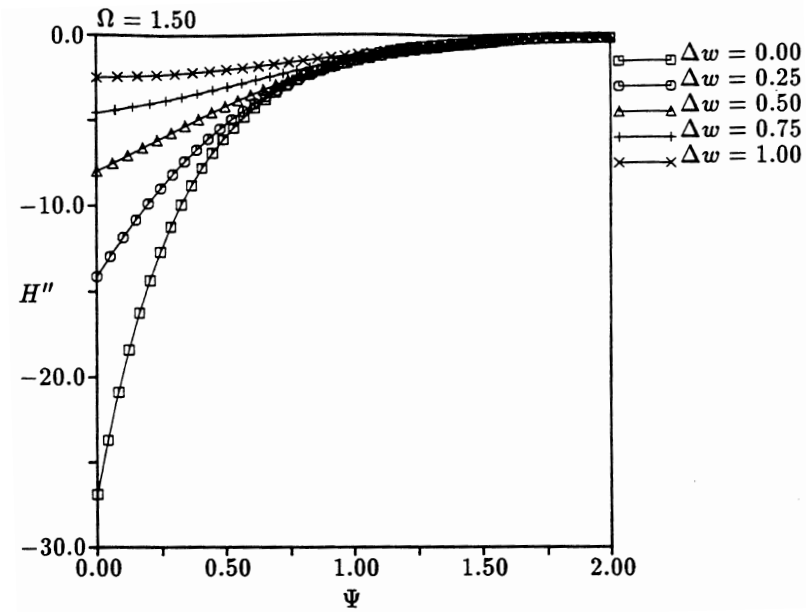


Figure 3.4: H'' vs Ψ from Darmofal [8].

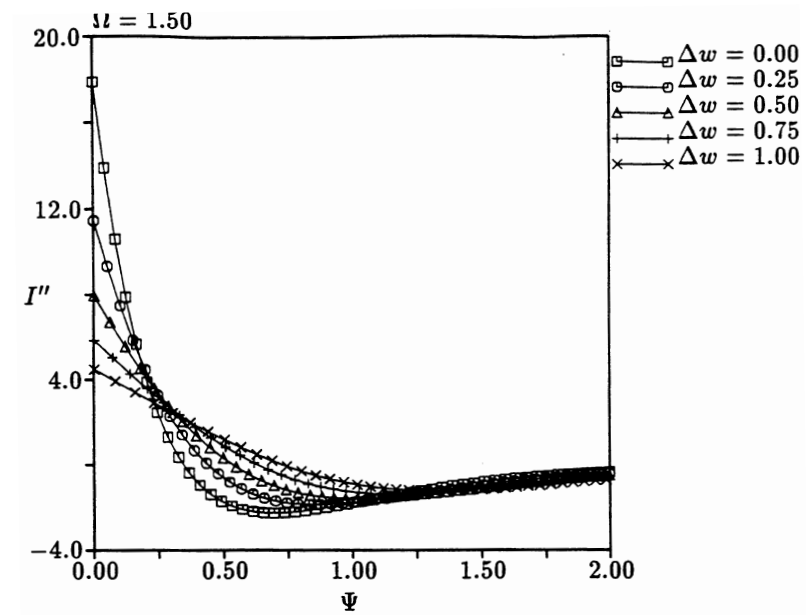


Figure 3.5: I'' vs Ψ from Darmofal [8].

Δw is the Δu defined in equation 4.16 for the axial velocity profile (in chapter 4). From figure 3.4 it can be seen that an increase in $-H''$ follows decreasing Ψ . Also, in figure 3.5, decreasing Ψ from a certain value Ψ_{max} results in increasing I'' . On the other side of Ψ_{max} the opposite trend is observed.

In a diverging flow Ψ decreases with increasing x at a particular radial distance r , due to divergence of the streamlines. Hence streamline divergence increases the magnitude of the coefficient of F in equation 3.13, and moves the flow toward criticality. Streamline divergence arises in pipe flows due to changes in the pipe radius, and in less confined geometries streamline divergence results from an adverse pressure gradient.

Once a region appears where the flow becomes subcritical downstream of a critical point, the potential for wave trapping is realised, as upstream travelling waves cannot move upstream past this point.

The formation of a shock in compressible flows is often used as an analogy to describe wave trapping in general, so it is useful to include a short discussion of shock formation here.

Consider a compressible fluid flow in an expanding nozzle, with speed u . Acoustic waves generated at some point in the flow will propagate both upstream and downstream, initially with speed say u' , relative to the flow. The wave travelling upstream will slow down as it progresses upstream. Wave fronts downstream of this wave will begin to catch up. At the sonic point, where the flow speed equals that of the acoustic waves (ie. $u =$ the speed of sound), the waves cannot progress any further upstream, and successive wave fronts pile up at the location where $u - u' = 0$. In the linear limit the wave amplitude tends to infinity. In reality a shock forms at the transition point, with supersonic flow upstream and subsonic flow downstream; the analogy with swirling flow is a supercritical flow upstream, and a subcritical flow downstream of the critical point.

Wave trapping and amplifying was visualised by Darmofal and Murman [9] in their numerical study of an open pipe flow, by plotting the perturbation azimuthal vorticity, $\delta\omega_\phi$ ($\tilde{\eta}_{2,k}$ in their study), near the pipe centreline. $\delta\omega_\phi$ is defined in equation 3.14

$$\delta\omega_\phi = \omega_\phi - \omega_\phi(i) \tag{3.14}$$

where ω_ϕ is the azimuthal vorticity at a particular time, and $\omega_\phi(i)$ is the initial azimuthal

vorticity. $\delta\omega_\phi$ along a line near the centreline was plotted with time, after an increase in Ω from an initial condition without breakdown to one where breakdown just evolves. The result of this simulation is shown in figure 3.6.

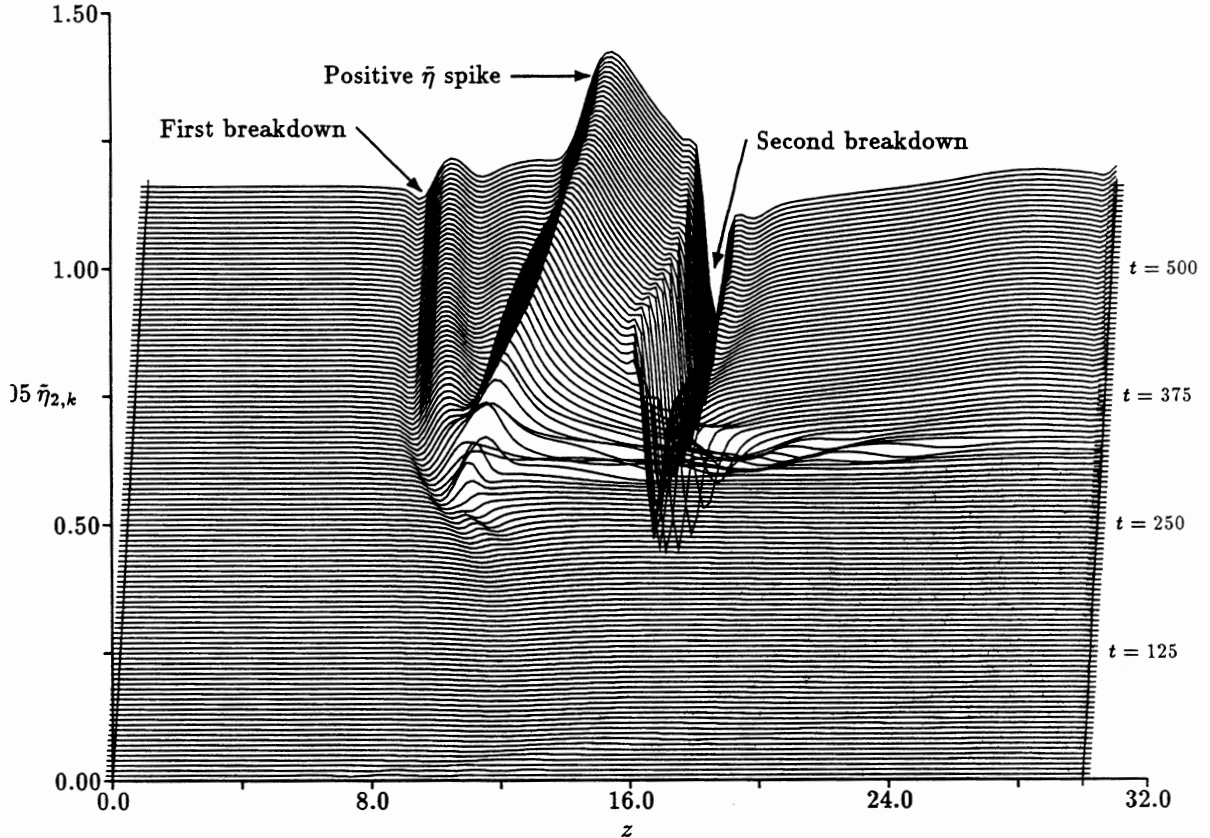


Figure 3.6: Perturbation azimuthal vorticity with time, from Darmofal [8].

The initial change in $\delta\omega_\phi$ is difficult to see in this plot; it begins to propagate downstream from the inlet at $t=0$. Some of the modes convect to the outlet, but some become trapped just downstream of the constricted section. These modes gradually grow in size as azimuthal vorticity is continually fed into the region from upstream, until two breakdown bubbles emerge in the final solution, as indicated in figure 3.6.

So far discussion of vorticity dynamics associated with breakdown has referred to the relatively open flow of the pipe. In the next chapter the evolution of breakdown in the torsionally driven cylinder will be examined via the vorticity dynamics and wave trapping approach described in this section. Comparing the generation of azimuthal vorticity in the

cylinder with that in the pipe will show that the mechanism by which negative azimuthal vorticity is generated and transported upstream of breakdown is similar to that in the open pipe.

Chapter 4

Method and Validation

4.1 Introduction

The approach taken in this study was to examine breakdown in laminar, incompressible flows by numerical analysis, ie. numerical solution of the fluid flow (Navier-Stokes) equations. The numerical approach was chosen because it offers the ability to more easily obtain details of the interior structures in the flow, and importantly for this study the possibility of constructing geometries and boundary conditions which are difficult to generate in reality.

Three distinct numerical codes were used at various stages throughout the analysis. The commercial product Fluent 4 was used to obtain most results for the vorticity dynamics studies for the open pipe and torsionally driven cylinder. The related code Fluent 5 was used to model the effect of placement of an aerofoil in the pipe, and for some of the experiments with different cylinder geometries, eg. the “streampipe”. One section of the study required computation of a 3 dimensional solution, as opposed to the axisymmetric solutions obtained for the other sections. Due to the high CPU time required for such computations using Fluent 4 and 5, a spectral-element code was substituted to obtain these 3D results. However the majority of the results presented in following chapters were obtained using Fluent 4, and it is this code which we describe briefly, and validate for the flows we consider, in this section. Validation of the other codes will be described in the later sections in which the results from them are reported.

4.2 Numerical method

In the flows we consider the complete state of the system is defined by the equations which describe conservation of mass and momentum, with appropriate boundary conditions. In this section we describe the formulation used to solve the equations. Further details can be found in Versteeg and Malalasekera [73].

The continuity (conservation of mass) equation which will be solved is shown in equation 4.1:

$$\frac{\partial \rho}{\partial t} = \nabla \cdot (\rho \mathbf{u}), \quad (4.1)$$

where ρ is the fluid density, and \mathbf{u} its velocity. We take the case $\rho = \text{constant}$, so this reduces to the continuity constraint:

$$\nabla \cdot \mathbf{u} = 0. \quad (4.2)$$

The following are the momentum equations to be solved, in component form:

$$\begin{aligned} \rho \frac{Du}{Dt} &= \frac{\partial \tau_{ii}}{\partial x} + \frac{\partial \tau_{ji}}{\partial y} + \frac{\partial \tau_{ki}}{\partial z} - \frac{\partial p}{\partial x} + S_x \\ \rho \frac{Dv}{Dt} &= \frac{\partial \tau_{ij}}{\partial x} + \frac{\partial \tau_{jj}}{\partial y} + \frac{\partial \tau_{kj}}{\partial z} - \frac{\partial p}{\partial y} + S_y \\ \rho \frac{Dw}{Dt} &= \frac{\partial \tau_{ik}}{\partial x} + \frac{\partial \tau_{jk}}{\partial y} + \frac{\partial \tau_{kk}}{\partial z} - \frac{\partial p}{\partial z} + S_z \end{aligned} \quad (4.3)$$

where the τ_{mn} are the viscous shear stress components (in the n direction, on a surface with normal m), (u, v, w) the velocity components in the (i, j, k) directions, and p is the pressure. The S_i terms represent body forces. For a Newtonian fluid, the viscous stress components are given in equation 4.4:

$$\tau_{ij} = \mu \left(\frac{\partial u_i}{\partial x_j} + \frac{\partial u_j}{\partial x_i} \right) - \frac{2}{3} \mu \frac{\partial u_l}{\partial x_l} \delta_{ij}, \quad (4.4)$$

where μ is the dynamic viscosity ($\mu = \rho \nu$, where ν is the kinematic viscosity), and the term incorporating δ_{ij} represents volume dilation, set to zero here as this study relates only to incompressible flows.

Substituting this expression for the τ_{ij} into equations 4.3, after some rearrangement the Navier-Stokes equations are obtained:

$$\begin{aligned}\rho \frac{\partial u}{\partial t} + \nabla \cdot (\rho u \mathbf{u}) &= -\frac{\partial p}{\partial x} + \nabla \cdot (\mu \nabla u) \\ \rho \frac{\partial v}{\partial t} + \nabla \cdot (\rho u \mathbf{v}) &= -\frac{\partial p}{\partial x} + \nabla \cdot (\mu \nabla v) \\ \rho \frac{\partial w}{\partial t} + \nabla \cdot (\rho u \mathbf{w}) &= -\frac{\partial p}{\partial x} + \nabla \cdot (\mu \nabla w).\end{aligned}\tag{4.5}$$

This form of the equations illustrates the similarities between the continuity and momentum equations; in fact both equations are special cases of a general form, shown in equation 4.6:

$$\frac{\partial(\rho\phi)}{\partial t} + \nabla \cdot (\rho\phi\mathbf{u}) = \nabla \cdot (\mu\nabla\phi) + S.\tag{4.6}$$

This equation describes the transport of a quantity ϕ , where for the momentum equations ϕ is either u , v , or w , and for the continuity equation $\phi = 1$. The S term incorporates the pressure gradient terms from the momentum equations.

The essence of the finite-volume method to be used involves dividing the computational domain into control volumes, then integrating the transport equations 4.6 over each control volume. Hence the next step is to determine an integral form for each of the terms in the transport equation which renders the result appropriate for discretisation. We begin by integrating over a control volume V :

$$\int_V \frac{\partial(\rho\phi)}{\partial t} dV + \int_V \nabla \cdot (\rho\phi\mathbf{u}) dV = \int_V \nabla \cdot (\mu\nabla\phi) dV + \int_V S dV.\tag{4.7}$$

Using the divergence theorem, the integrals for the convective and diffusive terms can be re-written as integrals over the surface A of the volume.

$$\frac{\partial}{\partial t} \int_V \rho\phi dV + \int_A \mathbf{n} \cdot (\rho\phi\mathbf{u}) dA = \int_A \mathbf{n} \cdot (\mu\nabla\phi) dA + \int_V S dV.\tag{4.8}$$

This equation describes the rate of change of the quantity $\rho\phi$ in the control volume V ; in words (Versteeg and Malalasekera [73]):

$$\begin{array}{ccccccc}
 \text{Rate of increase} & + & \text{Rate of decrease} & = & \text{Rate of increase} & + & \text{Rate of creation} \\
 \text{of } \phi & & \text{of } \phi \text{ from} & & \text{of } \phi \text{ from} & & \text{of } \phi \\
 & & \text{convection across} & & \text{diffusion across} & & \\
 & & \text{boundaries} & & \text{boundaries} & & \\
 \text{(Rate of change)} & & \text{(Convection)} & & \text{(Diffusion)} & & \text{(Source)}
 \end{array}$$

For steady-state problems the first (time-dependent) term on the left is not solved for. For time-dependent problems it is necessary to integrate each equation over a timestep Δt , as shown in equation 4.9

$$\int_{\Delta t} \frac{\partial}{\partial t} \int_V \rho \phi dV dt + \int_{\Delta t} \int_A \mathbf{n} \cdot (\rho \phi \mathbf{u}) dA dt = \int_{\Delta t} \int_A \mathbf{n} \cdot (\mu \nabla \phi) dA dt + \int_{\Delta t} \int_V S dV dt. \quad (4.9)$$

4.3 Discretisation

Having obtained an appropriate form of the Navier-Stokes equations, the next step is to discretise the equations so that they may be solved numerically. We use a one-dimensional steady flowfield (the time-dependent term is dropped) to illustrate the discretisation. The convection and diffusion of ϕ , in the absence of sources, can then be represented by:

$$\frac{d}{dx} (\rho u \phi) = \frac{d}{dx} \left(\mu \frac{d\phi}{dx} \right). \quad (4.10)$$

Continuity is provided by:

$$\frac{d}{dx} (\rho u) = 0. \quad (4.11)$$

We will use nomenclature introduced for the control volume V shown in figure 4.1.

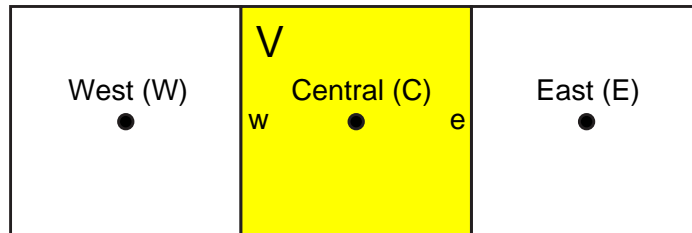


Figure 4.1: Control volume strategy used in Fluent 4.

We substitute $F = \rho u$ and $D = \frac{\mu}{\delta x}$. The convection-diffusion equation can then take the discretised, central difference form in equation 4.12 (Versteeg and Malalasekera [73]):

$$F_e \phi_e - F_w \phi_w = D_e (\phi_E - \phi_C) - D_w (\phi_C - \phi_W), \quad (4.12)$$

and the continuity equation:

$$F_e - F_w = 0, \quad (4.13)$$

where δx is the node spacing, assumed constant here. This assumes that the velocities on the faces are known; how these values are determined will be explained in section 4.4 on the SIMPLE method.

Next the values of ϕ_e and ϕ_w need to be calculated. A number of methods exist for this purpose. The Quadratic Upwind Interpolation for Convective Kinetics (QUICK) differencing scheme, as developed by Leonard (in Versteeg and Malalasekera [73]) is used in this study. The QUICK scheme uses a quadratic fit through the node on each side of the reference cell (W and E), along with the reference cell node (C), plus another quadratic fit which includes an upstream node (WW, not displayed in figure 4.1 but to the left of W), W, and C. Details of this method are described in Leonard (in [73]). The resulting scheme has greater accuracy than central differencing. QUICK is third-order accurate for flux interpolation resulting in second-order accuracy for the discretisation. However the truncation error coefficient of the third-order term is smaller than for central differences. QUICK also has increased stability due to the upwinding component (which includes node WW or EE, depending on flow direction), ie. a reduced tendency to produce “wiggly” solutions for high cell Reynolds numbers. However for time-dependent problems the QUICK scheme is still only conditionally stable.

4.4 Pressure-velocity coupling

If the pressure gradient ∇p is known, it is now possible using the QUICK scheme outlined above to determine the velocity field, \mathbf{u} . However at the beginning of the calculation the pressure field is also unknown. Since we only consider incompressible fluids, the velocity and pressure fields are coupled, and this can be used in an iterative scheme to calculate both the pressure and velocity fields.

A modified version of the SIMPLE algorithm of Patankar and Spalding [53], called SIM-
PLEC, was used (see Versteeg and Malalasekera [73]). The SIM-
PLEC method is an iterative procedure, which begins with an initial guess p^* for the pressure field. By substituting p^* into the discretised momentum equations an initial approximation to the velocity \mathbf{u}^* can be obtained. Since the pressure and velocity fields must also satisfy continuity, substituting \mathbf{u}^* into the continuity equation results in a pressure correction term, p' , where $p = p^* + p'$. Substituting the corrected pressure back into the momentum equations completes an iteration. This process is continued until the required level of convergence is reached.

4.5 The open pipe geometry

A typical pipe geometry used to study vortex breakdown is shown in figure 4.2. It is typical in the sense that it has the characteristics of many of the pipes used in experimental and numerical studies, ie. a constricted inlet section, a test section where breakdown is produced, and a constricted outlet.

The purpose of the constricted inlet is to provide an adverse pressure gradient in the axial direction; pressure increases along the length of the pipe. This adverse pressure gradient has been found in previous studies to play an important part in vortex breakdown initiation. It also fixes the location of the bubble in the pipe, as a range of swirl levels can be found for which the bubble cannot traverse the constriction.

Some open pipe studies have involved a straight section pipe (eg. Lopez [45]). In this case the breakdown may be held in place by the inlet boundary conditions. Here instead we use the more physical alternative of providing an adverse pressure gradient by constricting the pipe just downstream of the inlet. This keeps the bubble well downstream of the inlet for all swirls (Ω) and Reynolds numbers (Re) of interest.

Sarpkaya's [57] and Faler and Leibovich's [17] experimental pipe, and Beran and Culick's [4] and Darmofal's [8] numerical pipes are similar to the type displayed in figure 4.2. Beran and Culick's [4] and Darmofal's [8] pipe geometry is more suited to numerical work because the pipe walls are defined as streamlines, and so there is no need to accommodate boundary layers.

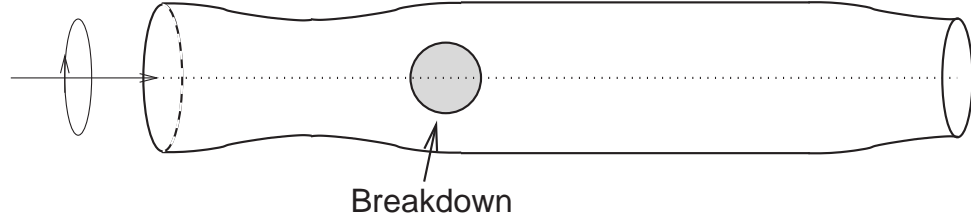


Figure 4.2: Open pipe geometry.

The precise definition of the pipe wall used in the present study is that provided by Darmofal [8], and is described by equations 4.14 and 4.15.

$$\begin{aligned}
 R(z) = & R_i + (R_t - R_i) g(z, z_t) & 0 < z < z_t \\
 & R_t + (R_0 - R_t) g(z - z_t, z_0 - z_t) & z_t < z < z_0 \\
 & R_0 & z_0 < z < z_c \\
 & R_0 + (R_{max} - R_c) g(z - z_c, z_{max} - z_c) & z_c < z < z_{max}
 \end{aligned} \tag{4.14}$$

$$\text{where } g(z, \Delta z) = \frac{1}{2} (1 - \cos[\pi(z/\Delta z)]), \tag{4.15}$$

and the R and z values are defined in figure 4.3. We use the values: $z_i = 0$, $z_t = 5$, $z_0 = 10$, $z_c = 25$, $z_{max} = 30$, $R_i = R_0 = R_c = 2$, $R_t = R_{max} = 1.8$.

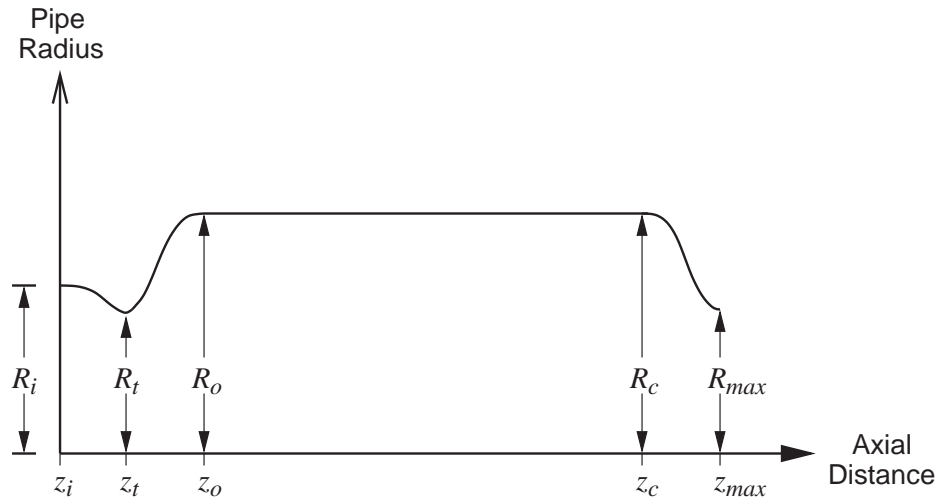


Figure 4.3: Open pipe geometry.

The converging outlet prevents an unphysical solution evolving, where the bubble length increases until it impinges on the outlet. The converging outlet causes the flow to accelerate

and become supercritical again.

The inlet boundary conditions are based on those observed experimentally for a q-vortex (see for example Leibovich [42]), and are defined in three-component form:

$$\begin{aligned} u_0(r) &= 1 + \Delta u e^{-r^2} \\ v_0(r) &= 0 \\ w_0(r) &= \frac{\Omega}{r} [1 - e^{-r^2}] \end{aligned} \tag{4.16}$$

where $u_0(r)$, $v_0(r)$, and $w_0(r)$ are the axial, radial, and azimuthal velocity components respectively. Here $\Omega = \frac{\Gamma_\infty}{\delta u_\infty}$, where Γ_∞ is the freestream circulation, u_∞ is the freestream axial velocity, and δ is the radius of the core. In the cases we consider Δu is zero, so the velocity in the axial direction does not vary radially. The w_0 profile has a form as shown in figure 4.4:

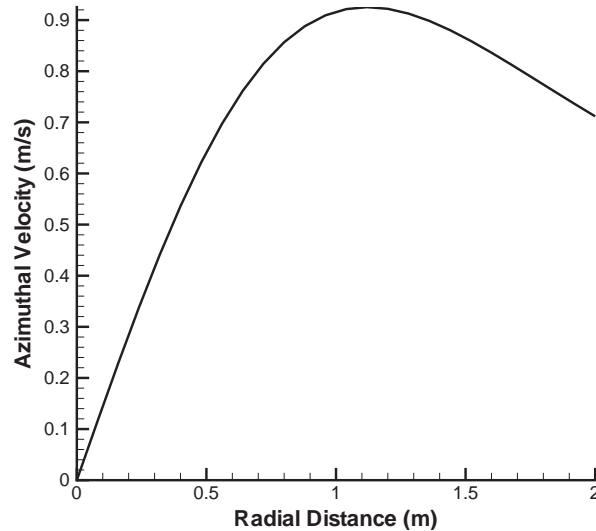


Figure 4.4: Inlet azimuthal velocity (w) profile.

The Reynolds number Re is defined in terms of the axial component of velocity at the inlet and the vortex core radius; both are set to 1 in all the cases considered here.

$$Re = \frac{u_0 \delta}{\nu} \tag{4.17}$$

where ν is the kinematic viscosity. Re is varied by changing ν . The axial velocity is set to $u = 1$ across the entire inlet, and the radial velocity to zero. The azimuthal velocity

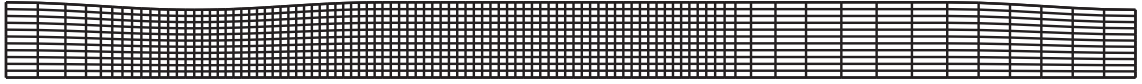


Figure 4.5: Example of the compression strategy used for the open pipe. This example has 12 nodes in the radial (y) direction and 94 nodes in the axial (x) direction (ie. a 94×12 grid).

is defined using a piecewise continuous curve described by 25 points. The function that generates the points is described in the expression for $w_o(r)$ in equations 4.16.

4.6 Grid resolution and verification of numerical results

4.6.1 Grid resolution

Six grids for the open pipe geometry were tested. All of the grids were compressed around the region where breakdown was expected in order to capture better the larger gradients in velocity which arise in this region. The areas outside the breakdown region have relatively small velocity gradients. The coarsest grid consisted of 94×12 nodes, and this grid is shown in figure 4.5 - it gives an indication of the compression strategy used for all of the grids.

In these tests the minimum streamfunction value is the measure used in the grid comparisons. This parameter has been used in previous studies, since it is a sensitive indicator of the grid resolution's effect on the solution. The point in the domain at which the minimum streamfunction value occurs is within the breakdown bubble, so it gives an indication of how well the bubble has been resolved. Also, it is around 5 orders of magnitude smaller than the streamfunction value in the general flow, and is of opposite sign, so it is relatively easy to identify. Hence for this test a regime is chosen where a breakdown bubble is present. In these cases $\Omega = 1.45$ and $Re = 1000$.

Iterations continued for each grid until the sum of the normalised pressure and velocity residuals was less than 2×10^{-5} . This level of convergence was deemed sufficient as the solution change was less than 2 percent for more highly converged runs.

Figure 4.6 indicates the level of convergence of each grid. The negative of the minimum

streamfunction value is plotted against the number of nodes. The 295×37 grid gives a result within 1% of the finest grid tested (602×75).

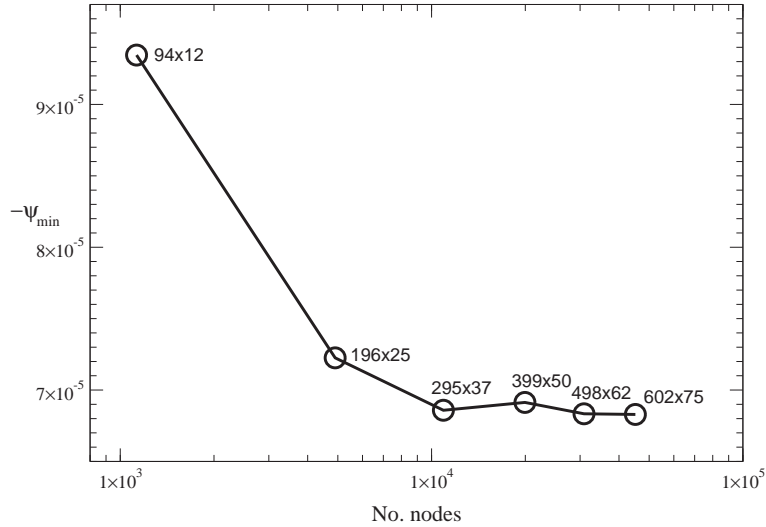


Figure 4.6: Open pipe grid convergence.

Also, table 4.1 shows the performance of the various grids.

Grid	Ψ_{min}	% difference from 602×75 grid
94×12	-9.34583×10^{-5}	36.856
196×25	-7.22547×10^{-5}	5.806
295×37	-6.85827×10^{-5}	0.429
399×50	-6.91333×10^{-5}	1.236
498×62	-6.83360×10^{-5}	0.068
602×75	-6.82895×10^{-5}	-

Table 4.1: Open pipe grid convergence.

The minimum streamfunction value is very sensitive to changes in the flow, so it is a good indicator of grid accuracy. Since the minimum streamfunction value changes by less than 1% relative to the finest grid studied for the three finest grids, and its value changes only slightly during the transition from 295×37 through to 602×75 , we conclude that the 602×75 solution is sufficiently well resolved to not warrant the testing of finer grids. The result for the 295×37 grid gives a sufficiently resolved result for it to be used in this study;

using a finer mesh will result in negligible change in the solution, and increase significantly the time required to obtain a converged solution.

4.6.2 Comparison with other numerical results

The accuracy of the solutions is checked by comparing sample results with those from Darmofal [8] and Beran and Culick [4]; these studies make use of geometries and boundary conditions which are in most respects identical to ours. However the outlet in our study converges; the results we compare with are for a straight-section outlet. The difficulty in obtaining a physically reasonable steady solution without the converging outlet was referred to earlier.

For the grid used in this study breakdown occurs at a swirl value of approximately $\Omega = 1.4605$. Darmofal's [8], [9] study cites initial breakdown onset at a swirl of $\Omega = 1.51$. To better compare results, the coarser grid used in that study is repeated using Fluent (Darmofal's grid has 31 nodes in the radial direction and 151 in the axial direction, and has constant spacing). It is found that breakdown for the coarser grid using Fluent occurs at $\Omega = 1.48$, a higher value than is found for the finer grid used in the main part of this study. A trend can be seen here - in increasing the coarseness of the grid, the breakdown is delayed until a higher swirl value. Hence Darmofal's [8] different swirl value for breakdown may be a result of the coarser grid used. The values of Ω required for breakdown onset only differ by $\sim 3\%$ in any case.

In figure 4.7 we plot streamfunction contours for the steady results of Darmofal [8] for $Re = 1000$, $\Omega = 1.51$, and Beran and Culick [4] for $Re = 1000$, $\Omega = 1.48$, along with our steady result for $Re = 1000$, $\Omega = 1.4605$.

The pipe sizes and aspect ratios are scaled in the images so that the pipe dimensions are comparable. The bubble sizes, shapes, and locations are in reasonable agreement, although the bubble in Beran and Culick's [4] result is significantly smaller than the other two. The values of Ω are slightly different, but in each case the flow represented is the one for which breakdown has just evolved, so in this sense the flows are more comparable than is evident from the values of Ω .

As an additional check, a straight-sided pipe was implemented using Fluent 5, with the same node density as was used for the grid in the previous section. Fluent 5 is used here

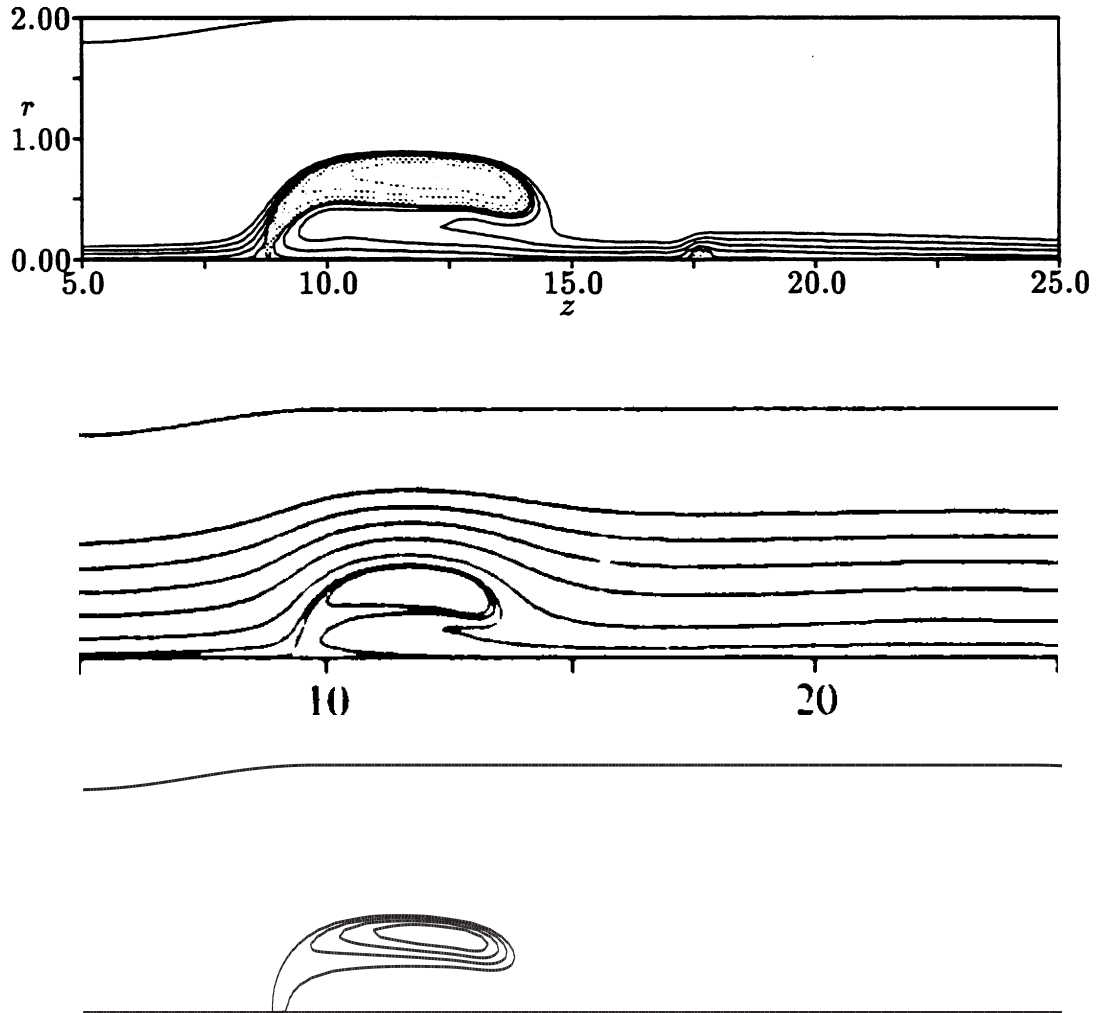


Figure 4.7: Comparison between Darmofal's [8] ($Re = 1000$, $\Omega = 1.51$) bubble, Beran and Culick's [4] ($Re = 1000$, $\Omega = 1.48$) bubble, and the bubble produced in the present study ($Re = 1000$, $\Omega = 1.4605$).

because it is capable of producing a converged solution without requiring a converging outlet. Here we will compare the velocity components near the centreline with those reported by Beran and Culick [4]. For comparison results from grid G3 in Beran and Culick's study was chosen; it consists of a converging/diverging section at the inlet, followed by a straight test section, and without a converging outlet. The node density of the G3 grid is 301×27 , which is comparable to the 295×37 grid used in our study. Three runs were conducted using this geometry. Results for $Re = 250$ and swirl $\Omega = 1.45$, $\Omega = 1.50$, and $\Omega = 1.55$ are presented. The resulting centreline axial velocity profiles are compared in figure 4.8. Beran and Culick's results are plotted as dashed lines, and our results as solid lines.

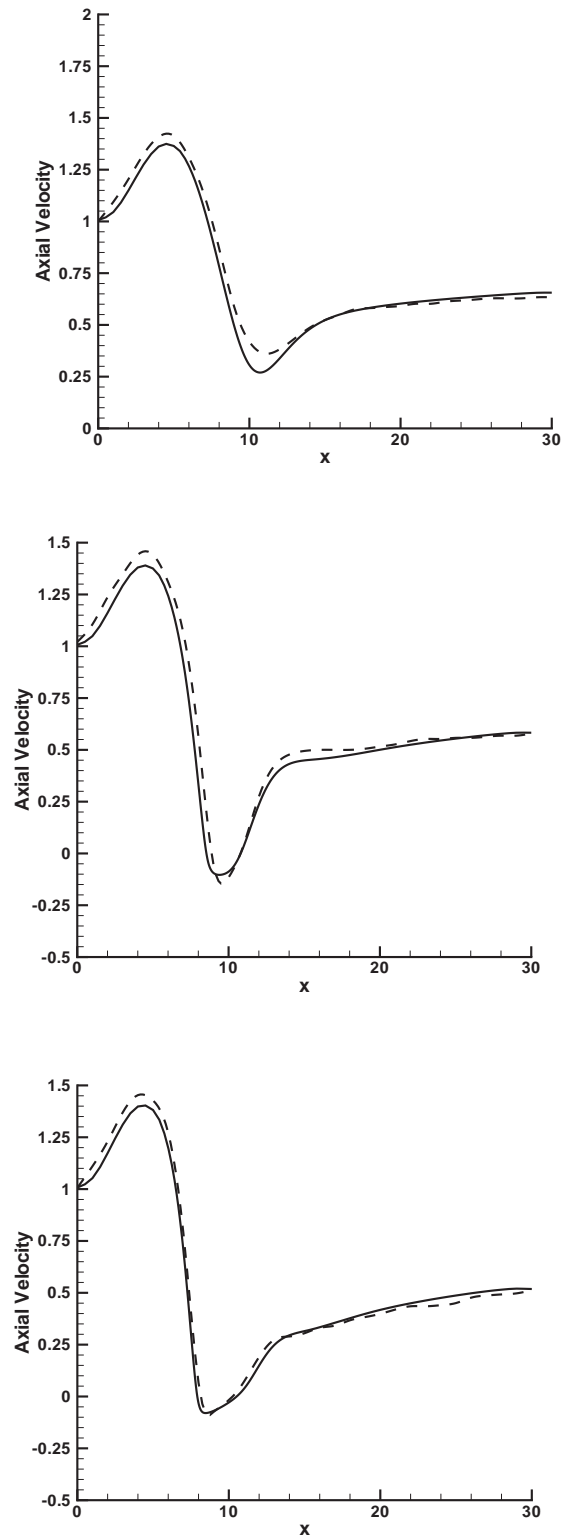
Figure 4.8: $Re = 250$, $\Omega = 1.45, 1.50, 1.55$.

Figure 4.8 shows that the results from this study compare well with those produced by Beran and Culick. This also indicates that the difference noted in the previous comparison was likely due to the different outlet conditions.

4.6.3 Timestep tests

A later chapter on the manipulation of breakdown by transient changes to the upstream swirl ratio requires time-dependent simulations. In this section we determine an appropriate timestep for this problem, which again involves the open pipe geometry.

The time resolution was tested at the following levels: $dt = 0.025, 0.01, 0.005, 0.0025,$ and 0.001 , where dt is defined in equation 4.18

$$t = n dt \frac{r_{core}}{u_{\infty}}. \quad (4.18)$$

Here t is the time, n the number of timesteps. r_{core} (the radius of the vortex core) and u_{∞} (the freestream velocity) both equal 1. A timestep which accurately resolves the transient features of the flow is required; in order to determine an appropriate timestep we plot the minimum axial velocity at a point along the centreline for each of the timesteps considered. In this case the initial condition has $Re = 600$ and $\Omega = 1.45$ in the open pipe defined in section 4.5. A perturbation is introduced by increasing Ω to 2.9 until $t = 1.5$, then decreasing Ω back to 1.45. The resulting plots are shown in figure 4.9, where the minimum axial velocity along the centreline is plotted.

The plot shows that timesteps smaller than $dt = 0.005$ result in little change in the minimum axial velocity over the $dt = 0.005$ solution. We therefore adopt this timestep for the period following initial swirl changes. With increasing time a larger timestep is capable of sufficiently resolving subsequent behaviour. Since this swirl change is the maximum that we will use in the later perturbation study, this timestep should provide sufficient resolution of transients for all of the perturbations tested.

4.6.4 Validation against experimental results

In this section we compare the results generated by Fluent 5 with experimental results published by Faler and Leibovich [18]. Faler and Leibovich [18] investigated the breakdown

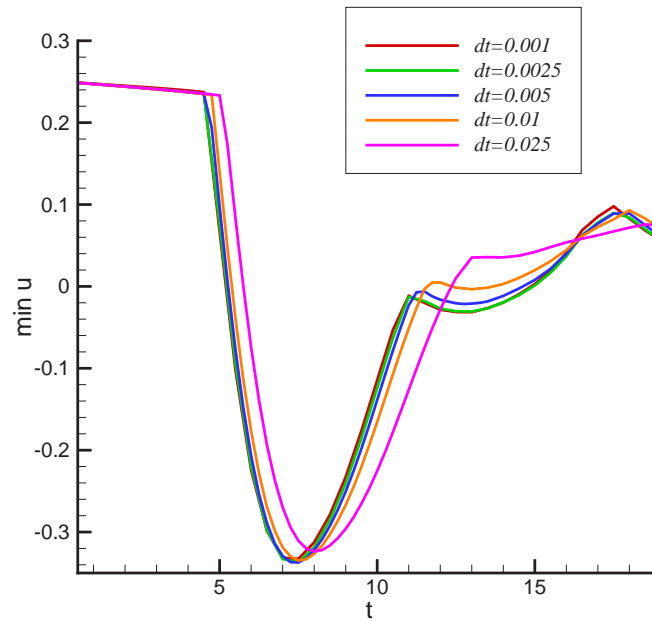


Figure 4.9: Timestep validation.

structures produced in an open pipe, where swirl was introduced by swirl vanes positioned upstream; the geometry is illustrated in figure 4.10. The figure is not to scale; the z and R values are provided in table 4.2.

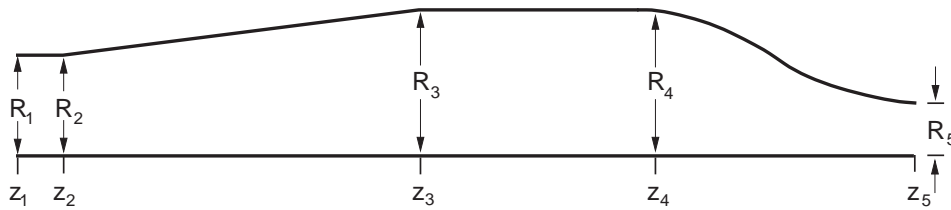


Figure 4.10: Apparatus of Faler and Leibovich [18].

i	1	2	3	4	5
z_i	0.0	1.763	15.097	22.967	33.467
R_i	1.0	1.0	1.333	1.333	0.667

Table 4.2: z and R values for Faler and Leibovich [18] pipe definition.

Further details of the experimental apparatus can be found in Faler and Leibovich [18]. For our purposes the geometry consists of a tube with varying cross section. A section of

straight pipe downstream of the inlet is followed by a gradually diverging section, then a straight test section. This test section is followed by another constriction. We represent this constricted section, but bring it further upstream to eliminate the need to solve for an excessively long domain.

Faler and Leibovich [18] observed a number of different forms of breakdown in their experiments. For our verification purposes we are concerned only with the axisymmetric bubble form.

We reproduce computationally a geometry identical to that of the experiment, except for the truncation applied to the extended straight section, and apply boundary conditions at the inlet consistent with the velocity profiles measured upstream of breakdown in the experiment. Faler and Leibovich [18] determine functions which closely match the velocity profiles observed; we use these functions to define the axial and swirl velocity profiles at the inlet. The functions are repeated below in equations 4.19 and 4.20:

$$u(r) = u_1 + u_2 \exp \left[\frac{-\alpha r^2}{r_t^2} \right] \quad (4.19)$$

$$w(r) = \frac{K r_t}{r} \left[1 - \exp \left[\frac{-\alpha r^2}{r_t^2} \right] \right], \quad (4.20)$$

where $\alpha = 11.84$, $u_1 = 5.53$ cm/s, $u_2 = 7.95$ cm/s, and $K = 4.1$ cm/s.

These velocity profiles are specified at the inlet to the left of the geometry in figure 4.10 which corresponds to a location 30.6mm upstream of breakdown in the experimental pipe.

In figure 4.11 we plot the Fluent 5 computational solution and the experimental solution. The computational solution is steady in the bubble regions, but produced using a time-dependent scheme. At the bottom of figure 4.11 are Faler and Leibovich's [18] averaged streamlines.

In both plots there are 2 recirculation bubbles, one above the other. The sizes of the bubbles are significantly different - the numerical bubble spans approximately half the pipe radius, but the experimental bubble only spans roughly one third the pipe radius. Generally the vortex core reformed behind the bubble, then broke down into the spiral form (Faler and Leibovich [17]). Our calculations are axisymmetric, so we are incapable of producing a spiral, but downstream of breakdown a vortex core does re-form (not shown here), and then another breakdown bubble follows at about the point where a spiral is

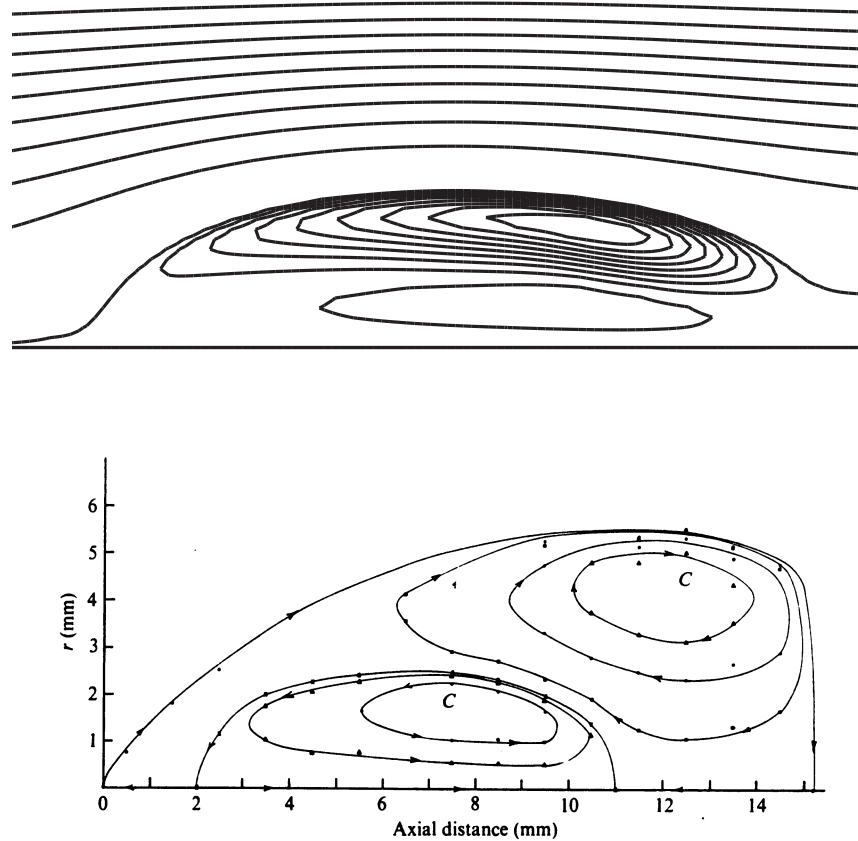


Figure 4.11: Comparison of Fluent 5 computational solution with Faler and Leibovich's [18] experimental averaged streamlines.

expected in the experiment. In work to follow we conduct a three-dimensional study of this pipe.

4.7 Azimuthal vorticity generation

In chapter 3 the vorticity dynamics associated with the onset of breakdown was described. It has been shown (Lopez [44], Darmofal [8]) that the onset of breakdown depends on the production of negative azimuthal vorticity. Once this vorticity is generated a feedback mechanism results in the generation of more negative azimuthal vorticity, to the point where the axial flow stagnates and a breakdown bubble forms.

A recurring theme in this thesis will be a comparison between the breakdowns produced in differing geometries, particularly the open pipe and torsionally driven cylinder, and whether the breakdown observed in the cylinder is indeed breakdown. If the phenomenon

observed in the cylinder is breakdown, then it is expected to have the same behaviour, and examination of vorticity generation and transport should reveal similar mechanisms.

In the following chapter an analysis will be presented of the vorticity dynamics associated with breakdown in the torsionally driven cylinder, to compare with the equivalent analysis for the open pipe. We aim to determine whether trapping of azimuthal vorticity is involved in the onset of breakdown in the cylinder.

The purpose of the remainder of this chapter is to validate our procedure for determining the vorticity components and describe in more detail the process of azimuthal vorticity generation in the pipe.

4.7.1 Validation of vorticity calculations

The first section compares plots of vorticity components determined for the open pipe in this study with those from Darmofal [8].

4.7.1.1 Components of vorticity

In this test case we use $Re = 600$ and $\Omega = 1.49$. In figures 4.12 to 4.15 streamlines and the three components of vorticity (axial, radial, and azimuthal) are plotted. On top are Darmofal's results, and below are our results for comparison. In the vorticity component plots the contour levels are kept the same for each pair of plots.

The streamline plots of figure 4.12 show good agreement in terms of bubble size, shape, and location between the two studies. The converging outlet will tend to reduce the size of the bubble in our solution.

Figures 4.13 to 4.15 show a close correspondence between the vorticity components computed in the two studies. The range of the vorticity components in our study exceed to a small extent those in Darmofal's, but the agreement as shown above is still very good, given geometrical and resolution differences between the meshes used.

We next compare terms from the vorticity equation.

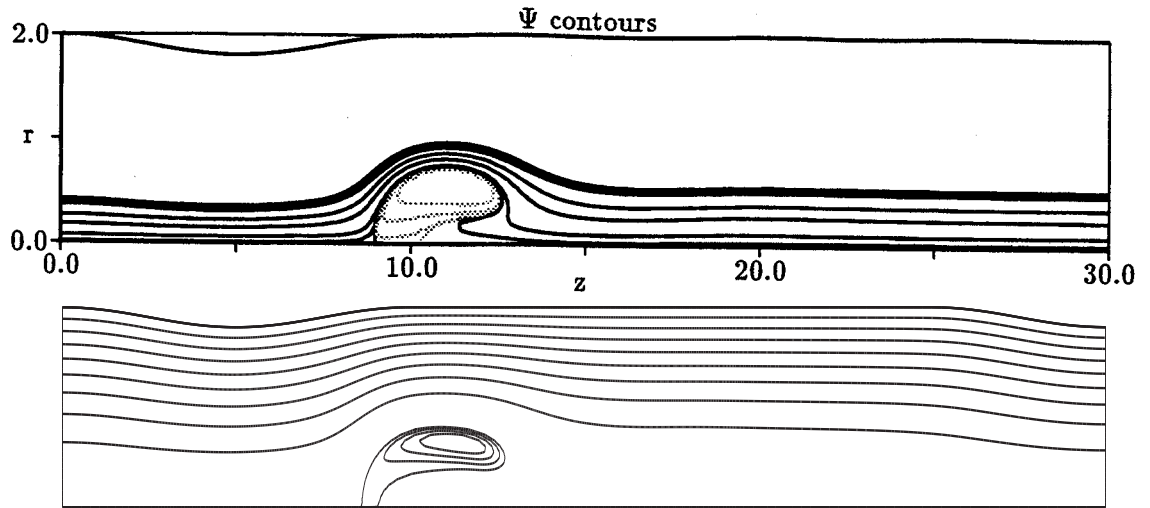


Figure 4.12: Streamfunction contours from Darmofal [8] (top), and the present study (bottom), for $Re = 600$, $\Omega = 1.49$.

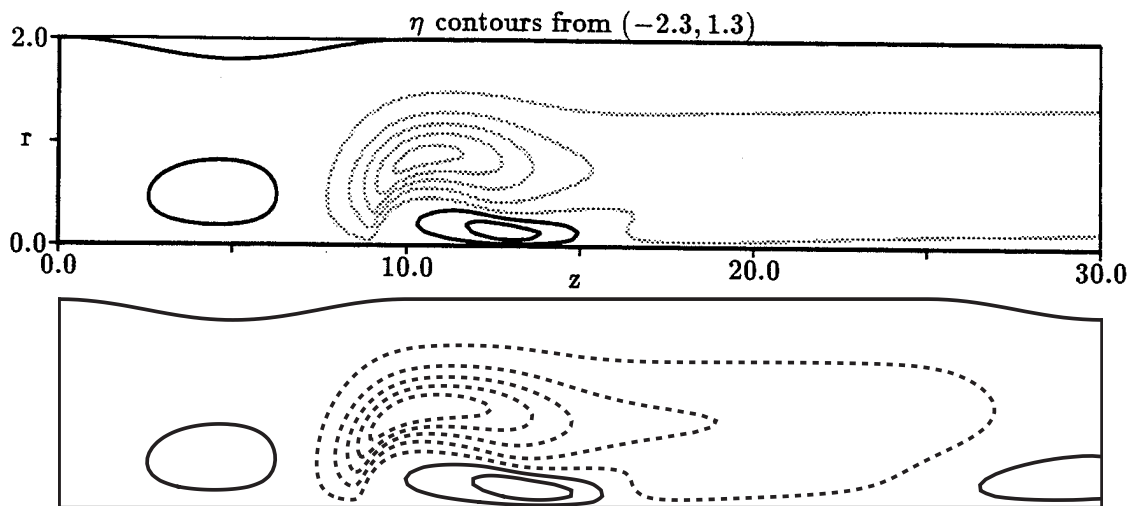


Figure 4.13: Azimuthal vorticity contours from Darmofal [8] (top), and the present study (bottom). Contour levels -2.3 to 1.3 for both plots, for $Re = 600$, $\Omega = 1.49$.

4.7.1.2 Azimuthal vorticity generation terms

We are primarily interested in the generation of azimuthal vorticity in this study. Here we plot 5 terms: total azimuthal vorticity generation without diffusive effects (figure 4.16), generation by stretching (figure 4.17) and turning (figure 4.18), total azimuthal vortic-

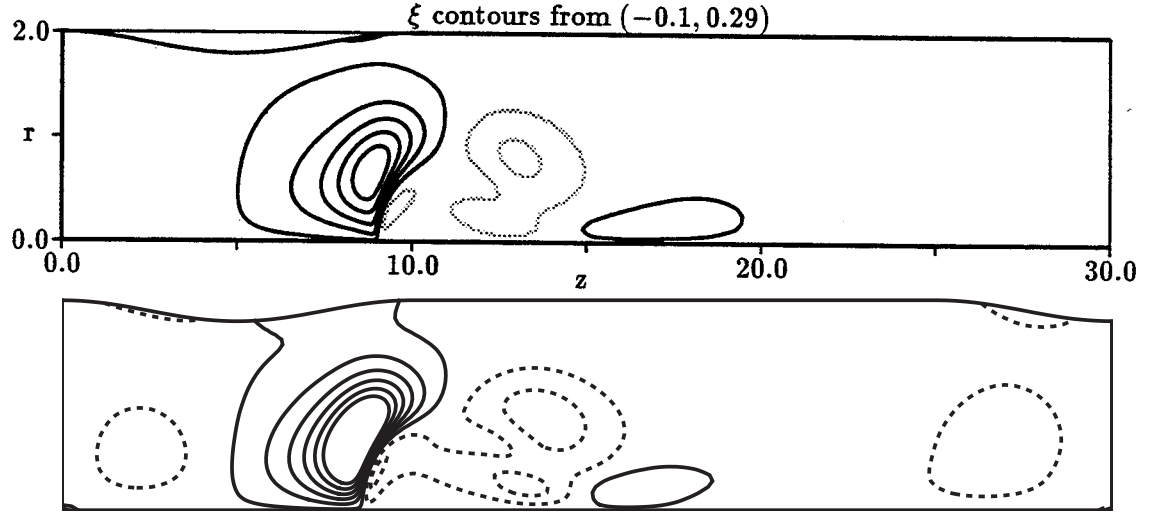


Figure 4.14: Radial vorticity contours from Darmofal [8] (top), and the present study (bottom). Contour levels -0.1 to 0.29 for both plots, for $Re = 600$, $\Omega = 1.49$.

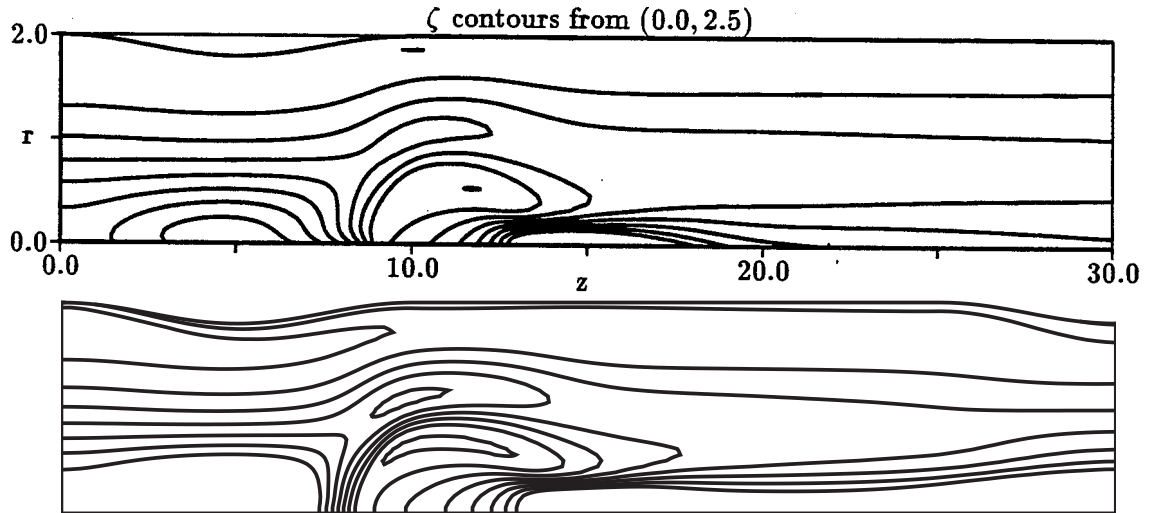


Figure 4.15: Axial vorticity contours from Darmofal [8] (top), and the present study (bottom). Contour levels 0.0 to 2.5 for both plots, for $Re = 600$, $\Omega = 1.49$.

ity generation including diffusive effects (figure 4.19), and the diffusion term alone (figure 4.20). These terms come directly from the azimuthal component of the vorticity generation equation, repeated in equation 4.21 without the diffusion term:

$$\frac{D\omega_\phi}{Dt} = \omega_r \frac{\partial u_\phi}{\partial r} + \omega_x \frac{\partial u_\phi}{\partial x} - \frac{u_\phi \omega_r}{r} + \frac{u_r \omega_\phi}{r}. \quad (4.21)$$

The four terms on the right hand side of equation 4.21 show the contribution to azimuthal vorticity generation by stretching and turning. The viscous term will reveal the relative importance of diffusion. It will be shown to have little contribution at this Reynolds number.

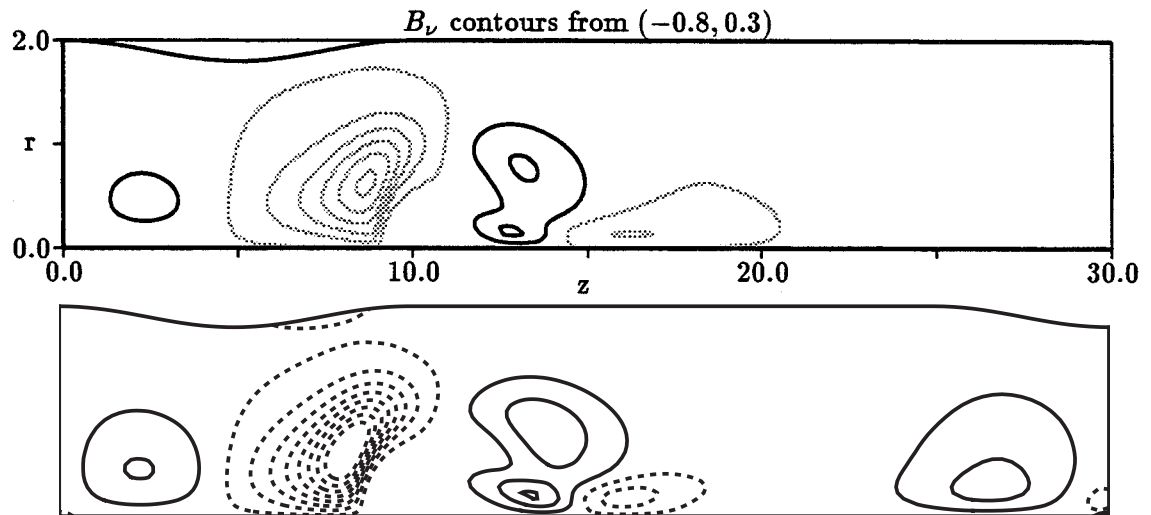


Figure 4.16: Total azimuthal vorticity generation contours without diffusion from Darmofal [8] (top), and the present study (bottom). Contour levels -0.8 to 0.3 for both plots.

The previous chapter on vorticity discussed in general terms the production of negative azimuthal vorticity in vortex cores. We can now use the plots of this section to describe in more detail how this process applies to azimuthal vorticity generation in the pipe.

Figure 4.18 shows that azimuthal vorticity generation begins in the pipe with production by turning, as turning occurs further upstream than the stretching process of figure 4.17. Negative azimuthal vorticity is produced at an increasing rate as the axial location where breakdown is expected is approached. Just in front of the bubble the turning begins to drop off, and stretching begins to take over. Previous investigations (as outlined in chapter 3) have shown that stretching increases the amplitude of the azimuthal vorticity generated in the turning process.

The contribution from the diffusion term is also plotted, in figure 4.20, for comparison. As shown by Darmofal [8], diffusion of azimuthal vorticity plays a relatively small part in the flow at this Reynolds number and swirl, compared to the other mechanisms. Diffusion

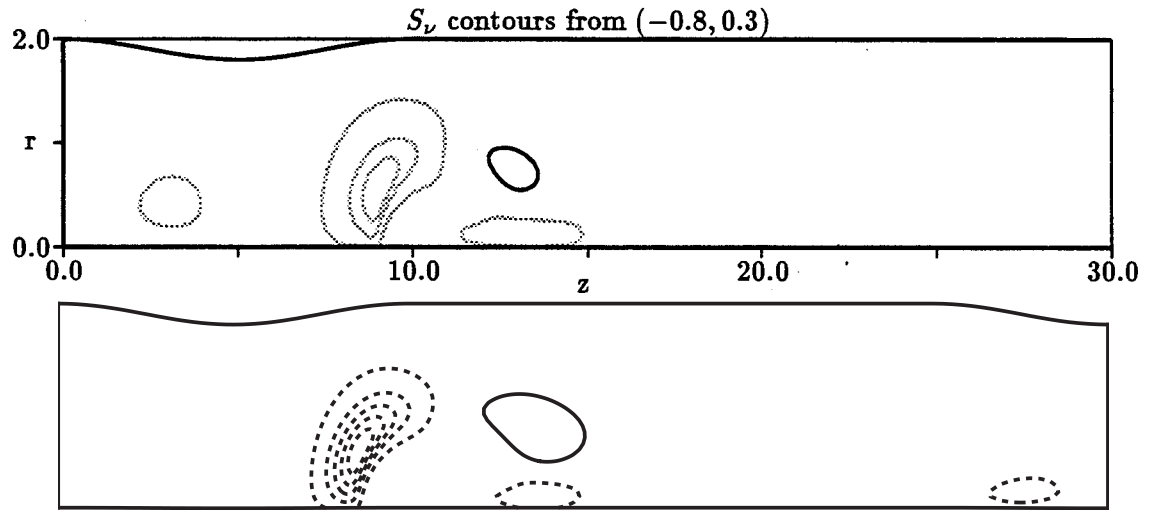


Figure 4.17: Contours of generation of azimuthal vorticity by stretching, from Darmofal [8] (top), and the present study (bottom). Contour levels -0.8 to 0.3 for both plots.

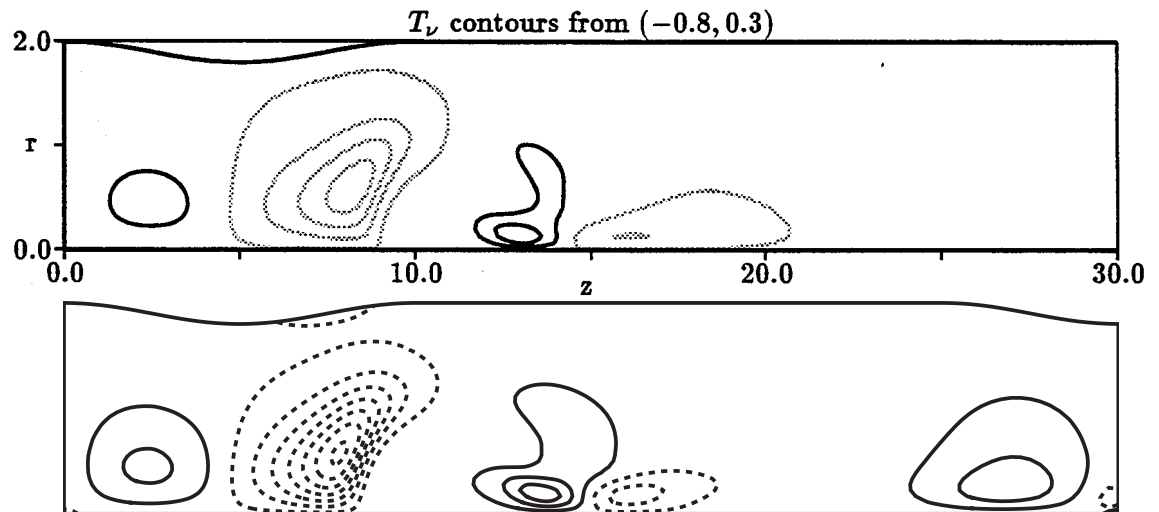


Figure 4.18: Contours of generation of azimuthal vorticity by turning, from Darmofal [8] (top), and the present study (bottom). Contour levels -0.8 to 0.3 for both plots.

has the largest effect downstream of the bubble, so it plays a minor part in the generation of vorticity leading to breakdown.

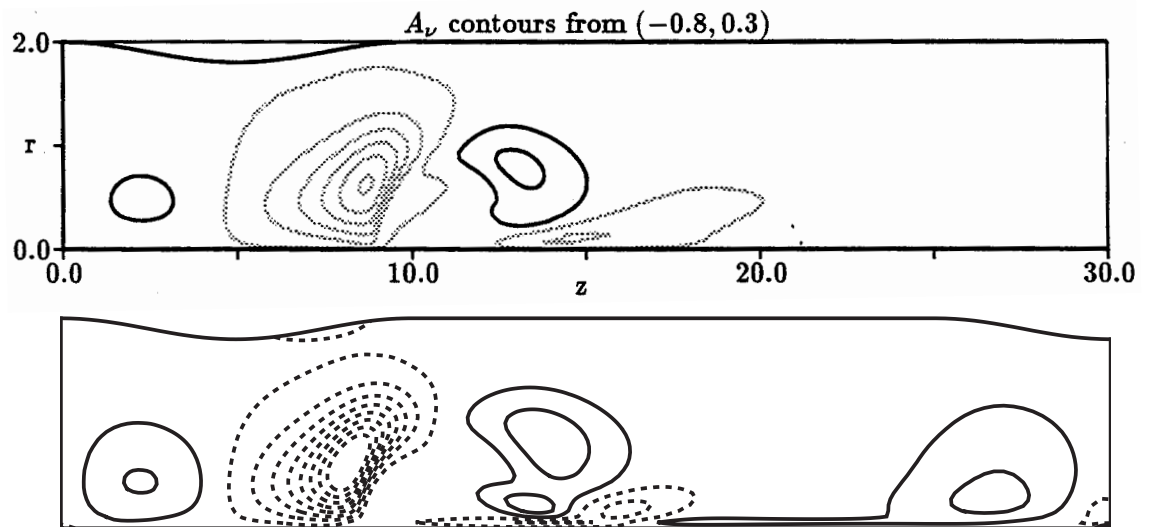


Figure 4.19: Contours of generation of azimuthal vorticity including the diffusion term, from Darmofal [8] (top), and the present study (bottom). Contour levels -0.8 to 0.3 for both plots.

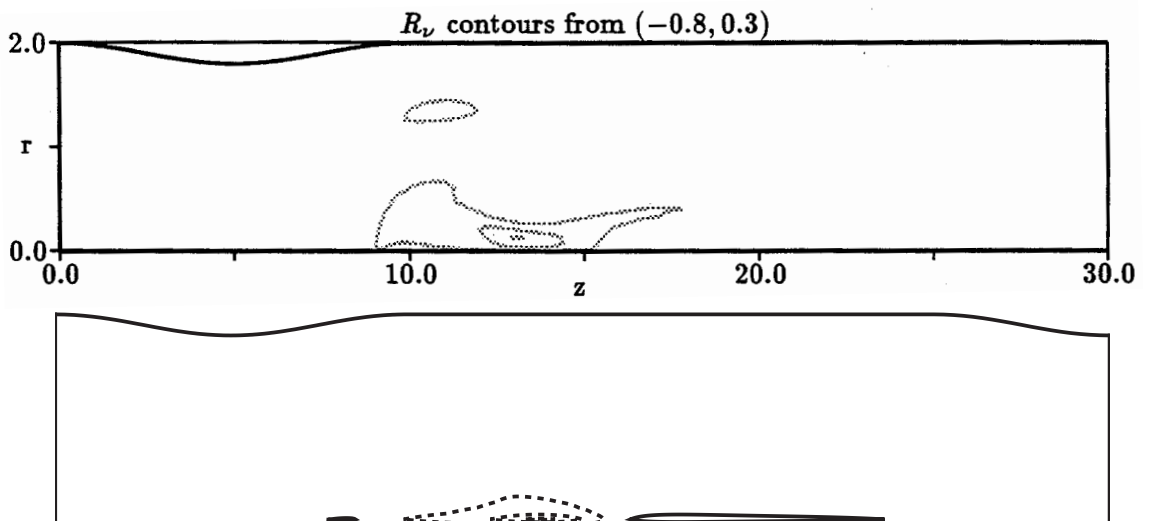


Figure 4.20: Contours of generation of azimuthal vorticity by diffusion, from Darmofal [8] (top), and the present study (bottom). Contour levels -0.8 to 0.3 for both plots.

4.7.2 Tilting of axial and radial vorticity

The contribution from the tilting term to azimuthal vorticity production in the open pipe was described in the review of chapter 3. In this section we split the turning term into

its two components; the contribution from turning of axial vorticity, and from turning of radial vorticity. A geometrical description of the effect of the turning terms is also provided to clarify the process. It turns out that while there is a nett negative generation of azimuthal vorticity via tilting, the axial and radial contributions are not of the same sign in the region of greatest azimuthal vorticity generation, just in front of the bubble.

The tilting of axial and radial vorticity are represented in equations 4.22 and 4.23 below:

$$\text{Tilting of axial vorticity} = \omega_x \frac{\partial u_\phi}{\partial x}, \quad (4.22)$$

$$\text{Tilting of radial vorticity} = \omega_r \frac{\partial u_\phi}{\partial r} - \frac{u_\phi \omega_r}{r}. \quad (4.23)$$

We briefly look at the geometrical interpretation of these processes.

4.7.2.1 Tilting of axial vorticity

The term we are interested in here is $\omega_x \frac{\partial u_\phi}{\partial x}$, ie. turning of axial vorticity by a gradient in u_ϕ in the axial direction. We can illustrate how ω_ϕ is generated by this term using figure 4.21.

At the top are contours of azimuthal velocity u_ϕ , and below contours of axial vorticity ω_x . In both cases selected contours have been annotated with their numerical value.

In the region just downstream of the point where the pipe radius is a minimum, $\frac{\partial u_\phi}{\partial x} < 0$. In this same region $\omega_x > 0$; in fact over the entire domain $\omega_x > 0$.

Hence the result is nett negative production of azimuthal vorticity ω_ϕ , as shown in figure 4.21(c)

4.7.2.2 Tilting of radial vorticity

This time we first consider the term $\omega_r \frac{\partial u_\phi}{\partial r}$ (the turning of radial vorticity by a gradient in u_ϕ in the radial direction). Again we plot contours of azimuthal velocity, in figure 4.22 (top), along with radial vorticity contours (bottom).

This time $\frac{\partial u_\phi}{\partial r} > 0$ in the region just downstream of the point of minimum pipe radius, and $\omega_r > 0$ in this region. Hence the term $\omega_r \frac{\partial u_\phi}{\partial r} > 0$, and the nett contribution to

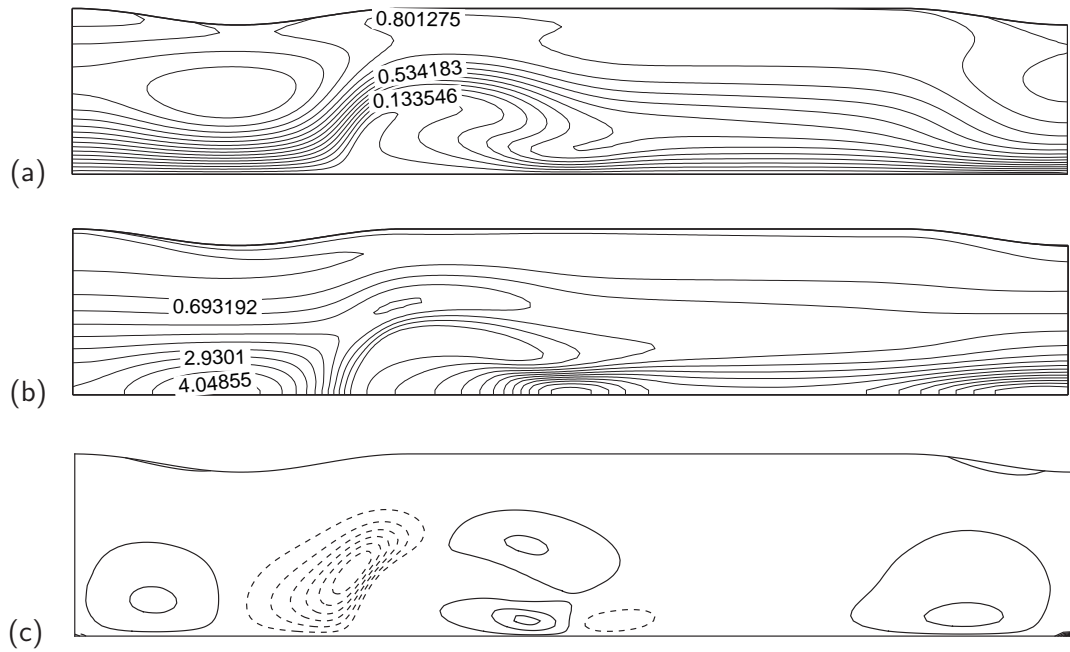


Figure 4.21: (a) Azimuthal velocity, (b) axial vorticity, (c) tilting of axial vorticity, for $Re = 600$, $\Omega = 1.49$.

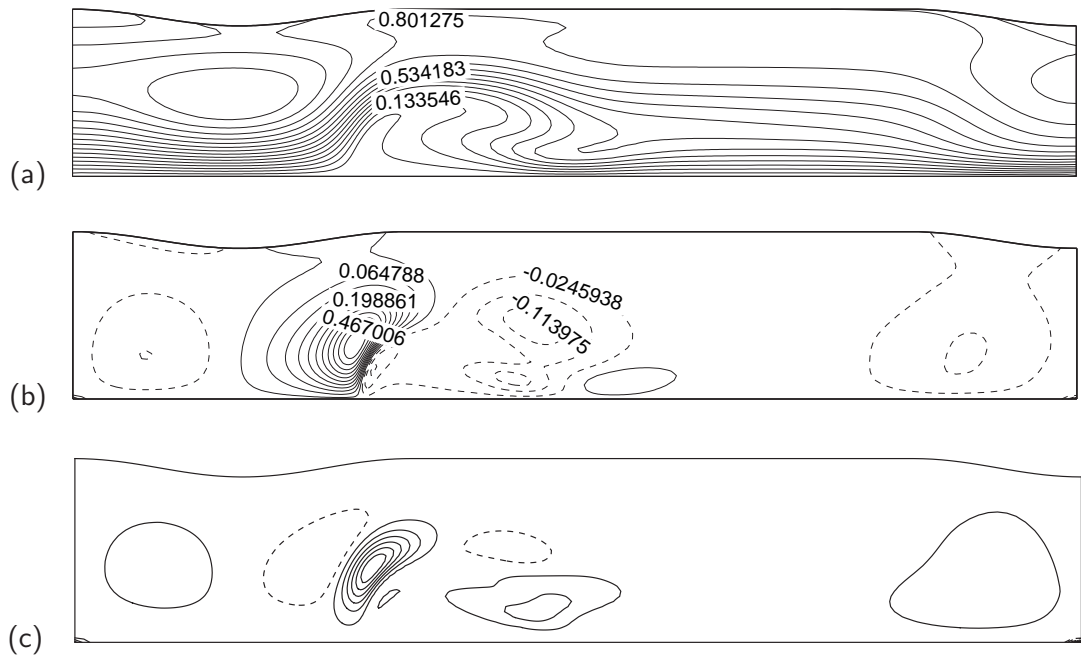


Figure 4.22: (a) Azimuthal velocity, (b) radial vorticity, (c) tilting of radial vorticity, for $Re = 600$, $\Omega = 1.49$.

the generation of azimuthal vorticity is positive, as shown in figure 4.22(c). The effect of the term $-\frac{u_\phi \omega_r}{r}$ is more minor, but it is opposite in sense to that of $\omega_r \frac{\partial u_\phi}{\partial r}$, and hence moderates the effect of tilting of radial vorticity.

Hence turning of both the axial and radial components of vorticity introduces azimuthal vorticity into the region in front of the breakdown bubble, but each contribution is of opposite sign; the two mechanisms which generate azimuthal vorticity by turning compete. The turning of axial vorticity works toward bringing about breakdown, whereas the turning of radial vorticity moves the flow away from a breakdown state.

For $Re = 600$ and $\Omega = 1.47$, production of ω_ϕ by axial vorticity turning dominates. It may be that for other Reynolds numbers and swirls the radial vorticity turning dominates, and breakdown is suppressed. Examination of the tilting contributions at other values of Re and Ω is relegated to future work.

Chapter 5

Vortex breakdown in the driven cylinder

A version of the torsionally driven cylinder (referred to from here on simply as the cylinder) was the first apparatus in which vortex breakdown has been documented (in Maxworthy [49]). At the time of this first observation the significance of the phenomenon would perhaps not have been realised, and even in modern times the relevance of breakdown in the cylinder to higher Reynolds number flows of practical interest has been questioned. This is due to differences in the manifestation of breakdown in the cylinder compared to its behaviour in more open geometries. Some of these differences are summarised in table 5.1.

With regard to the question of asymmetry, work published by Sotiropoulos *et al.* [63] indicated possible asymmetric modes of oscillation in a computational solution for a torsionally driven cylinder. Spiralling vortical structures were observed in the Stewartson layer on the cylinder sidewall. A similar observation of spiralling structures near the sidewall was made for some of our three-dimensional pipe visualisations (not presented here).

The observation of asymmetric modes in the cylinder for $Re = 2500$ has subsequently been confirmed in an experiment by Hirta *et al.* [31].

Hence some attention is now being focused on possible asymmetric modes of breakdown in the cylinder. We touch on asymmetry in chapter 7; a more in-depth study of the onset of three-dimensionality in the cylinder is beyond the scope of this thesis.

Cylinder	Pipe
Onset appears gradual with increasing Re	Onset appears sudden with increasing swirl (Ω)
Only bubbles have been observed	Bubbles, spirals, and helices have been observed
Hysteresis is generally not reported*	Hysteresis is prevalent
The vortex core flow reappears downstream	The flow downstream evolves to a spiral or turbulence
Multiple bubbles can exist on a single core	Only one bubble is generally observed
The bubble is axisymmetric	The bubble generally has some asymmetry
The downstream end of the bubble is closed	The downstream end of the bubble is often open

Table 5.1: Differences between breakdown in the cylinder and breakdown in the pipe. (*Hysteresis has been reported in the cylinder in at least one study [67].)

Note also that some of the other differences are not universally agreed on in the literature, for instance Spohn *et al.* [64] propose that cylinder breakdowns have open bubbles.

However given that there are differences in the manifestation of breakdown, it is apparent that efforts to find a single theory to explain breakdown should also explain why these differences occur. It is not the aim of this chapter to address these differences; this is left to chapter 7. In this chapter we discuss the vorticity dynamics of the torsionally driven cylinder, in the context of vorticity dynamics in the open pipe previously considered by Darmofal [9], [7], as discussed in chapters 4 and 3. If some understanding of breakdown in the pipe can be derived by considering the generation of azimuthal vorticity, then an examination of the dynamics of azimuthal vorticity in the cylinder may also shed some light on breakdown in that geometry.

First we define the cylinder, and describe how it will be studied numerically. We then validate results obtained from this geometry against other numerical and experimental results. In the previous chapter calculations of the components and generation of vorticity were verified by comparison with other work. We use the same numerical codes to calculate the vorticity components and generation terms here.

5.1 The cylinder geometry

A schematic of the cylinder was presented in figure 2.1 of chapter 2. In most of the visualisations to be presented in this thesis the cylinder will have the orientation shown in this figure, ie. rotating lid at the base. The Reynolds number Re is based on the cylinder radius R , the angular velocity of the lid Θ , and the fluid viscosity ν :

$$Re = \frac{\Theta r^2}{\nu} \quad (5.1)$$

The aspect ratio (AR) is simply height/radius. Re and AR uniquely define the flow.

5.2 Grid resolution and convergence considerations

For the Reynolds numbers considered the flow is axisymmetric about the cylinder axis, so it is sufficient to consider a single plane which includes the axis of the cylinder, as shown in figure 5.1.

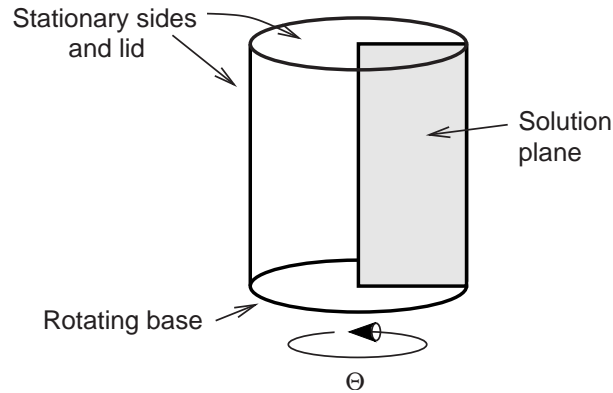


Figure 5.1: Solution domain for the axisymmetric torsionally driven cylinder problem.

A number of rectangular grids, both compressed and uncompressed, were tested for their ability to accurately represent the cylinder flow. A sample compressed grid (in this case 50×20) is shown in figure 5.2.

For the compressed grids the first 10% of elements (those closest to the rotating lid) were compressed sinusoidally, as were the last 10% of elements (those closest to the stationary lid). Also 10% of the elements in the radial direction were compressed using the same

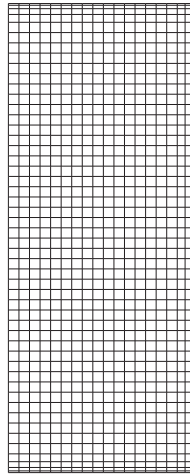


Figure 5.2: 50x20 torsionally driven cylinder mesh (cylinder axis is at the left edge.)

sinusoidal compression but only against the outer wall. The grid is compressed near the walls in order to capture the behaviour more accurately there - large gradients in velocity exist in the Ekman layer which forms near the rotating the lid and in (Stewartson) boundary layers associated with the cylinder walls, and these regions, especially the Ekman layer, play a large part in determining the solution for the entire domain.

Calculations were performed using the Fluent 4 code. Predictably, the compressed grids proved to be much better at resolving the boundary layers on the rotating end wall and the other stationary walls, so only compressed grids were considered for the rest of this study.

The selection of an appropriate grid was made by considering the change in the minimum streamfunction value as grid resolution was increased. As for the pipe, the minimum streamfunction value has commonly been used as it is a very sensitive measure of the flow state when breakdown is present. For the cylinder the maximum streamfunction value becomes the equivalent of the pipe minimum streamfunction value. All of the solutions have converged to a normalised velocity residual level of at least 3×10^{-7} . By this level of convergence the maximum ψ is accurate to within better than 1%. Table 5.2 shows the maximum streamfunction values for each grid considered.

Figure 5.3 shows in graphical form the variation in ψ_{max} with increasing grid resolution.

Based on these results the 202×82 grid was chosen, as it gives the required level of accuracy

Grid	ψ_{max}	% difference from 402x162 grid
52x22	2.059×10^{-7}	86.33
75x30	9.879×10^{-7}	34.40
102x42	1.431×10^{-6}	4.96
125x52	1.341×10^{-6}	10.91
152x62	1.387×10^{-6}	7.90
202x82	1.469×10^{-6}	2.43
252x102	1.488×10^{-6}	1.16
302x122	1.496×10^{-6}	0.64
402x162	1.506×10^{-6}	-

Table 5.2: Open pipe grid convergence.

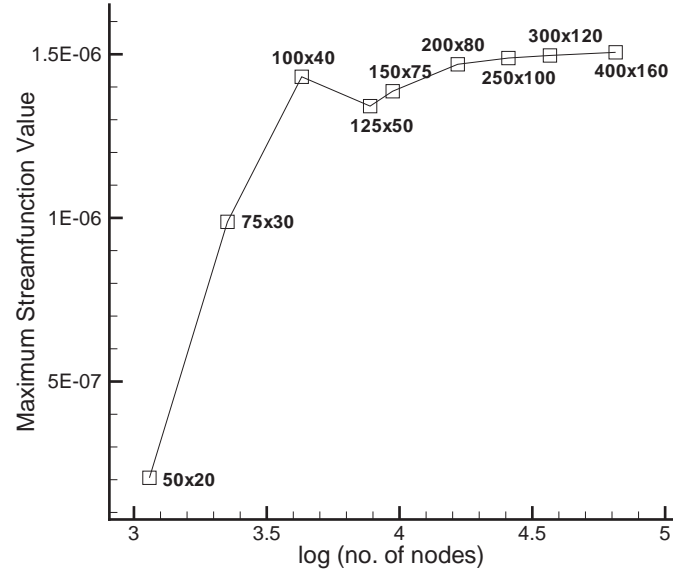


Figure 5.3: Open pipe grid convergence.

within a practical timeframe.

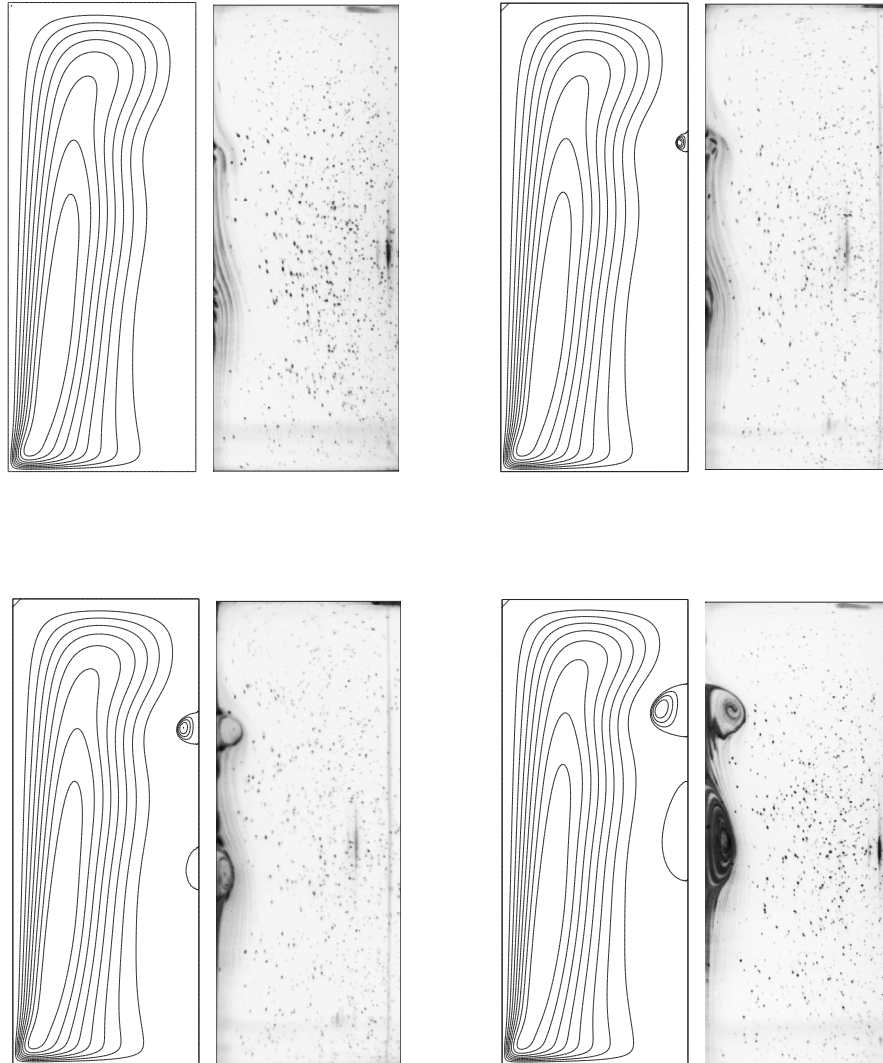


Figure 5.4: Numerical versus experimental results for $Re = 1902, 1933, 2001, 2252$.

5.3 Comparison of computational with experimental results

Figure 5.4 displays comparisons between the numerical results obtained here, with experimental results due to Graham *et al.* [24] for an aspect ratio of $AR=2.5$, and at $Re = 1902, 1933, 2001$, and 2252 . The streamline plots show very good agreement with the experimental dye visualisations.

In figure 5.5 we compare the results of Fluent 4 and Fluent 5 computations for aspect ratio $AR=1.5$ with results obtained by Gelfgat *et al.* [21]. The results are comparable, in

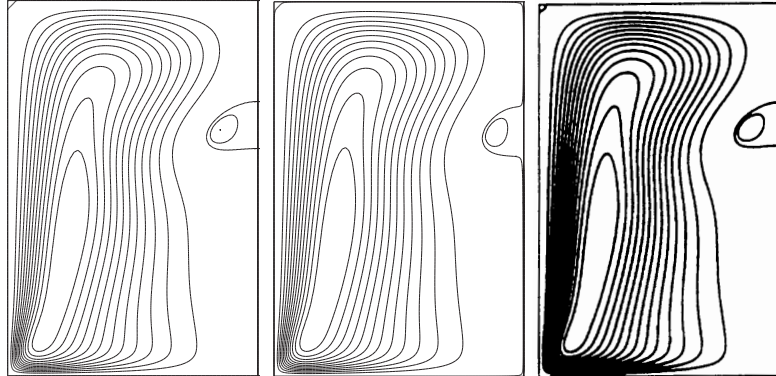


Figure 5.5: Comparison of results between Fluent 4 (left), Fluent 5 (centre) and Gelfgat *et al.* [21] (right) at $Re = 1500$, and $AR = 1.5$.

terms of the shape of the general flow, and recirculation bubble location and size. for both Fluent 4 and Fluent 5. However, there are distinct differences in bubble shape between Fluent 5 results and the other two; the cause of these differences is unknown.

5.3.1 Time dependence validation

To track the azimuthal vorticity generation and transport we will model behaviour of the flow in the cylinder with time. Initially we test Fluent's accuracy in modelling time dependent flows in the cylinder at the Reynolds numbers to be considered. Only Fluent 4 will be tested as this is the only code which will be used for the time dependent studies.

Comparison is made with streamline plots from Gelfgat *et al.* [21] for a cylinder with aspect ratio 1. Gelfgat *et al.*'s [21] results are for a Reynolds number of 3600. We obtain similar results for $Re = 3690$, a difference in Re of 2.5%. These results are presented in figure 5.6, to be compared with those from Gelfgat [21] in figure 5.7.

The order of progression is clockwise, and the plots are evenly spaced in time. The results compare well with those of Gelfgat *et al.* [21]. The flow is oscillatory, with a breakdown bubble evolving near the stationary wall of the cylinder. The bubble when it evolves is of comparable size and location to Gelfgat *et al.*'s [21] bubble, and the streamlines external to the bubble region have a very similar structure.

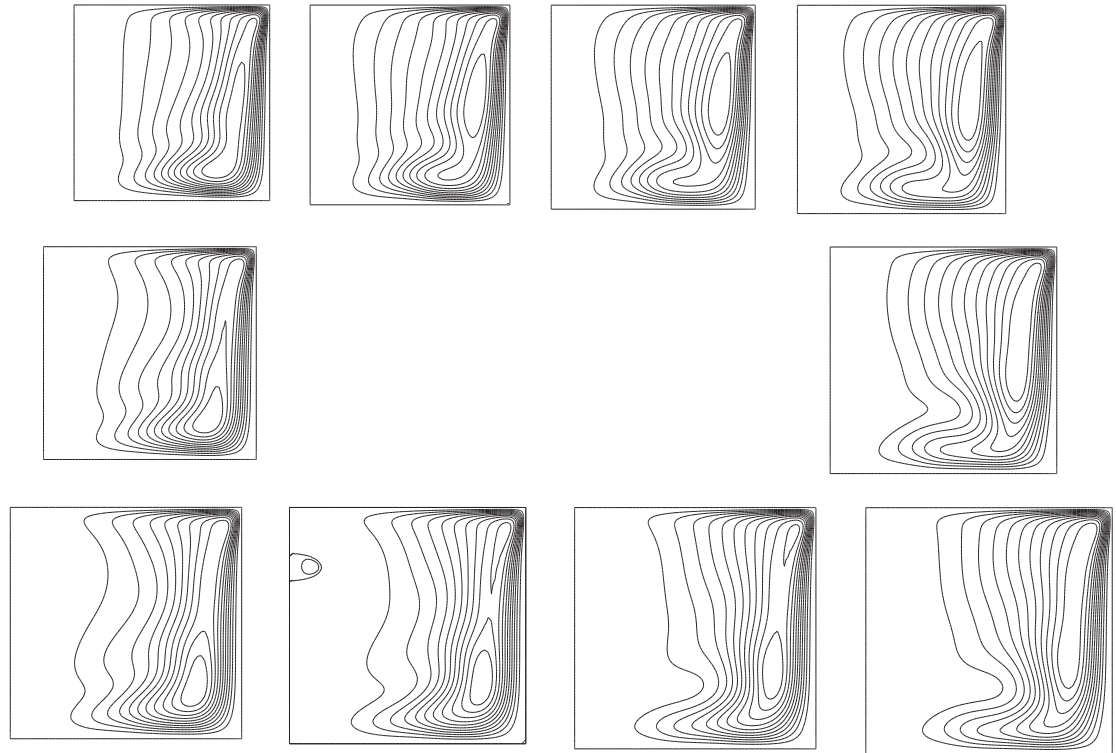


Figure 5.6: $AR = 1.0$ cylinder time dependent simulation. $Re = 3690$. Time increases in the clockwise direction.

5.4 The wave trapping hypothesis: present study

In this section we track the generation and transport of azimuthal vorticity in the torsionally driven cylinder. The aim is to compare azimuthal vorticity generation and transport in this geometry with that in the open pipe. Although the phenomenon of breakdown is the same, observations of vorticity dynamics in the cylinder are expected to be different to that in the pipe as a direct result of the differences in geometry:

- In the open pipe, there is one inlet from which all vorticity changes originate and propagate downstream. In the torsionally driven cylinder, the system is closed so flow downstream of breakdown recirculates to affect the flow upstream. Hence propagation of various elements in the cylinder is not as simple as in the open pipe

- The open pipe wall in the numerical experiments of Derrafel [7] is assumed to be

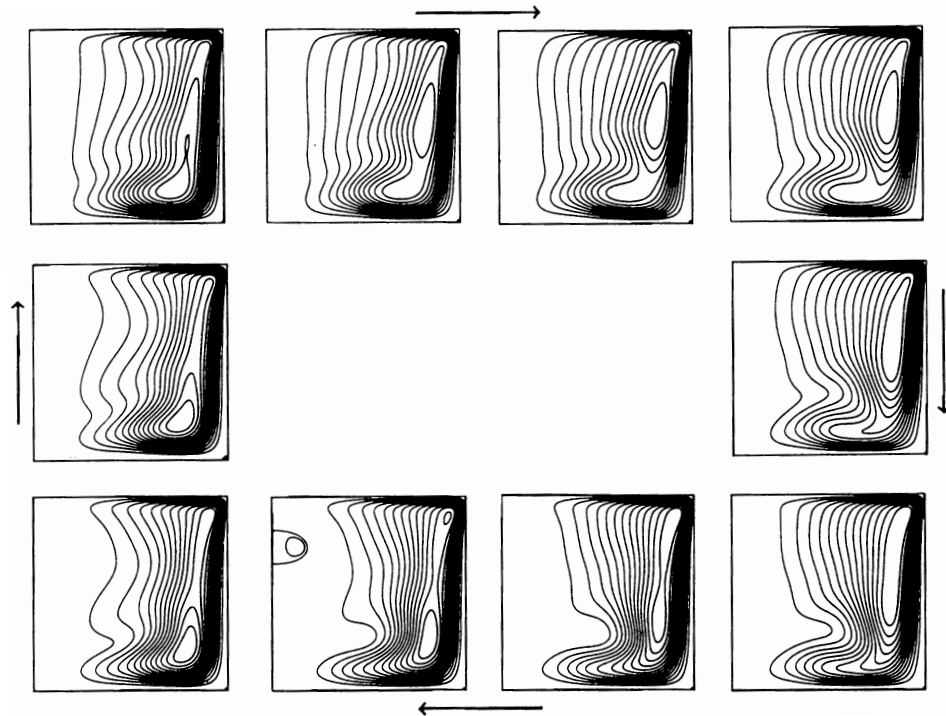


Figure 5.7: $AR = 1.0$ cylinder time dependent simulation from Gelfgat *et al* [21].
 $Re = 3600$. Time increases in the clockwise direction.

a significant role in the onset of breakdown.

5.5 Method

Expressions for calculating the vorticity components and generation terms in cylindrical polar coordinates were set out in chapter 4, along with verification of the method for the open pipe.

The aim here is to use these expressions to examine the generation and transport of the three components of vorticity individually for two scenarios:

1. a Reynolds number transition from a no-breakdown flow state (but some divergence of streamlines) to a flow with a single breakdown bubble, and;
2. an increase in Reynolds number which results in no change in streamline topology.

The second case is used as a baseline in order to identify elements of vorticity dynamics

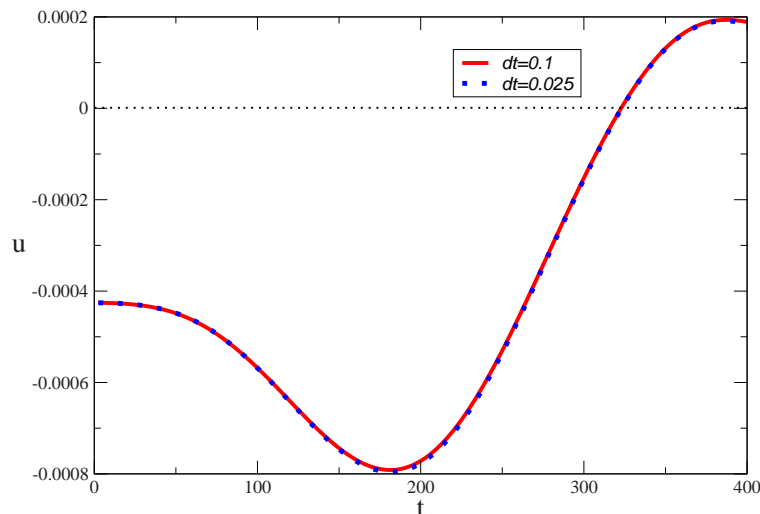


Figure 5.8: Timestep test: $dt = 0.1$ and $dt = 0.025$.

in the no-breakdown to breakdown transition which result from an increase in Reynolds number, without breakdown onset.

The initial (pre-breakdown) state is reached via a steady state calculation. For the first case, an initial condition Reynolds number of $Re = 1870$ is used, and for the second case $Re = 1400$. From these initial conditions the lid rotation rate is increased in a single step so that Reynolds number increases by 60 in both cases. The change has been kept relatively small to limit the size of transients. For the $Re = 1400$ to 1460 transition this results in only a small change in the $Re = 1400$ velocity field. At $Re = 1930$ breakdown appears, so the flow field which is initially at $Re = 1870$ undergoes transition to breakdown.

Runs conducted with two timesteps ($dt = 0.1$ and 0.025) for the 1870 to 1930 transition showed that a timestep of $dt = 0.1$ sufficiently resolves the temporal evolution of the flow. In figure 5.8 the axial velocity at a point in the domain where a breakdown bubble evolves is monitored. Each case is evolved to the point where the breakdown bubble appears (indicated by the change in sign of the axial velocity from negative to positive). The traces from the two timesteps are indistinguishable; hence the use of the timestep $dt = 0.1$.

The initial and final streamline plots are shown in figures 5.9 and 5.10. It should be noted that the states shown in figures 5.9 and 5.10 are not the final steady states - at this stage only the vorticity behaviour up to the point of evolution of the breakdown bubbles is being examined, so the final solutions are not required to be steady. Figure 5.11 illustrates how

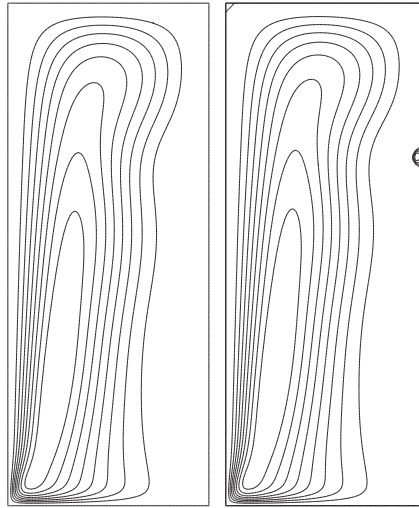


Figure 5.9: Initial (left) and final (right) streamfunction contours, $Re = 1870$ to 1930 transition.

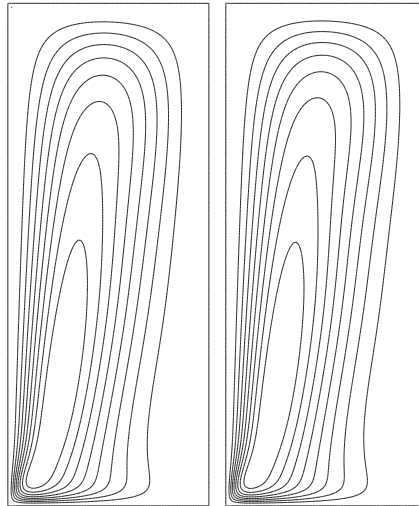


Figure 5.10: Initial (left) and final (right) streamfunction contours, $Re = 1400$ to 1460 transition.

the maximum and minimum streamvalues change with time. The two flat minima for the curve in figure 5.11(b) are caused by a small recirculation region at the corner furthest from the centre of the rotating lid - this region can be seen in figure 5.9 in the streamline plot with breakdown. This recirculation results in a small positive streamfunction value which provides a background to the positive streamfunction value produced at the bubble.

We focus on the behaviour of the azimuthal vorticity by plotting the perturbation az-

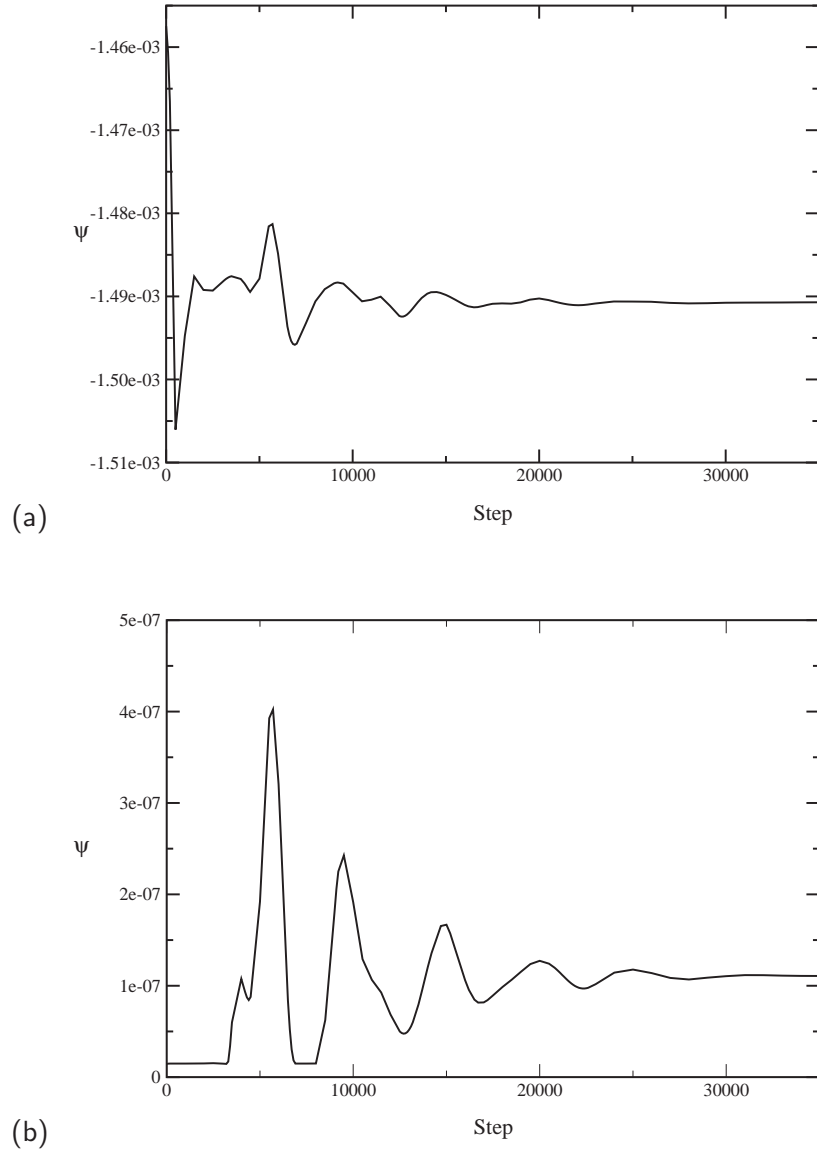


Figure 5.11: (a) Minimum and (b) maximum streamfunction value evolution against step number for the $Re = 1870$ to 1930 transition.

imuthal vorticity, $\delta\omega_\phi$, as defined in section 3.8, but the definition is repeated here:

$$\delta\omega_\phi = \omega_\phi - \omega_\phi(i) \quad (5.2)$$

where $\omega_\phi(i)$ is the azimuthal vorticity field for the initial condition.

Initially we plot the change in the azimuthal vorticity near the centreline of the cylinder as the Reynolds number is increased, in the same fashion as in Darmofal and Murman's [9] study. They observed a change in azimuthal vorticity which travelled downstream

following an increase in the swirl. A fraction of this downstream travelling wave became trapped near the location where vortex breakdown subsequently developed. In our study it is not possible to introduce a change in the swirl so cleanly as in the pipe, since there is no inlet from which changes are swept downstream, and the enclosed nature of the geometry means that downstream effects will eventually propagate back to the front of the bubble.

In figure 5.12 we plot the perturbation azimuthal vorticity along a line just offset from the centreline for successive timesteps in the same fashion as for the pipe study in chapter 3. (The initial results shown in figures 5.12 were produced using another commercial code, CFX. All further results in this section were produced using fluent.) Note that the orientation in these plots has the cylinder on its side, with the rotating lid to the left.

The upper plot displays the perturbation azimuthal vorticity for the $Re = 1400$ to $Re = 1460$ change. The final state displayed (top line) has a significant deficit in azimuthal vorticity. The development toward this state involves an initial decrease near the left (rotating lid) end, which propagates to the right, its progression slowing and amplitude increasing as the stationary end of the cylinder is approached. Hence the propagation of azimuthal vorticity change near the axis is in the reverse direction to the general flow along the axis.

The $Re = 1870$ to $Re = 1930$ transition appears quite different. The change in azimuthal vorticity becomes established near the location where breakdown is expected from $t=0$ (as evidenced by the small wiggles in the lines corresponding to the first few timesteps). The development of a large azimuthal vorticity deficit is apparent after some time, along with a surplus in azimuthal vorticity further from the stationary lid.

In the cylinder propagation of swirl and vorticity is complicated by the recirculation. Initially, convection could be expected to transport changes in vorticity around the outside walls of the cylinder to the top wall, then radially inward, and along the axis, as this is the general flow direction (this neglects production of vorticity along the way). At the point upstream of breakdown a situation analogous to that in the pipe was anticipated, where diverging streamlines result in the generation of more azimuthal vorticity, and, if sufficient azimuthal vorticity is generated, the formation of a breakdown bubble. The presence of a change in the azimuthal vorticity before sufficient time is allowed for convection to transport vorticity to that point on the axis indicates that this notion is overly simplistic.

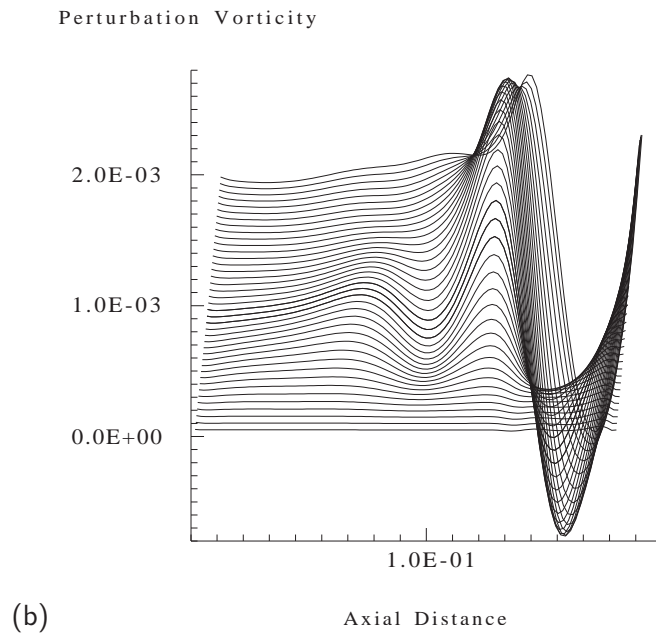
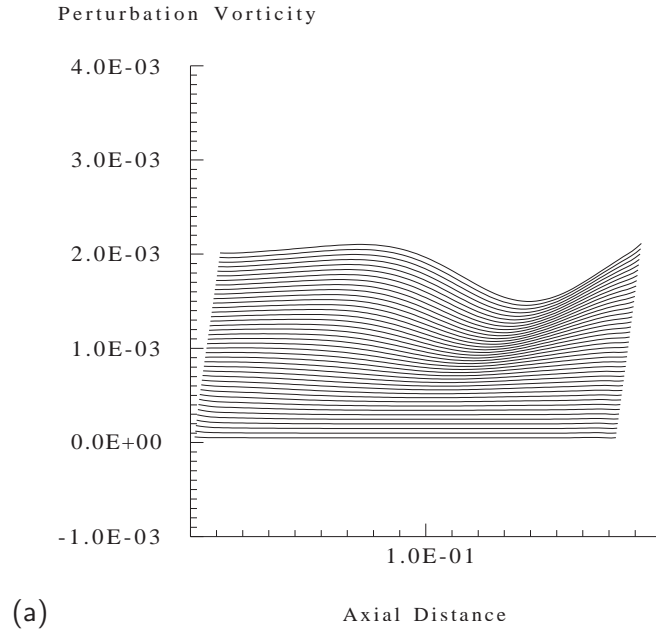


Figure 5.12: Perturbation azimuthal vorticity, $Re = 1400$ to 1460 (top) and $Re = 1870$ to 1930 (bottom) transition.

The method by which azimuthal vorticity is generated in the cylinder is also influenced by the fact that increasing the rotation rate of the lid not only increases the degree of swirl in the flow, but also axial velocities along the side wall and axis. Continuity determines that changes in the axial velocity near the rotating lid (produced by increased pumping of fluid away from the axis at the rotating lid end) are immediately communicated to the

opposite end of the cylinder. Hence changing the rotation rate results in the potential for an immediate change in various flow quantities, including the vorticity, at the stationary lid end of the cylinder.

This complicates the flow, and the analysis. It is not possible to gain sufficient insight into the production of azimuthal vorticity near the bubble location by examining solely the near-centreline azimuthal vorticity. It becomes necessary to examine azimuthal vorticity production over the entire domain. We pursue this analysis in the following section.

5.6 Vorticity propagation

Figures 5.13 to 5.15 show streamfunction, and changes in azimuthal vorticity, axial vorticity, and radial vorticity, from left to right, as time increases, for the $Re = 1870$ to 1930 transition. The equivalent plots for the $Re = 1400$ to 1460 transition are shown in figures 5.16 to 5.18. The centreline of the cylinder in all plots is to the right. Positive contours are represented by solid lines, and negative contours by dashed lines.

Inspecting $t = 50$ for the $Re = 1870$ to 1930 transition, all components are seen to grow at the lid and propagate from the corner where the rotating lid meets the stationary side wall. The contour levels are restricted to show how changes in vorticity propagate through the cylinder, so some areas, especially in the Ekman layer, have no contours plotted. Large velocity gradients exist at the lid and where the lid joins the wall, so we expect this region to be the dominant source of vorticity. Initially every component has a significant value along the side wall, and this is also expected - the change in pressure gradient along the wall caused by an increase in the rotation rate of the lid results in vorticity generation, as described in Morton [52].

The region of increased azimuthal vorticity sits next to a deficit along the wall until about half way along the wall, where it moves toward the centre of the cylinder. It becomes more significant on the centreline at about $t=200$. This explains why the attempt in the previous section to examine vorticity only along the centreline did not reveal how azimuthal vorticity is generated in front of the bubble. As opposed to the open pipe flow, vorticity in the cylinder needs to negotiate corners, so a one-dimensional examination does not capture its transport.

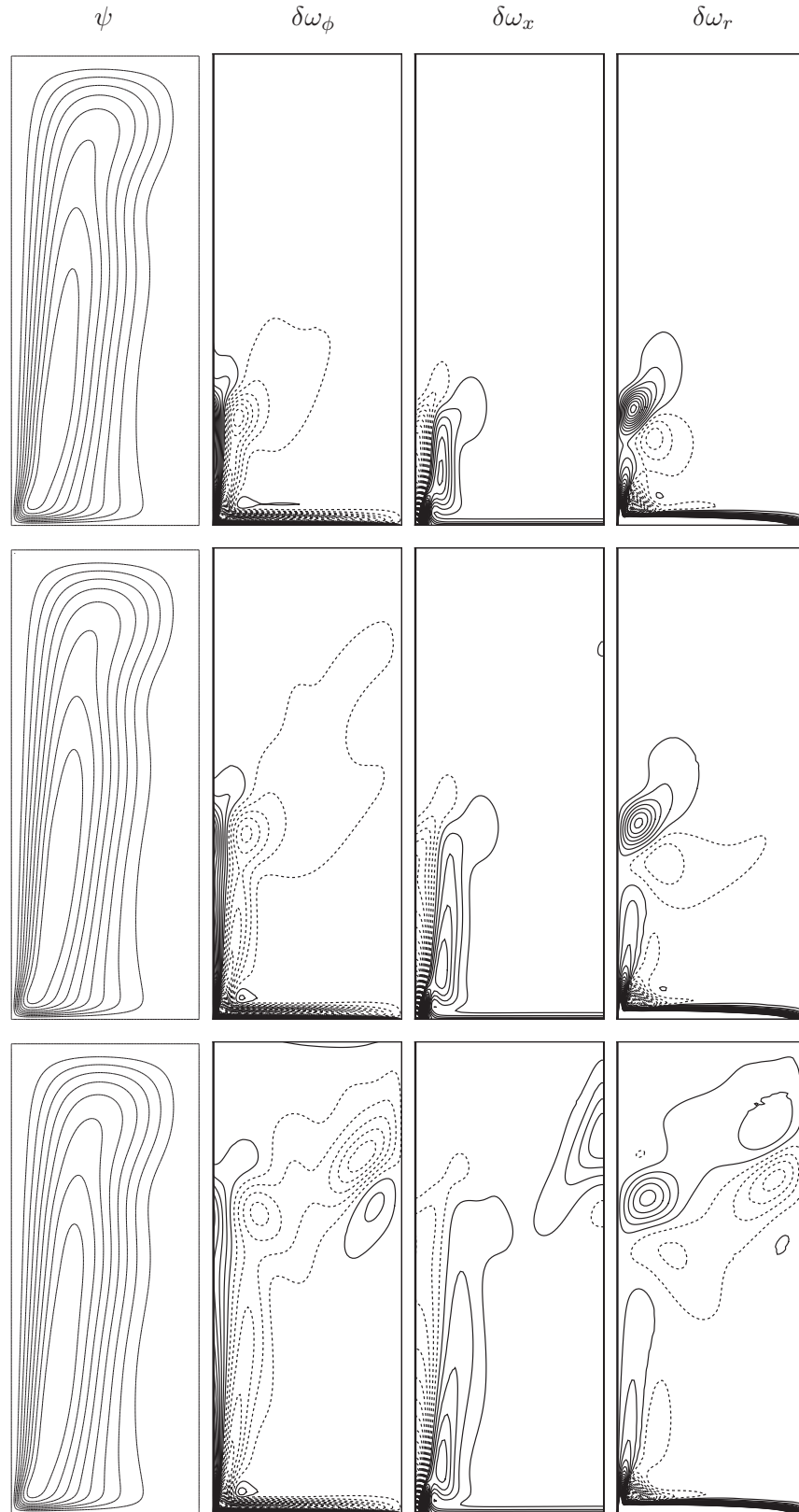


Figure 5.13: Streamlines and perturbation vorticity contours for $Re = 1870$ to 1930 transition. From top to bottom: $t = 50, 100,$ and 200 . From left to right: streamfunction, changes in azimuthal vorticity, axial vorticity, and radial vorticity.

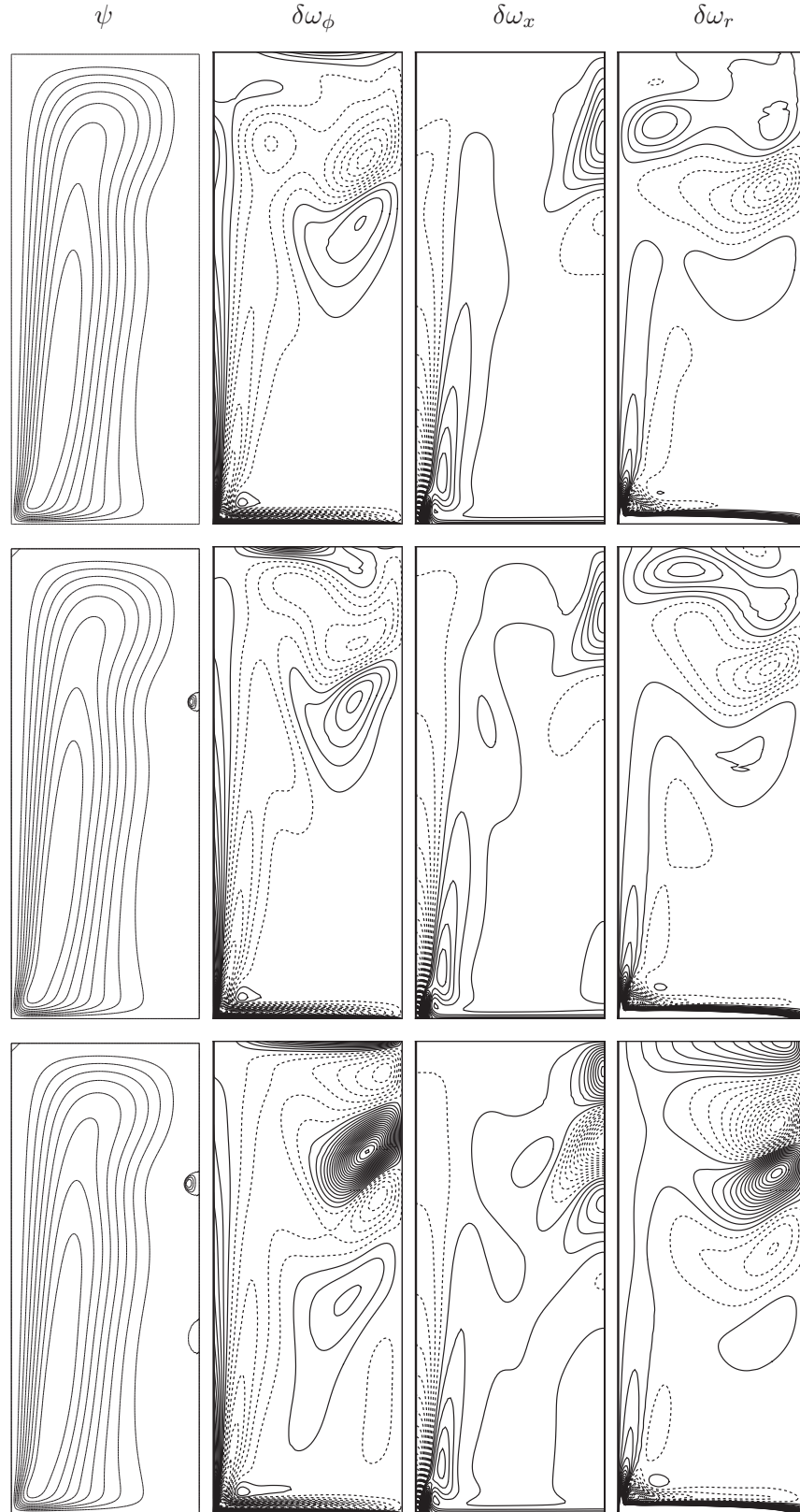


Figure 5.14: Streamlines and perturbation vorticity contours for $Re = 1870$ to 1930 transition. From top to bottom: $t = 300, 400,$ and 600 . From left to right: streamfunction, changes in azimuthal vorticity, axial vorticity, and radial vorticity.

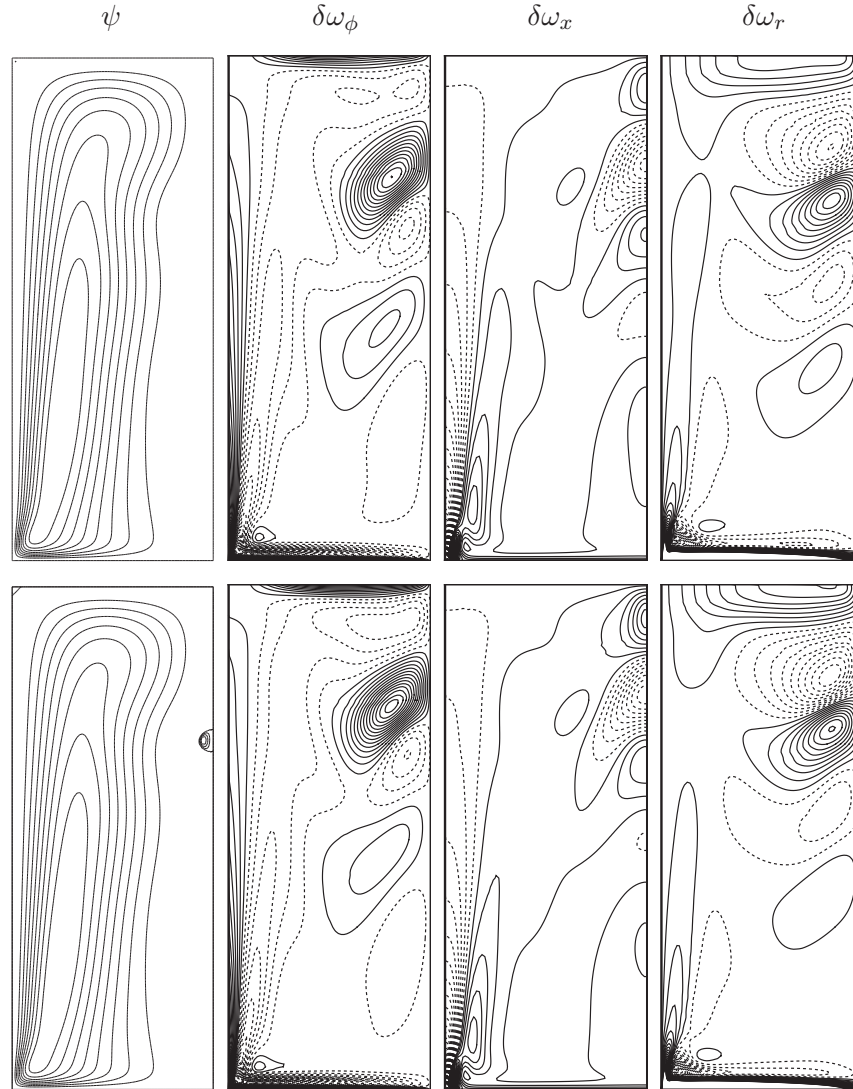


Figure 5.15: Streamlines and perturbation vorticity contours for $Re = 1870$ to 1930 transition. From top to bottom: $t = 750$ and 900 . From left to right: streamfunction, changes in azimuthal vorticity, axial vorticity, and radial vorticity.

It was expected at the start of this study that the generation of negative azimuthal vorticity along the cylinder walls and stationary lid would contribute significantly to the decrease in azimuthal vorticity on the axis and the subsequent evolution of a breakdown bubble. Figures 5.13 to 5.15 show that this azimuthal vorticity deficit decays as it propagates through the cylinder and becomes magnified in the region upstream of breakdown.

While there is a significant azimuthal vorticity deficit upstream of breakdown, another feature of these plots is the large increase in azimuthal vorticity at the breakdown bub-

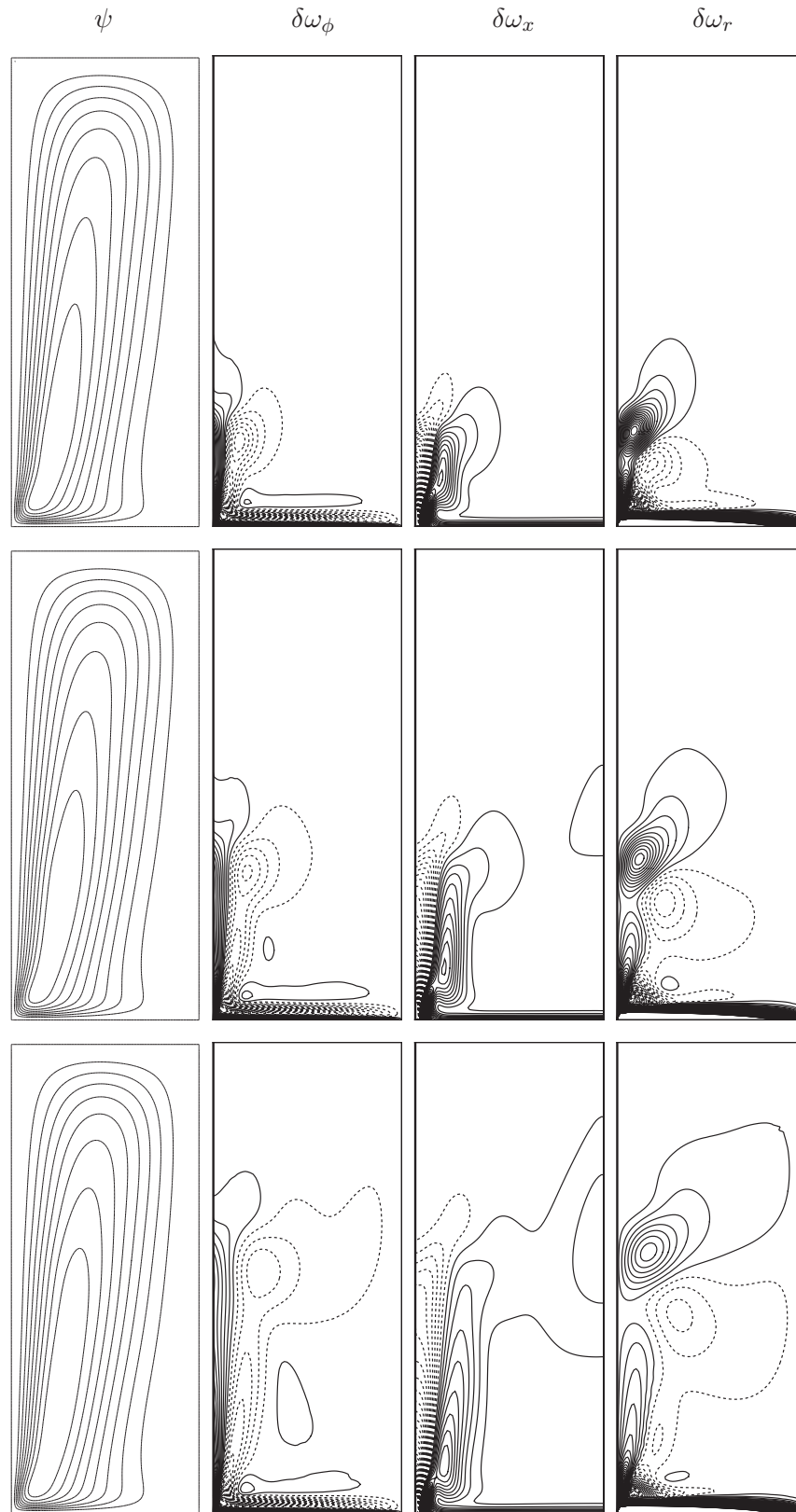


Figure 5.16: Streamlines and perturbation vorticity contours for $Re = 1400$ to 1460 transition. From top to bottom: $t = 50, 100,$ and 200 . From left to right: streamfunction, changes in azimuthal vorticity, axial vorticity, and radial vorticity.

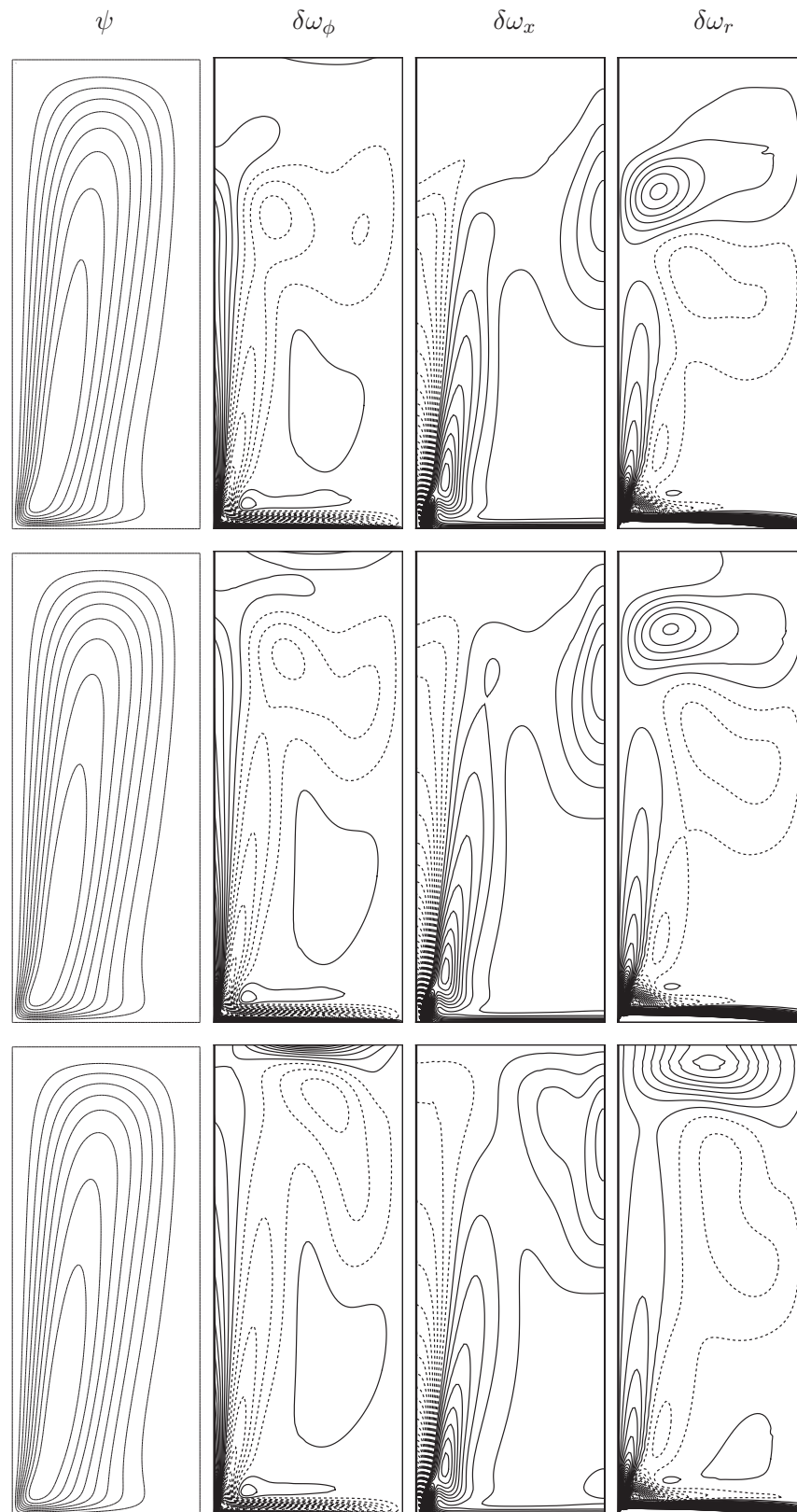


Figure 5.17: Streamfunction and perturbation vorticity contours for $Re = 1400$ to 1460 transition. From top to bottom: $t = 300, 400,$ and 500 . From left to right: streamfunction, changes in azimuthal vorticity, axial vorticity, and radial vorticity.

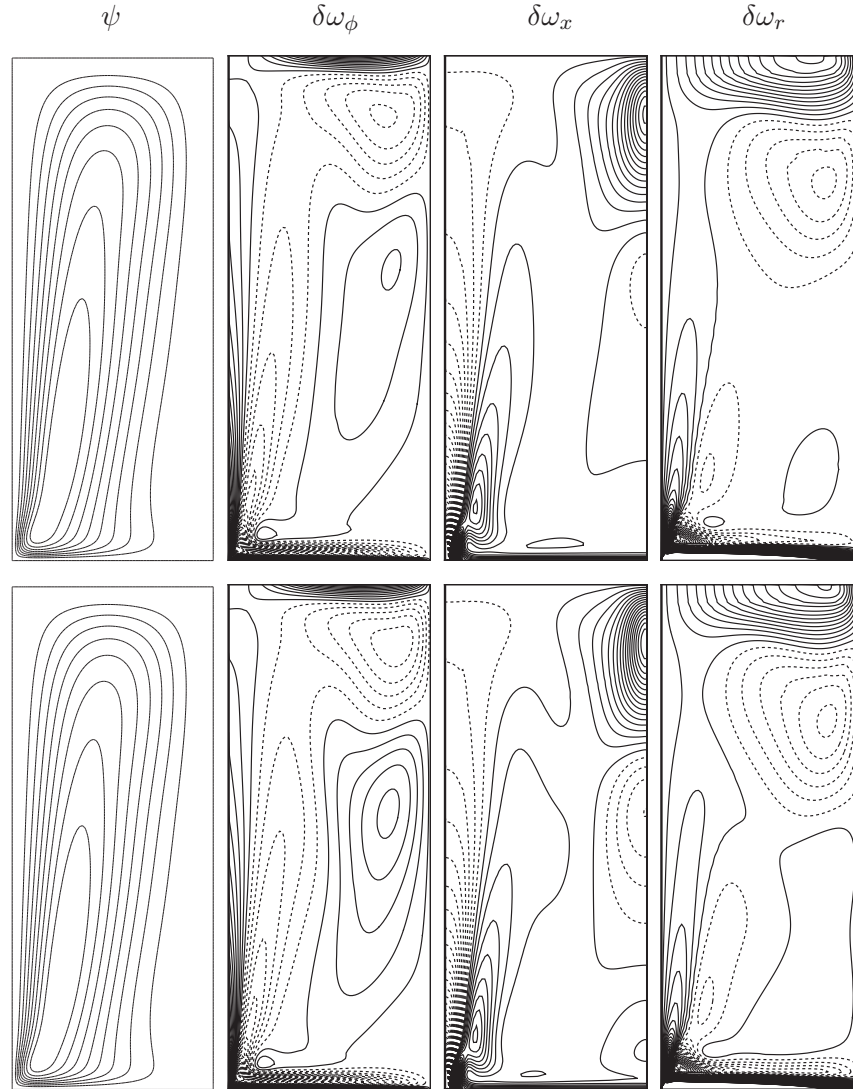


Figure 5.18: Streamfunction and perturbation vorticity contours for $Re = 1400$ to 1460 transition. From top to bottom: $t = 750, 900$. From left to right: streamfunction, changes in azimuthal vorticity, axial vorticity, and radial vorticity.

ble. The production of this positive azimuthal vorticity is necessary to return the vortex structure downstream of breakdown.

The axial vorticity behaves in a similar manner to the azimuthal vorticity. It propagates along the wall, then detaches half way and becomes established on the centreline. In the $Re = 1400$ to 1460 transition (figures 5.16 to 5.18) the vorticity change establishes a larger footprint on the centreline.

For the $Re = 1400$ to 1460 transition, the azimuthal vorticity travels through the cylinder

in a similar fashion to the $Re = 1870$ to 1930 case. The vorticity change reaching the centreline does so closer to the stationary lid for the $Re = 1870$ to 1930 breakdown case, and confines itself to a smaller region. The change in vorticity is more concentrated in the breakdown region for the transition at higher Reynolds number.

The most obvious difference between the two transitions is the absence of the region of increased azimuthal vorticity at the breakdown bubble for $Re = 1400$ to 1460 .

5.6.1 Velocity change propagation

The propagation of vorticity through the cylinder is partly a function of how the change in velocity propagates. Hence an examination of how the velocity change moves through the cylinder should help illustrate the vorticity dynamics. In figures 5.19 and 5.20 are plotted the change in axial and azimuthal velocity. Again the streamfunction contours are plotted on the left, and velocity change contours on the right.

From these figures it can be seen that the change in azimuthal velocity starts at the corner where the rotating lid meets the cylinder wall and propagates in the axial direction and diagonally toward the axis - The axial velocity change is communicated along the axis as well. So the azimuthal vorticity change moves through the cylinder in similar fashion to the azimuthal velocity change, i.e. it is convected initially along the outside wall of the cylinder, then is transported across the streamlines onto the centreline.

5.6.2 Vorticity generation

The propagation of extant azimuthal vorticity is one way of providing sufficiently negative azimuthal vorticity for the production of a breakdown bubble. The plots of figures 5.13 to 5.15 indicated that azimuthal vorticity is also being produced upstream of breakdown. This section examines the generation terms from the vorticity equation to show how sufficient azimuthal vorticity arrives upstream of breakdown.

In figure 5.21 we plot contours of the streamfunction (left), azimuthal vorticity (centre), and azimuthal vorticity generation.

The pattern of ω_ϕ generation in this aspect ratio $AR = 2.5$ cylinder is consistent with that observed in Gelfgat *et al.* [21] for an aspect ratio $AR = 1.7$ cylinder. There are large

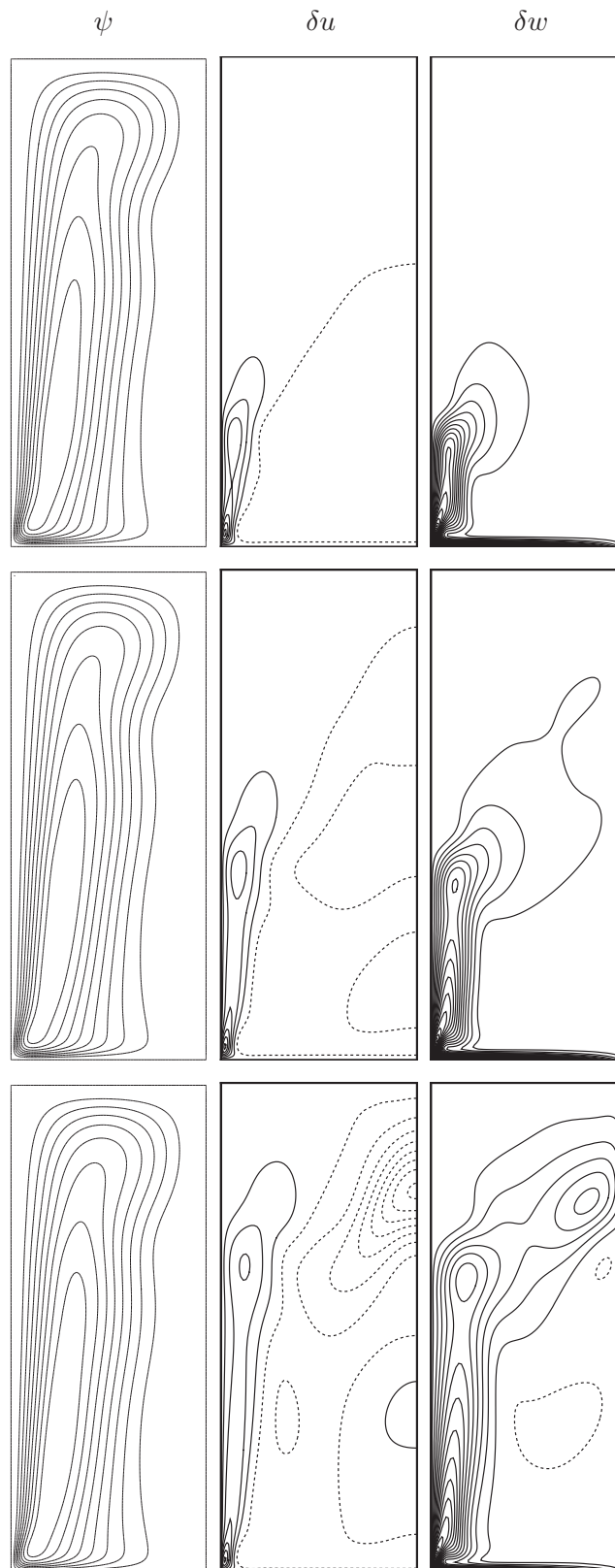


Figure 5.19: Streamlines and perturbation velocity contours for $Re = 1870$ to 1930 transition. From top to bottom: $t = 50, 100$, and 200 . From left to right: streamfunction, axial velocity, and azimuthal velocity.

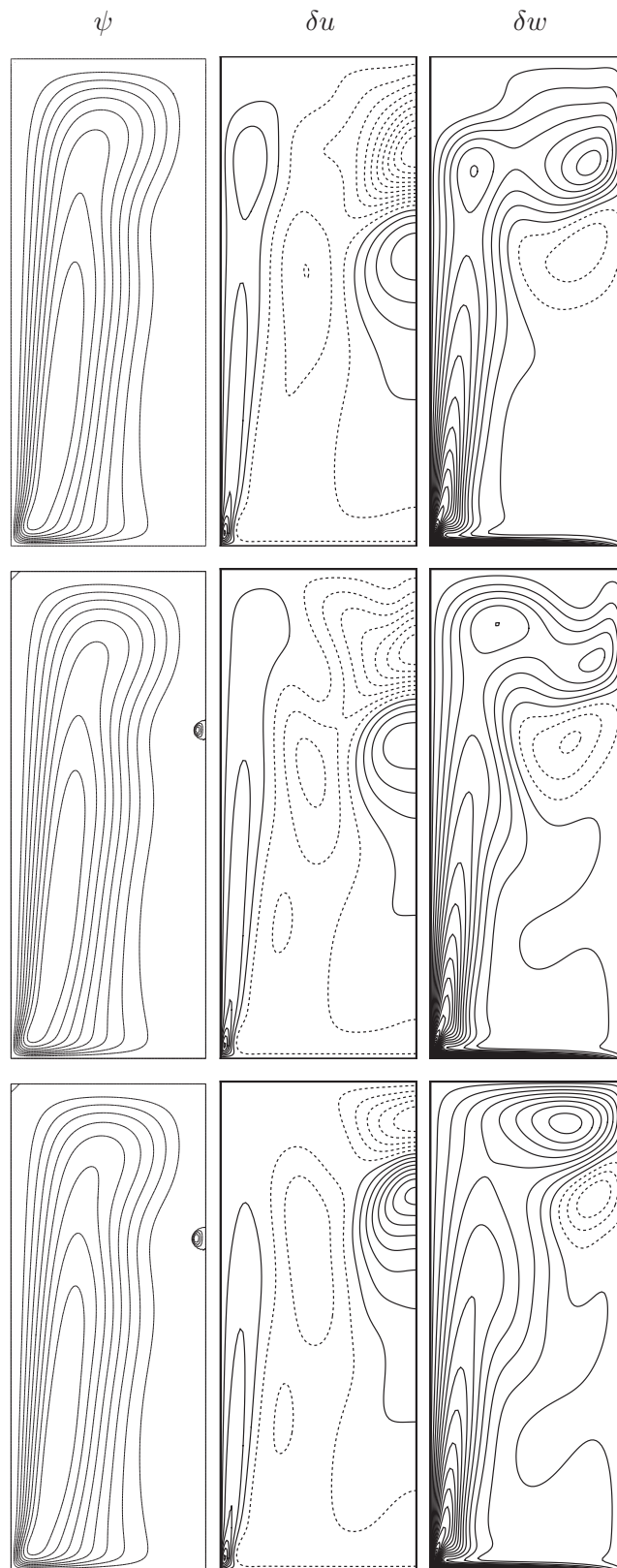


Figure 5.20: Streamlines and perturbation velocity contours for $Re = 1870$ to 1930 transition. From top to bottom: $t = 300, 400,$ and 500 . From left to right: streamfunction, axial velocity, and azimuthal velocity.

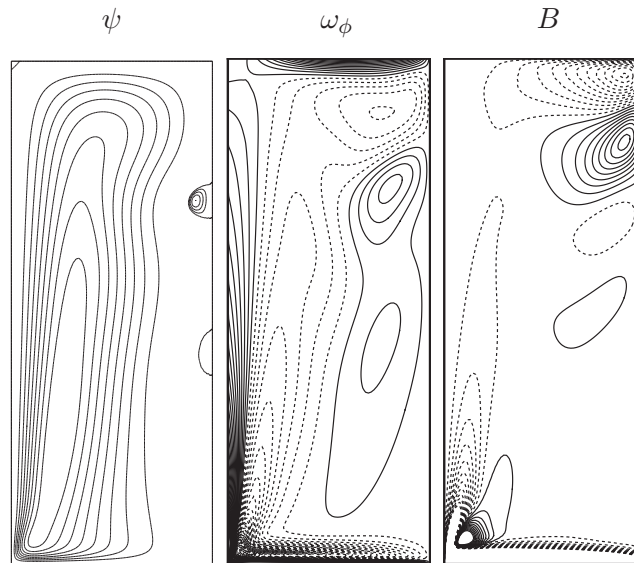


Figure 5.21: From left to right: streamlines, azimuthal vorticity, generation (without diffusion.)

amounts of negative ω_ϕ and negative ω_ϕ generation at the rotating lid, and at the corner where the rotating lid meets the stationary sidewall.

The high values in the Ekman layer have been excluded; most of the azimuthal vorticity is generated at the rotating lid and corner where the lid meets the stationary wall. It was expected that the axial and radial vorticity generation terms would have large magnitudes in this region, because they are directly affected by an increase in the lid rotation rate. The azimuthal component was not expected to be so directly affected by the lid because the lid's rotation has no component in the direction normal to its surface, although it does induce a gradient in u in the axial direction as flow away from the centreline is increased.

To allow visualisation of ω_ϕ generation near the breakdown bubble we exclude contours of the generation terms in this and future plots in the vicinity of the rotating lid. The plot of ω_ϕ shows that along the sidewall there is positive azimuthal vorticity due to the meridional flow boundary layer. Positive azimuthal vorticity is also present at the stationary end for the same reason.

The plot of ω_ϕ generation shows that away from the wall there is nett negative azimuthal vorticity generation. This approximately coincides with the region of negative ω_ϕ . Both ω_ϕ and the generation term reduce in magnitude as the flow convects toward the stationary

lid. Along the stationary endwall generation of negative ω_ϕ picks up again, so that in front of the breakdown bubble a region of negative ω_ϕ persists. In the returning axial flow the generation term changes sign, resulting in the generation of positive ω_ϕ just upstream of where the bubble forms, consistent with the presence of a large increase in ω_ϕ at the bubble shown in figure 5.15. The requirement for the flow to return to the axis requires more positive azimuthal vorticity; fluid around the bubble will have the same vorticity sense as that in the bubble.

Before drawing comparisons between the mechanisms of turning and stretching in the pipe and cylinder, we first examine the contribution from diffusion. Later work will show that the Reynolds number associated with the vortical core flow in the cylinder is much lower than that for the pipe. Hence diffusion is expected to play a more significant part in breakdown in the cylinder.

Figure 5.22 has on the left the generation term excluding diffusion, the diffusion term in the centre, and the generation term including diffusion on the right.

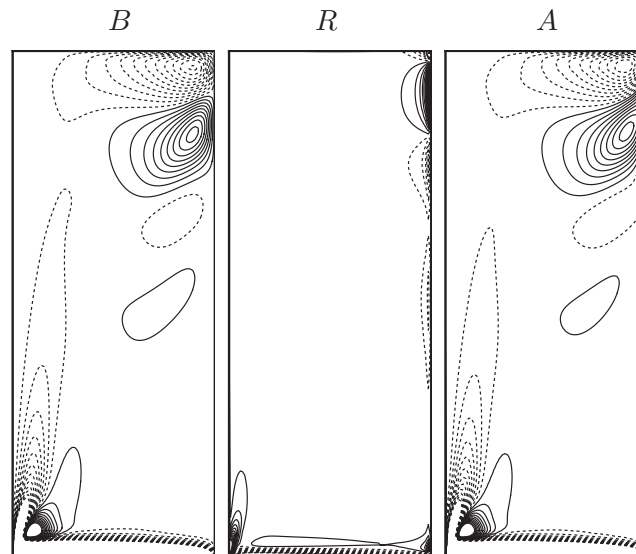


Figure 5.22: Left to right: azimuthal vorticity generation by stretching and turning B , contribution from the diffusion term R , and total azimuthal vorticity generation A (including diffusion.)

The diffusion term results in generation of positive ω_ϕ and is confined to the axis, as in the pipe flow. The Reynolds number is much lower here than at the lid, and hence viscous

diffusion of ω_ϕ becomes more significant, although the mechanism for breakdown has been shown in earlier studies to be fundamentally inviscid. However viscosity here appears to result in the moderation of negative ω_ϕ generation along the axis in front of the bubble, consistent with the pipe.

5.6.3 Stretching and turning

In the next series of plots the contributions to the generation term by stretching and turning are differentiated; we begin by plotting the contributions from these two terms in figure 5.23.

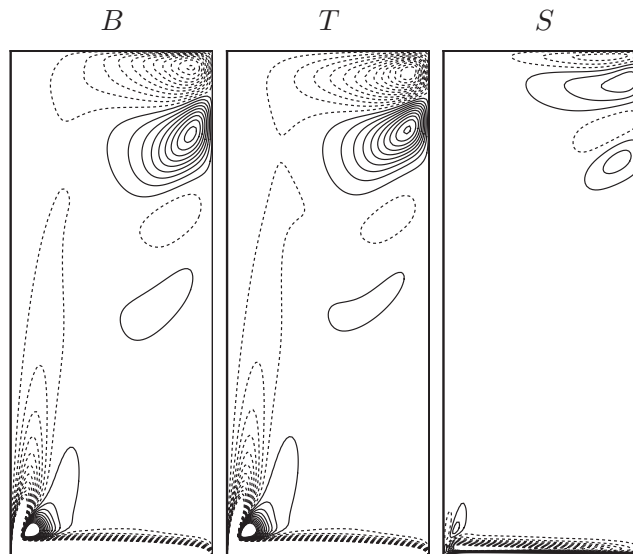


Figure 5.23: Left to right: azimuthal vorticity generation B , contribution from the turning term T , and contribution from the stretching term S .

Again the total ω_ϕ generation term (minus diffusion) is plotted on the left. In the centre is the contribution from the turning terms, and to the right the contribution from stretching. It is apparent from the figure that the majority of ω_ϕ generation upstream of breakdown arises through turning. This is in contrast to the situation for the open pipe, where initial negative ω_ϕ came from turning, and then a feedback process which depended on stretching took over. The requirement for the meridional flow, which transports the axial and radial vorticity through the cylinder, to negotiate corners most likely results in this discrepancy between generation mechanisms in the two geometries. Given that the turning

term appears to be the dominant mechanism for ω_ϕ generation in the cylinder, we further split it into its axial and radial turning components; see figure 5.24.

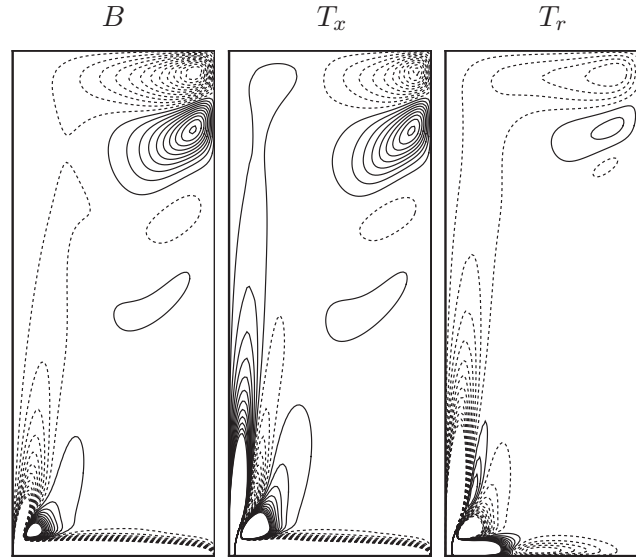


Figure 5.24: Left to right: azimuthal vorticity generation B , contribution from the turning of axial vorticity T_x , and contribution from turning of radial vorticity T_r .

Near the side wall the contribution from turning of axial vorticity is positive, while the contribution from turning of radial velocity is negative, so the two terms cancel each other out to some extent, and $|\omega_\phi|$ generation is reduced. Part way along the stationary endwall the axial vorticity turning term changes sign. From this point the two terms contribute to negative ω_ϕ generation, until the change in sign of both terms in front of the bubble. The turning of axial vorticity appears to contribute most to negative ω_ϕ production. This is not surprising given the base flow contains considerably more axial than radial vorticity; see figure 5.25.

Hence it appears that the same mechanism which dominates in the pipe, ie. stretching and turning of vorticity, contributes significantly to generation of negative azimuthal vorticity in the cylinder. The relative importance of these mechanisms is reversed in the cylinder though. Turning of vorticity, especially of axial vorticity, dominates negative ω_ϕ production upstream of breakdown.

The cylinder also has significant production at the lid, and this negative ω_ϕ does make

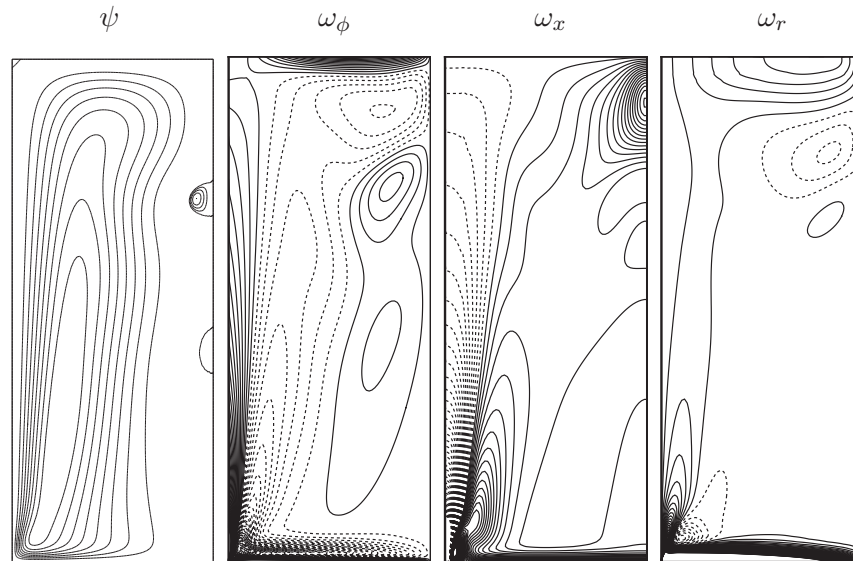


Figure 5.25: Left to right: streamfunction, azimuthal vorticity, axial vorticity, radial vorticity.

some contribution to the ω_ϕ found in the region upstream of where breakdown appears. It would be interesting to observe the effect on breakdown of removing the contribution from the lid; this is attempted in the “streampipe”, to be introduced in section 7.2.

5.6.4 Dependence of generation term on Reynolds number

The contributions from stretching and turning become more obvious if these terms are plotted with increasing Re ; see figures 5.26 to 5.30, which show ψ , ω_ϕ , B (total generation), S (stretching), and T (tilting), for $Re = 500, 1000, 1500$, and 2000 . For consistency all the generation term quantities are plotted with the same contour levels.

Between $Re = 500$ and 1000 the contour levels plotted do not show a significant change in B , S , and T near the centreline. ω_ϕ is negative along the centreline, as shown in the streamlines’ concave orientation away from the axis.

Increasing Re to 1500 results in a visible change on the axis. Turning is starting to produce ω_ϕ upstream of where breakdown is expected. The contribution from stretching is more minor, and is opposite in sense to turning away from the endwall. By $Re = 2000$ ω_ϕ generation is significant enough to result in the formation of two breakdown bubbles. The wavy nature of the axial flow is reflected in all the variables plotted. There is a large

amount of negative ω_ϕ generated near the endwall, followed by positive ω_ϕ generation just in front of and at the bubble. Production by stretching is largely opposite in sense and smaller in magnitude than that from turning, upstream of breakdown.

At $Re = 2500$ the region of ω_ϕ generation is becoming compressed axially as the bubble combination moves upstream.

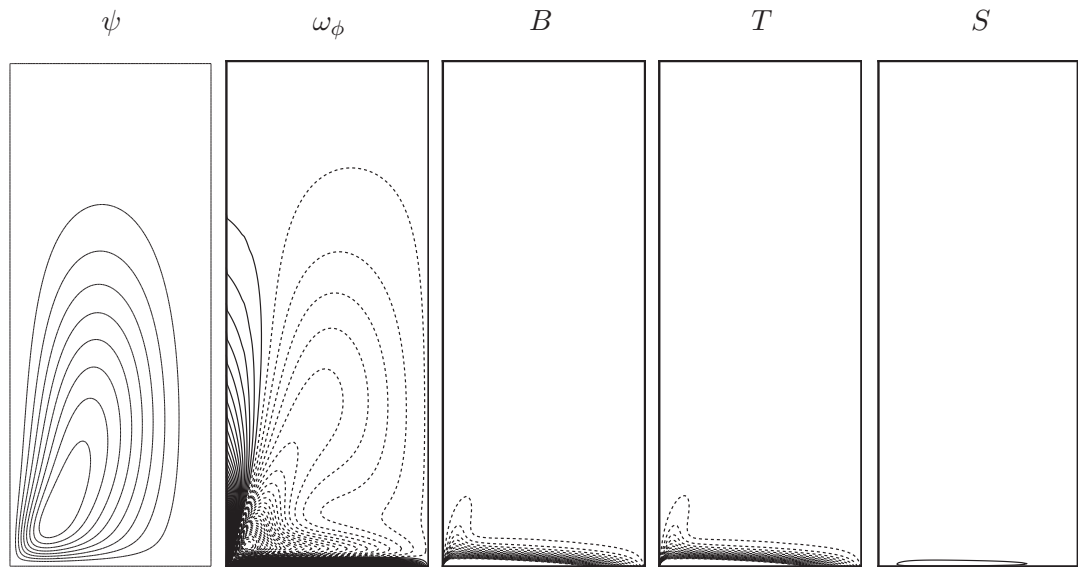


Figure 5.26: $Re=500$, from left to right contours of streamfunction, azimuthal vorticity, azimuthal vorticity generation, turning term, and stretching term. (B , T , and S plotted with 40 contour levels between -0.02 and 0.02).

5.7 Conclusions and further work

Although it is difficult to interpret wave trapping for the torsionally driven cylinder, a direct correlation can be seen between the generation mechanisms in the open pipe and in the torsionally driven cylinder. The most significant azimuthal vorticity generation in the cylinder occurs at the rotating lid, but of more relevance to breakdown is the region of vigorous negative azimuthal vorticity generation just in front of the bubble. This generation is the result of turning of axial and radial vorticity and the stretching of existing azimuthal vorticity, as for the open pipe. The relative importance of the tilting and stretching terms is reversed in the cylinder, with turning dominating the production of negative ω_ϕ .

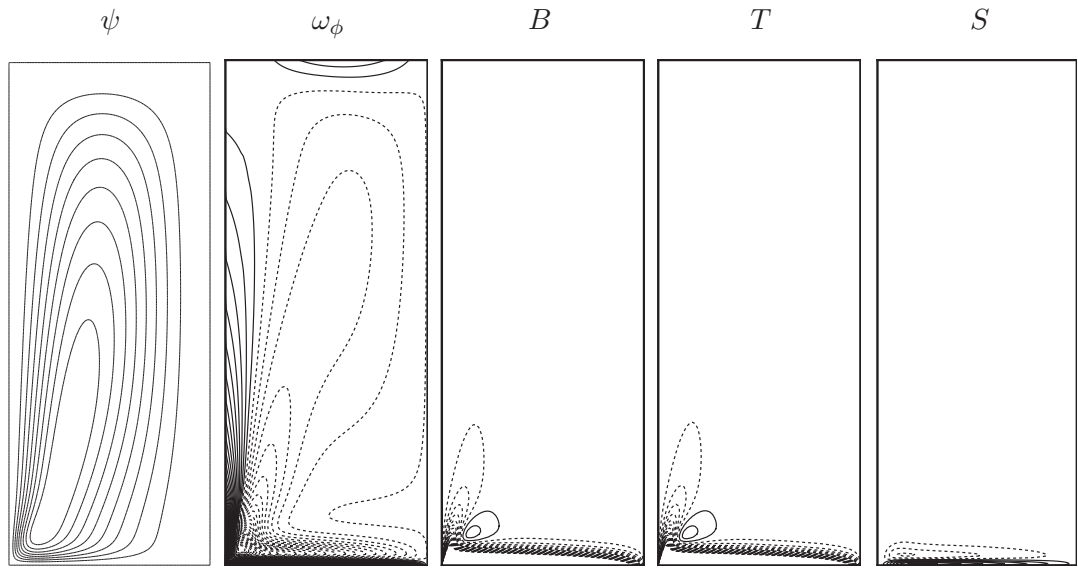


Figure 5.27: $Re = 1000$, from left to right contours of streamfunction, azimuthal vorticity, azimuthal vorticity generation, turning term, and stretching term. (B , T , and S plotted with 40 contour levels between -0.02 and 0.02).

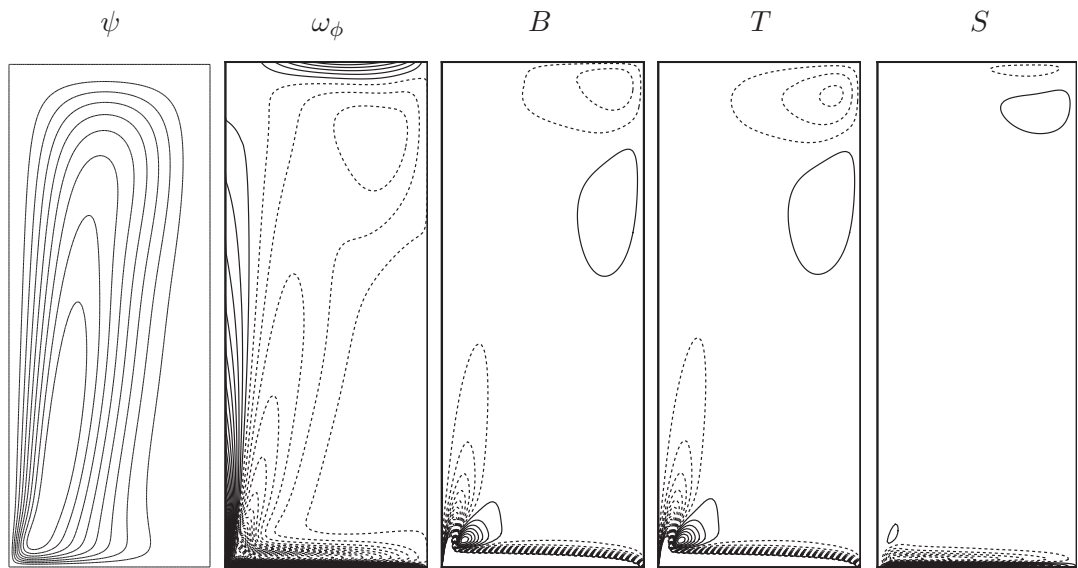


Figure 5.28: $Re = 1500$, from left to right contours of streamfunction, azimuthal vorticity, azimuthal vorticity generation, turning term, and stretching term. (B , T , and S plotted with 40 contour levels between -0.02 and 0.02).

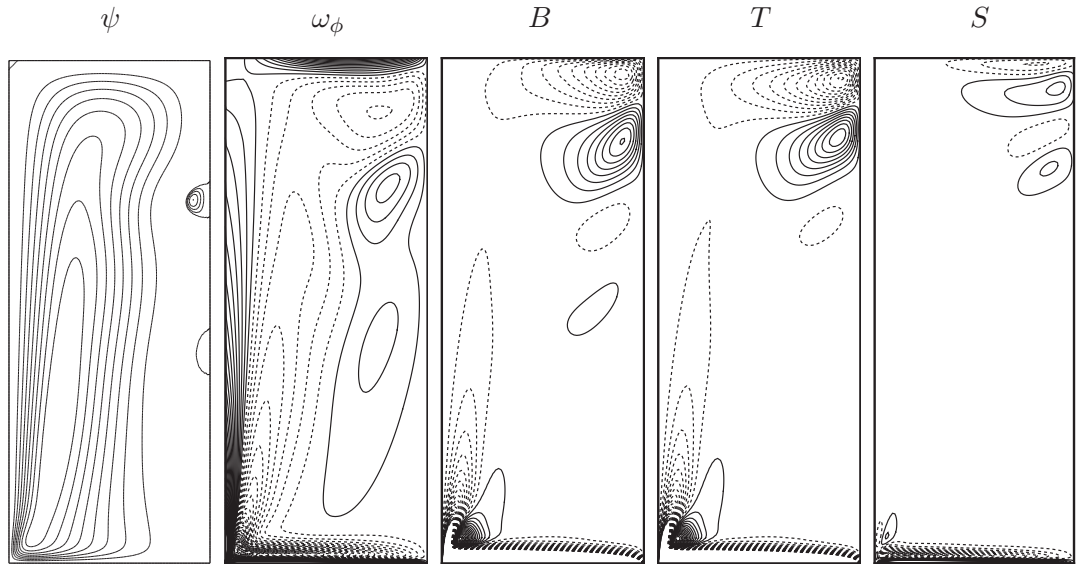


Figure 5.29: $Re = 2000$, from left to right contours of streamfunction, azimuthal vorticity, azimuthal vorticity generation, turning term, and stretching term. (B , T , and S plotted with 40 contour levels between -0.02 and 0.02).

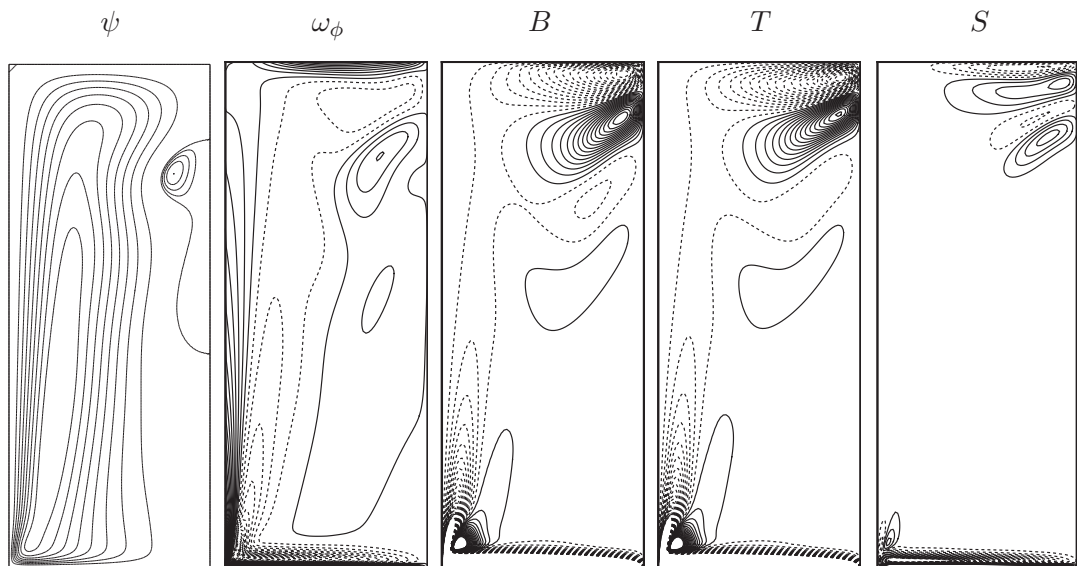


Figure 5.30: $Re = 2500$, from left to right contours of streamfunction, azimuthal vorticity, azimuthal vorticity generation, turning term, and stretching term. (B , T , and S plotted with 40 contour levels between -0.02 and 0.02).

Chapter 6

Breakdown control by a slip aerofoil

Chapters 3, 4, and 5, and the work of others have highlighted the role of the production of negative azimuthal vorticity in the mechanism for vortex breakdown. In this section we aim to effect some control on breakdown by directly influencing azimuthal vorticity production in the pipe.

The vorticity equation in chapter 3 described the contribution to the onset of breakdown of turning and stretching. Stretching refers to the generation of additional azimuthal vorticity by a change in the radial velocity. The equation which describes this component is repeated in equation 6.1:

$$S = \frac{\omega_\phi v_r}{r}. \tag{6.1}$$

Once turning of vorticity into the azimuthal direction has occurred, Darmofal [8] showed that the main mechanism for the generation of azimuthal vorticity in the pipe is stretching. By reducing the magnitude of the stretching term it is anticipated that a reduction in azimuthal vorticity, and a delay in the onset of breakdown, would result. In this study we attempt to control the production of $-\omega_\phi$, and hence the onset of breakdown, by directly influencing the stretching mechanism. Since stretching is dependent on a radial outflow u_r , contributions from stretching may be controlled by modifying u_r .

A number of methods were considered for modifying u_r in the pipe. These include:

- placing a flow modifier in the vortex core;
- blowing fluid radially inward;
- sucking fluid from the pipe axis.

In this section we study the effect of a flow modifier. The device we use is an artificial aerofoil. It is artificial in the sense that it is not a practical device, but is only used here as a method of directly affecting the radial outflow.

The aerofoil introduced here has zero shear stress specified on its surface. This ‘slip’ aerofoil is used because it has the effect of altering the radial velocity, which is its purpose, while having a much smaller effect on the flow than a normal aerofoil. A normal aerofoil results in significantly retarded axial flow downstream, and large flow structures which complicate the situation. Since the geometry is again axisymmetric, the aerofoil actually corresponds to a cylindrical structure around the vortex core.

Initial studies using a flat plate at various angles to the flow effected little control over the bubble, and often made the situation worse as the bubble would frequently become attached to the plate. Hence only results for the aerofoil are presented.

A NACA0012 aerofoil with unit length is used. The pipe at $\Omega = 1.45$ and $Re = 500$ is used initially because it results in a flow which only marginally enters the breakdown regime - the bubble is relatively weak. Hence the effect of the aerofoil is expected to be more obvious.

6.1 Mesh study

The introduction of an object into the pipe results in an added degree of complexity when it comes to mesh considerations.

In the grid resolution study the Reynolds number and swirl are set at $Re = 500$, and $\Omega = 1.45$. Given the sensitivity of the bubble to resolution, a solution with breakdown should give a good indication of grid convergence. Because of the larger meshes required to accurately represent flow around the aerofoil it was necessary to further optimise the meshes external to the aerofoil in order to achieve a result within a reasonable timeframe. First compression is applied upstream, downstream, and radially away from the location

where breakdown is expected without the aerofoil. The result is greater node spacing for regions external to the breakdown bubble than was used for the earlier studies. Table 6.1 and table 6.2 show that this grid optimisation still gives adequate resolution for the pipe with no aerofoil.

Mesh	No. of nodes	u_{min}	% diff.
358×41	14,678	-0.1521099	0.3%
358×62	22,196	-0.1516608	

Table 6.1: Radial grid convergence test.

Mesh	No. of nodes	u_{min}	% diff.
358×62	22,196	-0.147032	0.4%
496×62	30,752	-0.1476081	

Table 6.2: Axial grid convergence test.

In addition, three quantities based on bubble location and dimensions were compared with those in Beran and Culick's [4] study. The comparison is shown in table 6.3. Again no aerofoil is present.

Mesh	Distance to stagnation point	Distance to trailing edge	Maximum width
358×41	0.2929	0.5080	0.0275
B&C [4]	0.3154	0.4538	0.0248
Difference	7%	12%	11%

Table 6.3: Comparison with Beran and Culick [4].

The last row indicates the difference between our measurements and those from Beran and Culick [4]. The match between these breakdown locations and sizes is reasonable, given the difference in the outlet geometries (this study has a converging outlet; Beran and Culick's [4] pipe does not).

Based on the above study the 358×41 mesh was used as the basis for resolving the flow external to the aerofoil.

Next the aerofoil is introduced. It was decided that the most efficient strategy would be

a combination of structured and unstructured meshes, and consists of triangular elements in the region surrounding the aerofoil, and rectangular elements elsewhere; the mesh in figure 6.1 is representative of those tested.

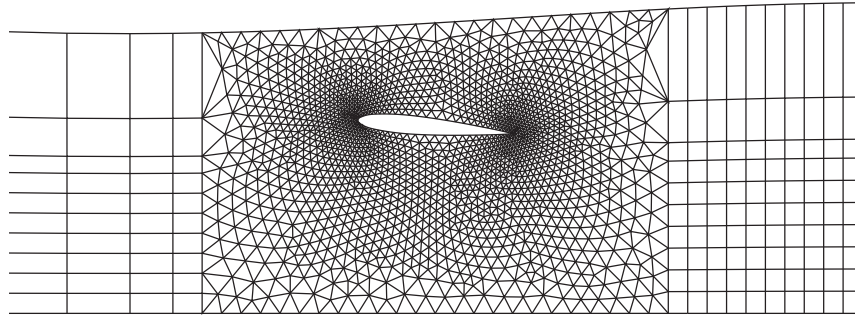


Figure 6.1: Example of tri/quad mesh used for aerofoil in pipe study.

The mesh in figure 6.1 has a node density much lower than that of the actual mesh used, but it shows the grid strategy used for this study. Various unstructured meshes were inserted into the 358×41 external mesh; In this test we use a monitoring point within the bubble region to reveal the velocities present there; this region is very sensitive to grid resolution (for reference the monitoring point is at $x = 10.7$, $y = 0.17$). An aerofoil is positioned so that its centre is at $x = 6.5$ and $y = 0.4$. The grid performances in table 6.4 were recorded.

Mesh	Number of nodes	Monitoring point axial velocity	% diff
1.50mesh	51519	-0.052521132	2.7%
2.25mesh	96774	-0.051098809	

Table 6.4: Aerofoil trimesh convergence test.

Of the grids tested the 1.50 grid gave sufficient accuracy; it provides a result for the monitoring point axial velocity within 3% of that for the finest mesh.

6.2 The effect of varying angle of attack

We begin by investigating the effect of angle of attack when the centre of the aerofoil is at $x = 6.5$, $y = 0.4$, where x and y are the axial and radial ordinates, respectively. This is just upstream of where breakdown is observed, and at 40% of the vortex core radius. The test is conducted at $\Omega = 1.45$, $Re = 500$, as breakdown is present in the pipe with no aerofoil at these values. Streamline plots in figure 6.2 show that with increasing angle of attack the bubble size decreases, and the leading edge of the bubble moves downstream. The largest effect on the bubble is realised by the 7.5° aerofoil; the bubble nearly disappears in this case.

It was not possible to obtain converged steady solutions for angles of attack greater than 7.5° . Unsteady calculations showed that beyond this angle of attack the bubble began to attach itself to the aerofoil, and shedding from the trailing edge of the bubble was observed. Results for angles of attack beyond 7.5° were not pursued any further.

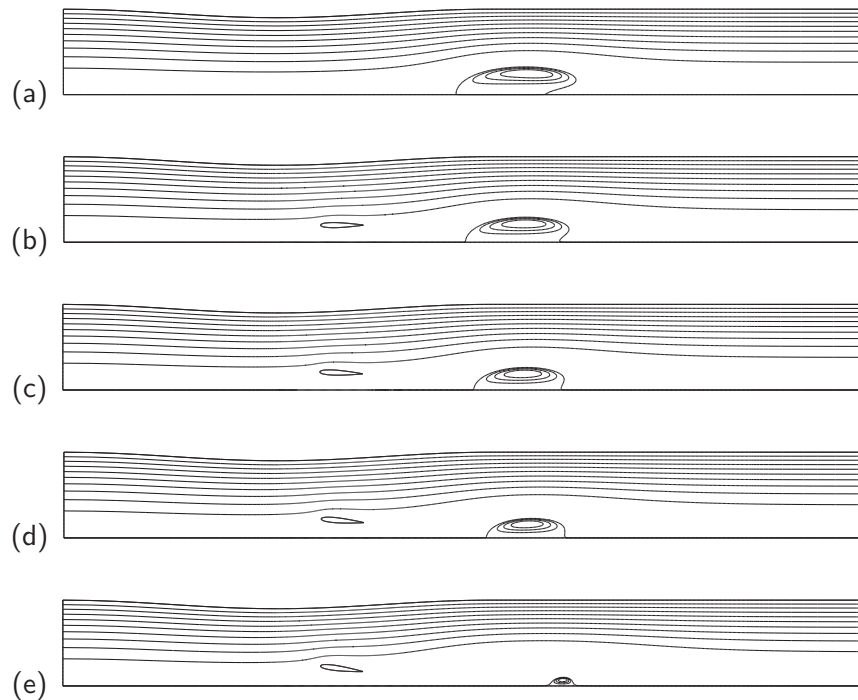


Figure 6.2: Streamline contours for the open pipe with: (a) no aerofoil, (b) aerofoil at $AOA = 0^\circ$, (c) $AOA = 2.5^\circ$, (d) $AOA = 5^\circ$, (e) $AOA = 7.5^\circ$, $\Omega = 1.45$, $Re = 500$.

The centreline axial velocity profile for each of the cases in figure 6.2(a) - (e) is plotted in

figure 6.3.

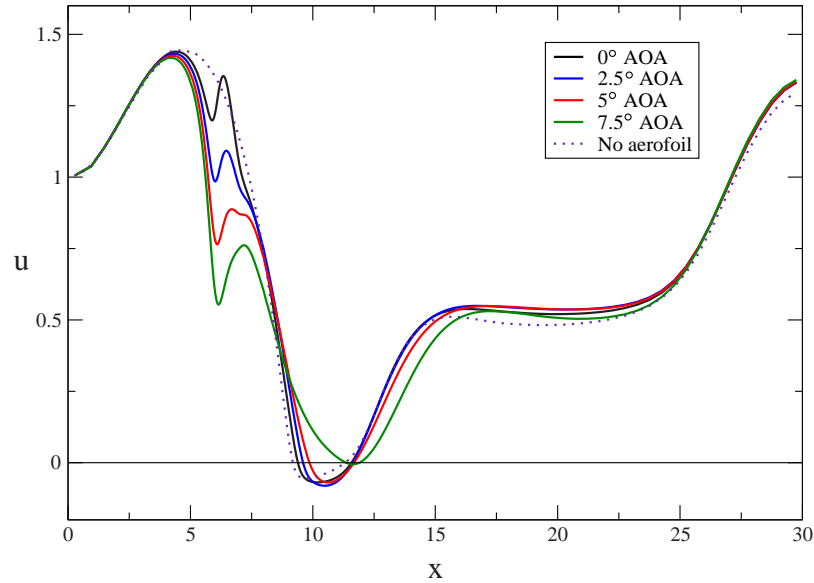


Figure 6.3: Axial velocity along the centreline for various aerofoil AOA: AOA = 0° , 2.5° , 5° , 7.5° . $\Omega = 1.45$, $Re = 500$.

The case without an aerofoil present is represented by a dotted line. The effect of the aerofoil at $x = 6.5$ is obvious in this plot; the axial velocity decreases, then peaks again before stagnating at the front of the breakdown bubble. The 0° , 2.5° , and 5° angle of attack cases appear to slightly decrease (make more negative) the minimum axial velocity, compared to the no-aerofoil case. This would normally imply that the bubble is becoming larger, however the streamlines in figure 6.2 show that all of these angles of attack result in a reduction in size of the breakdown bubble.

The result for angle of attack 7.5° is more dramatic, with the minimum axial velocity approaching zero.

It transpired in later runs for varying aerofoil position that unsteady solutions for angle of attack 7.5° showed the same shedding behaviour observed for angle of attack greater than 7.5° . Given this response of the flow to angles of attack of 7.5° and greater, the optimum angle of attack probably lies in the region 5° to 7.5° .

For the remainder of this study we use an angle of attack of 5° , which still has a significant effect on breakdown. It will be shown in subsequent sections that it is possible to eliminate breakdown using the AOA = 5° aerofoil by varying the aerofoil location.

6.3 The effect of varying aerofoil radial location

In the next series of tests the angle of attack is fixed at 5° , and the aerofoil is progressively moved further away from the axis. The axial location is still set at $x = 6.5$.

The results in plots 6.4(a) to (f) show the effect on the breakdown bubble for $\Omega = 1.45$ and $Re = 500$.

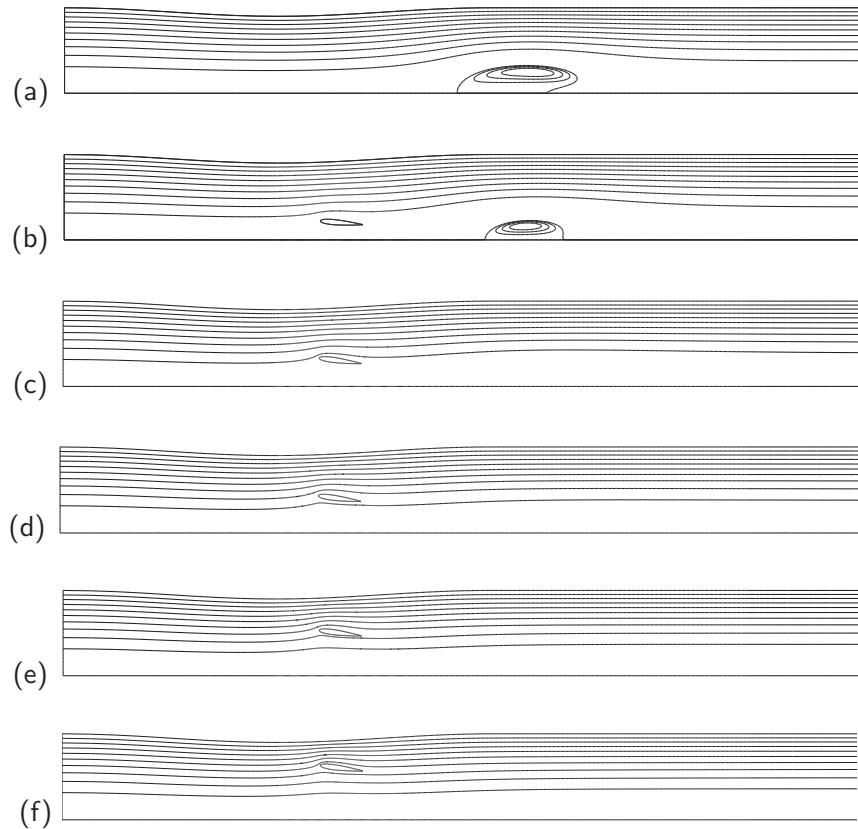


Figure 6.4: Streamline contours for the open pipe (a) without aerofoil, then with aerofoil at 5° AOA, varying location of aerofoil centre: $x = 6.5$, (b) $y = 0.4$, (c) $y = 0.6$, (d) $y = 0.8$, (e) $y = 1.0$, (f) $y = 1.2$. $\Omega = 1.45$, $Re = 500$.

The solution without an aerofoil is represented in plot 6.4(a). The first case with an aerofoil installed, plot 6.4(b), was included in the previous figure 6.2 for angle of attack 5° . With each successive plot the aerofoil is moved further from the axis.

In plot 6.4(c) the bubble has already disappeared. Further increasing the radial distance results in a noticeable straightening of the streamlines downstream of the aerofoil. The radial location is not increased beyond $y = 1.2$ as wall effects are probably becoming

more significant, although we are not too concerned with these effects since this is only a qualitative look at the effect of the aerofoil. We are not measuring lift or drag, for example.

In figure 6.5 the axial velocity along the centreline is again plotted to more clearly resolve the effect of the aerofoil once the bubble has disappeared.

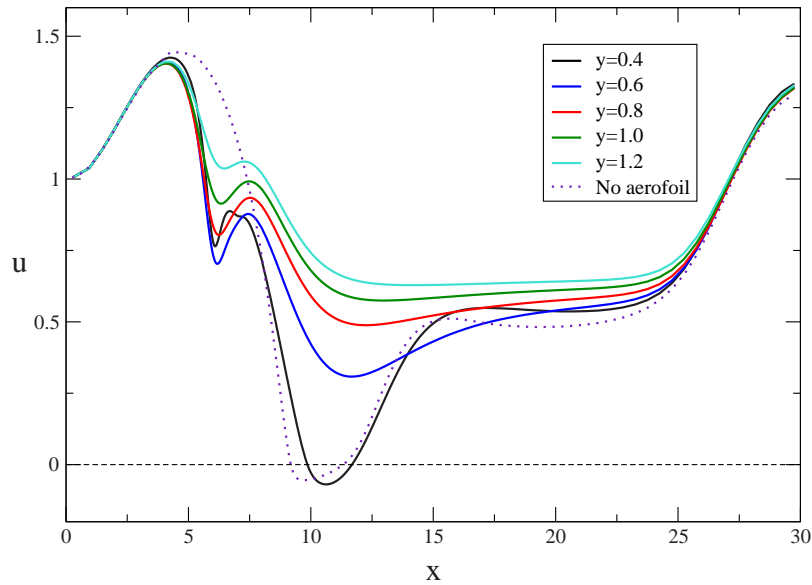


Figure 6.5: Axial velocity along the centreline for various aerofoil positions: 5° AOA, $x = 6.5$, y varies: $y = 0.4, 0.6, 0.8, 1.0, 1.2$. $\Omega = 1.45$, $Re = 500$.

In each case, except for $y = 0.4$, the minimum axial velocity increases as the aerofoil moves away from the centreline, and the progression is again nonlinear. The largest jump in minimum axial velocity occurs for the change from $y = 0.4$ to $y = 0.6$. Beyond that transition the effect of increase in radial distance reduces with increasing y .

6.4 The effect of varying aerofoil axial location

In this final series of plots the response of breakdown to changes in the aerofoil axial location is explored. It was seen in the previous section that the aerofoil has the greatest effect on breakdown at $y = 1.2$, so this value of y will be used here. Since the pipe has a constriction, and we wish to have a reasonable gap between the aerofoil and the pipe wall, the radial position of the aerofoil at each axial location will be adjusted depending

on the pipe radius. Hence the radial distance will be a minimum when the aerofoil is in the centre of the constriction.

Streamline plots in figure 6.6 show the effect on the flow of adjusting the axial location of the aerofoil.

Surprisingly the bubble is removed by an aerofoil at $x = 2$, far upstream of where breakdown is expected. Moving the aerofoil downstream continues to suppress breakdown until $x = 9$, at which point a bubble forms directly underneath the aerofoil. The aerofoil has little influence on the upstream vortex core when it is at $x = 9$, hence the reappearance of the bubble. Moving the aerofoil to $x = 10$ results in a larger semi-detached bubble more like that which occurs at higher Reynolds number.

The centreline axial velocity plot (figure 6.7) reveals non-monotonicity in the axial velocity trend as the aerofoil is moved along the axis. At $x = 2$ there is no breakdown. The aerofoil is moved to $x = 3$, resulting in a reduction in the axial velocity at the axial location of the aerofoil, but otherwise the profile is indistinguishable from that for $x = 2$. For the $x = 4$ profile there is a large drop in the axial velocity between $x = 10$ and $x = 15$, where breakdown normally forms. Moving the aerofoil to $x = 5$ increases the axial velocity again, signifying a move away from breakdown. For $x = 6$, $x = 7$, and $x = 8$ the trend is the same. At $x = 9$ a bubble evolves, and the minimum axial velocity becomes negative. For $x = 10$ the bubble has partly detached from the axis, and the minimum axial velocity undergoes a slight increase.

The decrease then increase in axial velocity corresponded approximately with the movement of the aerofoil toward then away from the axis through the converging section. So it is possibly this normalising of the radial location by the pipe radius which resulted in the non-monotonic behaviour.

6.5 Discussion

The purpose of this chapter was to investigate a potential mechanism for controlling the breakdown bubble produced in the open pipe, by reducing the contribution from the stretching term in the vorticity equation. Azimuthal vorticity production in the pipe is dominated by stretching, once the turning of axial and radial vorticity has resulted in

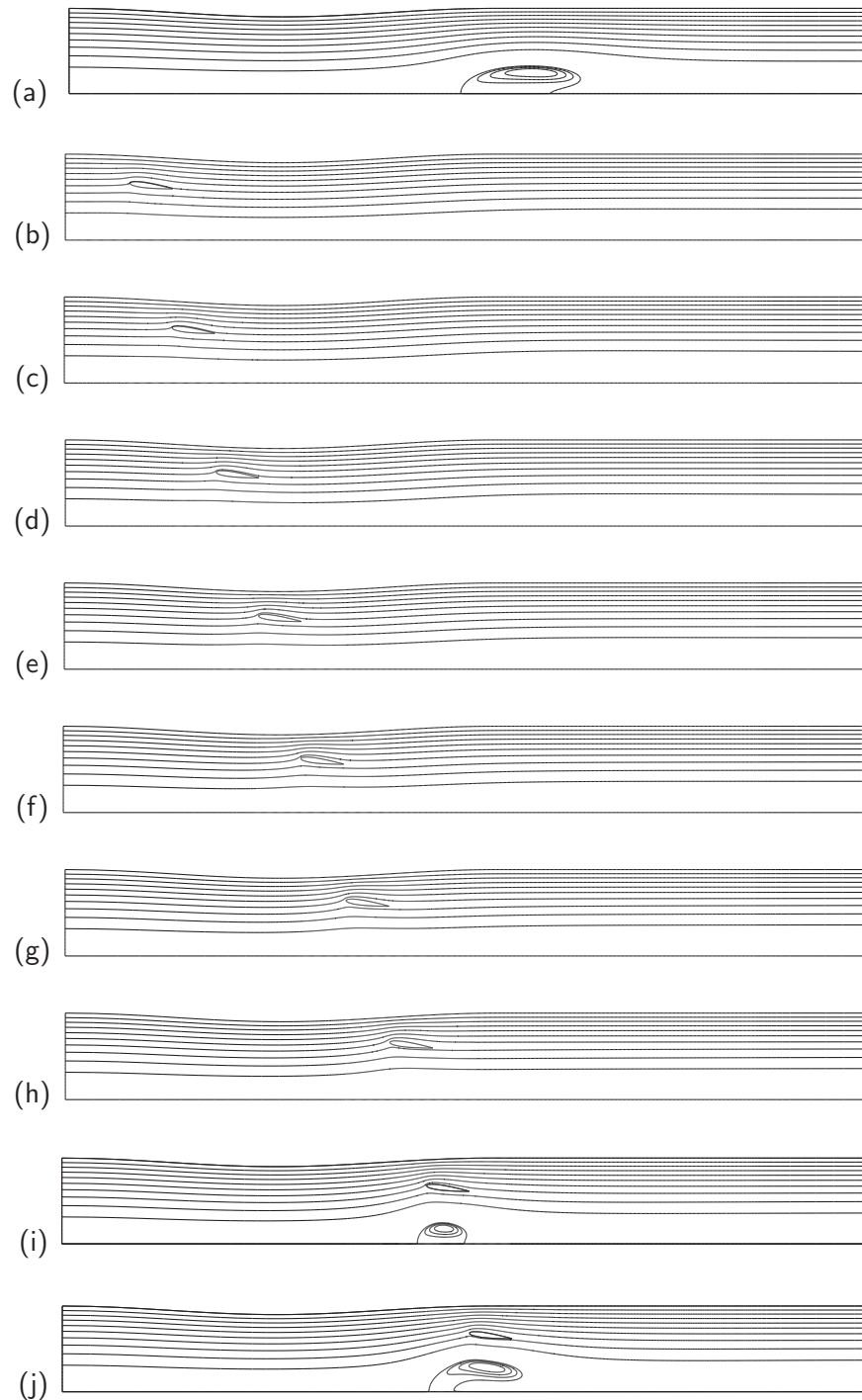


Figure 6.6: Streamline contours for the open pipe (a) without aerofoil, then with aerofoil at 5° AOA, varying location of aerofoil centre: $y = 1.2$, (b) $x = 2$, (c) $x = 3$, (d) $x = 4$, (e) $x = 5$, (f) $x = 6$, (g) $x = 7$, (h) $x = 8$, (i) $x = 9$, (j) $x = 10$. $\Omega = 1.45$, $Re = 500$.

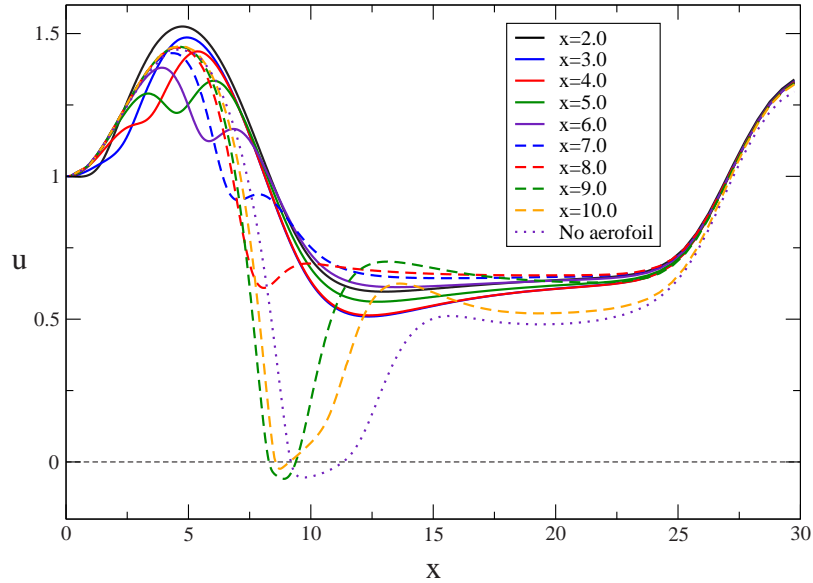


Figure 6.7: Axial velocity along the centreline for various aerofoil positions: 5° AOA, $y = 1.2$, x varies: $x = 2, 3, 4, 5, 6, 7, 8, 9, 10$. $\Omega = 1.45$, $Re = 500$.

the production of an azimuthal component. The onset of stretching results in a nonlinear feedback, which leads to stagnation of the axial flow and vortex breakdown. It has been demonstrated here that breakdown in a pipe can be controlled by the addition upstream of a small control device, which has the effect of impeding the radial outflow. The full range of states, from parallel streamlines to a full partially-detached breakdown bubble, could be realised by judicious placement of the aerofoil.

This study was performed at very low Reynolds number compared with flows of practical interest. However, the use of a non-slip aerofoil possibly makes these results more relevant to higher Reynolds number flows. In any case the purpose here was to determine the response of breakdown to control of the radial outflow. In practice other methods, such as withdrawal of fluid from the axis, could be applied to similar effect.

Chapter 7

Geometry dependence of breakdown

It has already been noted that vortex breakdown is observed in a variety of different geometries. The multitude of circumstances in which breakdown can occur is made possible by the fact that breakdown seems to be largely a product of the makeup of the vortex core. The susceptibility of a flow to breakdown is only influenced indirectly by the external flow, in that the external flow has a part to play in determining the profile of the vortex core.

The Reynolds number Re and swirl ratio Ω are commonly used to determine the susceptibility of the vortex to breakdown. However, many authors define Re and Ω differently depending on the peculiarities of their geometry or the flow produced in that geometry. Darmofal [8] and Beran and Culick [4] base their Re on the freestream velocity and vortex core radius. Khoo *et al.* [41] use a rotating drum apparatus to generate breakdown, and define their Re in terms of an average axial velocity and drum radius. Faler and Leibovich [17] use the average axial velocity and pipe diameter to determine Re . Given the different geometries used in all of these studies, this eclecticism in variable definition is understandable. However, these differing definitions compound the difficulty in drawing a direct comparison between the different flows which result in breakdown.

Maxworthy [49] went some way toward solving this problem by describing a generic apparatus, which has elements common to most of the geometries considered. This apparatus is illustrated in figure 7.1. Its purpose is to describe laboratory models for atmospheric vortex generators, and is not intended for vortex breakdown flows specifically. For geome-

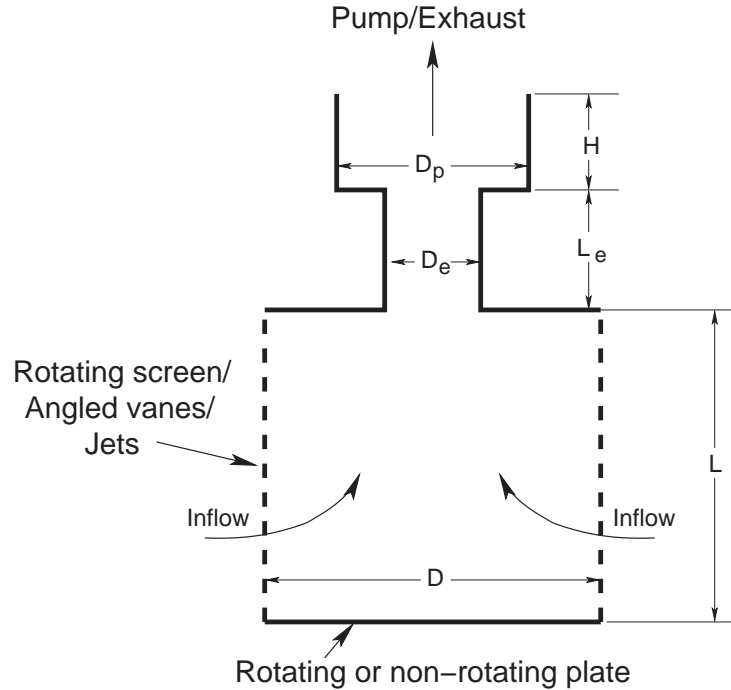


Figure 7.1: Maxworthy's [49] generic apparatus.

tries which support breakdown the transitions between the three sections of the apparatus are assumed smooth, and the system is arranged so that breakdown is observed in the section with length L_e .

Khoo *et al.* [49] used the definitions provided by this apparatus to compare results obtained in their swirling tank geometry with those obtained for open pipe flows. However, this apparatus still does not enable a direct comparison to be made between the various breakdown-susceptible flows, as approximations have had to be made in order to accommodate some geometries, such as the open pipe of Faler and Leibovich [17]. Also, it is not possible to include breakdown produced in a geometry such as the torsionally driven cylinder as it is difficult to define a mean axial velocity when all of the flow recirculates.

In the work discussed in this chapter we attempt to completely remove consideration of the geometry which produces breakdown by examining only the vortex core. As was stated at the start of this chapter, vortex breakdown is really only a product of the vortex core, so it makes sense to consider just the vortex core when comparing breakdowns produced in differing geometries.

In this section the breakdown forms produced in the torsionally driven cylinder and two

open pipes are compared. The aim is to compare the flows which support breakdown and determine whether any general conclusions can be drawn based on these comparisons. The parameters swirl Ω and Reynolds number Re are used, but both of these quantities are defined in terms of velocity profiles in the vortex core. In this way consideration of the apparatus external to the flow, and flow outside the vortex core, is eliminated.

First the velocity profiles upstream of breakdown in the torsionally driven cylinder and an open pipe flow are compared qualitatively. In the following section the application of velocity profiles upstream of breakdown to the inlet of a pipe is considered. The aim is to determine whether the vortex core profile of the cylinder would result in breakdown in an open pipe flow. Since it has been suggested that breakdown in the cylinder is actually an internal separation ([30],[22]) and not the same phenomenon as that observed in other geometries, the application of the same velocity profile upstream of breakdown in the cylinder to the open pipe should provide some insight into this question. Also, the influence of the rotating lid on the flow can be removed, as anticipated in chapter 5.

Following that study, a quantitative comparison is drawn between the various flow geometries which produce vortex breakdown. Appropriate geometry-independent quantities are determined which allow direct comparison between the different flows with respect to the onset of breakdown.

The final section summarises the arguments regarding classification of vortex breakdown. It has been proposed that the recirculation observed in the cylinder is not vortex breakdown; by the end of this chapter we will be able to address this question.

7.1 Cylinder and pipe velocity profiles

This investigation begins with an examination of the axial (u), radial (v), and azimuthal (w) velocity profiles in both geometries. Figures 7.2 and 7.3 display profiles of the three velocity components for the cylinder and the pipe. These plots show the velocity profiles at a number of axial locations in the cylinder and open pipe, however we are most concerned with the velocity profiles just upstream of breakdown.

The axial velocity profile in the cylinder is of the opposite sign to that in the pipe - for the cylinder, positive axial velocities are shown to the right of the baseline, and for the

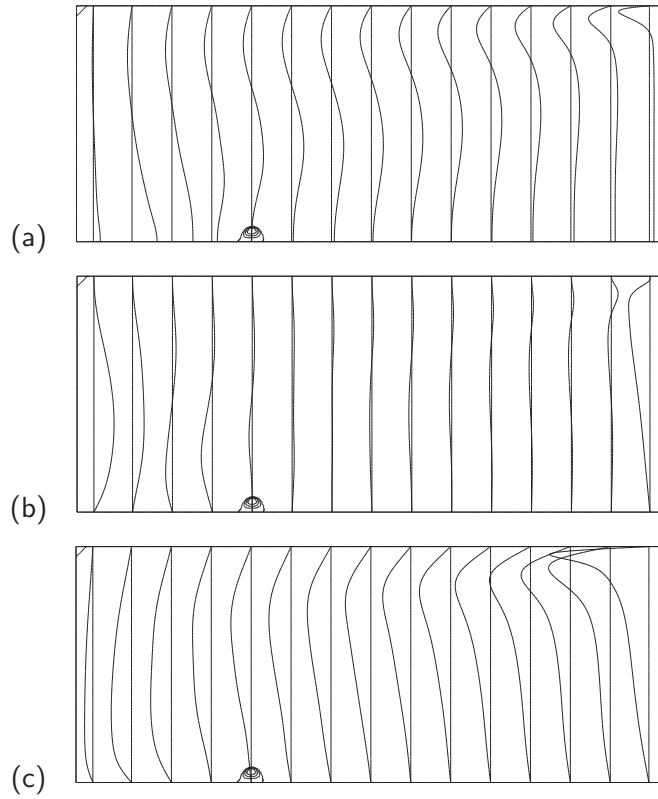


Figure 7.2: (a) u , (b) v , (c) w profiles and breakdown bubble streamlines. $Re = 1933$. Velocity magnitudes are not to scale.

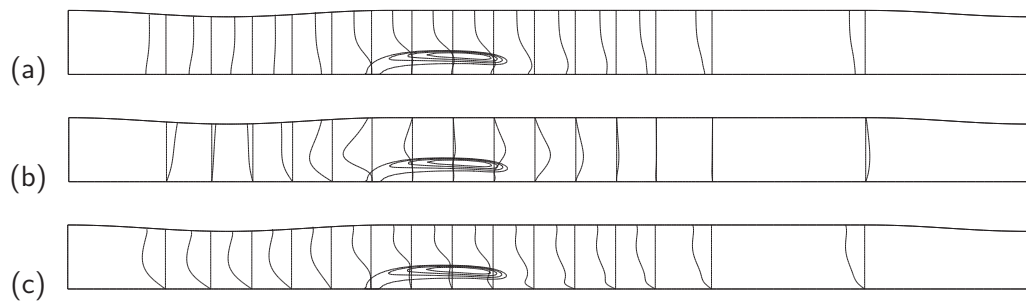


Figure 7.3: (a) u , (b) v , (c) w profiles and breakdown bubble streamlines. $Re = 1000$, $\Omega = 1.45$. Velocity magnitudes are not to scale.

pipe, positive axial velocities are shown to the left of the baseline.

7.1.1 Axial velocity

The axial velocity begins in the pipe as a jet-type flow - a higher axial velocity prevails at the centre of the vortex core, decreasing gradually with radial distance from the axis. This type of profile has been observed experimentally in open pipe studies, and is described approximately by the equation:

$$u = 1 + \Delta u e^{-r^2}. \quad (7.1)$$

This is the profile applied to the inlet of the open pipe here, but in the present case Δu is zero, so the profile is uniform - the nonuniform jet type flow develops as a result of the geometry. The cylinder also displays this jet-type flow well upstream of breakdown. Closer to breakdown, for both geometries the axial flow begins to stagnate.

7.1.2 Radial velocity

The role of the radial velocity profile in the onset of vortex breakdown has been discussed in its capacity to introduce generation of $-\omega_\phi$ through stretching. The radial velocity has a similar profile in both geometries. In the cylinder the radial velocity changes rapidly as a result of the flow's turn from the radial into the axial direction, and in the pipe the constricted section has a direct influence on the radial velocity.

7.1.3 Azimuthal velocity

The azimuthal velocity profile in both cases is also similar. In both geometries the profile upstream of breakdown is approximately solid-body near the axis, changing to a constant velocity profile further from the axis in the cylinder, and decaying slightly toward the wall in the open pipe. This is characteristic of other flows which exhibit breakdown, including the intense vortices which form over delta wings

7.1.4 Other derived quantities

The axial and radial velocity profiles in the pipe for $Re = 2560$ and $\Omega = 1.777$ measured by Faler and Leibovich [18] in their experiments, at an axial location just upstream of

breakdown, are shown in figure 7.4. In figure 7.5 the equivalent velocity profiles in the cylinder just upstream of breakdown are reproduced for comparison.

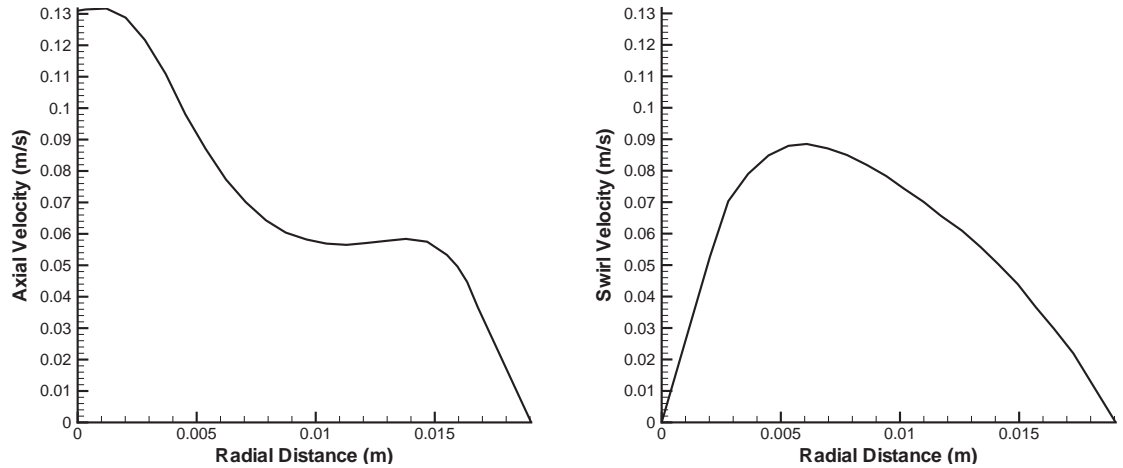


Figure 7.4: Faler and Leibovich's [18] $Re = 2560$, $\Omega = 1.777$ axial and swirl inlet velocity profiles.

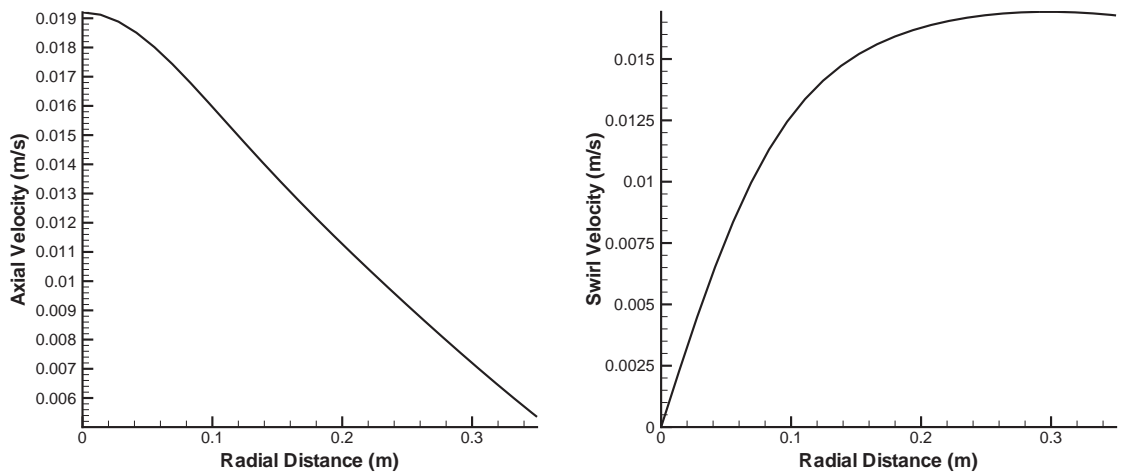


Figure 7.5: Cylinder axial and swirl velocity profiles upstream of breakdown.

It can be seen from these figures that close to the axis the axial and swirl velocities are similar. Again, both the Faler and Leibovich pipe and the cylinder have a jet like axial velocity profile. Away from the axis the velocity drops off smoothly but rapidly with radial distance. The swirl velocity plots show the same, roughly solid-body, profile, which in the case of Faler and Leibovich's experiment changes at a radial distance of about 0.0025, then reduces to zero at the pipe wall. The cylinder profile rounds off more smoothly, but

has a similar form (ie. solid-body) near the axis to the experimental pipe result.

In figure 7.6 we plot the profiles of another swirl parameter, the helix angle γ , for a profile from the pipe, and from the cylinder, upstream of breakdown. γ is defined:

$$\gamma = \text{artan} \left(\frac{w}{u} \right). \quad (7.2)$$

Delery [10] notes that the value of the helix angle γ can be used to predict breakdown onset. It can be seen that for small radial distances from the axis, the γ profiles for both geometries are similar.

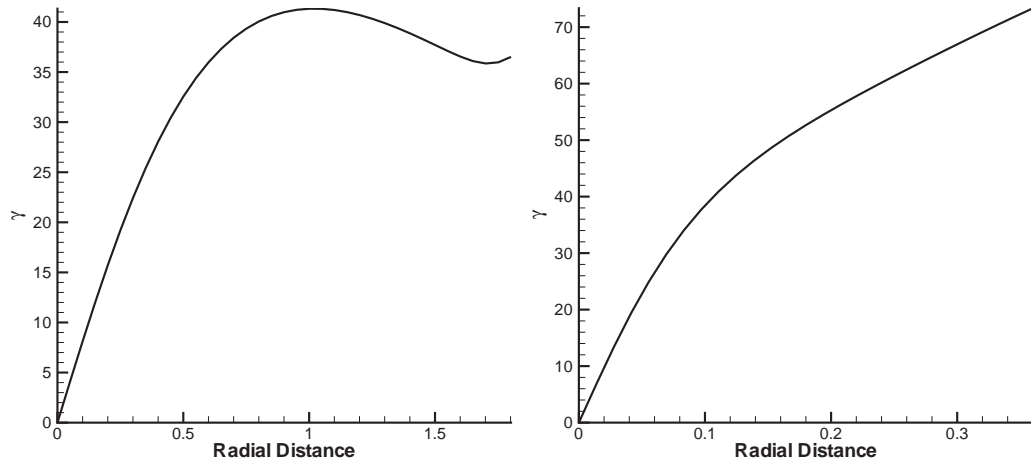


Figure 7.6: Pipe $Re = 600$, $\Omega = 1.49$ γ profile, cylinder $Re = 1933$ γ profile.

Of interest also is the circulation profile; Delery [10] observes that the circulation variation with radial distance in breakdown-susceptible flows is parabolic near the axis and tends toward a constant value in the outer region of the flow. This characteristic profile is revealed both in the open pipe and cylinder profile plots of figure 7.7 where we simply plot $\Gamma = V_\theta \times y$.

These simple comparisons confirm qualitatively the similarities between the flows upstream of breakdown in two very different geometries. Although the velocity profiles at a distance from the axis are different, in the near-axis region the axial and azimuthal velocity profiles have a similar form.

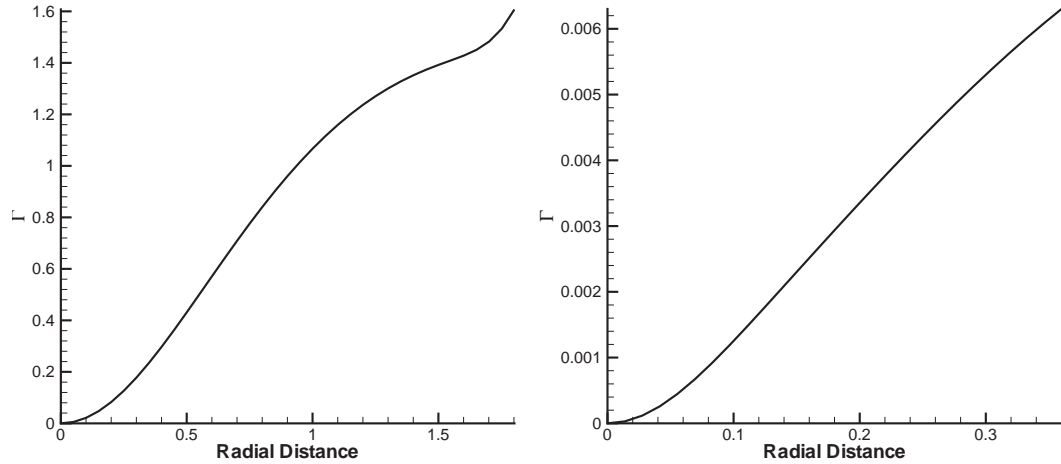


Figure 7.7: Pipe $Re = 600$, $\Omega = 1.49$ circulation (Γ) profile, cylinder $Re = 1933$ circulation (Γ) profile.

7.2 Streampipe

In studies of vortex breakdown in open pipes and similar unconfined geometries, the vortex flow state is determined by two factors, the Reynolds number Re and swirl Ω . These two parameters may be adjusted independently of one another. The Reynolds number is governed by the axial velocity and can be manipulated by adjusting the mass flow rate. The swirl is the ratio of the azimuthal velocity to the axial velocity, and is changed by varying the angle of swirl vanes, for example.

In the torsionally driven cylinder of fixed aspect ratio we have only one parameter with which to manipulate the flow - the Reynolds number, which is based on the rotation rate of the lid. Changing the rotation rate affects both the swirl and Reynolds number - there is no way to independently manipulate these two quantities. Hence it is difficult to compare the flow regimes in the pipe and cylinder with respect to breakdown. The Re/Ω region the cylinder operates in compared to the pipes is unknown, as it is difficult to define the equivalent parameters to the pipe Re and Ω , for the cylinder. In a later section we will define quantities which enable a direct comparison between the cylinder and pipe flows with respect to the core flow. In this section we examine the region of the flow in the cylinder where vortex breakdown occurs, and by applying the velocity profile found there to the more open conditions of the pipe are able to draw a more direct comparison between the two geometries.

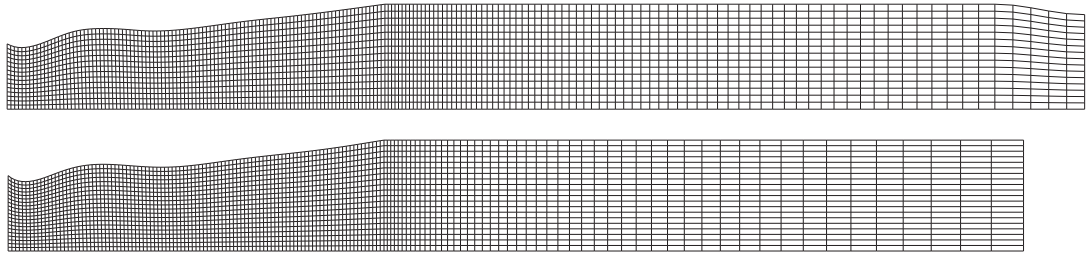


Figure 7.8: Pipes defined by $Re = 1933$ cylinder streamline.

In order to most accurately simulate the flow which occurs in the cylinder, it is necessary to change the pipe geometry so that the wall of the pipe corresponds to a streamline in the cylinder. Hence the flow in the pipe will be like that in the cylinder, but with an outlet instead of a rotating endwall downstream.

A streamline is extracted from the cylinder boundary and used as a slip wall in the open pipe. A streamline is chosen which is sufficiently far away from the axis to contain most of the vortex core region, and which begins at an axial location where the streamlines are most parallel to the cylinder axis; the radial velocity is at a minimum.

The geometries considered are shown in figure 7.8 - only every second grid line is shown.

In this figure the inlet is to the left. Following the inlet is a region whose outer wall is defined by a streamline taken from the torsionally driven cylinder flow at $Re=1933$. The inlet boundary condition is defined by the 3 velocity components extracted from the cylinder at a point just upstream of breakdown, corresponding with the start of the streamline. Downstream of this streamline-defined wall the geometry becomes a straight pipe. At the outlet two geometries were considered: an outlet with a 10% constriction as for the pipe used in chapter 4, and an outlet with no constriction. The constriction of the outlet was required previously in the pipe to prevent the bubble length increasing until the downstream end of the bubble reached the outlet. In the streampipe presented here the bubbles do not extend past the streamline-defined section of the pipe for the straight outlet case, and hence a constricted outlet is not necessary. In keeping with the wall's origin as a cylinder streamline, the streampipe wall is defined as slip. The cylinder has a radius of 1; the pipe was constructed to have a radius equal to the radius of the starting point of the streamline considered, which is 0.36 in this case. Hence the dimensions of the flow are equivalent between the cylinder and the pipe. The Reynolds number was also

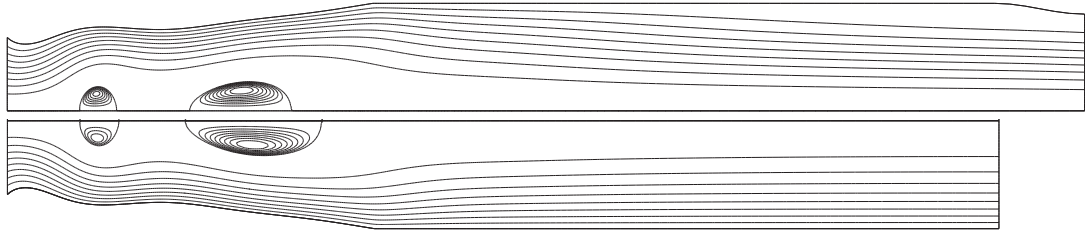


Figure 7.9: Streamlines for $Re = 1902$ cylinder profile applied to streamline-defined geometries.

kept the same by using the same viscosity and applying the velocity profile just upstream of breakdown to the pipe.

The velocity profiles for $Re = 1902$ are extracted from the cylinder at the starting point of the streamline used to define the pipe wall, so the inlet represents the conditions present in the cylinder at an axial location just upstream of breakdown.

Results of steady computations for both $Re = 1902$ pipes are shown in figure 7.9. The $Re = 1902$ steady cylinder result is displayed in figure 5.4 of chapter 5. In both cases two bubbles evolve for the same Reynolds number where only one bubble was observed in the torsionally driven cylinder. The bubbles have a similar form to those observed in the cylinder - they are different to the form commonly observed in pipes, which tend to have a more elongated structure and a recirculation region further displaced from the axis (see figure 4.7 in chapter 4). The flow in the pipe appears more like that at higher Reynolds number in the cylinder - compare the cylinder results at $Re = 2001$ and 2252 (figure 5.4 in chapter 5). The presence of the rotating lid in the cylinder appears to have the effect of increasing the Reynolds number at which breakdown is observed.

Although this will not be investigated in detail, it can be seen that decreasing the adverse pressure gradient downstream of the breakdown bubble decreases the bubbles' size. It has been well documented that an adverse pressure gradient promotes breakdown formation, so this effect of a more favourable pressure gradient is not unexpected. As a more favourable pressure gradient is applied, by moving the converging outlet closer to the region where bubbles develop, it is expected that the bubbles' size will decrease further.

Figures 7.10 to 7.13 show plots of streamfunction contours for the cylinder against those for the streampipe. The cylinder and streampipe of equivalent Re are placed side by side

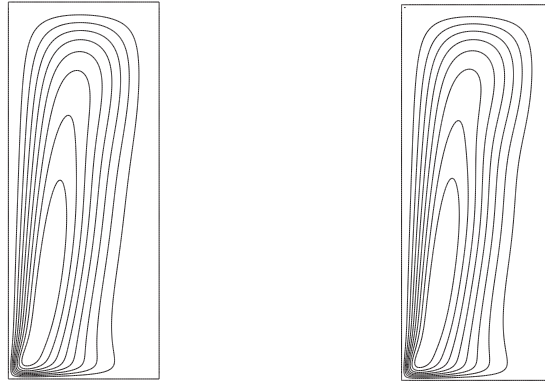


Figure 7.10: Cylinder streamlines on the left and streamampipe streamlines on the right. Left: $Re = 1500$, right: $Re = 1600$.

for direct comparison. In each case the streamampipe is placed so that its inlet is at the approximate axial position relative to the cylinder where the streamline which defines the pipe originates.

Plots are provided for eight Reynolds numbers: $Re = 1500, 1600, 1700, 1800, 1902, 1933, 2001,$ and 2252 . Following is a comment on each of these results, followed by a discussion of their implications:

1. $Re = 1500$: At this Re no bubble exists in either the cylinder or streamampipe. However in both cases there is significant streamline divergence, a precursor to breakdown at higher Re .
2. $Re = 1600$: Two waves in the streamline closest to the axis become evident in both geometries, indicating the approximate axial location where 2 recirculation bubbles will form for higher Re .
3. $Re = 1700$: A recirculation bubble forms in the streamampipe, at the approximate axial

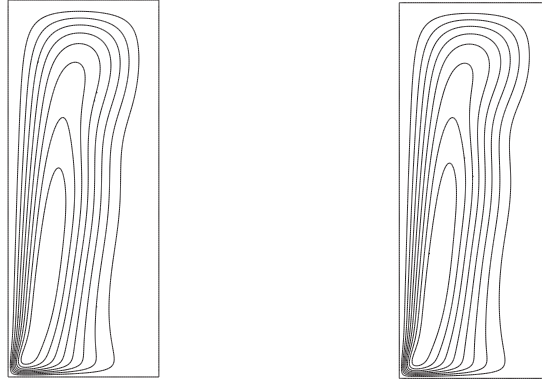


Figure 7.11: Cylinder streamlines on the left and streamampipe streamlines on the right. Left: $Re = 1700$, right: $Re = 1800$.

location where the downstream bubble for the cylinder will form at higher Re . In the streamampipe the pattern of bubble evolution is reversed; the downstream bubble evolves first, whereas this bubble evolves second in the cylinder.

4. $Re = 1800$: With increasing Re the bubble in the streamampipe increases in size. Upstream another bubble evolves, although it is tiny at this Re . Still there is no bubble present in the cylinder. Increasing streamline divergence is evident however, and the development of two regions where breakdown is expected becomes slightly more pronounced.
5. $Re = 1902$: The streamampipe now contains two fully developed breakdown bubbles, of the same form as those observed in the cylinder for higher Re ; a glance at the cylinder flow for $Re = 2001$ reveals an upstream bubble of comparable size to that in the streamampipe for $Re = 1902$. The downstream bubble in the streamampipe is however much larger than the corresponding bubble in the cylinder at $Re = 2001$.

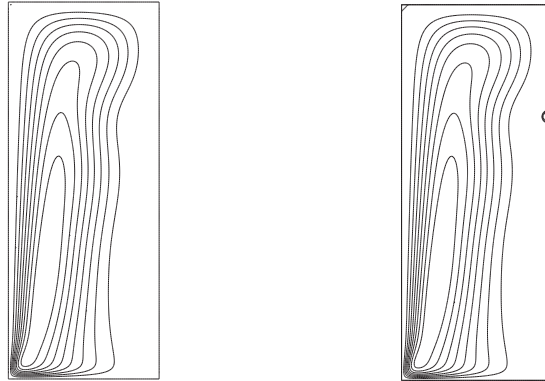


Figure 7.12: Cylinder streamlines on the left and streamampipe streamlines on the right. Left: $Re = 1902$, right: $Re = 1933$.

6. $Re = 1933$: The streamampipe flow remains relatively unchanged, as this Re change is smaller than that applied in the previous plots. The change is large enough to herald the onset of the first breakdown bubble in the cylinder though. As was mentioned earlier, the first bubble develops upstream, the reverse of the order of occurrence in the streamampipe.
7. $Re = 2001$: With increasing Re the second bubble evolves in the cylinder, while the bubbles in the streamampipe grow in size.
8. $Re = 2252$: In these last plots the two bubbles in the streamampipe begin to merge. This also occurs in the cylinder for higher Re , but for this Re the two bubbles in the cylinder just grow larger.

Figure 7.14 shows the minimum axial velocity measured along the centreline for the streamampipe and the cylinder. For the cylinder, the minimum axial velocity is extracted from the region away from both endwalls so that only the region of interest is included;

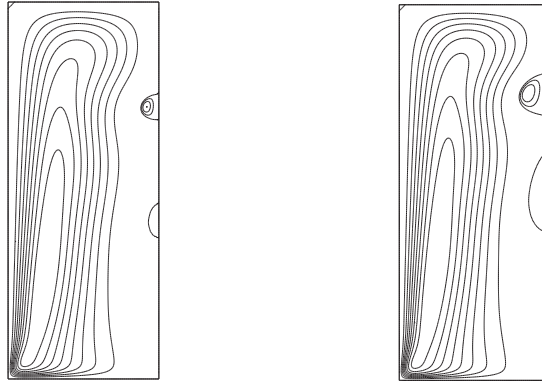


Figure 7.13: Cylinder streamlines on the left and streampipe streamlines on the right. Left: $Re = 2001$, right: $Re = 2252$.

the centreline axial velocity goes to zero at the endwalls. For the streampipe the whole domain is considered.

In both cases there are two local minima in u for Re approaching breakdown, but only the global minimum is plotted here.

Since the Re for each geometry is defined in the same way and the length scale and viscosity are the same, the velocity magnitudes are also comparable.

These results clearly show the tendency of the streampipe flow to suffer breakdown before the cylinder; minimum axial velocity becomes negative at $Re \sim 450$ less than for the cylinder. The progression toward lower minimum u is monotonic for the streampipe except at $Re = 1933$, where the minimum u in the second bubble begins to dominate the first - this is evident in the kink in minimum axial velocity between $Re = 1902$ and $Re = 2001$.

We can conclude from these results that it is possible to produce a breakdown bubble in an open pipe geometry at comparable parameter (Re, Ω) values to those used for breakdown

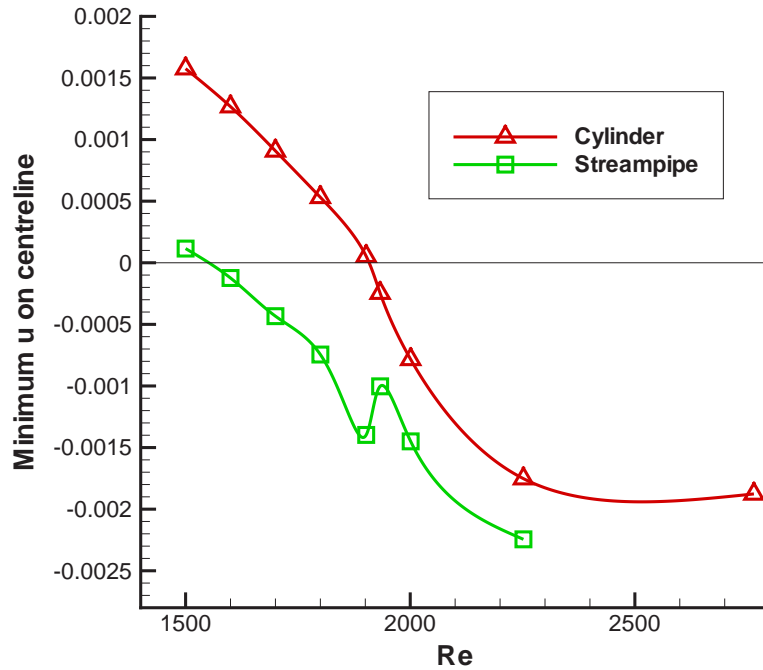


Figure 7.14: Minimum axial velocity on the centreline vs. Re for the streampipe (green squares) and the cylinder (red triangles).

simulations in the torsionally driven cylinder. This lends support to the view that the breakdown observed in the cylinder is related to the phenomenon which occurs in the open pipe.

7.3 Equivalence of Ω and Re in different geometries

The next aim of this study is to find a set of parameters by which the open pipe and torsionally driven cylinder can be directly compared. For the pipe we specify the Reynolds number and swirl, and they can be varied independently. This is impossible in a cylinder with constant aspect ratio, because the swirl and Reynolds number are linked through the rotation of the spinning lid. If we consider only the vortex core flow, which is the most important region of the flow with respect to vortex breakdown, then it is possible to determine a Reynolds number and swirl equivalent to that used in open pipe studies. We will determine these quantities for the cylinder by examining the axial and azimuthal

velocity profiles just upstream of breakdown.

Khoo *et al.* [41] addressed the problem of defining Re and Ω in different geometries, as mentioned in the previous section. Their study examined the breakdown forms produced in a unique unconfined geometry, consisting of a cylinder with a stationary circular base, a rotating outer wall (a section of which allows inflow), and a suction tube to extract fluid from the axis. In order to compare the results from their study with those from open pipes, Khoo *et al.* [41] define a Reynolds number $Re = \frac{\Gamma}{2\pi\nu}$ and swirl ratio $S = \frac{r_0\Gamma}{2Q}$, where Γ is the circulation, defined by $\Gamma = 2\pi V_0 r_0$, and V_0 is the tangential velocity at the radius r_0 of the drum, Q is the flow rate, and ν is the viscosity. They supply a plot of Re vs S for the various types of breakdown observed in their geometry. Approximately equivalent quantities were calculated based on the Reynolds number and circulation supplied by Faler and Leibovich (1977) [17].

Maxworthy (1982) [49] provides a generic apparatus (see figure 7.1) which can be used to quantify the swirl and Reynolds numbers for most unconfined geometries in which breakdown is observed. However as mentioned previously it is difficult to ascertain what parameters from the torsionally driven cylinder flow can be used to define the same quantities used in Maxworthy's apparatus.

An attempt at a direct comparison between pipe and cylinder flows containing breakdown was made by Spohn *et al.* [64]. Their definitions of Re and S (swirl) for the torsionally driven cylinder are provided by Lewellen (in [64]):

$$Re_Q = \frac{Q}{L\nu}, \quad (7.3)$$

$$S = \frac{2\pi\Gamma a}{Q}, \quad (7.4)$$

where Q is the flow rate along the cylinder axis, L is a characteristic length, taken to be the height of the cylinder, ν is the viscosity, Γ is the maximum circulation, and a is a characteristic radius, taken to be the radius of the cylinder. The resulting values of Re and S are presented in table 7.1.

There is no Re quoted for B&A (Brücker and Althaus, in [64]) because the length of the pipe is unknown.

Based on the above results, the cylinder has a comparable Re_Q to the experimental pipes

Author	Geometry	S	Re_Q
F&L [17]	Pipe	0.4-0.7	75-150
Escudier [14]	Pipe	0.5	200
B&A in [64]	Pipe	0.6	(?)
Spohn <i>et al.</i> [64]	Cylinder	10	100

Table 7.1: S and Re_Q values from various studies, from Spohn *et al.* [64].

at breakdown, but the swirl S is much higher in the cylinder. This observation is offered as an explanation for the differences between manifestations of breakdown in the cylinder and in the pipe.

There are some problems with these definitions. It is difficult to see why the length of the pipe should be used to determine Re_Q , as it has no direct consequence for the type of breakdown observed; one could construct a pipe of great length, entailing a large Re_Q , with little change to the pipe flow at breakdown. Also, S appears to have little relation to the vortical core; it is merely an indication of the size of the cylinder, and is difficult to relate to the definition of core size used for the open pipes of the other studies.

7.3.1 Billant *et al.*'s [5] criterion

Billant *et al.* [5] deduced a criterion for vortex breakdown in a swirling jet. Their geometry consisted of a more open arrangement than has been considered so far. It involved a swirling jet discharging into a large tank; this geometry is less confined than the open pipe. The flow which results is depicted schematically in figure 7.15.

Billant *et al.*'s criterion is based on the assumption, first made by Escudier and Keller [15], that the velocities inside the breakdown bubble are negligible, and hence the interior of the bubble is at stagnation pressure. A derivation of this criterion, from Billant *et al.*, is provided below):

From Bernoulli,

$$H = \frac{P_0}{\rho} + \frac{V_x^2(0, x_0)}{2} = \frac{P_1}{\rho}, \quad (7.5)$$

where the quantities are as defined in figure 7.15. Far upstream of the stagnation point,

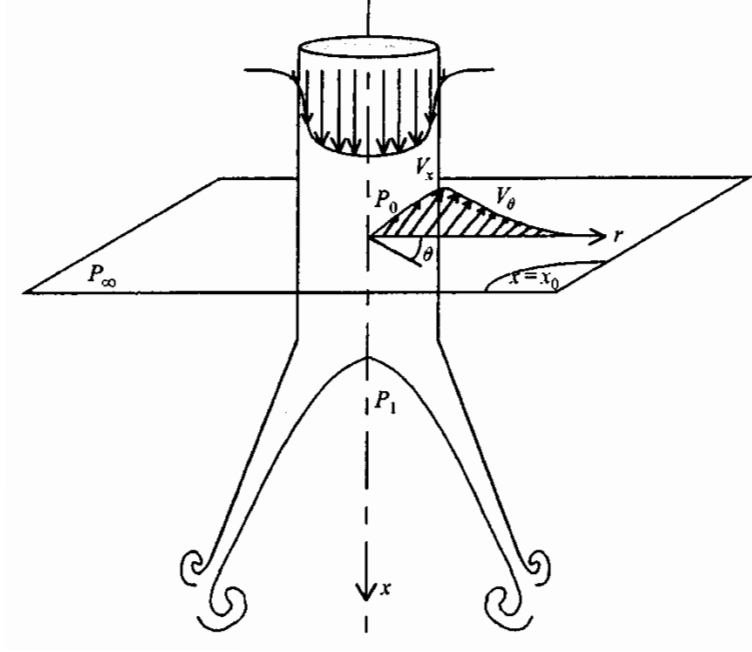


Figure 7.15: Schematic of the flow induced in Billant *et al.*'s [5] apparatus.

within the vortex core, the centrifugal force balances the radial pressure gradient, and so after some work we arrive at the following:

$$P_0 = P_\infty - \int_0^\infty \frac{\rho V_\theta^2(r, x_0)}{r} dr, \quad (7.6)$$

where P_0 is the pressure on the axis at point x_0 , P_∞ is the pressure at infinity, V_θ is the azimuthal velocity, and r is the radial ordinate. Since the pressure inside the bubble (P_1) is assumed equal to that at infinity, from the above two equations Billant *et al.* [5] arrive at the following criterion C_B for breakdown:

$$C_B = \frac{\int_0^\infty \frac{\rho V_\theta^2(r, x_0)}{r} dr}{V_x^2(0, x_0)} \geq \frac{1}{2}. \quad (7.7)$$

This is a lower bound, hence breakdown onset may occur for higher values of C_B , but for all $C_B < \frac{1}{2}$ breakdown will not be present. It should be noted that this expression contains no allowance for viscosity, and hence is Reynolds number independent, reflecting the assumed inviscid nature of breakdown. This is a reasonable assumption for high Reynolds numbers, but for lower Re viscosity has a large effect on the velocity ratio which will result in breakdown, as will be seen later.

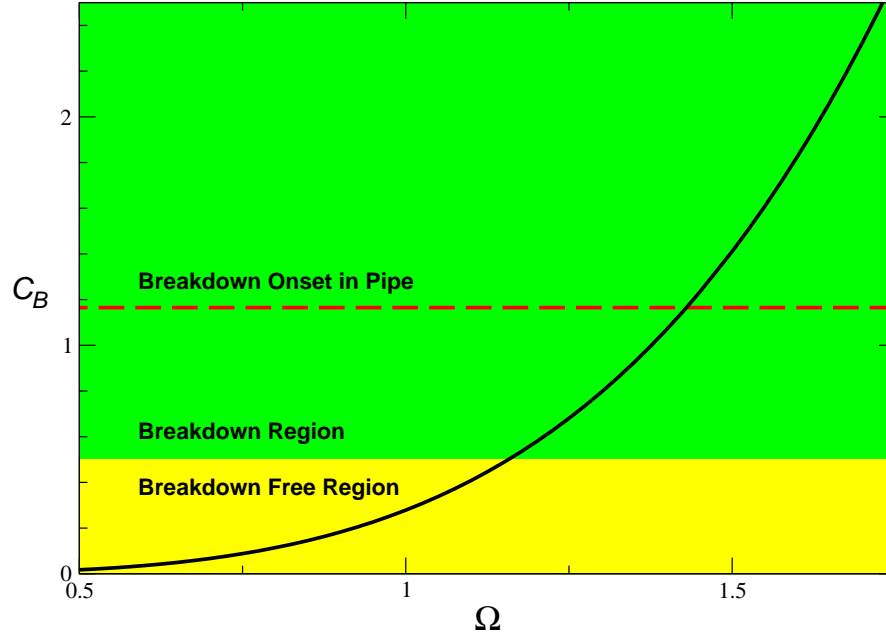


Figure 7.16: Billant *et al.*'s [5] breakdown onset criterion.

It is a simple matter to apply this criterion to the pipe inlet velocity profiles used in this study; the result is plotted in figure 7.16.

For the q-vortex (used to define the pipe inlet velocity profile) the integral was evaluated out to the point where the swirl velocity is close to zero, after which there is no further contribution to the integral. In the figure Billant *et al.*'s [5] breakdown criterion is calculated for the range $0.5 < \Omega < 1.75$. At $C_B = \frac{1}{2}$ there is a transition to flows which can support breakdown. For the pipe we consider, breakdown is observed at $\Omega = 1.43$, which translates into $C_B = 1.165$, which is greater than $C_B = \frac{1}{2}$, and hence consistent with Billant *et al.*'s criterion.

Unfortunately this criterion cannot be so directly applied to the torsionally driven cylinder, as the flow is tightly constrained by the cylinder walls; it is not possible to integrate out to infinity, and the swirl velocity does not have sufficient space to taper off gradually to zero before it is rapidly reduced to zero at the wall.

In the next section we propose alternative definitions for Re and Ω which can be applied to the open pipe and torsionally driven cylinder flows. These definitions provide a more consistent comparison between the two flows, and show that the Ω at which breakdown occurs in both geometries is similar. However Re in the cylinder will be shown to be

different by at least an order of magnitude compared to most of the reported experimental results, and this, we suggest, accounts for the different appearance of breakdown in the cylinder. We are able to confirm this by reducing Re in the pipe to the level of that in the cylinder. The result is a closed bubble with a strong resemblance to the cylinder bubble. This will be used to substantiate the claim that the pipe and cylinder breakdowns are the same phenomenon, and that differences in manifestation of breakdown are probably a result of the different Reynolds number regimes which the two flows inhabit.

7.3.2 Some definitions

We define some geometry independent quantities in this section. The Reynolds number will be defined by the maximum axial velocity along the centreline (u_{max}), the radius of the point of maximum azimuthal velocity at the axial location of maximum axial velocity (r) (r defines the vortex core), and the viscosity (ν):

$$Re = \frac{u_{max}r}{\nu}. \quad (7.8)$$

The swirl Ω is defined as the maximum azimuthal velocity (w_{max}), at the axial location of maximum axial velocity, divided by the maximum axial velocity:

$$\Omega = \frac{w_{max}}{u_{max}}. \quad (7.9)$$

These definitions are not new; the maximum azimuthal velocity has been used by Garg and Leibovich [20] and Delery [10], for example, to define the level of swirl in the vortex core, and the radius of the vortex core has also previously been defined as the point at which the azimuthal velocity becomes a maximum. We explain the reasoning for the use of these definitions in this study in the following.

Previous studies (Darmofal [8], and others) of pipe geometries have based the Reynolds number on the freestream axial velocity. In those studies the freestream axial velocity is an easily obtained quantity. But vortex breakdown affects the core of the vortex, and a flow's susceptibility to breakdown is a function of the core axial and swirl velocity profiles - the velocity outside the core is not directly relevant. Also, for the cylinder, there is no way to define a freestream axial velocity because the flow recirculates. Hence it proves to be more convenient and more consistent to use the above equations based on core velocities

for our definition of Ω and Re . We use u_{max} in order to determine the flow as far along the axis as possible from the influence of the breakdown bubble, as the bubble causes the axial flow to stagnate. In the cylinder this is important because the bubble is located so close to the stationary lid. So determining the swirl and Reynolds number at the location of maximum axial velocity gives a position of least influence from both the stationary lid and breakdown bubble in the cylinder. The length scale r is defined by the radius of the vortex core, ie. the radius at which the azimuthal velocity begins to decrease with radial distance from the axis.

Using the definitions above it is now possible to compare the pipe and cylinder flow regimes quantitatively, in terms of the swirl parameter Ω and the Reynolds number Re . (Where it becomes necessary to refer to the previously defined pipe Re and Ω and cylinder Re , we will use the subscript P for the pipe and C for the cylinder.)

Table 7.2 presents some values of the core Reynolds number and Ω calculated for the torsionally driven cylinder.

Cylinder Re_c	Breakdown state	Core Re	Ω
1902	no bubble	60.2	0.8787
1933	1 bubble	59.9	0.8936
2001	2 bubbles	59.0	0.9299
2252	2 bubbles	61.1	1.1250

Table 7.2: Newly defined core Re and Ω for the torsionally driven cylinder.

The first point to notice is the very low core Re compared with the cylinder Re . This is an indication of the relatively small velocity magnitudes in the secondary recirculating flow in the cylinder.

Also, the core Reynolds number Re does not vary much with increasing cylinder Reynolds number Re_c . Ω increases roughly linearly with increasing cylinder Reynolds number Re_c .

The equivalent properties calculated for the pipe are shown in table 7.3.

It can be seen from tables 7.2 and 7.3 that the core Reynolds number regimes at which breakdown is observed in the two geometries are quite different. However the values of Ω which breakdown occurs are comparable, even at these very different values of core Re .

Pipe Ω_p	Breakdown state	Core Re	Ω
1.40	no bubble	1282	0.2836
1.45	1 bubble	1433	0.6944
1.49	1 bubble	1426	0.7126

Table 7.3: Newly defined core Re and Ω for the open pipe.

The plot in figure 7.17 illustrates graphically the region in Re/Ω space which the pipe and cylinder flows inhabit.

Pipe results are shown for $Re_p = 1000$ and $\Omega_p = 1.0, 1.45,$ and $1.49,$ along with a Faler and Leibovich [18] pipe result. Four cylinder results are plotted for $AR=2.5,$ $Re_c = 1902,$ $1933,$ $2001,$ and $2252.$

Note the large difference in Re between the geometries. The pipes all inhabit the region $Re > 800,$ whereas all of the cylinders have $Re < 62.$ Given the scarcity of results plotted here it is difficult to determine the value of Ω at which breakdown first occurs in the pipe. However, the swirl Ω at which breakdown is first observed in the cylinder is $\sim 0.9,$ whereas for the pipes it is potentially much lower, in the range $0.35 < \Omega < 0.70.$ If we look at figure 7.18 the reason for this becomes apparent.

In figure 7.18 only cylinder results are plotted, and results for varying aspect ratio have been included; the first number in the label for each data point is the aspect ratio, the second number is the cylinder $Re_c.$

This plot shows that as Re decreases, the value of Ω required for breakdown increases. Also, if the Re scale of this plot is taken into account, compared to figure 7.17 the rate of increase in Ω required for breakdown is also increasing as Re is reduced.

A dashed line is drawn to indicate the approximate transition point; it is meant only as an aid to the eye. There is some discrepancy in the results near the line dividing breakdown and no-breakdown results - the $Re = 1902$ result has a slightly higher Ω and Re than the $Re = 1933$ result, so if the trend were to be consistent we should expect that at $Re = 1902$ there would be breakdown.

We will return to this analysis soon after a short diversion.

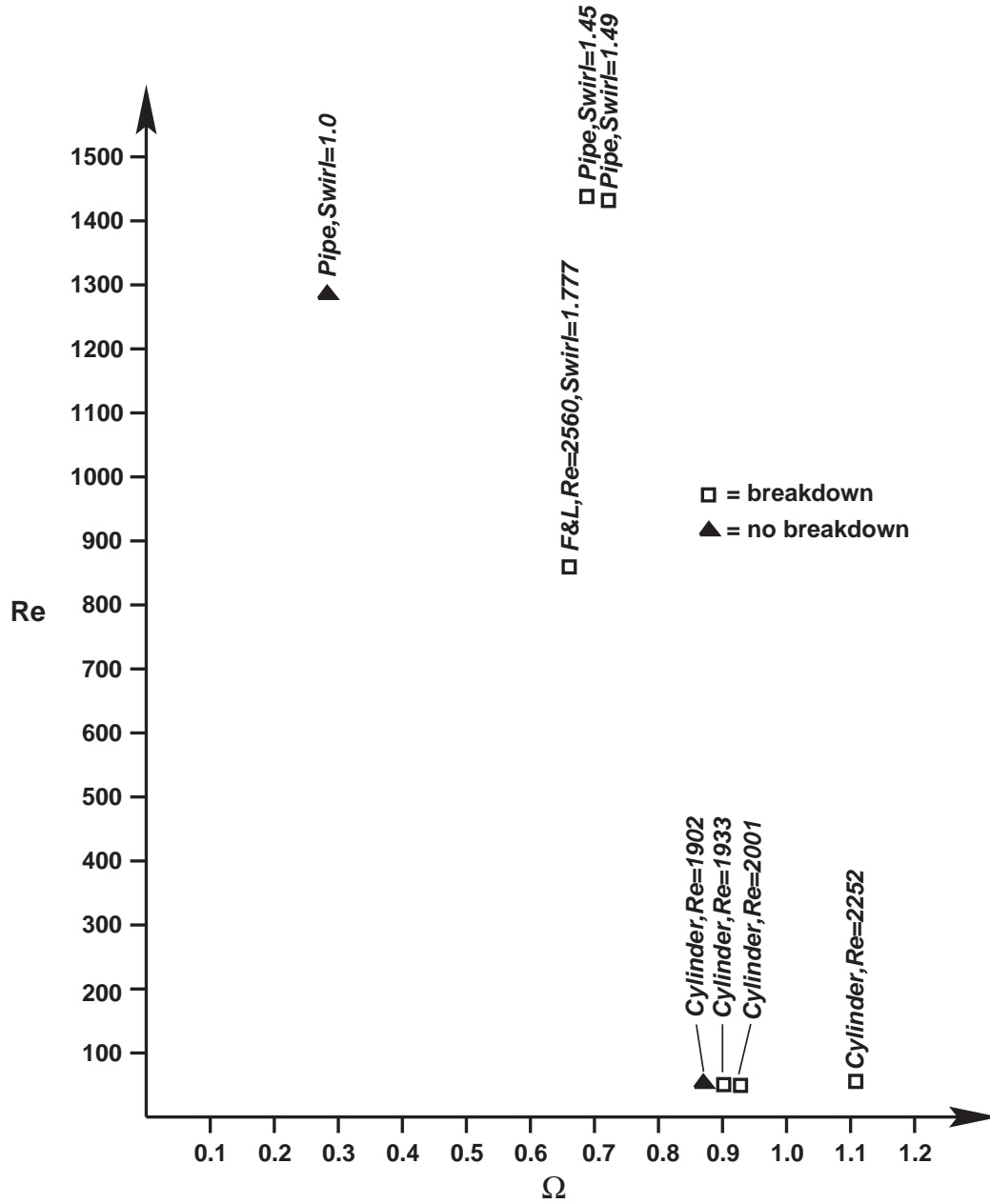


Figure 7.17: Re vs Ω for the various geometries. Both quantities are defined in terms of the vortex core. Point labels: the first number is the commonly defined Re for that geometry (for the pipe, $Re = 1000$), and the swirl is that commonly defined for that geometry.

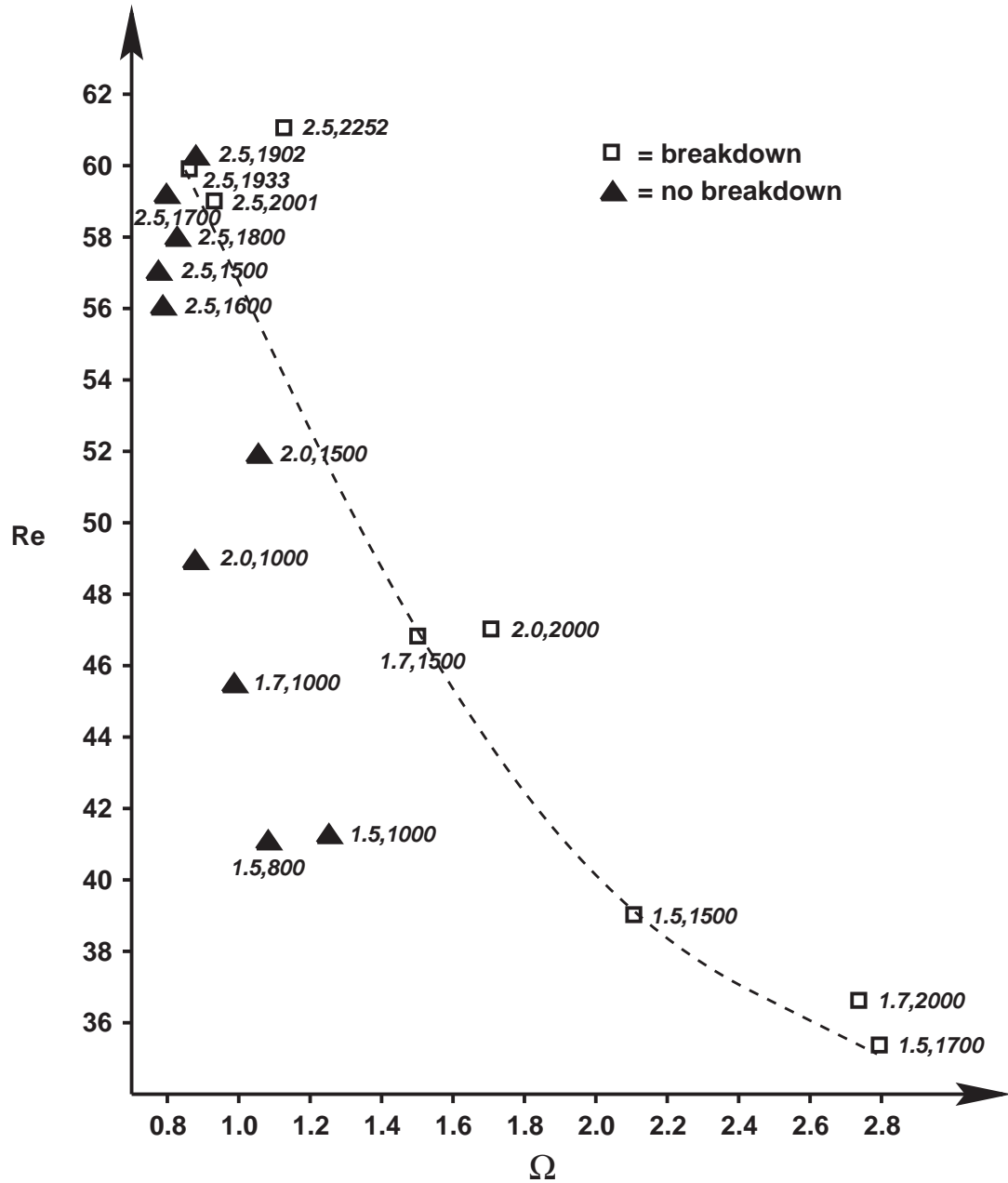


Figure 7.18: Re vs Ω for the cylinder. Both quantities are defined in terms of the vortex core. Points labels: the first number is the cylinder aspect ratio, the second number is the cylinder Reynolds number Re_c .

7.3.3 Effect of sloping cylinder walls

As was mentioned earlier, a limiting factor in the torsionally driven cylinder studies is the inability to independently alter the Reynolds number and swirl. The result of this limitation is that it is only possible to explore a very limited range of flows in the cylinder. For example, we cannot visit the region in Re/Ω space where the spiral and other types of breakdown occur. Perhaps this is why only the axisymmetric bubble is seen in the cylinder.

In order to make independent changes to the Reynolds number and swirl in the cylinder, it will be necessary to make some change to the cylinder geometry. Two methods are suggested here:

1. inject some flow along the cylinder axis to directly have some influence on the axial velocity, and hence the core Reynolds number;
2. change the slope of the cylinder sidewalls and determine the effect this has on the Reynolds number and swirl measured in the core.

For the next part of this study the second alternative is explored. The new geometry considered is shown in figure 7.19. The rotating lid is at the right hand end of the cylinder, and cylinder Re_c is still determined by its rotation rate. For this study the ratio of the endwall (stationary lid) radius to the rotating lid radius will be varied; define this as the wall ratio:

$$\alpha = \frac{\text{stationary lid radius}}{\text{rotating lid radius}} \quad (7.10)$$

For each α various Reynolds numbers will be tested. We use the Reynolds number range: $1000 \leq Re_c \leq 7000$. For $Re_c \geq 2700$ (see eg. Lopez [44]) in the straight-sided cylinder the flow has been observed to become unsteady. In this study we only consider steady state solutions however. The unsteadiness is probably not related to breakdown, but is most likely a product of the overall flow at these higher Re_c , as shown by Tsitverblit *et al.* [72], hence we are not concerned with unsteadiness.

A complete analysis should average the streamlines over time; we use the steady solution as a proxy for this to obtain some indication of the trends expected for higher Re .

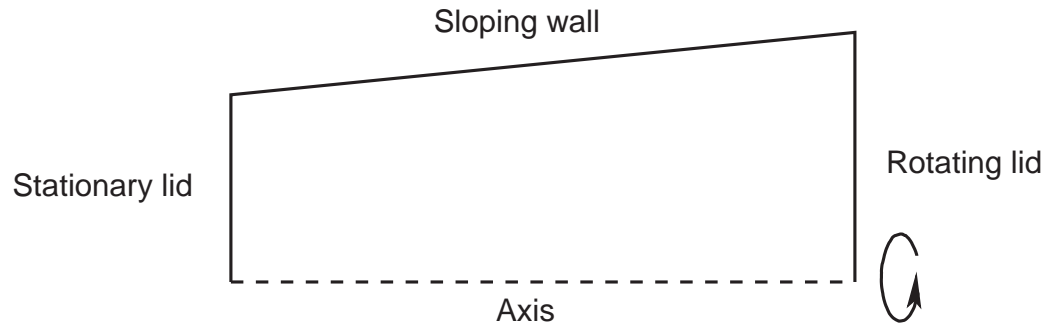


Figure 7.19: Sloped cylinder definition.

Results for $0.25 \leq \alpha \leq 1.25$ are considered; this includes the straight-sided cylinder and results on both sides of this case. Note that the more highly sloped wall begins to approximate the situation in cyclone separators.

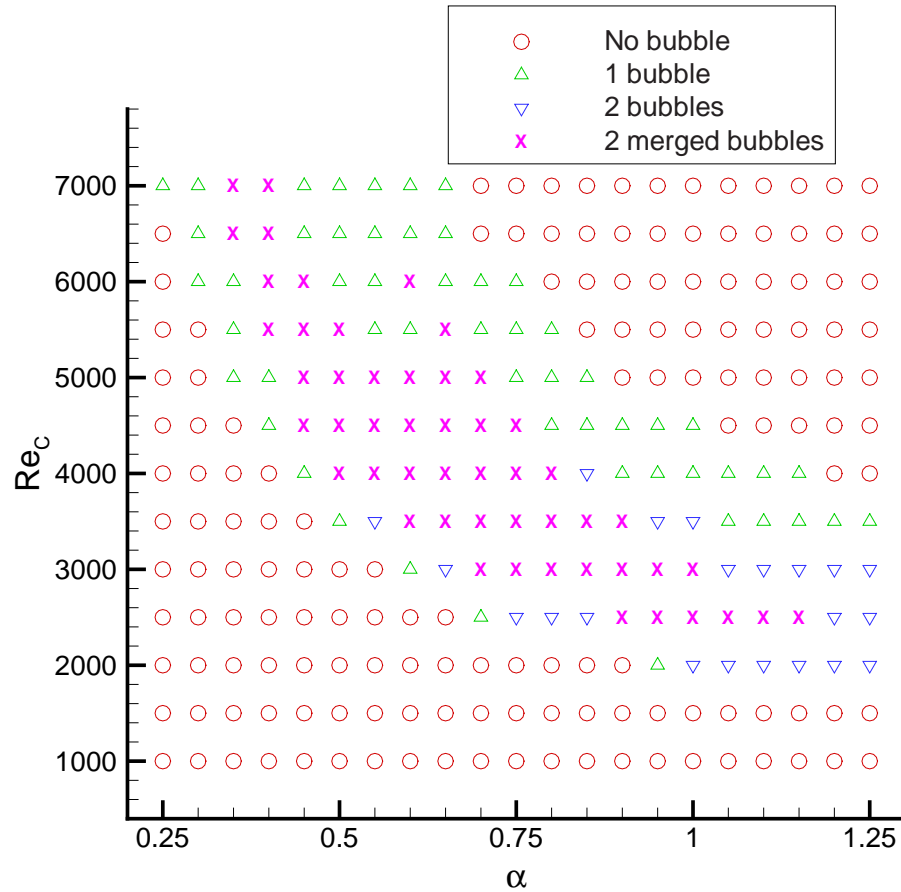
Fluent 5 was used to generate all of the following results. In the case of the $\alpha = 1$ cylinder the results match those previously generated using Fluent 4. The same grid was used as for the $\alpha = 1$ case, but it was compressed to allow for the changing cylinder radius.

Figure 7.20 summarises the breakdown onset characteristics of each α/Re_c combination. Four distinct classes of flow are represented:

1. no breakdown bubble (red circles);
2. one breakdown bubble (green deltas);
3. two distinct breakdown bubbles (blue inverted deltas).
4. two merged breakdown bubbles (purple crosses);

The two latter classes are characterised by two separate regions of recirculation. For class 3, the two bubbles are not connected in that a vortical flow similar to that upstream of the first bubble re-forms between them. In class 4 the two bubbles are in some way connected, ie. the vortical core does not re-form between them. In figure 7.21 a typical progression of solutions is shown for $\alpha = 0.95$.

The plot of figure 7.20 has as its lower limit $Re_c = 1000$. For this Re_c at all the α values considered no breakdown bubble is present. It is conceivable, given the trends to

Figure 7.20: Sloped cylinder breakdown incidence with Re_c and α .

be discussed, that this Re_c could yield breakdown for higher α . We will not explore this possibility however.

For $\alpha = 0.25$ no bubble evolves until $Re_c = 7000$. This Re_c is much higher than that for which breakdown is first observed in the cylinder without sloped sides, ie. ~ 1900 . Increasing α brings the Re_c required for all of the transitions lower. At $\alpha = 0.30$ two merged bubbles appear, and at $\alpha = 0.55$ another mode of breakdown becomes apparent: two separated bubbles (case 4). This state only appears for one Re_c at $\alpha = 0.55$. For $\alpha > 0.55$ the transition from no bubble to 2 bubbles tends to proceed through the 1, 2 separated, or 2 merged bubbles, to the extent that it is suspected the flow may go through all these modes before settling on the 2 merged bubble arrangement. The resolution in the Re_c direction is not sufficient to determine whether or not this is the case. At the higher Re_c end there is also some non-monotonic behaviour for $\alpha = 0.60$, as the flow transitions

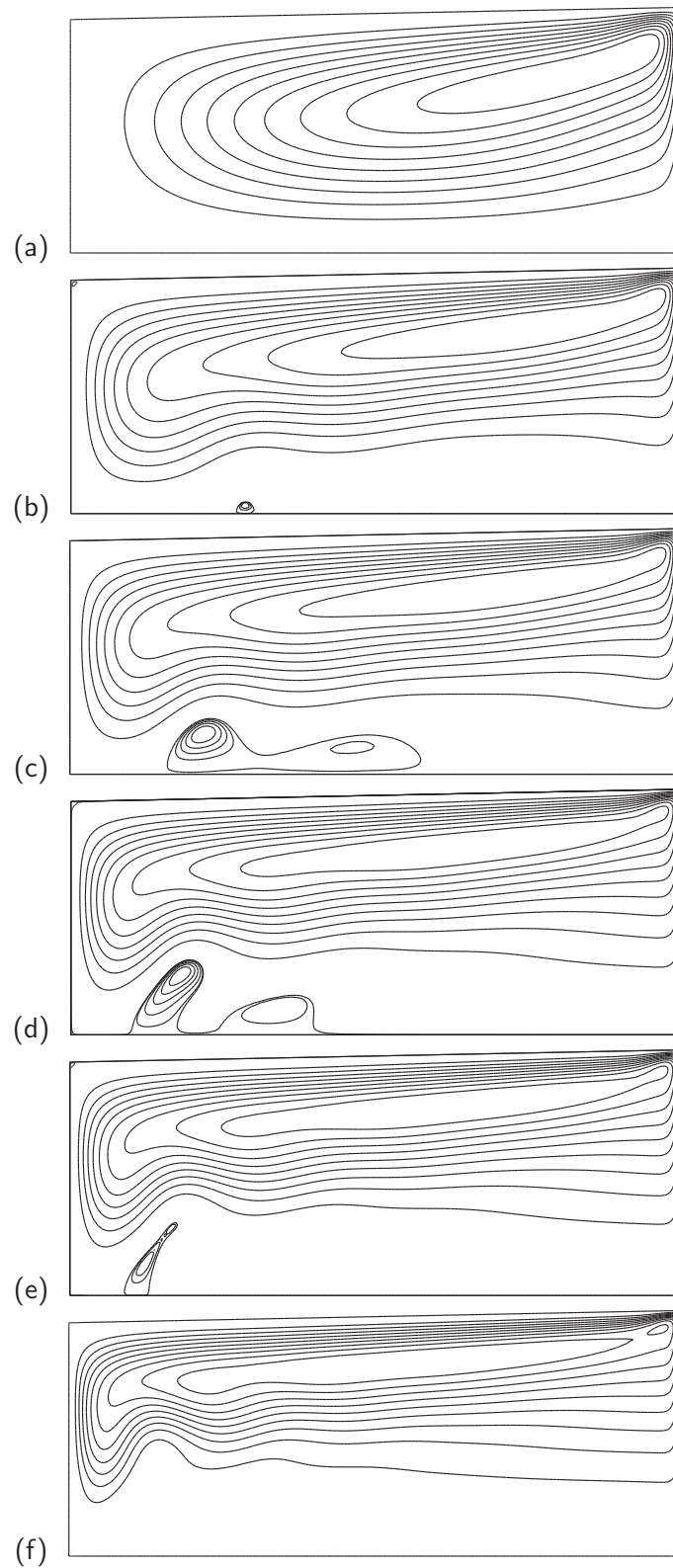


Figure 7.21: $\alpha = 0.95$ sloped cylinder streamlines for $Re_c =$ (a) 1000, (b) 2000, (c) 2500, (d) 3500, (e) 4000, (f) 6000.

from 2 merged bubbles to one, then to two and back to one again. This is due to a small intermittent bubble which appears downstream of the upstream bubble.

Increasing α narrows the Re_c range over which breakdown bubbles exist: for $\alpha = 0.75$, bubbles are present over $2500 \leq Re_c \leq 6000$, whereas at $\alpha = 1.25$ bubbles are only present over the range $2000 \leq Re_c \leq 3500$.

For all $\alpha > 4.0$, increasing Re_c beyond the two-bubble flow Re results in a transition to one bubble, which is situated close to the stationary lid. The bubble finally disappears for higher Re_c , although again streamline divergence persists, often well away from the centreline, for every α .

Some points which appear to be anomalous exist at the edges of some of the case regions. These are more likely a result of the inadequate resolution in these areas, rather than erratic behaviour in the flow itself. Smaller Re_c and α increments should clear up these regions. They do not play a significant part in our analysis in any case.

Based on these results we come to the conclusions that:

1. Increasing the wall ratio α decreases the lid rotation rate (Re_c) required for breakdown onset.
2. The range of Re_c over which breakdown exists reduces with increase in α .
3. As α approaches $\alpha = 1$ the flow is predisposed toward separated rather than merged bubbles.

An outcome of the sloped cylinder investigation is a new set of results to test the core Re and Ω definitions against. In figure 7.22 the breakdown states of the sloped cylinders are plotted as a function of core Re and Ω .

The aim of influencing Re and Ω with some independence has been achieved. An initial glance reveals a large spread in Ω . There are no results below $\Omega = 0.80$. But the spread of Ω into the high Ω end is much more extensive than has previously been studied in the open pipe. Ω ranges up to $\Omega \sim 8.5$, the result of a very high ratio of azimuthal to axial velocity. It is possible that the core Re and Ω definitions break down here, as it becomes difficult to differentiate a core since the streamline divergence associated with breakdown is so close to the stationary lid. With increasing Ω the maximum Re decreases,

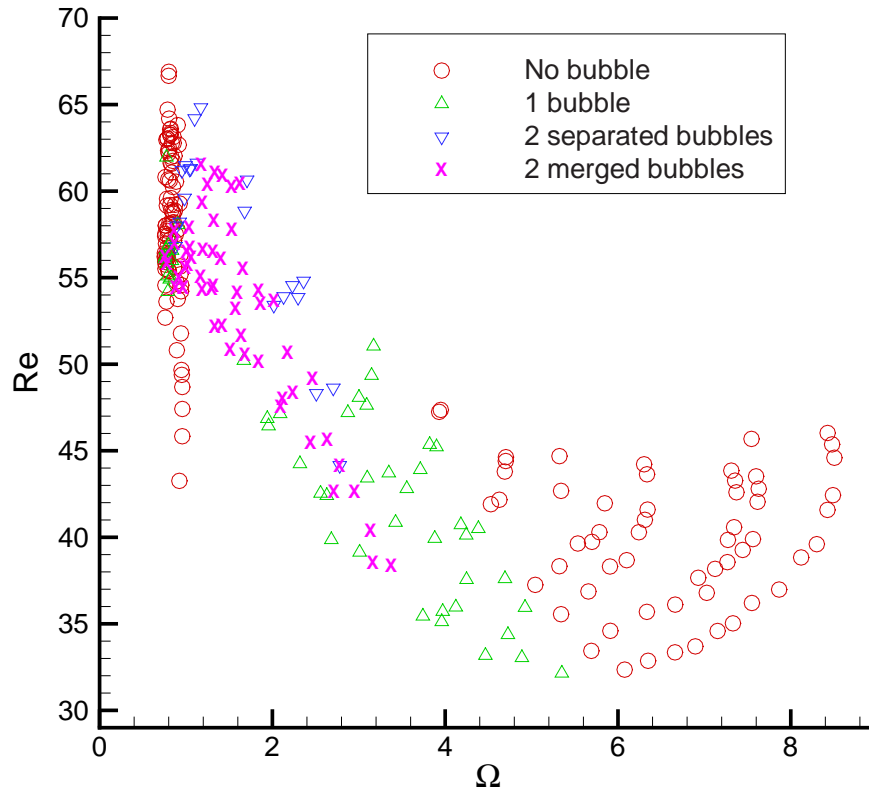


Figure 7.22: Sloped cylinder comparison of Re and Ω for breakdown.

even though these high Ω results correspond to high cylinder Re_c . Increases in cylinder Re_c appear to translate into increases in swirl for a particular slope α . The effects of three-dimensionality and time-dependence are not illustrated due to the two-dimensional steady analysis used. The disappearance of the bubble is expected for high Re_c however, as this occurs in the straight-sided cylinder. It is not known what structures will form at these high Re_c , but the observation of no bubbles is consistent with experimental observation. Also, a study by Al-Abdeli and Masri [1] found that in a swirling jet flow beyond a certain swirl level breakdown disappeared.

At the higher swirls ($1.2 < \Omega < 8.5$), there is a definite band structure. A fair degree of scatter does exist, but on the whole the breakdown occurrences tend to fit into distinct regions.

The low swirl results ($\Omega < 1$) are dominated by solutions with no breakdown, as expected.

There are incidences of breakdown for these low Ω for some values of α though. As swirl is increased (for $1 < \Omega < 2$), a band comprised of multiple breakdown bubble solutions appears. The definition of merged and separated bubbles was mentioned earlier, and serves as a way to further classify the types of breakdown occurring in the cylinder. But the physical relevance of this definition has not been considered, and is not particularly relevant to this discussion. We note that the occurrences of two separated bubbles are limited to the upper Re end of the two-bubble observations.

The band of multiple bubbles persists from $\Omega > 1$ to a gradual petering out at $\Omega \sim 3.5$. As the multiple bubbles peter out the single bubbles start to appear. At $\Omega = 3$ the single bubble occurrences dominate. This band persists until $\Omega = 5.5$.

In figure 7.23 the cylinder Re and Ω results are plotted against those obtained for the pipe defined in section 4.5.

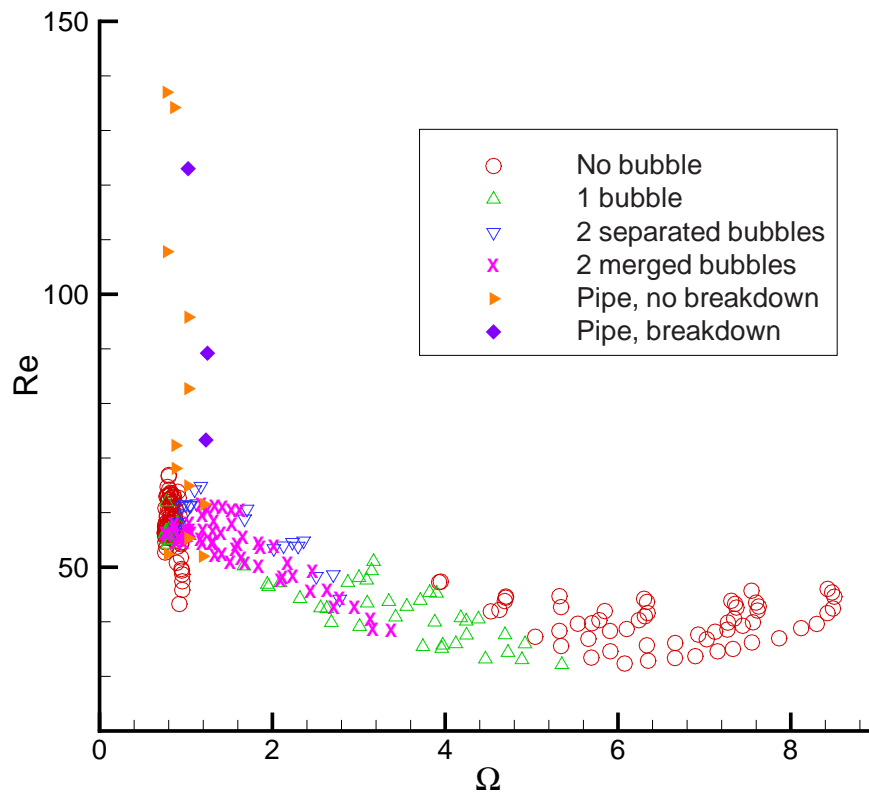


Figure 7.23: Sloped cylinder vs. pipe, comparison of Re and Ω for breakdown.

To obtain results for the pipe which would inhabit a similar core Re range to the cylinder, it was necessary to reduce Re_p to a much lower level than is usually considered; it turned out to be quite difficult to obtain useful results at such low Re_p . The range of Ω which can be explored for the pipe is also greatly restricted in comparison to the cylinder, as imposing too high a swirl at the inlet results in breakdown propagating past the diverging section. Nevertheless, the limited data plotted in figure 7.23 indicates that breakdown in the pipe and cylinder occurs at a similar swirl Ω , and that this Ω decreases with increasing Re .

In figure 7.24 the scale is expanded to allow closer inspection of the low Ω region. As expected, low Ω results in many solutions with no breakdown bubbles. There are some solutions with breakdown at low swirl though. The erratic behaviour for $\alpha = 0.25$ results in one breakdown bubble appearing among no-breakdown solutions. This point is not far removed from a cluster of single breakdown solutions at $Re \sim 55$.

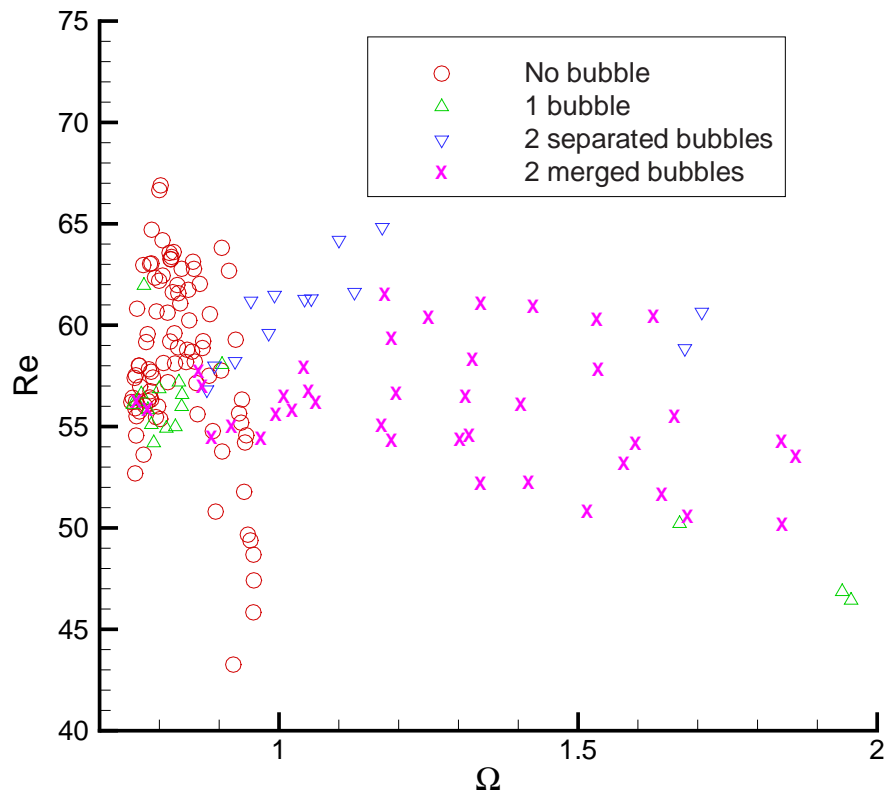


Figure 7.24: Sloped cylinder Re and Ω comparison.

A single stream of no-breakdown solutions extends downward (ie. decreasing Re) for roughly constant Ω . These solutions result from high slope ($\alpha = 0.25$ to ~ 0.75) and low cylinder Re_c cases. Beyond $\Omega = 1$ there are only breakdown solutions, until much higher cylinder Re_c .

The progression of Re/Ω for each cylinder as Re_c is increased is shown in figure 7.25

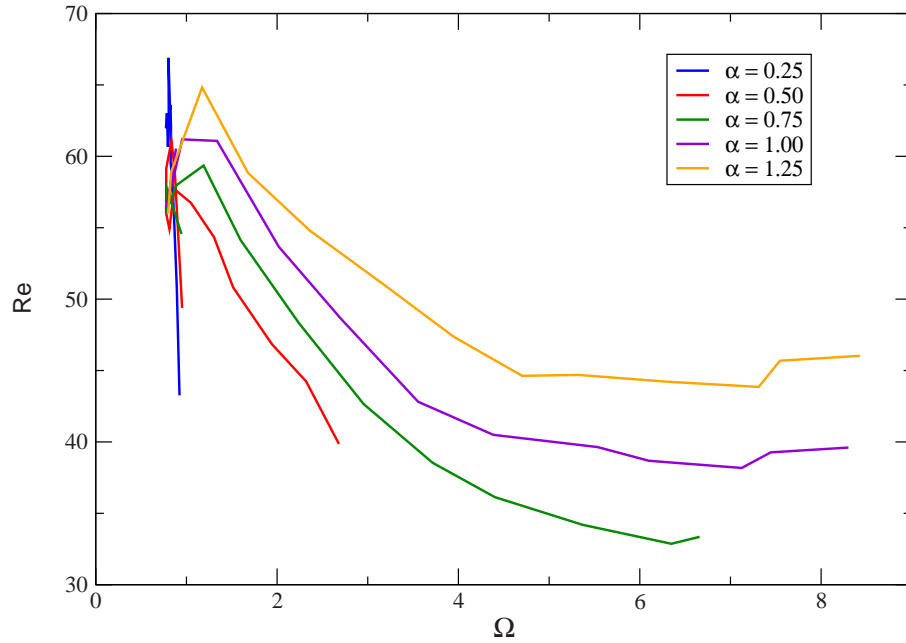


Figure 7.25: Sloped cylinder Re and Ω progression.

For $\Omega > 1.5$, progressive increases in cylinder Re_c result in a decrease in Re and increasing Ω , until $Re_c = 600$, for some cylinders, where Re starts to increase. So increases in Re_c push the flow closer to breakdown by increasing the swirl Ω . Hence we observe the onset of breakdown forms for increasing cylinder Re_c . This is consistent with observations in the pipe. However in the pipe Re generally remains unchanged while swirl is increased.

The decreasing core Re as a result of increasing Re_c is due to the stagnation in front of the bubble moving upstream, toward the stationary lid, and hence allowing less space for the flow to accelerate away from the wall.

7.3.4 Some conclusions

The various swirl definitions in the literature result in questionable comparisons between the swirl levels at which breakdown is expected in various geometries. Maxworthy's [49] description of a generalised geometry goes some way to improving the situation, but is not completely general in that some geometries, eg. the torsionally driven cylinder, do not fit the description. Since the core flow seems to be the most important factor in the development of vortex breakdown, defining the swirl and Reynolds number in terms of this core flow results in more meaningful comparisons between breakdown in differing geometries. Hence we considered only the core, ie. the region in which the swirl is increasing with radial distance from the axis. The edge of the core was defined to be the radial distance at which the change in the swirl velocity with radius first becomes zero. In all cases considered here the swirl velocity initially increased linearly away from the axis. (A disadvantage of this definition is that the swirl can only be defined if the axial and swirl velocity profiles are known just upstream of breakdown - this requires data to be extracted from the flow, and this data is not obtainable in all cases.)

However, the value even of this calculation is questionable - how can these numerical values be compared when the swirl and axial velocity profiles, though similar, vary significantly in shape? As argued by Delery [10], is it valid to reduce these complex profiles to a single parameter? The definition becomes especially vague when this parameter seems to be defined differently depending on the geometry in which breakdown is generated. Darmofal [8] calculates a swirl based on Faler and Leibovich's results which varies from the value obtained by Faler and Leibovich's calculation.

Despite these factors, some correspondence between the pipe and cylinder in terms of Re and Ω for breakdown onset is apparent.

7.4 Absence of hysteresis in the cylinder

Another difference between the cylinder and open pipe flows is the observation of hysteresis. Hysteresis is often observed in open pipe experiments and over delta wings. However, hysteresis is not generally observed in the cylinder (Sorensen [62] observed hysteresis, but only for Re_c higher than that generally used in breakdown studies). This observation is

claimed by some to indicate that the recirculation observed in the cylinder is fundamentally different and should not be classified as breakdown.

It has been noted that the hysteresis range is a function of Reynolds number. Our conclusion that the fundamental difference between pipe and cylinder breakdowns is Reynolds number is consistent with this observation; hysteresis is not associated with breakdown in the cylinder because the Reynolds number is too low, according to the more consistent core definition of Reynolds number.

Hence one possible interpretation is that the hysteretic transition that occurs at high Reynolds number in pipe flows is smoothly converted to a non-hysteretic transition as the Reynolds number is decreased toward that characteristic of cylinder breakdown.

To test this we use a two-dimensional spectral-element code to simulate Faler and Leibovich's [18], [17] pipe. Initially we begin with a flow with a pipe Reynolds number similar to that used by Faler and Leibovich, and determine the range of Ω_p over which breakdown can be found. This range is found by gradually increasing the swirl from an initial low-swirl solution without breakdown to one with breakdown, and then gradually reducing the swirl to determine the level at which breakdown disappears again. This procedure is repeated for decreasing Reynolds numbers until hysteresis is no longer observed. This provides a lower bound on the hysteresis region. The test will determine whether this (core) Reynolds number is greater than the (core) Reynolds number at which breakdown is typically observed in the cylinder, and hence whether or not hysteresis should be expected in the cylinder.

In figure 7.26 the regions corresponding to no breakdown, breakdown, and hysteresis (where both breakdown and no-breakdown solutions are obtained) are plotted.

In figure 7.26 the region to the left of the low Ω_p curve indicates solutions with no breakdown, to the immediate right of the high Ω_p curve is a region with breakdown only. Between the two curves is a region where solutions with breakdown and without breakdown are possible; the hysteresis region.

The Reynolds number range tested was $250 < Re_p < 2000$. Within the resolution of the study ($0.005\Omega_p$) hysteresis was not observed for $Re_p \leq 1250$. From $Re_p = 1250$ to $Re_p = 2000$ the region over which hysteresis is observed grows with Re_p ; at $Re_p = 1250$ the hysteresis region has a width of (at most) $\Delta\Omega_p = 0.005$, and at $Re_p = 2000$ this region

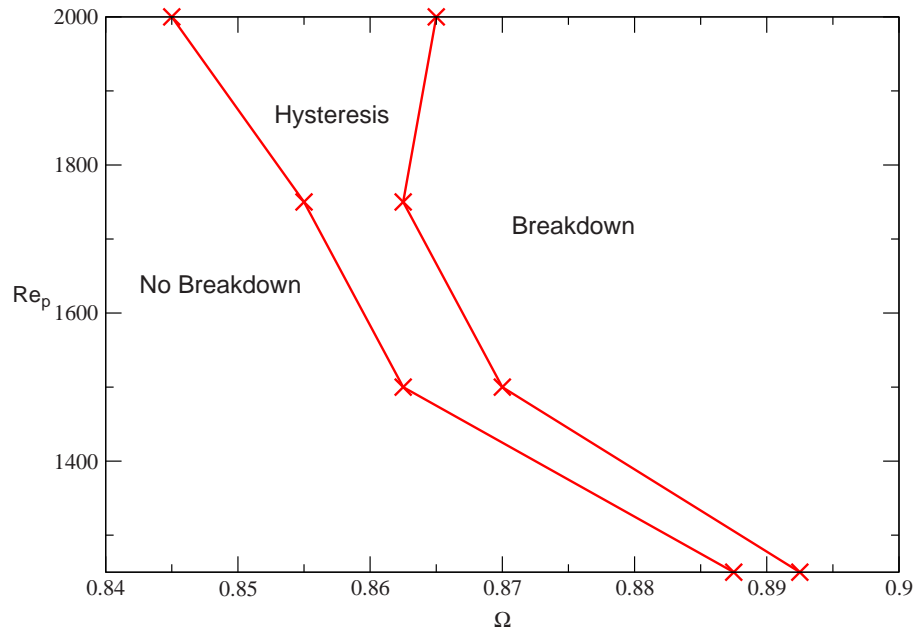


Figure 7.26: Breakdown, no-breakdown, and hysteresis regions in numerical computations based on an implementation of Faler and Leibovich's [18], [17] pipe.

has a width of $\Delta\Omega_p = 0.02$. Also, as Re_p increases, it appears from these limited data that the rate of expansion of the hysteresis region is also increasing with increasing Re_p .

Also to be noted from figure 7.26 is the tendency of the value of Ω_p at which breakdown appears to increase with decreasing Re_p .

Since the core Re is based on the axial velocity on the centreline, the core Re at which hysteresis disappears will have a value larger than the pipe $Re_p = 1250$, since the flow is jet-like. So the lack of hysteresis in the cylinder, where Re is typically < 100 , is not surprising.

7.5 Is the cylinder 'breakdown' really breakdown?

If a mechanism for vortex breakdown is to be better understood then there must be confidence that what is being studied in different geometries *is* a manifestation of the same physical phenomenon. Much work has concentrated on the flow in the cylinder, as it is relatively easy to set up experimentally and computationally, with the expectation that the same phenomenon is occurring in the cylinder as that which occurs over wings. This

however may not be the case. Since a major motivation for studying vortex breakdown is to understand its occurrence over a delta wing, it is important to determine whether what occurs in the cylinder is breakdown or not.

Goldshtik and Hussain [23] give the name ‘vortex breakdown’ to the phenomenon observed in open pipes and over delta wings. In order for breakdown in any other geometry to satisfy their definition it must have the following characteristics:

1. The entire steady flow must experience a jump transition to another steady flow state, in the sense of figure 7.27;
2. The flow usually displays hysteresis.

(a)

(b)

Figure 7.27: (a) Jump transition vs. (b) gradual change.

Goldshtik and Hussain [23] claim that according to this definition, the recirculation bubbles which occur in the torsionally driven cylinder cannot be classed as vortex breakdown. This is because the transition from parallel streamlines to the development of a recirculation bubble on the axis is a smooth one; see the collection of visualisations in figure 7.28.

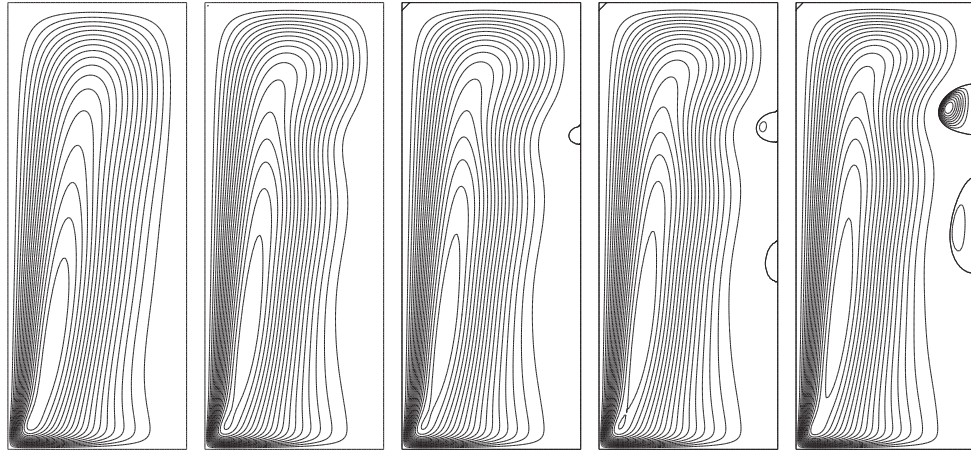


Figure 7.28: Streamlines for (from left to right) $Re = 1500, 1902, 1933, 2001, 2252$.

It can be seen from these images that the transition from no breakdown to breakdown in the cylinder appears gradual - there is a steady increase in streamline divergence, until eventually the axial flow stagnates and a recirculation bubble appears.

Another (likely related) claimed point of difference between the cylinder and pipe/wings is the hysteretic behaviour observed in pipes and over wings, and the general absence of this behaviour for cylinders. A possible reason for the absence of observations of breakdown hysteresis in the cylinder was mentioned in the previous section. In any case the hysteresis argument is not a strong one, as vortex breakdown in the more open geometries (pipes and wings) does not necessarily display hysteresis.

Leibovich [42] asserts that the evidence produced by experiments in pipes shows that the spiral and bubble types of breakdown are distinct, in the sense that they are the results of different generation mechanisms. Leibovich [42] quotes the experiments by Sarpkaya [57] and Faler and Leibovich [17], in which the transition from the spiral mode to the axisymmetric bubble mode of breakdown was observed. With increasing swirl, the spiral gradually progressed upstream, until at a critical swirl an axisymmetric bubble formed and this bubble jumped several vortex core diameters upstream. Leibovich [42] argues that this discontinuity in the axial position/swirl relationship provides evidence that the two breakdown forms are distinct. Leibovich [42] also notes that the most prevalent form of breakdown over delta wings is the spiral.

So:

- if the bubble and spiral forms are not manifestations of the same phenomenon, and:
- the form most prevalent over delta wings is the spiral, and:
- the only form seen in cylinders is the bubble, then:
- how relevant is what happens in cylinders to breakdown over delta wings?

ie. is it possible to relate studies of vortex breakdown in a cylinder to those of breakdown over delta wings?

Despite the above concerns regarding the validity of the approach, research continues into the cylinder phenomenon, and conclusions drawn from these cylinder studies are applied to vortex breakdown theory generally. How can this be justified given the above assertions?

Figure 7.29: Left: pipe at $\Omega_p = 1.45$, $Re_p = 500$; right: cylinder at $Re_c = 2252$.

We begin by stating that the bubbles in the torsionally driven cylinder resemble in many ways the bubbles produced in pipes, and also those resulting from the breakdown of vortex cores over delta wings. See figure 7.29; the bubbles appear similar - there is a stagnation point on the axis, and a region of recirculation downstream. At low Re the observations by Sarpkaya [57] of the bubble form in the pipe match closely images of the bubble in the torsionally driven cylinder, although Leibovich [42] notes that there is some asymmetry in the downstream end of the bubbles.

We also question the assertion by Goldshtik and Hussain [22] that the open pipe transition to breakdown is fundamentally different to the transition to breakdown in the cylinder. For the open pipe at low Re_p , the breakdown onset path is similar (figure 7.30). Here we consider pipe flow at $Re_p = 500$, which is outside the hysteresis range (see figure 7.26). At $\Omega_p = 1.44$ there is some streamline divergence, and at $\Omega_p = 1.445$ the divergence has increased slightly. At $\Omega_p = 1.45$ a small bubble has formed on the axis of the pipe, and

by $\Omega_p = 1.48$ a large bubble has appeared. This gradual bubble evolution is similar to the progression that occurs in the cylinder; figure 7.28.

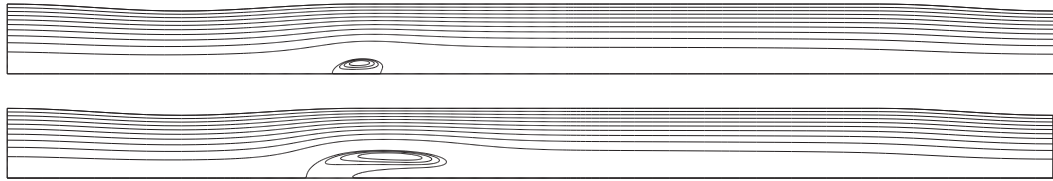


Figure 7.30: From top to bottom: results for $\Omega_p = 1.44, 1.445, 1.45, 1.48$ ($Re_p = 500$).

The previous section highlighted the different Re/Ω regimes occupied by the pipe and cylinder flows. This potentially provides an explanation for the absence of the spiral form in the cylinder, and a way to test this hypothesis.

The reason that the (completely) axisymmetric bubble is not observed in the pipe, and the spiral form is only observed in the pipe, is the much higher Re at which pipe studies have been conducted. Experimentally it is very difficult to obtain results in the pipe for the (core) Re and Ω values which in the cylinder result in breakdown. However it is possible to investigate very low Re values in the pipe numerically. This will be attempted in the next section.

7.6 Three-dimensional simulation of the pipe flow

For this work, the increased computational requirements for 3d simulations resulted in a change of code. A more efficient spectral-element code was used in order to provide three-dimensional results of adequate resolution within a feasible timeframe. A description of the spectral-element code employed is given in Tan [69], and a similar method is used in Karniadakis and Triantafyllou [40]. Fundamentally a spectral-element scheme is employed to obtain 2D solutions, and this is extended to a 3D method via a Galerkin Fourier expansion. Integration forward in time is provided by a three-step time splitting technique

described in Karniadakis *et al.* [39].

7.6.1 Method

Here we model numerically the pipe used by Faler and Leibovich [17] in their experimental work. The pipe is similar to that used by Sarpkaya [57], illustrated in figure 2.3. To reduce computation time the test section is truncated; the resulting pipe is illustrated in figure 7.31; the R_i and z_i are defined in table 7.4.

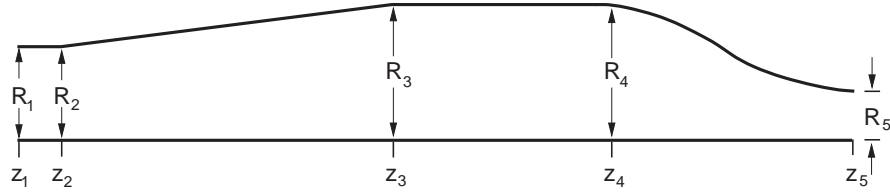


Figure 7.31: Pipe geometry from Faler and Leibovich [17] (truncated here).

Variable / i	1	2	3	4	5
R_i	1.0	1.0	14.0	21.87	32.37
z_i	0.667	0.667	1.333	1.333	0.667

Table 7.4: Table of R_i and z_i , $i = (1, \dots, 5)$.

Swirl and axial velocity profiles specified at the inlet are described by functions fitted to the velocity profiles measured by Faler and Leibovich upstream of breakdown in their experiment. The functions are represented in equations 7.11 and 7.12.

$$u(r) = u_1 + u_2 \exp\left(-\frac{\alpha r^2}{r_t^2}\right) \quad (7.11)$$

$$v(r) = k \left(\frac{r_t}{r}\right) \left[1 - \exp\left(-\frac{\alpha r^2}{r_t^2}\right)\right] \quad (7.12)$$

where $u(r)$ and $v(r)$ are the axial and radial velocities at radius r , and r_t is the radius of the tube at the inlet. The other quantities in these equations are constants, with the following values for the $Re_p = 2560$, $\Omega_p = 1.777$ flow: $u_1 = 5.53$ cm/s, $u_2 = 7.95$ cm/s, $\alpha = 11.84$, and $k = 4.1$ cm/s. These functions are a good approximation to the actual velocity profiles away from the wall. They are applied at the axial location in the pipe

corresponding to the axial location the profiles were extracted from in the experimental pipe.

From the base case of $Re_p = 2560$ and $\Omega_p = 1.777$ we vary Re_p and Ω_p by scaling. Re_p is varied by changing the viscosity, ν . Ω_p is varied by applying a scaling factor β to the equation for the swirl velocity. A value $\beta = 1$ corresponds to $\Omega_p = 1.777$ in the experimental pipe. Both Re_p and β need to be varied as it is anticipated that decreasing Re_p will require a corresponding increase in β to obtain breakdown.

7.6.2 Varying Re_p

To test our hypothesis, we now need to reduce Re_p and see whether the flow (with breakdown) becomes axisymmetric. For each value of Re_p solutions were obtained for a number of different values of β in the two-dimensional pipe to determine the point at which breakdown evolves. These values of β were then used as a starting point to look for breakdown in the three-dimensional pipe. As expected, decreasing Re_p led to a large increase in the value of β required for breakdown. For reference the values required for breakdown in the two-dimensional simulations are presented in table 7.5.

Re_p	Breakdown β
2000	0.865
1750	0.8625
1500	0.87
1250	0.8925
1000	0.94
500	1.135
250	1.335
125	1.63

Table 7.5: The value of β at which breakdown is first observed for each Reynolds number tested.

The resulting three-dimensional visualisations for $(Re_p, \beta) = (160, 1.75)$, $(320, 1.375)$, and $(1280, 1.0)$ are presented in figure 7.32. In figure 7.32 we plot the region where the median eigenvalue λ_2 of the term $S^2 + \Omega^2$ is negative, where S and Ω are the symmetric and

antisymmetric parts of the velocity gradient tensor. This quantity provides visualisation of vorticity structures. For more details see Jeong and Hussain [35]. The approximate locations of the pipe walls are indicated in the figure.

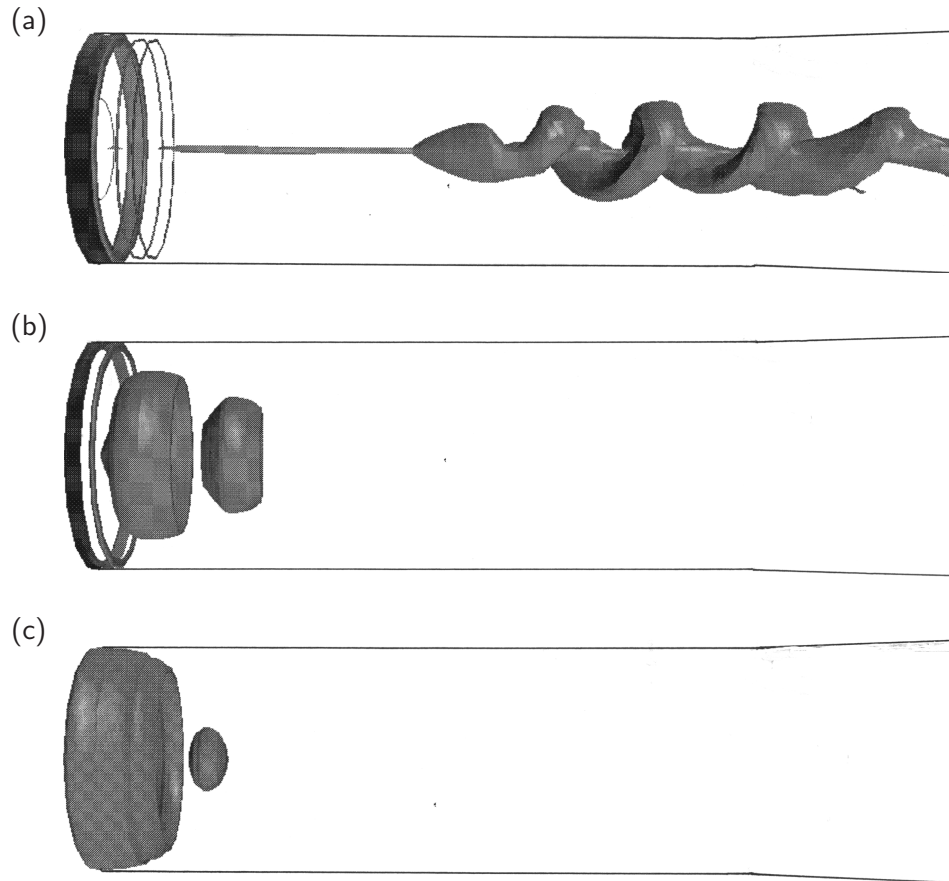


Figure 7.32: Results for (a) $Re_p = 1280$, $\beta = 1.0$, (b) $Re_p = 320$, $\beta = 1.375$, (c) $Re_p = 160$, $\beta = 1.75$.

These plots show that as Re_p is reduced (and β increased to ensure breakdown) the three-dimensionality which dominates the high Re_p case completely disappears by $Re_p = 320$. Also note the appearance of the bubble for $Re_p = 160$. The back of the bubble has become closed, and it resembles much more the type of bubble observed in the torsionally driven cylinder.

For low Re_p , the bubble is very close to the inlet - compare with the cylinder, where breakdown is also close to the cylinder wall. This type of breakdown is difficult to produce in the pipe experimentally because it would swim upstream past the inlet (in our case the bubble is fixed by the inlet boundary condition.) Hence the absence of axisymmetric

breakdown in the pipe.

7.7 Summary

Examination of the velocity profiles upstream of breakdown in the cylinder and open pipe has revealed the similarities between the vortical core flows, despite the differences in geometry. The subsequent implementation of more consistent definitions for the two parameters Re and Ω , based on these velocity profiles, has enabled a direct comparison to be made between the open pipe and cylinder flows with respect to their susceptibility to breakdown. The cylinder and pipe flows typically studied have been shown to operate in very different Reynolds number regimes. This observation is put forward as an explanation for the different manifestations of breakdown in these geometries.

To test this idea, the Reynolds number in a three-dimensional pipe simulation was reduced to the level of that found in the cylinder, with the result that a bubble with the characteristics of the cylinder type breakdown was observed. This confirms the hypothesised dependence of breakdown form on Reynolds number.

This observation, along with others outlined in this section, indicates that as the Reynolds number for the pipe flow is reduced, the hysteretic open spiral mode of breakdown commonly observed in pipes is replaced by a non-hysteretic closed bubble breakdown observed in the closed cylinder. This does not imply that the two types of mode are the same. It seems more likely that the helical mode becomes less unstable at low Reynolds number relative to the axisymmetric mode, for instance.

Chapter 8

Breakdown promotion by an upstream pulse

8.1 Hysteresis and delta wing vortex breakdown

One of the characteristics of vortex breakdown is the existence of regions of parameter space in which flow hysteresis is observed. Studies of vortex breakdown in flows over delta wings, in swirling pipe flows, and in confined cylinder flows have shown that multiple states can exist for a single set of parameter values.

In Lowson's [46] study of vortex breakdown in flow over a delta wing, breakdown displayed hysteresis with respect to its chordwise location as wing incidence (angle of attack) was varied. The apparatus used consisted of a 10° semi-apex angle wing with variable pitch placed in a water tunnel. The findings are represented graphically in figure 8.1, where breakdown location is plotted against wing angle of attack (AOA, or α). Breakdown location was measured from the wing apex, and expressed in terms of the wing chord length.

At an AOA of 30° no breakdown was observed. As AOA was increased to 34° breakdown appeared in the wake, downstream of the wing trailing edge. With further increase in AOA the breakdown moved gradually upstream until at $\text{AOA} = 40^\circ$ the breakdown was 0.4 chord downstream of the wing trailing edge. At $\text{AOA} = 41^\circ$ the bubble moved further upstream to 0.375 chord from the apex of the wing. A slow reduction of AOA back to $\text{AOA} = 34^\circ$ resulted in a gradual movement of breakdown toward the trailing edge, although

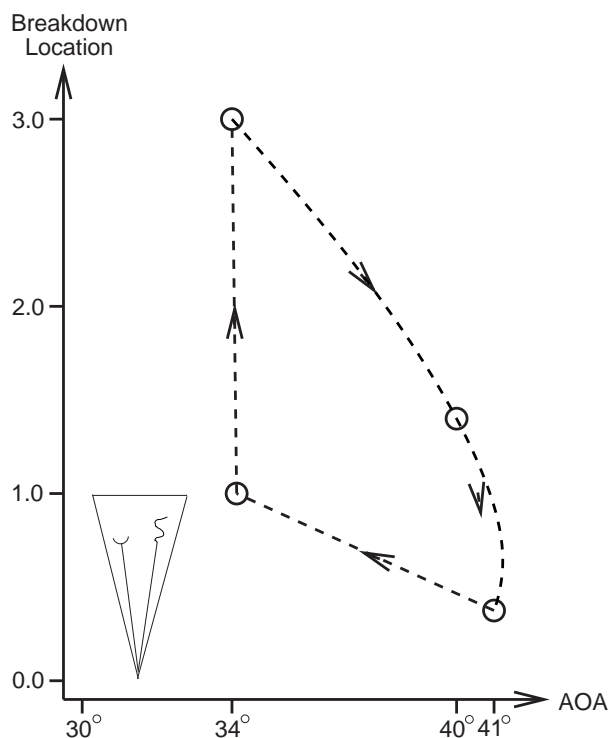


Figure 8.1: Lowson's [46] experimental results for location of breakdown as a function of Angle Of Attack (AOA).

it stayed above the wing. Then at $\text{AOA} = 34^\circ$ the bubble was blown slowly back to the location at which it first evolved.

This study was conducted at Reynolds number $Re = 3 \times 10^4$, which is low relative to that of practical applications, but it is noted by Lowson [46] that Reynolds number does not have a large effect on flows on slender wings; hence hysteresis is also expected for higher Reynolds number flows of practical interest. Since we consider only the pipe in this and the following chapter, we return to less cumbersome notation: $Re = Re_p$, $\Omega = \Omega_p$.

Traub and Galls [70] observed some Reynolds number dependence in their study of flow past a blunt-edged delta wing with a fuselage. Variation in Re through the range $6.8 \times 10^4 < Re < 2.03 \times 10^5$ led to a maximum variation in breakdown position of approximately 20% of the wing chord in that study. It is expected that wings with sharp leading edges would be less sensitive to Reynolds number changes due to a reduced dependence of leading edge separation from a sharp leading edge on Reynolds number [70]. Previous work has also identified breakdown hysteresis with respect to yaw of slender delta wings (in Lowson [46]).

It is evident that vortex breakdown in flows over delta wings is susceptible to hysteresis; this suggests the possibility of using a transfer between hysteresis states to control the location and incidence of breakdown over wings. It may be possible to make the flow jump to a state where breakdown occurs downstream of the wing leading edge, but at the same Reynolds number and swirl Ω . Also, if it is desirable to instead promote vortex breakdown, for example to destroy trailing vortices behind large aircraft, it may be possible to trigger a jump to the conjugate breakdown state. It turns out that the second transition is more easily brought about, at least in open pipe flows. This will be elaborated on in the main part of this chapter. However we first describe the incidence of hysteresis with respect to vortex breakdown in pipes.

8.2 Hysteresis and pipe vortex breakdown

Sarpkaya [57] noted the existence of vortex breakdown hysteresis in open pipe flow experiments. For a particular range of Reynolds number and Ω two breakdown states were possible, the bubble or spiral, and the flow would change from one form to the other within a certain Reynolds number and swirl range.

A numerical study of pipe vortex breakdown was provided by Beran and Culick [4]. They examined breakdown onset in a circular pipe with converging-diverging section just downstream of the inlet, and the same inlet velocity profile as that used in the present study:

$$\begin{aligned} u(0, r) &= 1 && \text{(axial velocity)} \\ w(0, r) &= \frac{V}{r} (1 - e^{-r^2}) && \text{(swirl velocity)} \end{aligned} \tag{8.1}$$

where V is the swirl Ω used in our study. These velocity profiles are representative of the profiles observed upstream of breakdown in experimental pipe studies.

The behaviour of the open pipe flow in the range $250 \leq Re \leq 2000$ and $1.45 \leq \Omega \leq 1.55$ was mapped out. Below a critical Reynolds number no hysteresis was observed, but at higher Reynolds number a cusp in the solution space was identified; up to 3 flow states could be produced for the same swirl V . Lopez [45] confirmed Beran and Culick's [4] Reynolds number and swirl range over which primary and secondary limit points could be defined.

The behaviour of vortex breakdown in flows over delta wings also forms a cusp in angle of attack/Mach number space. Shtern and Hussain [61] described the effect of angle of attack (AOA) and Mach number (M) on the pattern of vortex breakdown evolution; their schematic is redrawn in figure 8.2. The pattern matches that found for vortex breakdown in open pipe studies of Lopez [45] and Beran and Culick [4].

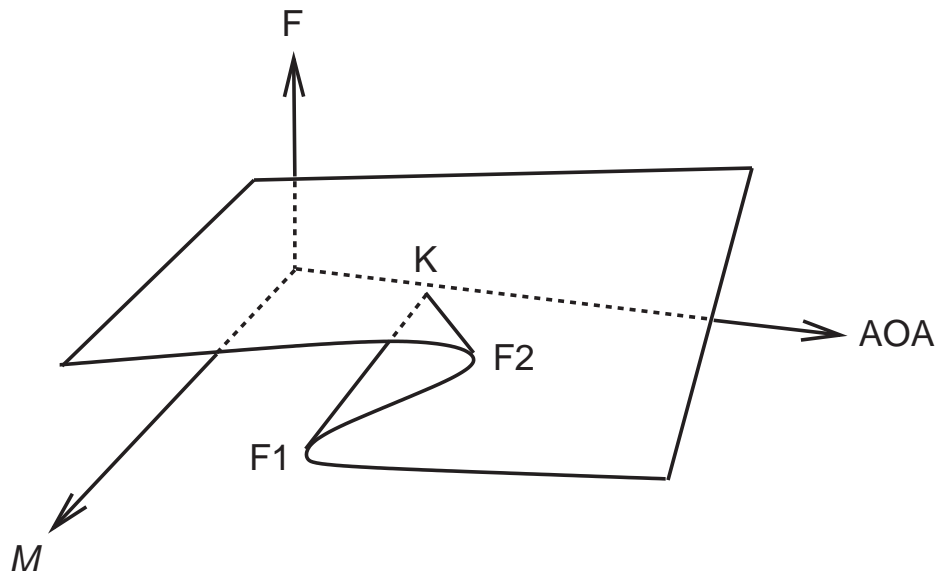


Figure 8.2: Schematic of the cusp and fold associated with hysteretic transitions over a delta wing (redrawn after Shtern and Hussain [61]).

So the behaviours in the two geometries are similar, but without measurements of the velocity profiles in the vortex core it is not possible to quantitatively compare the flows. In the case of the delta wing, the hysteretic jumps refer to abrupt shifts in vortex breakdown location, rather than the appearance and disappearance of breakdown.

8.3 This study

A method by which changes between the two conjugate states within the hysteresis region may be realised will now be considered. We aim to investigate whether transitions between states can be induced by applying perturbations to the inlet velocity profile. The perturbations will involve changing the swirl to axial velocity ratio at the inlet, and this is achieved by directly manipulating the value of Ω (V in equation 8.1). In this way only the

swirl ratio is changed, and the axial velocity (and hence the Reynolds number) remains the same.

There are two questions to be answered here:

1. Can a perturbation to a flow which is initially without breakdown induce a persistent breakdown?
2. Can a perturbation to a flow which begins with breakdown present result in the disappearance of breakdown?

The obvious answer to both of these questions is yes, if the perturbation is sufficiently large and sustained. For example, if the flow is pushed out of the hysteresis range and held there by the inlet boundary condition, only one flow condition can be manifest. However, it is unknown just how large (in amplitude and duration) the perturbation must be.

8.4 Problem formulation

The pipe geometry employed is defined in Darmofal and Murman [9] (1994), and was described in an earlier section.

The inlet velocity profile is the q-vortex, and is redisplayed below:

$$\begin{aligned}
 u_0(r) &= 1 + \Delta u e^{-r^2} \\
 v_0(r) &= 0 \\
 w_0(r) &= \frac{\Omega}{r} [1 - e^{-r^2}]
 \end{aligned} \tag{8.2}$$

where u , v , and w are the axial, radial, and azimuthal velocity components respectively. In each case we consider Δu is zero, so the velocity in the axial direction does not vary radially at the inlet.

All of the solutions presented here are results of time-dependent calculations. In order to obtain the initial steady solutions, the time dependent code is run until a steady state is reached.

We aim to map out the transitions as a function of Ω_P and dt . We define Ω_P as the change in Ω applied to the inlet, as follows:

$$\Omega_P = \frac{\Omega}{\Omega_i} \tag{8.3}$$

where Ω_i is the initial condition swirl.

The change will be applied step-wise, ie. initially we do not ramp up Ω ; the change is instantaneous. Δt is then the duration over which the perturbation is maintained.

Since this study will focus on the region in the Reynolds number/swirl parameter space where hysteresis occurs, an initial investigation has determined that for a Reynolds number of $Re = 1000$, hysteresis is observed in the range $1.43 < \Omega < 1.461$, where Ω is the swirl parameter defined in equations 8.2.

The procedure for determining this range is as follows. A steady solution is obtained at $\Omega = 1.43$, without breakdown, and the swirl steadily increased, with the axial velocity constant, until breakdown is observed at $\Omega = 1.461$. This process defines the limit on the upper branch for the no-breakdown state (see figure 8.4). Next the swirl is gradually reduced, so that the flow travels along the lower branch, until the breakdown bubble disappears at $\Omega = 1.43$. This defines the breakdown limit point on the lower branch. The second limit point is not as well defined as the first - the bubble seems to be more persistent once it has evolved, and the flow takes a considerable time to return to the original pre-breakdown state. This observation will also be borne out in the transitions described in the following sections.

The range over which hysteresis occurs ($1.43 < \Omega < 1.461$) compares with Beran and Culick's (1992) range of $1.465 < \Omega < 1.505$ for the same Reynolds number ($Re = 1000$). The relative range shift may be due to the slightly different geometries considered - both of the pipes are identical apart from a converging outlet in our study. The two ranges are of comparable size.

8.5 Steady initial condition

Now that the hysteresis range has been mapped out, the initial conditions for the transition study can be determined. All of the simulations begin with a swirl of $\Omega = 1.45$, near the centre of the hysteresis range; it will be necessary to obtain both the breakdown and no-breakdown steady solutions at this value of Ω ; the solution with breakdown will be used in chapter 9.

For the no-breakdown state, since the flow is sensitive to transients - which can easily

push the flow into the breakdown state - it is necessary to slowly increase the swirl from well below the breakdown region to $\Omega = 1.45$. An initial solution was obtained using a steady solver for $\Omega = 1.34$, which is well below that required for breakdown. Ω was then increased gradually by time-dependent calculations until $\Omega = 1.45$, ensuring that no breakdown bubble evolved. This solution was close to steady by $t=2.0 \times 10^4$. Iterating for a further 1.1×10^5 time units changed the solution by 0.05% (where the minimum axial velocity was monitored). This final solution was adopted as the initial condition.

Obtaining the initial breakdown solution was more straightforward; allowing the flow to develop from an initial condition with $\Omega = 0$ resulted in the development of a steady breakdown bubble at $\Omega = 1.45$. In this case the solution changed by 0.07% from $t=7.1 \times 10^4$ to $t=8.3 \times 10^4$. The solution at $t=8.3 \times 10^4$ was used for the initial condition for the transition from breakdown to no-breakdown, considered in the next chapter.

The two initial conditions thus obtained are displayed in Figure 8.3.

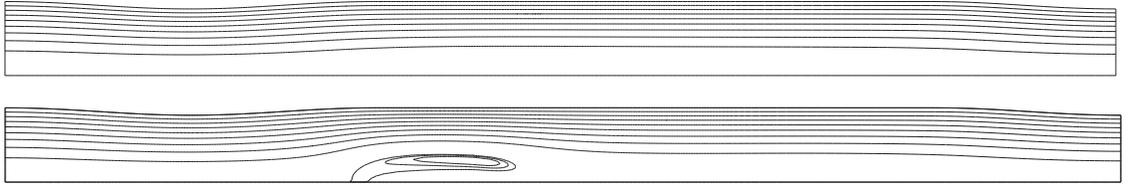


Figure 8.3: Solutions for $\Omega = 1.45$: no-breakdown state (top) and breakdown state (bottom).

$\Omega = 1.45$ at $Re = 1000$ is in the body of the hysteresis region. Although the $\Omega = 1.45$ solution with breakdown will not be used as an initial condition until the next study, it is included here to illustrate the expected flow state for the present study after a successful transition to breakdown.

We aim to trip the flow into the conjugate state by imposing an increase in swirl, at the inlet. The swirl change is maintained for varying periods of time; the pulse time dt is the time the pulse is left on, normalised by the pipe length and axial velocity; see equation 8.4:

$$dt = \frac{u\delta t}{L}, \quad (8.4)$$

where u is the axial velocity, L is the pipe length, and δt is the period over which the pulse is maintained. Various pulse times and amplitudes are tested.

The pulse amplitude is represented by the swirl increase divided by the initial condition swirl Ω_i , which is 1.45 in all cases:

$$\Omega_P = \frac{\Omega}{1.45} \quad (8.5)$$

Hence an increase in swirl is represented by $\Omega_P > 1$, and for a decrease in swirl $\Omega_P < 1$.

As mentioned, the initial condition for this part consists of the $\Omega = 1.45$ solution with no breakdown bubble present; this represents a solution on the lower branch in figure 8.4.

The aim is to determine a combination of the pulse amplitude and duration which will result in the persistence of a breakdown bubble in the final steady state. If the pulse is maintained indefinitely, breakdown is expected to evolve and remain, as all pulse magnitudes increase the swirl Ω to the point where the flow is outside the hysteresis region, and into the region where breakdown is present. It is uncertain whether the breakdown will remain once the swirl is reduced again.

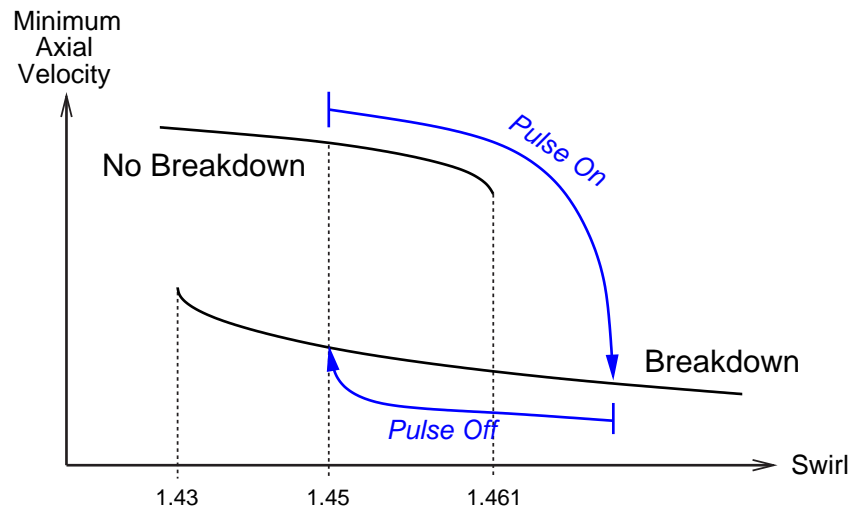


Figure 8.4: Possible path as a result of the $\Omega_P > 1$ pulse.

An initial study revealed that the following ranges of parameters Ω_P and dt should encompass the most interesting transitions :

$$\begin{aligned} 1.01 &\leq \Omega_P \leq 2.0 \\ 0.01 &\leq dt \leq 4.0 \end{aligned} \quad (8.6)$$

8.6 Flow behaviour for $\Omega_P > 1$

The first pulse applied amounts to a doubling of the swirl at the inlet; Ω is increased to $\Omega = 2.9$ (Hence $\Omega_P = 2$). This case is described here in some detail as it illustrates some points about the pipe transitions in general. In figures 8.5 and 8.6 streamfunction contours (top) and contours of the change in azimuthal velocity (bottom), δu_ϕ , are plotted, for $dt = 0.25$.

Figures 8.5 and 8.6 show the evolution of the flow following the increase and subsequent decrease in swirl. The contour levels remain constant for these plots. The streamfunction contours are not equally spaced - there are 4 contours of negative streamfunction values, and 8 contours of positive streamfunction values. This unequal partition is designed to ensure the breakdown bubble is visible when it evolves.

The increase in swirl velocity due to the imposition of the swirl increase at the left (the inlet) is obvious in the plot 8.5(a). Substantial streamline divergence is associated even at this early stage with the swirl increase, indicating a strong tendency toward the evolution of breakdown. By time $t=5$ in plot 8.5(b) a breakdown bubble has evolved on the centreline of the pipe. The swirl increase is maintained until $t=7.5$, so plot 8.5(c) shows the conditions just after the inlet swirl has reverted back to $\Omega = 1.45$. As the swirl change continues to propagate through the domain, the breakdown bubble lengthens and increases in radial extent.

By $t=25$ (plot 8.5(d)) the long bubble is moving downstream with the swirl change, but some streamline divergence remains upstream, with a tiny recirculation region present in the diverging section; this bubble is transient and has disappeared by the next plot (8.5(e)). A region of reduced azimuthal velocity, which has been present since $t=5$ but is now reduced in magnitude, now lingers near the diverging inlet section, and is accompanied by some streamline divergence (plot 8.5(f)).

Figures 8.6(a) to (c) show that with time this azimuthal velocity deficit slowly strengthens, and a new breakdown bubble evolves. In the final plot (8.6(c)) a bubble partly detached from the axis has formed; this bubble is of the form seen in the steady case for $\Omega = 1.45$, and the progression of the flow is now toward a steady state containing this partly-detached bubble.

The importance of azimuthal vorticity in elucidating the mechanism for onset of breakdown

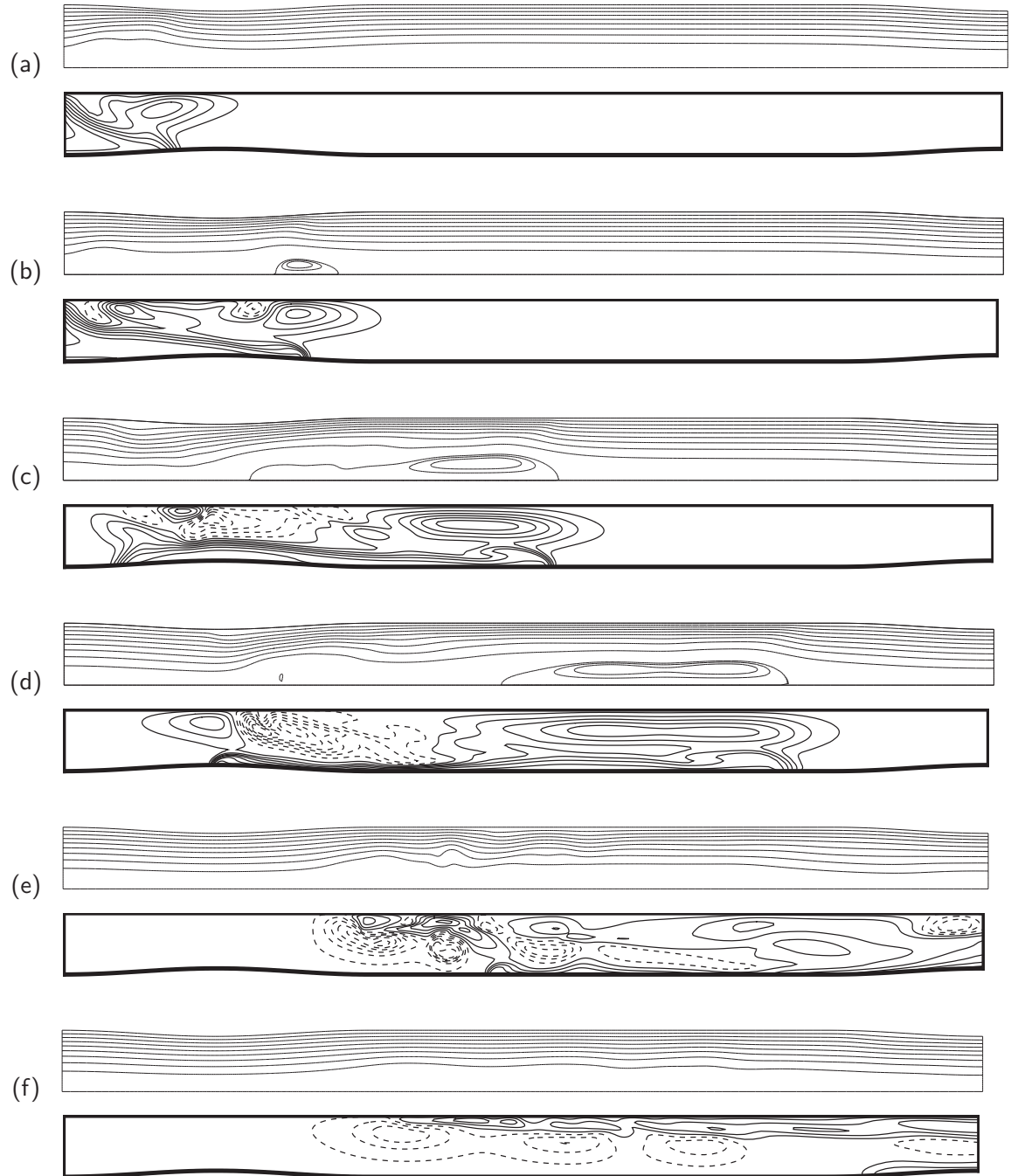


Figure 8.5: Flow evolution for $\Omega_P = 2.0$, $dt = 0.25$. Time $t =$ (a) 2.5, (b) 5, (c) 10, (d) 15, (e) 25, (f) 40. Top: streamlines, bottom: change in azimuthal velocity.

was mentioned previously, so we also plot the change in azimuthal vorticity with time, at the same times as for the previous plots: figures 8.7 and 8.8.

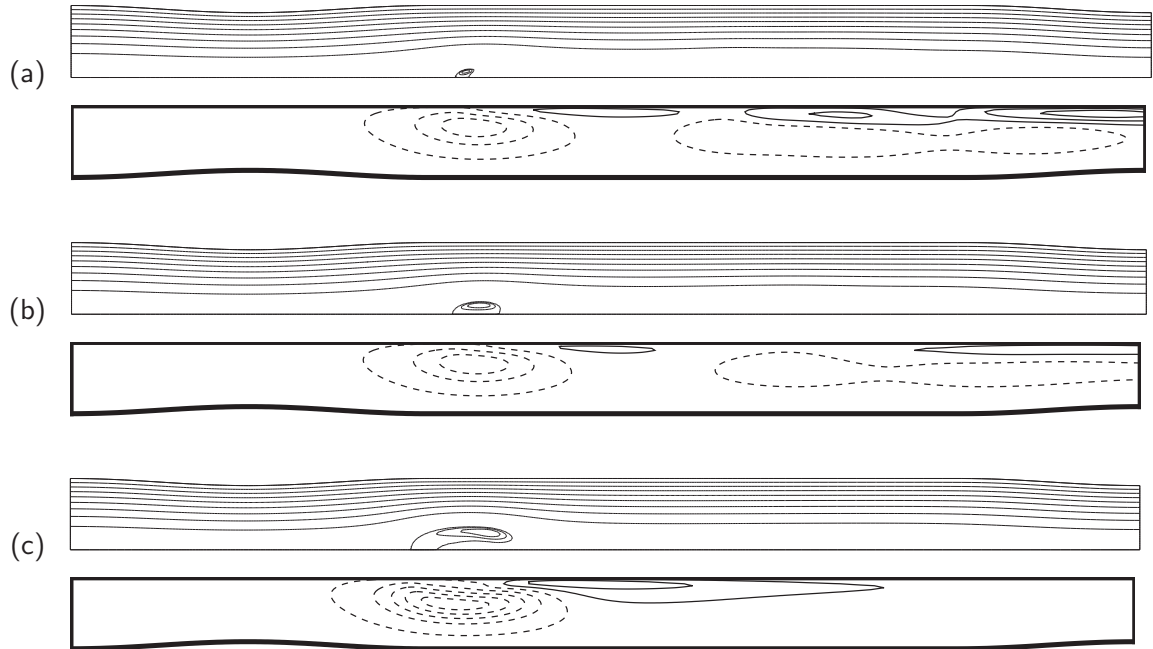


Figure 8.6: Flow evolution for $\Omega_P = 2.0$, $dt = 0.25$. Time $t =$ (a) 55, (b) 75, (c) 1102.5. Top: streamlines, bottom: change in azimuthal velocity.

The lower plot has contours of the change in azimuthal vorticity, $\delta\omega_\phi$, as defined in a previous section, but repeated here:

$$\delta\omega_\phi = \omega_\phi - \omega_\phi(i) \quad (8.7)$$

where ω_ϕ is the azimuthal vorticity at each timestep and $\omega_\phi(i)$ is the azimuthal vorticity of the initial condition. The azimuthal vorticity is plotted in equally spaced contours, and the contour levels are the same in each plot, so that the magnitude of the vorticity can be seen at each timestep. Dashed lines indicate negative azimuthal vorticity.

Again, the first plot 8.7(a) shows the increase in swirl entering the domain. Although only an increase in swirl velocity is introduced at the inlet, resulting in an increase in the axial component of vorticity, there is an immediate change in the azimuthal component as well, possibly due to the turning of axial or radial vorticity into the azimuthal direction. As the change in azimuthal vorticity propagates through the pipe constriction, its magnitude increases (plot 8.7(b)). This is expected - since circulation is conserved, the change in radius of the vortex tube must result in a change in the azimuthal vorticity magnitude.

By 8.7(c) the inlet swirl has been reduced to the initial condition of $\Omega = 1.45$, and the

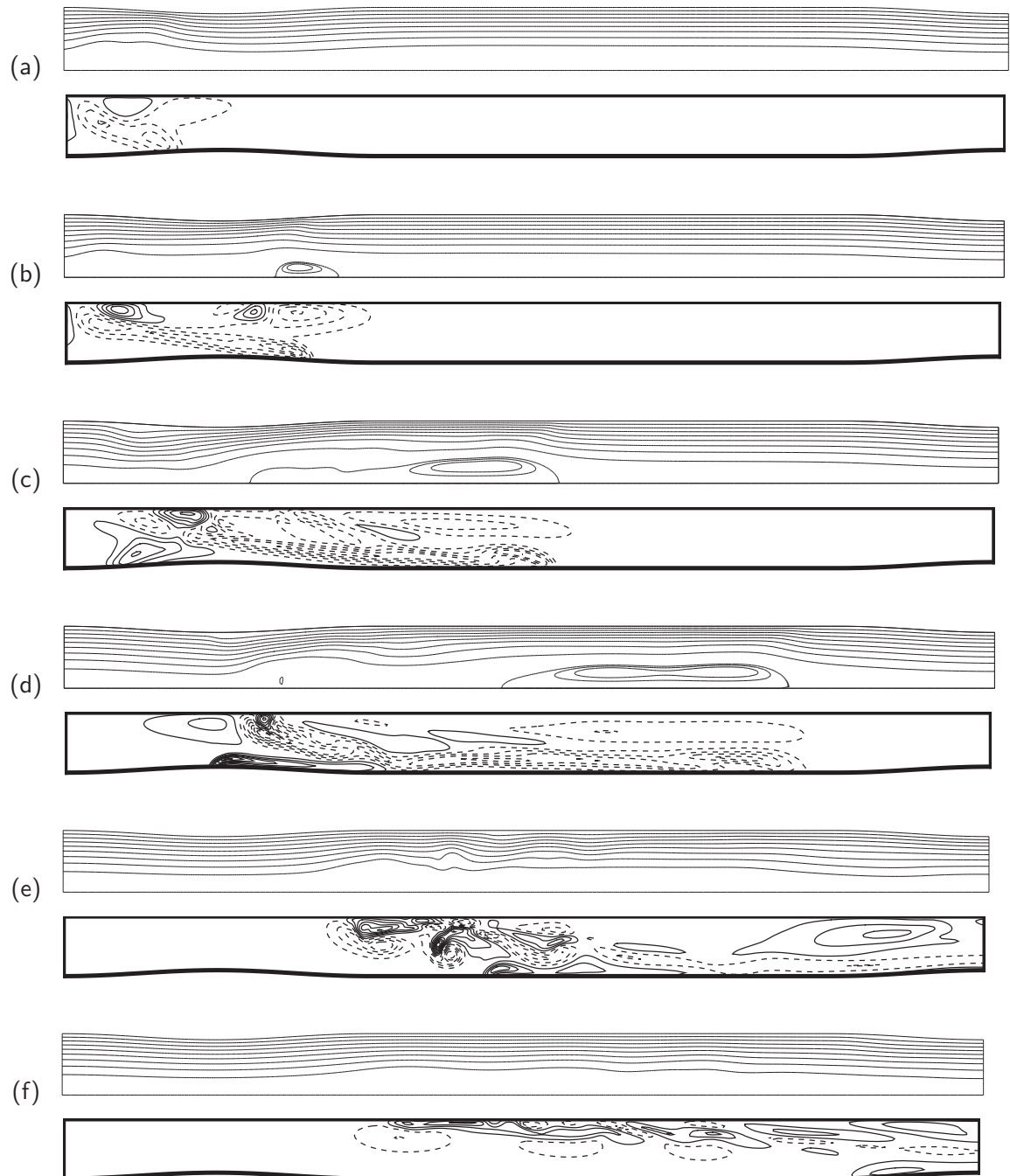


Figure 8.7: Flow evolution for $\Omega_P = 2.0$, $dt = 0.25$. Time $t =$ (a) 2.5, (b) 5, (c) 10, (d) 15, (e) 25, (f) 40. Top: streamlines, bottom: change in azimuthal vorticity.

change in azimuthal vorticity is propagating downstream.

At the diverging section in succeeding plots 8.7(d) to 8.7(f), some of the azimuthal vor-

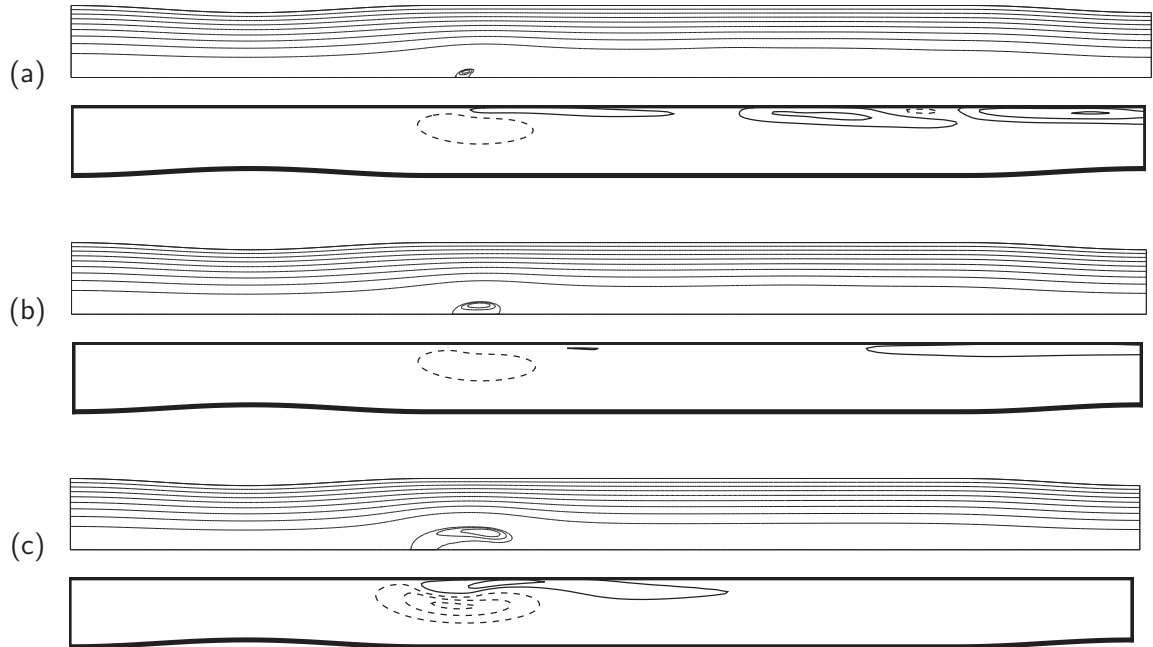


Figure 8.8: Flow evolution for $\Omega_P = 2.0$, $dt = 0.25$. Time $t =$ (a) 55, (b) 75, (c) 1102.5. Top: streamlines, bottom: change in azimuthal vorticity.

ticity continues to propagate downstream, while a portion slows near the location where breakdown subsequently evolves. This is the behaviour observed by Darmofal and Murman [9], where a portion of the azimuthal vorticity moves through the pipe, while some remains trapped at a certain axial location. In their study, this trapped portion grows in amplitude and eventually leads to the formation of a breakdown bubble. In the results presented here, the region of reduced azimuthal vorticity is not continually fed from upstream as in Darmofal and Murman [9] (since in their study the increased swirl is maintained), but stays relatively constant as most of the azimuthal vorticity continues to be swept downstream.

As was seen in plot 8.6(a), with increasing time a small bubble starts to evolve (plot 8.8(a)). The bubble continues to grow (relatively slowly) until it reaches a size close to its final state. In the final plot (8.8(c)) the necessary deficiency in the azimuthal vorticity lingers upstream of breakdown.

This then is the effect of introducing the largest pulse in swirl to the pipe, resulting in the evolution of a breakdown bubble in the final steady state. For the remainder of this chapter the effect of swirl change magnitude and pulse duration will be explored.

8.7 Results for varying Ω_P

Here we summarise the response of the pipe flow to the pulses Ω_P and durations dt in the ranges specified in equations 8.6. The appearance of negative minimum axial velocities along the centreline will be used to identify the recirculation associated with vortex breakdown in the pipe. The minimum axial velocity along the centreline has also been used in previous studies (eg. Tromp and Beran [71]) to indicate the onset of breakdown. As well as plotting the minimum axial velocity, an inspection of each of the cases was made to determine that the negative axial velocity was associated with a breakdown bubble; occasionally a region of reversed flow would detach from the axis, and the axial stagnation point would disappear. In the steady state, only the two flows described in figure 8.3 are possible, and the minimum axial velocity will enable differentiation between these two flows.

In this section the trends observed after the application of the various pulses will be described, then a discussion of the conclusions which can be drawn from these observations will be presented.

The response of the minimum axial velocity (to pulses of different duration) with time is summarised in figures 8.9, 8.11, and 8.12 - 8.18.

8.7.1 $\Omega_P = 1.10, 1.125$

The analysis begins with an examination of the response of the pipe flow to the $\Omega_P = 1.10$ pulse, displayed in figure 8.9

This pulse is maintained for values of dt between 0.01 and 4.00. The initial $dt = 0.01$ solution shows only a small decrease in u_{\min} , with a slow return to the initial condition value. The response for $dt = 0.02$ to 0.25 is similar, with an increasing divergence from the initial condition at first but a return after some time. At $dt = 0.50$ the behaviour changes, with u_{\min} almost dropping to zero. The flow rebounds, then heads toward breakdown again. It does not quite cross into a breakdown state, but hovers nearby, and slowly gravitates back toward the initial condition.

For $dt = 1.00$ there is a cross-over into breakdown, as shown in figure 8.10, where the streamfunction contours are plotted for the result at the time of minimum u_{\min} at $t = 35$.

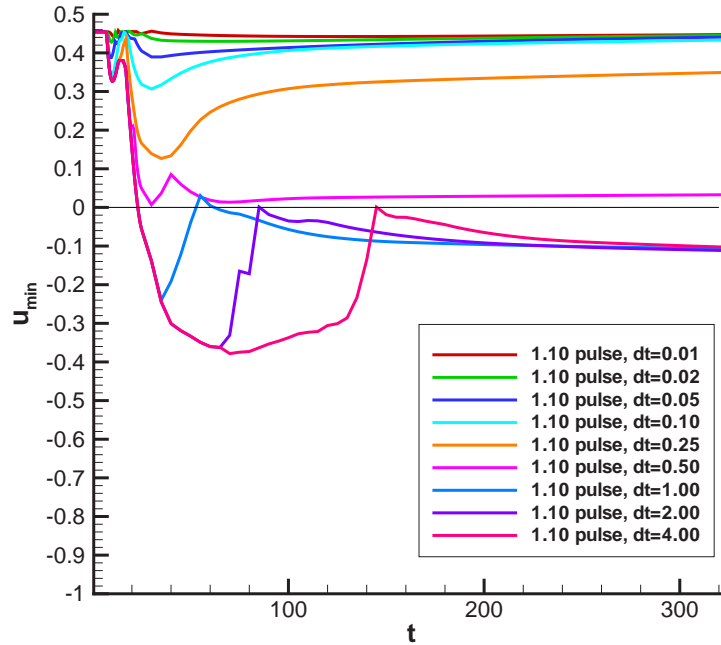


Figure 8.9: $\Omega_P = 1.10$, minimum axial velocity vs. time for pulse durations $dt = 0.01, 0.02, 0.05, 0.10, 0.25, 0.50, 1.00, 2.00, 4.00$.

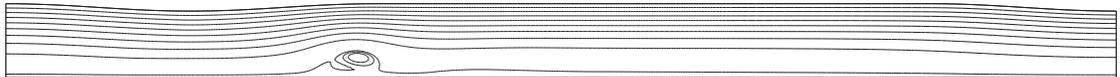


Figure 8.10: Streamline plot for $\Omega_P = 1.10$, $dt = 1.00$.

A small recirculation bubble has formed just off the axis. With increasing time this bubble disappears, as can be seen from the u_{\min} trace, but subsequently returns and stabilises as the steady state bubble of the conjugate $\Omega = 1.45$ state.

As the pulse duration is increased to $dt = 2.00$ and $dt = 4.00$, the minimum u_{\min} drops correspondingly, but there is on each occasion the return to slightly positive values before an evolution toward the steady breakdown state.

The results are consistent with the model discussed for the evolution of breakdown; increased pulse duration results in greater azimuthal vorticity generation and hence greater likelihood of eventual breakdown. One would expect, based on these observations, that increasing the pulse magnitude would result in bubble evolution for lower values of dt .

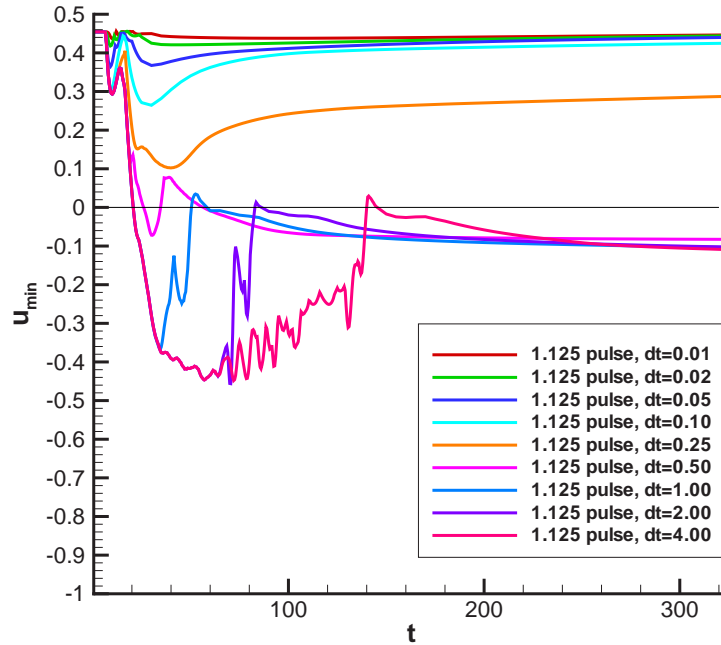


Figure 8.11: $\Omega_P = 1.125$, minimum axial velocity vs. time for pulse durations $dt = 0.01, 0.02, 0.05, 0.10, 0.25, 0.50, 1.00, 2.00, 4.00$.

This is the case for an increased change in swirl $\Omega_P = 1.125$ in figure 8.11; for this case $dt = 0.50$ also results in breakdown in the final steady solution.

The situation for larger pulses is not so simple however; further tests reveal some departure from the expected behaviour.

At this point we also mention the oscillations in the solution apparent in figure 8.11 for the $\Omega_P = 1.125$ pulse. These oscillations also appear for the higher Ω_P cases; they will be addressed in section 8.12.

8.7.2 $\Omega_P = 1.20, 1.25, 1.30$

For small dt , the progression of solutions for pulse sizes $\Omega_P = 1.20, 1.25$, and 1.30 is similar to that in the $\Omega_P = 1.10$ case.

For $\Omega_P = 1.20$ (figure 8.12), breakdown appears at $dt = 0.50$, and also for $dt = 1.00$. However, as Ω_P is increased further, while initially breakdown evolves, after the pulse is turned off the flow reverts back to the initial condition. This behaviour continues for all

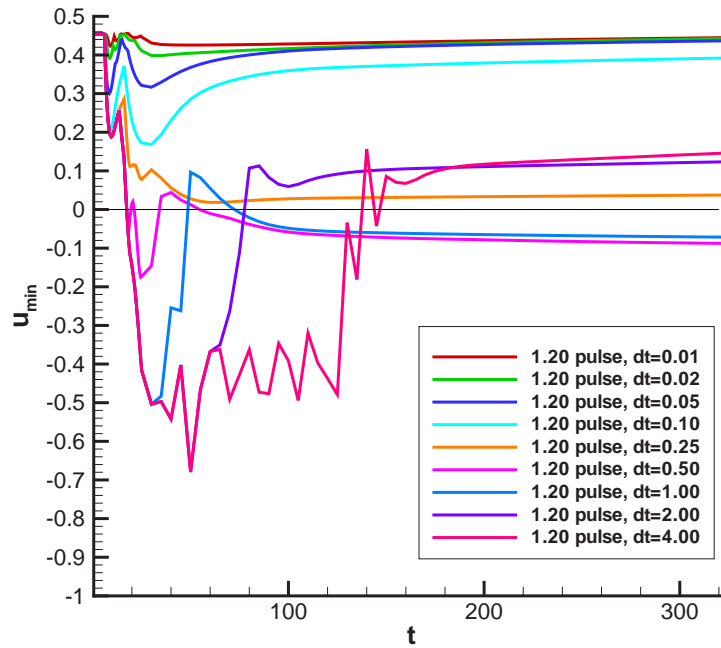


Figure 8.12: $\Omega_P = 1.20$, minimum axial velocity vs. time for pulse durations $dt = 0.01, 0.02, 0.05, 0.10, 0.25, 0.50, 1.00, 2.00, 4.00$.

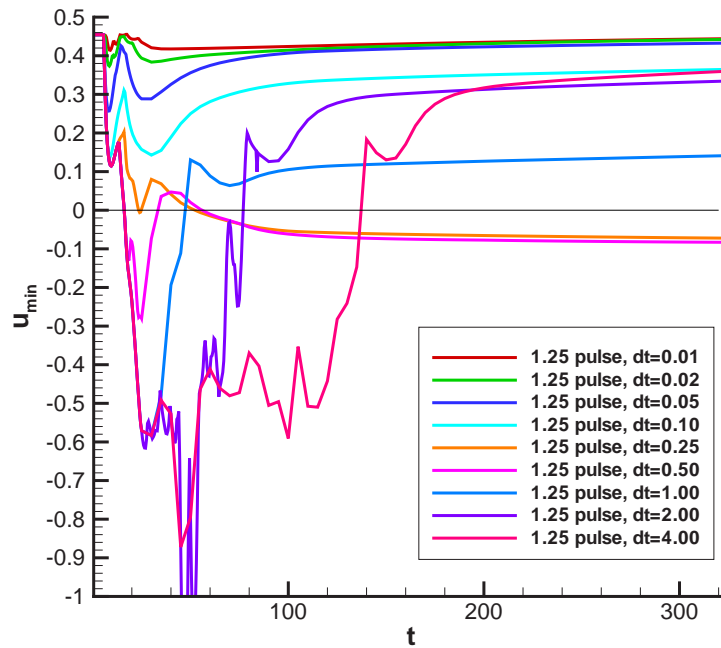


Figure 8.13: $\Omega_P = 1.25$, minimum axial velocity vs. time for pulse durations $dt = 0.01, 0.02, 0.05, 0.10, 0.25, 0.50, 1.00, 2.00, 4.00$.

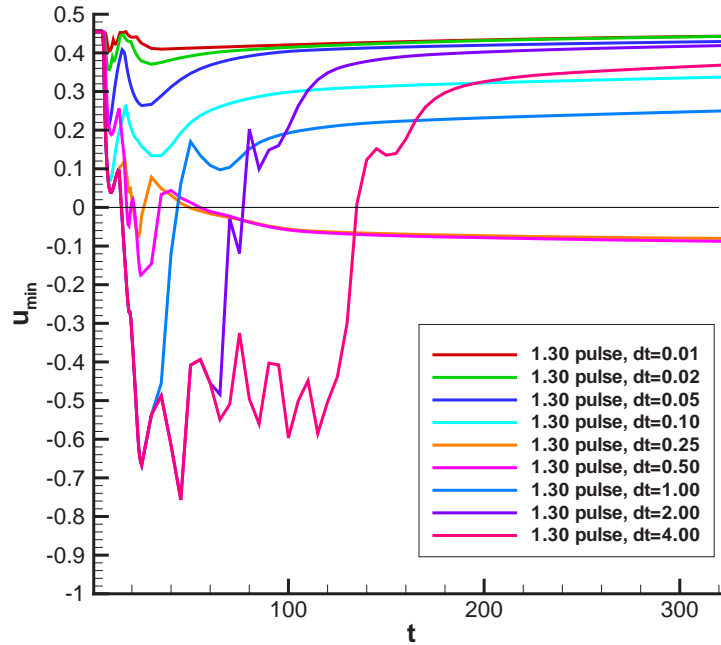


Figure 8.14: $\Omega_P = 1.30$, minimum axial velocity vs. time for pulse durations $dt = 0.01, 0.02, 0.05, 0.10, 0.25, 0.50, 1.00, 2.00, 4.00$.

the higher dt tested, up to $dt = 4.00$.

This pattern is repeated for $\Omega_P = 1.25$ and 1.30 (figures 8.13 and 8.14, with the transition to this new behaviour at $dt = 1.00$ in both these cases.

The result for $\Omega_P = 1.30$ is not significantly different from $\Omega_P = 1.25$, but shows that the anomalous behaviour with regard to the onset, then disappearance, of breakdown is not confined to one solution. It occurs through a band of pulse magnitudes.

8.7.3 $\Omega_P = 1.375$

For $\Omega_P = 1.375$ initially the same behaviour as for the 1.20 to 1.30 pulses is noted. A breakdown bubble is first observed in the $dt = 0.25$ test. For $dt = 0.25$ the bubble remains in the steady solution, and this is also the case for $dt = 0.50$. At $dt = 1.00$ the bubble appears, but subsequently disappears and in the final state the flow returns to the initial condition. As dt is increased to $dt = 2.00$ the u_{\min} plot shows a borderline breakdown result, but the solution progresses toward no-breakdown in the steady state. At $dt = 4.00$,

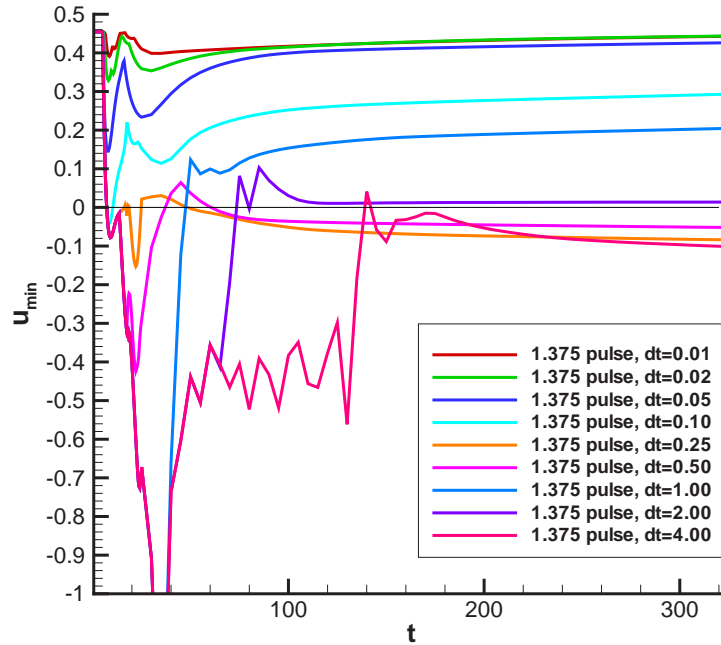


Figure 8.15: $\Omega_P = 1.375$, minimum axial velocity vs. time for pulse durations $dt = 0.01, 0.02, 0.05, 0.10, 0.25, 0.50, 1.00, 2.00, 4.00$.

however, a bubble evolves, disappears, then re-emerges and persists in the final steady solution.

8.7.4 $\Omega_P = 1.50$

For the $\Omega_P = 1.50$ case the region of non-monotonicity has disappeared. The rebound from the initial breakdown solution is for $dt = 0.25$ and $dt = 0.50$ sufficient to move the flow back to a state without breakdown, but not enough to keep the flow in that state. So we see a return to the monotonic behaviour observed for the initial low Ω_P runs.

8.7.5 $\Omega_P = 1.75, 2.00$

For higher swirls, $\Omega_P = 1.75$ and 2.00 , the large Ω_P value during the pulse resulted in a breakdown bubble that moved upstream, past the converging/diverging section, right up to the inlet. These larger dt solutions must be discounted, as the behaviour of the bubble near the inlet cannot be modelled, given the fixed inlet boundary condition used here.

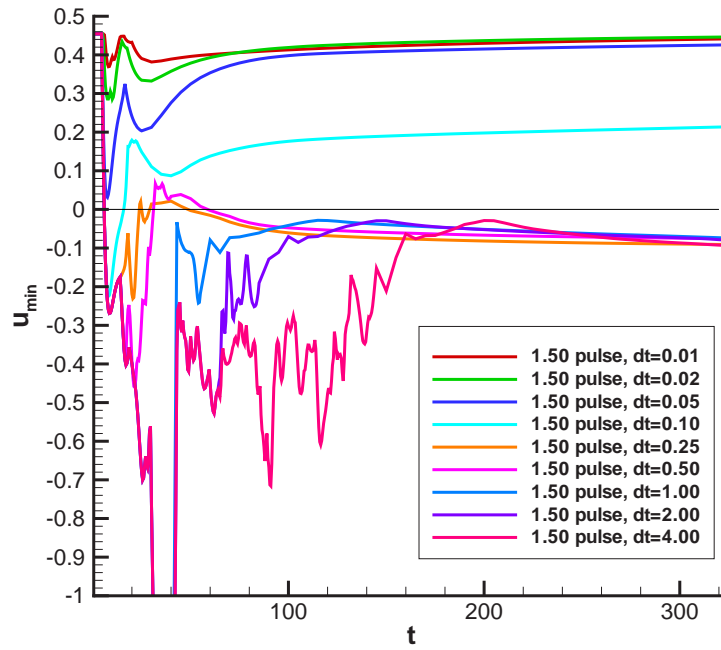


Figure 8.16: $\Omega_P = 1.50$, minimum axial velocity vs. time for pulse durations $dt = 0.01, 0.02, 0.05, 0.10, 0.25, 0.50, 1.00, 2.00, 4.00$.

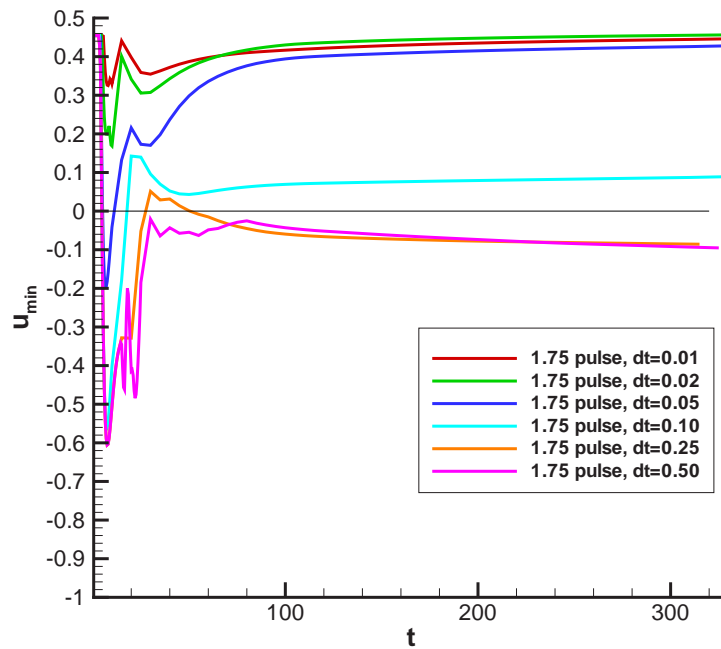


Figure 8.17: $\Omega_P = 1.75$, minimum axial velocity vs. time for pulse durations $dt = 0.01, 0.02, 0.05, 0.10, 0.25, 0.50$.

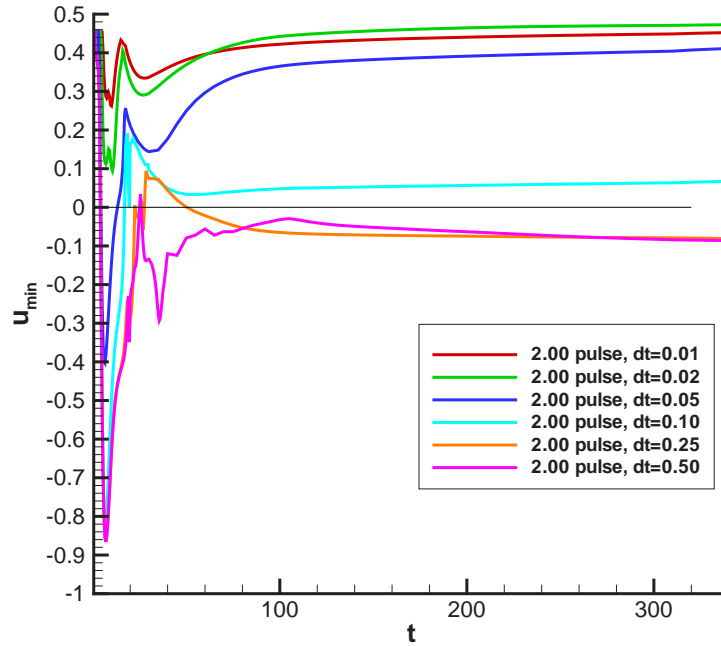


Figure 8.18: $\Omega_P = 2.00$, minimum axial velocity vs. time for pulse durations $dt = 0.01, 0.02, 0.05, 0.10, 0.25, 0.50$.

Hence the analysis for these larger Ω_P is limited to $dt < 0.50$; for the smaller pulse times the bubble remained a considerable distance from the inlet, and the solutions are valid.

The progression in behaviour for these two Ω_P is similar to that for the other Ω_P tests conducted, up to the point where the solutions become invalid for higher dt ; $dt = 0.25$ and $dt = 0.50$ result in breakdown in the steady state. Since the transition to the unexpected behaviour of the $\Omega_P = 1.20$ to 1.375 cases occurs at higher dt , it is not possible to determine for $\Omega_P = 1.75$ and 2.00 whether this occurs for these pulses as well.

8.8 Observed trends

In the results presented above some general trends can be discerned. For the smaller pulses the flow requires a longer time dt in order to develop a breakdown bubble; at $\Omega_P = 1.75$ a bubble evolves for $dt = 0.25$, whereas for $\Omega_P = 1.10$ a bubble does not evolve until $dt = 1.00$. The flow needs time to develop sufficient negative azimuthal vorticity in the region upstream of where breakdown is expected. If the pulse is turned off too soon a bubble will not form. If Ω_P is larger, the growth rate of azimuthal vorticity is greater, and hence

less time is needed to generate sufficient azimuthal vorticity to result in breakdown.

It can be seen from these plots that even if a breakdown bubble does develop, this does not guarantee that the bubble will persist. As was seen for the $\Omega_P = 1.75$ pulse, for example, a bubble evolves for all pulses with duration of $dt = 0.05$ or greater, but only persists for $dt = 0.25$ or greater. However, for all pulse magnitudes examined, the absence of a bubble in the initial evolution of the flow indicates the absence of a bubble in the final steady state.

We also note that for pulse magnitudes outside the range $1.20 < \Omega_P < 1.375$ once a dt is found for which breakdown exists in the steady state, any greater dt also results in breakdown in the steady state. For the range $1.20 < \Omega_P < 1.375$, this is not the case.

Thus it appears that whether or not a bubble appears in the final solution is not purely a function of the size and duration of the perturbation applied, as was initially expected. It may be that the timing of the return to the initial condition inlet may, for this pulse magnitude, have an influence on whether the flow reverts to the initial no-breakdown flow or results in the persistence of a breakdown bubble. The phase in the evolution of the bubble when the swirl changes are imposed may be a deciding factor in whether a bubble persists or not. The minimum axial velocity traces hint that the larger Ω_P flows are becoming time-dependent. The onset of time-dependence will be considered in a later section. It will be shown that in some cases soon after the bubble develops, the flow begins to oscillate in this geometry.

8.9 Ramped pulse

Two extremes of perturbation application have been considered; a gradual increase in swirl (to obtain the $\Omega = 1.45$ solution without breakdown), and the top hat swirl increase. In between it is feasible to vary the time over which the increased swirl is applied; the pulse can be ramped up and down, rather than the sudden increase and decrease applied here. Since the $\Omega_P = 1.25$, $dt = 2.00$ case is in the middle of the region which gives different results to those expected (ie. the non-monotonicity), we will use this case to test the effect of ramping. The hypothesis is that increasing the length of ramping time will favour breakdown in the final state. This is because the flow for $\Omega_P = 1.25$ contains breakdown, and gradually reducing the swirl from this state should result in a more gradual progression

toward the lower part of the curve in figure 8.4 and the steady $\Omega = 1.45$ breakdown state.

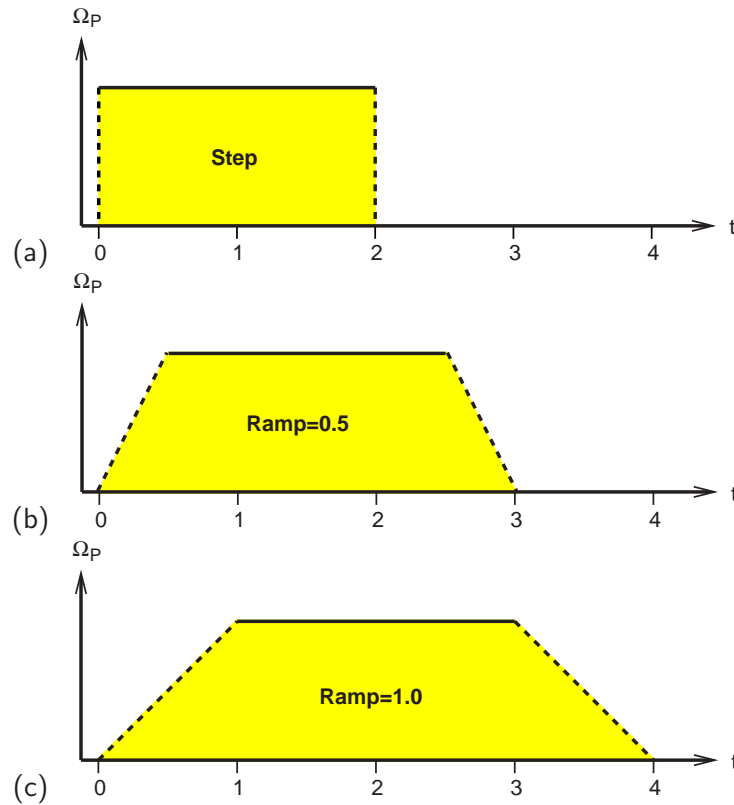


Figure 8.19: Ramping scenario: (a) no ramping, (b) ramping = 0.5, (c) ramping = 1.0.

Three cases are considered; the first case has no ramping; the pulse is simply turned on and off - this is the case which was presented in figure 8.13. The second case has a ramping time of $dt = 0.50$, then a pulse on-time of $dt = 2.00$, and a ramping down time of $dt = 0.50$. In the third case the ramping times are increased to $dt = 1.00$. The minimum axial velocity plot resulting from these tests is shown in figure 8.20.

It can be seen that as the ramping time is increased, in the final state breakdown is preferred. So ramping time is another parameter that can be used to effect some control on the final flow desired. Here a linear ramping has been used; the ramping profile can also be varied, but this will not be considered here.

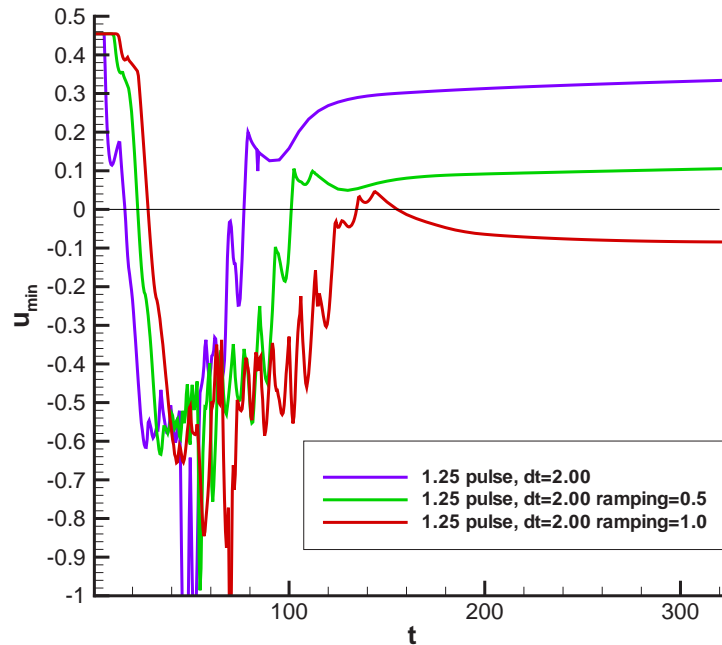


Figure 8.20: Ramping results: no ramping, ramping = 0.5, ramping = 1.0.

8.10 Onset of three-dimensionality

Tromp and Beran [71] linked the start of time-dependence in open pipe simulations containing breakdown with the onset of three-dimensionality. Their study compared the results from axisymmetric and asymmetric numerical methods, using an axisymmetric flow as the initial condition for the asymmetric solution. For their swirl parameter $\nu = 1.5$ ($\nu \equiv \Omega$ used in our study) and $Re = 250$, no asymmetry or time-dependence were observed in the three-dimensional computation. As the swirl was increased to $\nu = 1.53$, the flow became both time-dependent and asymmetric - a spiralling structure was observed. With increasing ν , the radius of the spiralling motion increased, until at $\nu = 2.3$ a structure akin to the spiral mode of vortex breakdown was observed. It is interesting that the spiral mode occurs for higher swirl than for the onset of the bubble in this numerical result, whereas in pipe experiments (eg. Sarpkaya [57]) the spiral mode occurs for lower swirl than the bubble mode.

These observations have implications for the results presented in this chapter. By increasing the degree of swirl beyond the value at which the flow is steady (ie. just above $\Omega = 1.45$), the flow may be moving into a region where three-dimensionality would become

apparent in a three-dimensional computation. This three-dimensionality may be manifest in our computations as time-dependence.

8.11 Note on bubble evolution

For pulses that only marginally produce a persistent breakdown, the bubble evolution in space begins at the axis. For a pulse that easily produces breakdown, the bubble originates away from the centreline of the pipe and reaches forward to touch down on the axis, from which point it grows into the full-sized bubble. This second case is illustrated in figures 8.21. The other case (where the bubble grows from the axis) is treated in the series of plots in figure 8.22.

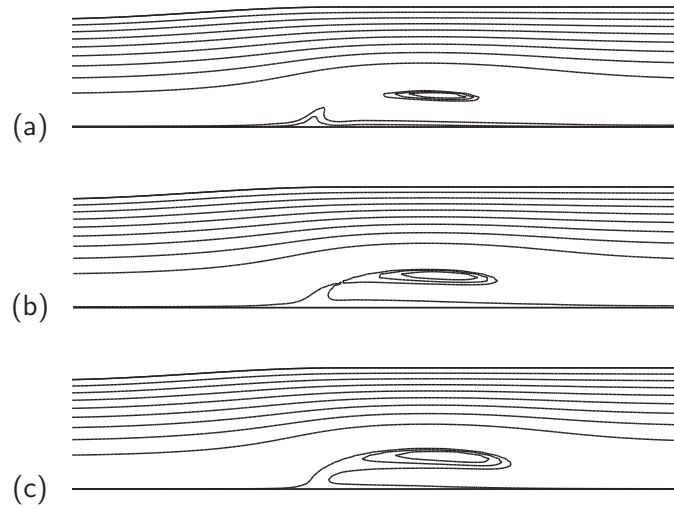


Figure 8.21: Evolution of the breakdown bubble when breakdown evolution is not marginal; $\Omega_P = 1.50$, $dt = 1.00$, $t =$ (a) 17.5, (b) 22.5, (c) 35.5.

Time increases from top to bottom in figure 8.21. The bubble in the top image is not attached to the axis - it forms as an isolated recirculation region in the body of the pipe. Streamlines pass under the bubble, showing its isolation from the axis. With time, the kink in the streamlines along the axis becomes more pronounced, and eventually meets the bubble. At this stage the axial flow between the bubble and the axis ceases and the flow proceeds around a stagnation point in front of the bubble, as is the situation for the final steady bubble.

For the more marginal case, where breakdown is only just produced by the pulse, the

situation at the axis is similar, in that a kink in the streamlines grows from the axis. However, there is no initial recirculation region in the body of the pipe - this develops once the kink has grown into the body of the pipe and recirculation develops inside it. The streamline plots of figure 8.22 illustrate this point.

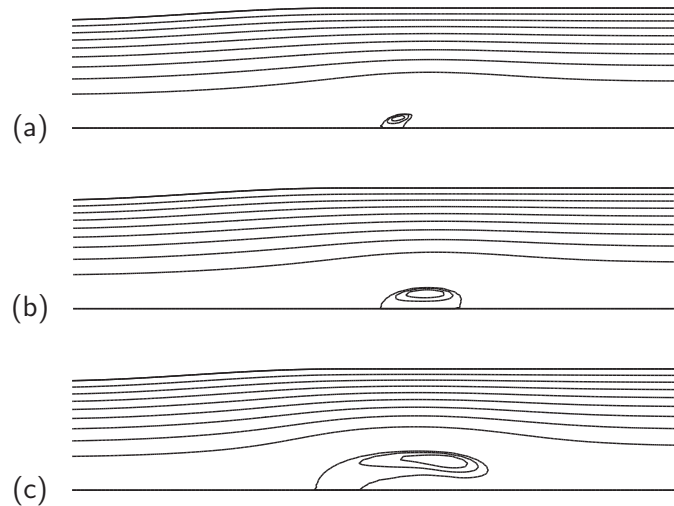


Figure 8.22: Evolution of the breakdown bubble when breakdown evolution is marginal; $\Omega_P = 2.00$, $dt = 0.25$, $t =$ (a) 55, (b) 75, (c) 710.

8.12 Flow state at Ω_P

The observation of time-dependence for some of the larger dt tests has prompted an examination of the longer-term development of the flow at higher swirls. The solutions for each Ω_P after the flow has settled down will be examined for time-dependence. Darmofal [8] observed time-dependent behaviour at Reynolds number $Re = 6000$ and $\Omega = 1.282$. The flows in our study become time-dependent at a lower Reynolds number of $Re = 1000$ due to the higher swirl level investigated.

We consider the pipe flow at the swirls Ω presented in table 8.1, with the corresponding Ω_P below. Only $\Omega_P < 1.75$ were considered, as for the higher swirls the bubble swims upstream to the inlet.

For all of these cases the initial condition has $\Omega = 1.45$. Time was stepped forward until either a steady state solution was obtained or the flow became periodic. Again the Reynolds number considered was $Re = 1000$.

Ω	1.479	1.5525	1.595	1.74	1.8125	1.885	1.99375	2.03	2.175
Ω_P	1.02	1.05	1.10	1.20	1.25	1.30	1.375	1.40	1.50

Table 8.1: Swirl levels tested.

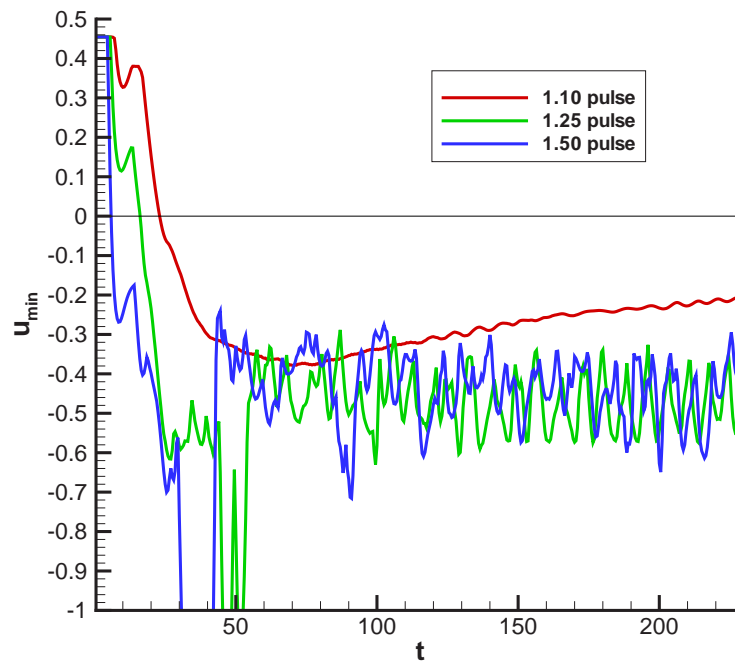
Figure 8.23: Onset of time-dependent behaviour for $\Omega_P = 1.10$, 1.25, and 1.50.

Figure 8.23 shows the minimum axial velocity plots for the cases $\Omega_P = 1.10$, 1.25, and 1.50. For $\Omega_P = 1.10$ the flow in the pipe is time-dependent. Solutions for increasing Ω_P are also time-dependent; the time-dependence is manifest as an oscillation in the bubble. For all Ω_P studied the upstream end of the bubble is stationary. For $\Omega_P = 1.10$, a single long bubble persists, and pulses travel along the length of this bubble. For $\Omega_P \geq 1.15$, a smaller bubble sits just downstream of the converging/diverging section, and bubbles are shed downstream from this location. The magnitude of the variations in the minimum axial velocity is roughly consistent between $\Omega_P = 1.25$ and $\Omega_P = 1.50$

The lower swirl magnitude case of $\Omega_P = 1.10$ stands out, as the flow has not yet settled down. It is necessary to iterate for longer to determine the fully-developed nature of this case; see figure 8.24. The minimum axial velocity plot for $\Omega = 1.05$ is also included.

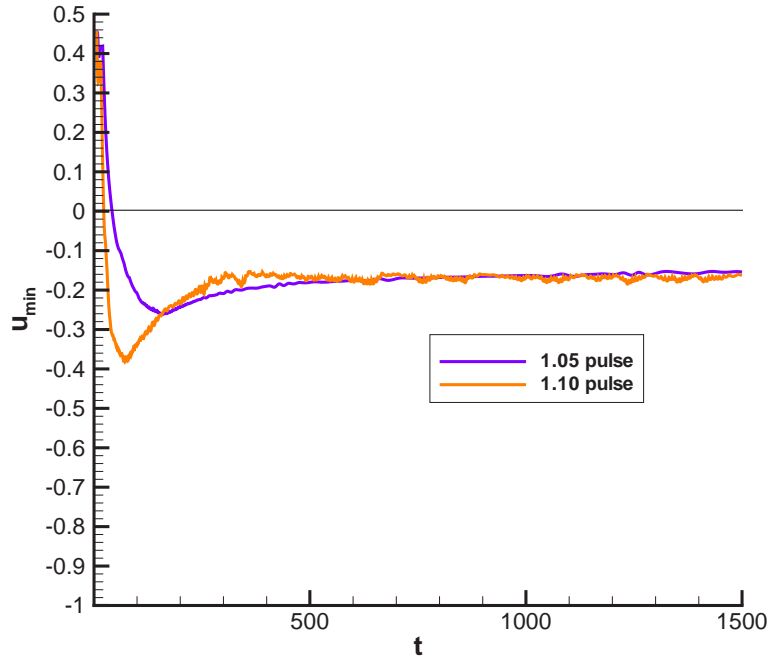


Figure 8.24: Onset of time-dependent behaviour with increasing Ω_P , for $\Omega_P = 1.05$ and $\Omega_P = 1.10$.

Both cases are still unsteady at large $t = 1500$, and the amplitude of the oscillations appears to decrease with decreasing Ω_P .

8.13 $dt \gg 4$

To determine whether the non-monotonic behaviour extended far above the values of dt used, it was decided to test the evolution of the flow for $dt \gg 4$. For these cases the initial condition is obtained by iterating forward in time until the flow either becomes steady or periodic. These initial condition solutions have already been obtained, and were described in the previous section; most of the solutions for these $\Omega > 1.45$ are time-dependent. In each case the higher Ω flow was used as the initial condition as soon as it becomes fully developed, ie. steady or periodic. No consideration was given to the phase of the bubble's oscillation here.

The result of applying $dt \gg 4$ is included in figure 8.25, which also contains a summary of the results from all the pulse amplitudes Ω_P and times dt applied in this study. It is

evident that the non-monotonic behaviour is not just an anomaly for small dt , but is the response of the flow to the pulse magnitude range $1.2 \leq \Omega \leq 1.3$.

8.14 Discussion

Figure 8.25 summarises the response of the pipe to the pulses applied.

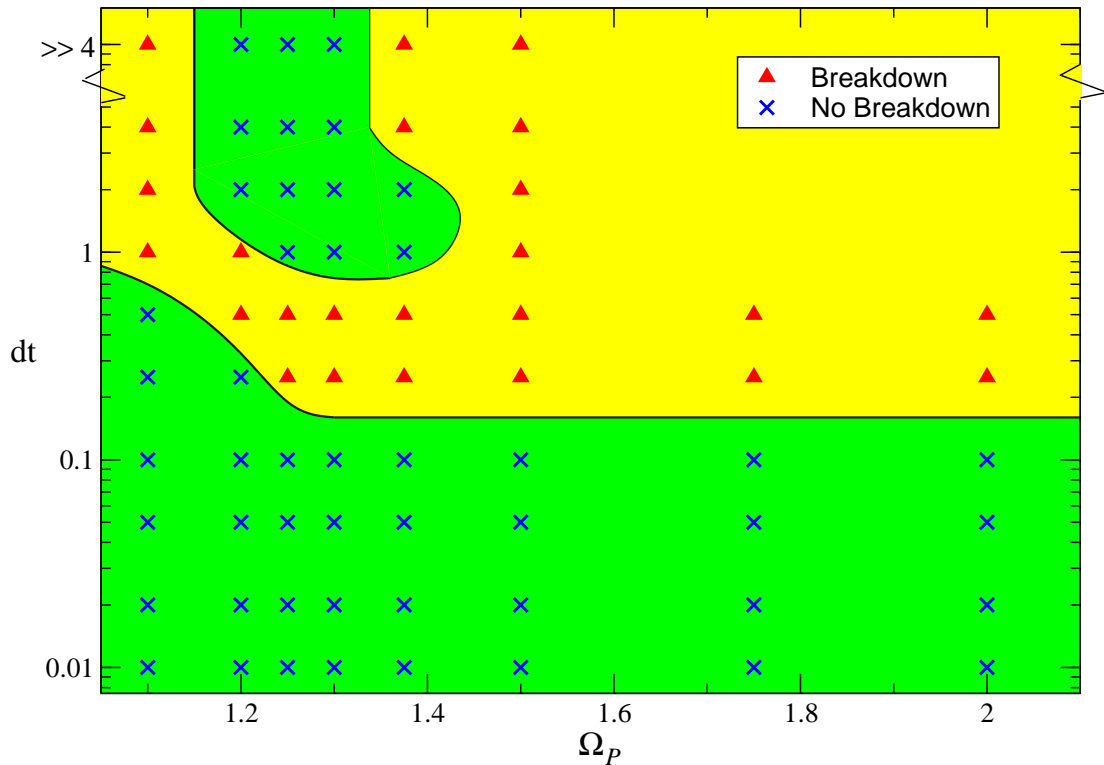


Figure 8.25: dt vs Ω_P , no-breakdown to breakdown transition. Red triangles represent solutions with breakdown, blue crosses represent solutions without breakdown.

The primary intention of this study was to determine whether it was possible to make the flow jump from an initial state where no breakdown was observed to a conjugate state at the same Reynolds number and swirl where a bubble exists. The evolution of a breakdown bubble after a swirl increase was expected - an increase in swirl would result in a bubble in any case, as long as the increase took the flow outside the hysteresis region. The question to be answered was whether the flow would then revert back to the initial condition, or stay in its new state and retain the breakdown bubble.

It has been seen that a pulse initially may or may not produce breakdown as it passes the potential breakdown location. If the pulse duration is too short, a bubble will not evolve at all, but if the pulse is maintained for long enough a bubble will appear. If the pulse is large enough and lasts for long enough, the bubble can work its way past the converging/diverging section and reach the inlet. In these cases the solutions are not considered past the point where the breakdown reaches the inlet (for $\Omega_P = 1.75$ and $\Omega_P = 2.00$, and $dt = 0.75$).

For cases where the bubble does not reach the inlet, the bubble in many cases disappears again. For certain combinations of Ω_P and dt the final solution contains breakdown; this region is delineated by red triangles in figure 8.25. Maintaining the increased swirl for long enough eventually resulted in a transition to breakdown in the final state. This was not true for a group of results at low Ω_P however. In the region including $1.2 \leq \Omega_P \leq 1.3$ for $2 < dt < \infty$, breakdown was not observed in the final state. It is possible that this non-monotonic response is due to the timing of the swirl reduction at the end of the pulse, with respect to the phase of oscillation of the flow at the higher swirls. This variable has not been tested here.

In the next chapter the transition from a flow with breakdown to one without is considered; the suppression of breakdown is attempted within the hysteresis region.

Chapter 9

Breakdown suppression by an upstream pulse

9.1 Introduction

In this chapter the transition opposite to that of the previous chapter will be studied - from the breakdown state to no-breakdown, as represented in figure 9.1

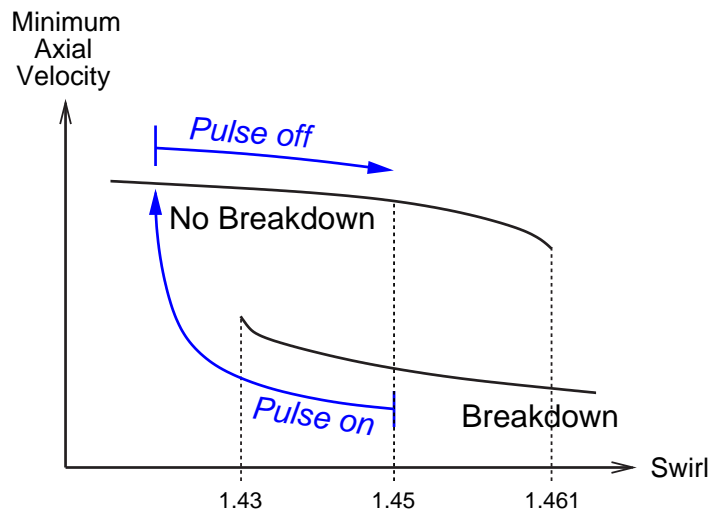


Figure 9.1: Possible path as a result of the $\Omega_P < 1$ pulse.

The initial condition again has $\Omega = 1.45$ and Reynolds number $Re = 1000$, and breakdown is present; see figure 8.3. From this state a pulse is applied, this time by reducing the

amount of swirl at the inlet. The Ω_P and dt ranges considered are shown in the limits 9.1:

$$\begin{aligned} 0.0 &\leq \Omega_P \leq 0.975 \\ 0.01 &\leq dt \leq 32.00 \end{aligned} \tag{9.1}$$

All of the pulses applied will have sufficient magnitude to take the flow outside the hysteresis region, ie. $\Omega_P > 1.45 - 1.43 = 0.02$, or 1.3% of the initial condition swirl. Hence in the limit $dt \rightarrow \infty$, for all of the Ω_P tested there would be no breakdown bubble in the final state.

9.2 Results for varying Ω_P

9.2.1 $\Omega_P = 0.0$

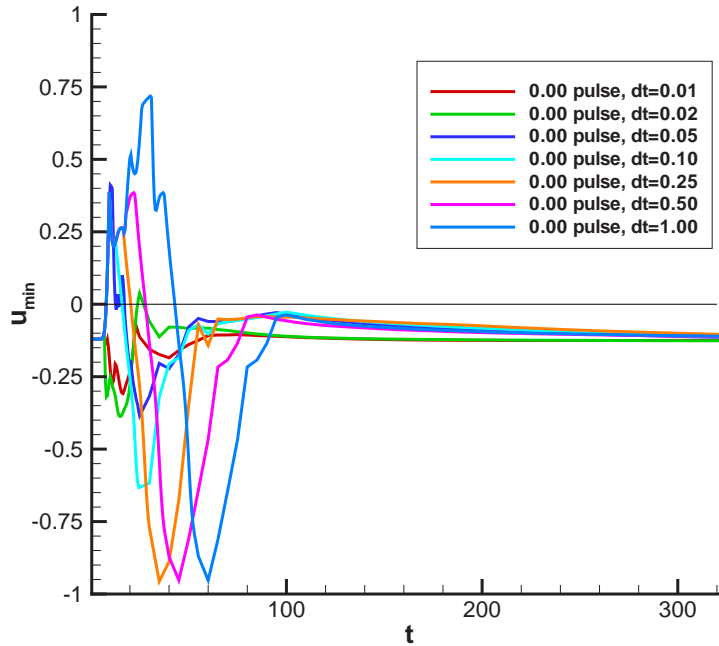


Figure 9.2: $\Omega_P = 0.0$: minimum axial velocity vs. time for pulse durations $dt = 0.01, 0.02, 0.05, 0.10, 0.25, 0.50,$ and 1.00 .

For all pulse durations for $\Omega_P = 0.0$, the bubble returns in the steady solution as expected; in determining the initial condition it was found that spontaneously increasing Ω to 1.45

resulted in breakdown. In figure 9.2 the minimum axial velocity (along the centreline) with time is plotted for the various values of dt .

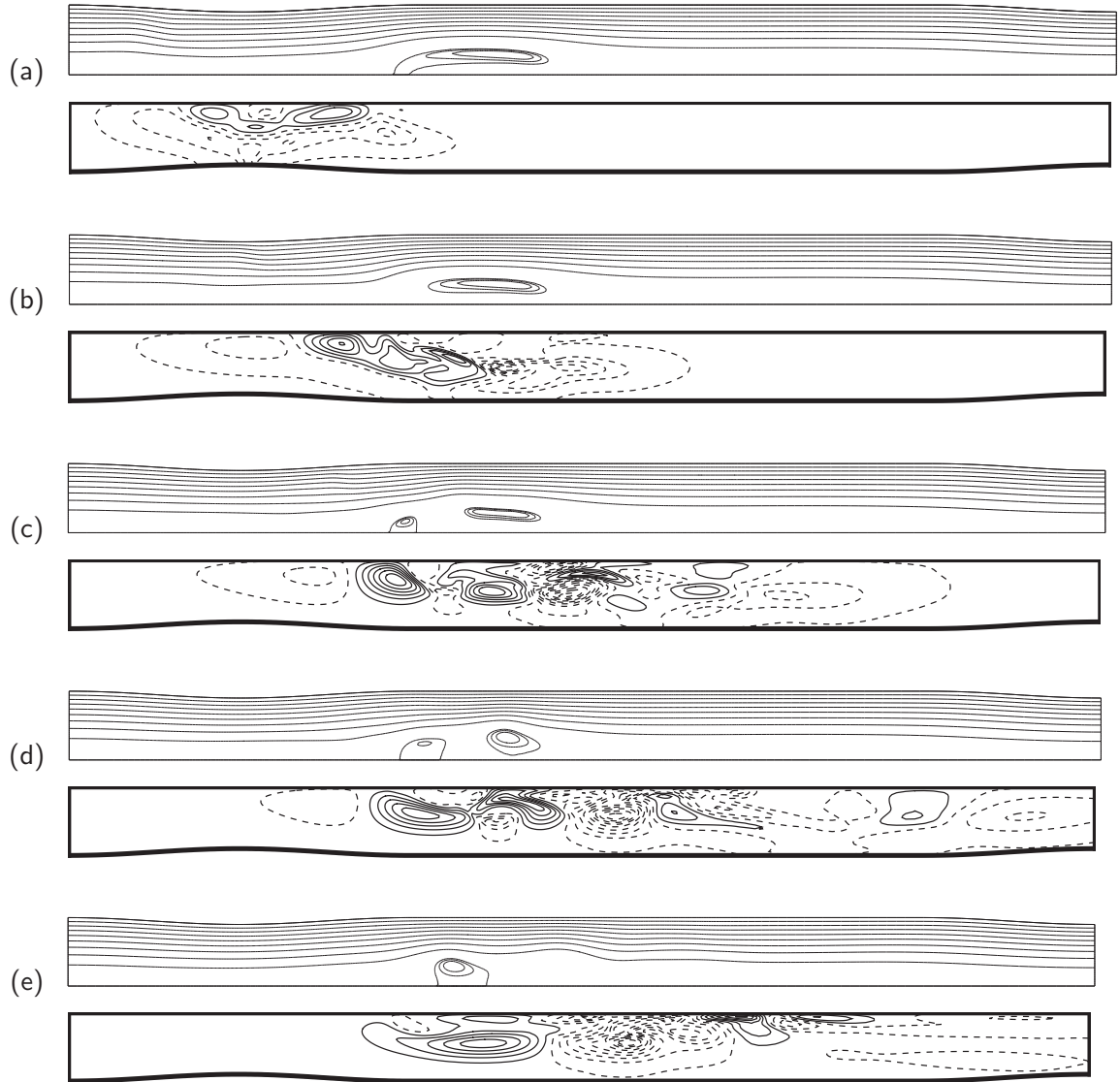


Figure 9.3: Flow evolution for $\Omega_P = 0.0$ pulse, $dt = 0.01$. Time $t =$ (a) 5, (b) 10, (c) 15, (d) 20, (e) 30. Top: streamlines, bottom: azimuthal velocity change.

In all cases the bubble was either pushed downstream or eliminated by decreasing the swirl to $\Omega_P = 0.0$; this is indicated by the movement of the minimum axial velocity above zero for some dt in figure 9.2. Returning the swirl to $\Omega = 1.45$ resulted in a return of the bubble in cases where it was removed.

Figures 9.3 and 9.4 illustrate the evolution of the flow with time for the $\Omega_P = 0.0$ transition, and $dt=0.01$. We plot this case as it is indicative of the way the flow responds to all $\Omega_P < 1$

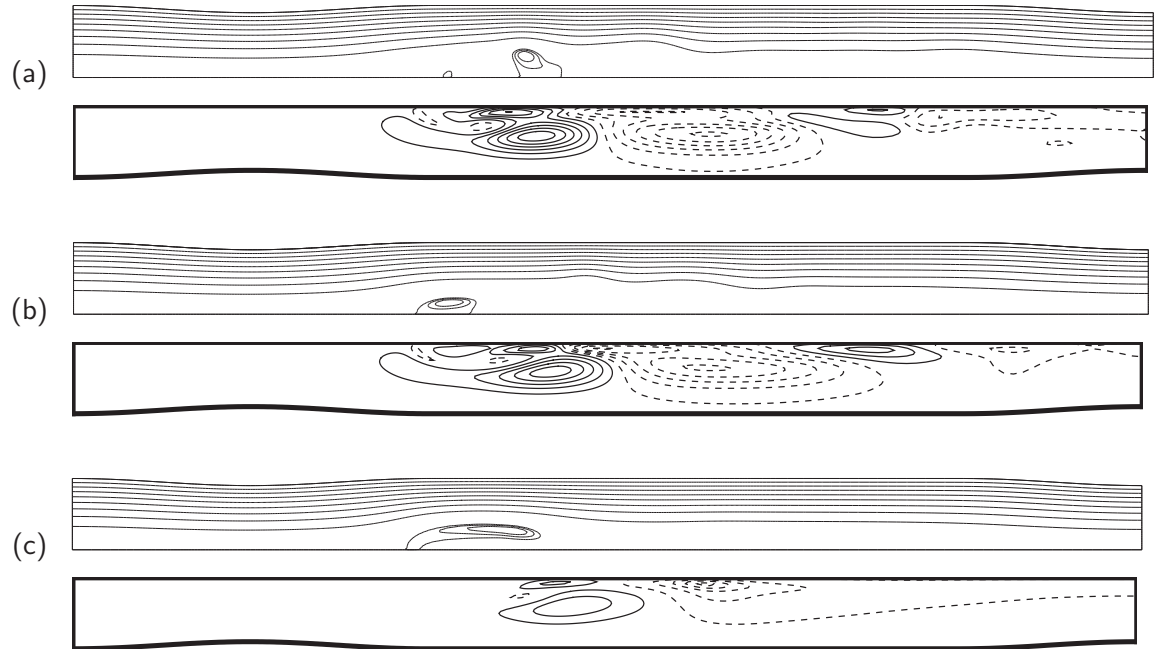


Figure 9.4: Flow evolution for $\Omega_P = 0.0$, $dt = 0.01$. Time $t =$ (a) 40, (b) 50, (c) 325. Top: streamlines, bottom: azimuthal velocity change.

perturbations tested.

In plot 9.3(a) an azimuthal velocity change, which encompasses the swirl reduction then increase, can be seen travelling downstream from the inlet. This first begins to affect the bubble at time $t = 10$ (plot 9.3(b)), and the bubble detaches from the axis. In the plots for later times (plots 9.3(c) to 9.4(a)) a process of shedding appears to take place, with bubbles continually regenerating from the axis. Eventually, at time $t = 50$ (plot 9.4(b)), a bubble slowly grows from the axis and develops into a breakdown bubble identical to that of the initial condition. By time $t = 325$ the bubble has become partially detached from the axis, and is slowly evolving toward a state identical to the initial condition.

The purpose is to determine how small the pulse needs to be before a transition to a final state without breakdown can be produced. If the swirl is at a level where increasing it suddenly will result in the onset of breakdown then it does not matter how long the pulse of lower swirl is kept on, the bubble will always return for these step changes.

In the following sections the pulse magnitude is successively reduced to the point where breakdown has been eliminated in the final state.

9.2.2 $\Omega_P = 0.50, 0.75$

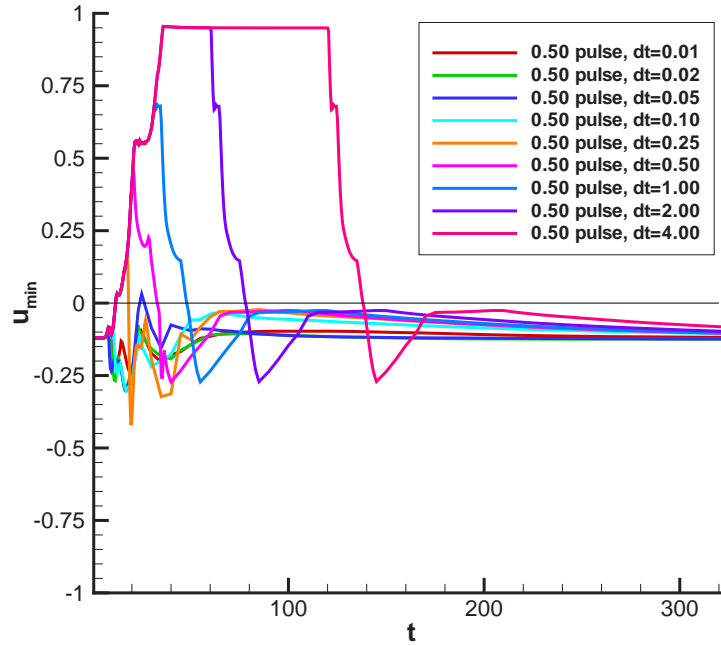


Figure 9.5: $\Omega_P = 0.50$: Minimum axial velocity vs. time for pulse durations $dt = 0.01, 0.02, 0.05, 0.10, 0.25, 0.50, 1.00, 2.00, 4.00$.

As for the $\Omega_P = 0.0$ pulse case the change in swirl by greater than 25% results in the immediate transition to a bubble; in this region of Re/Ω space all changes in swirl need to be small or gradual. These 2 cases will not be considered any further.

9.2.3 $\Omega_P = 0.85, 0.875$

Later results will show that the more interesting behaviours occur for larger dt , so for $\Omega_P \geq 0.85$ only results for $dt = 8.00$ to 32.00 will be included.

For $\Omega_P = 0.85$ (figure 9.7) the situation is similar to that for $\Omega_P = 0.75$. As Ω_P is increased to $\Omega_P = 0.875$ (figure 9.8) the flow just barely rebounds into breakdown. Results for all dt eventually evolve to breakdown, but the tendency for all the larger dt ($dt \geq 2.0$) is to just cross the axis.

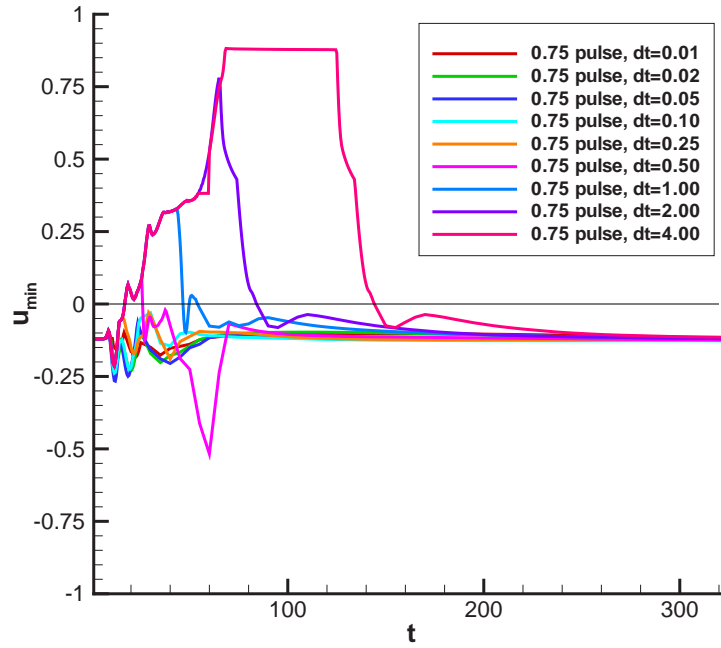


Figure 9.6: $\Omega_P = 0.75$: Minimum axial velocity vs. time for pulse durations $dt = 0.01, 0.02, 0.05, 0.10, 0.25, 0.50, 1.00, 2.00,$ and 4.00

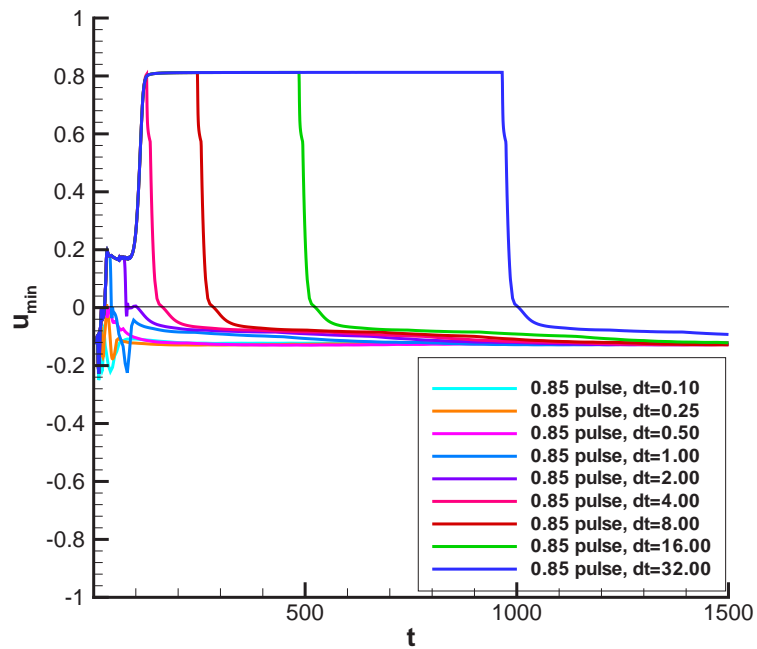


Figure 9.7: $\Omega_P = 0.85$: Minimum axial velocity vs. time for pulse durations $dt = 0.10, 0.25, 0.50, 1.00, 2.00, 4.00, 8.00, 16.00, 32.00$.

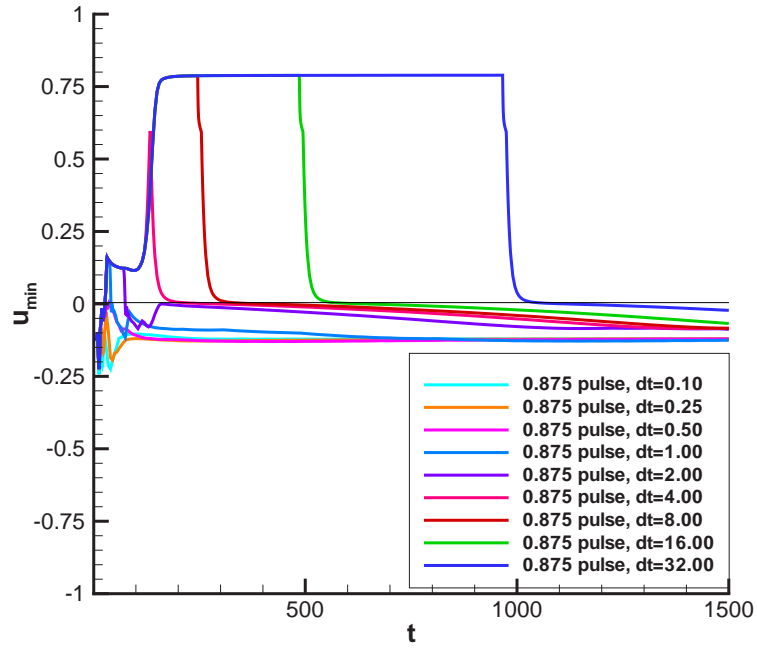


Figure 9.8: $\Omega_P = 0.875$: Minimum axial velocity vs. time for pulse durations $dt = 0.10, 0.25, 0.50, 1.00, 2.00, 4.00, 8.00, 16.00, 32.00$.

9.2.4 $\Omega_P = 0.90$

At $\Omega_P = 0.90$ for $dt < 2.00$ (figure 9.9) breakdown remains in the final solution. For $dt \geq 2.00$ the bubble is eliminated. For the larger dt values, the axial velocity stays positive - no bubble reappears. The flow initially rebounds toward the breakdown state after the swirl is increased again.

This case is the first one that can bring about a transition to the no-breakdown state. However, it requires a relatively long pulse time dt to accomplish the change, compared with the reverse transition.

9.2.5 $\Omega_P = 0.925, 0.95, 0.975$

These final cases reveal a trend toward requiring larger values of dt for increasing Ω_P in order to effect the removal of breakdown. This trend continues until the final case $\Omega_p = 0.975$.

At $\Omega_p = 0.975$ breakdown remained even for $dt = 32.00$. For this Ω_P the magnitude of

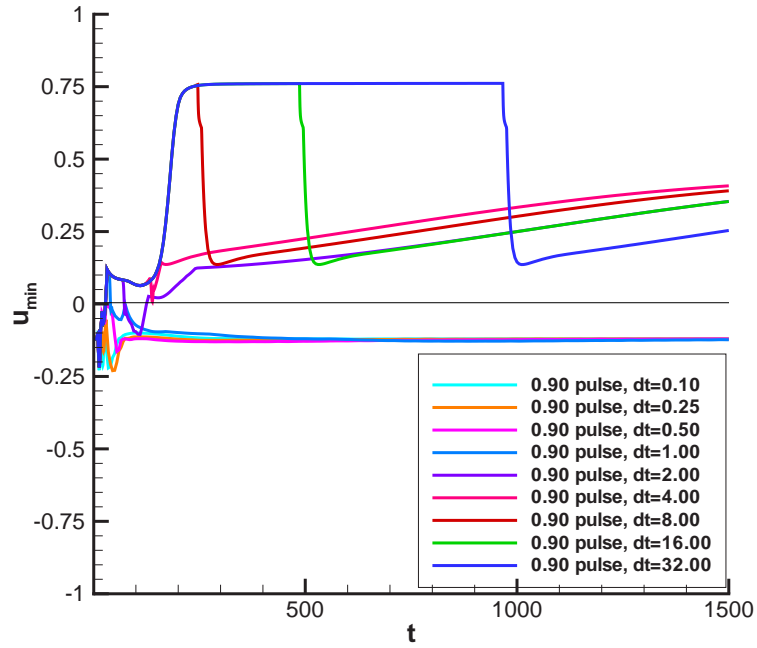


Figure 9.9: $\Omega_P = 0.90$: Minimum axial velocity vs. time for pulse durations $dt = 0.10, 0.25, 0.50, 1.00, 2.00, 4.00, 8.00, 16.00, 32.00$.

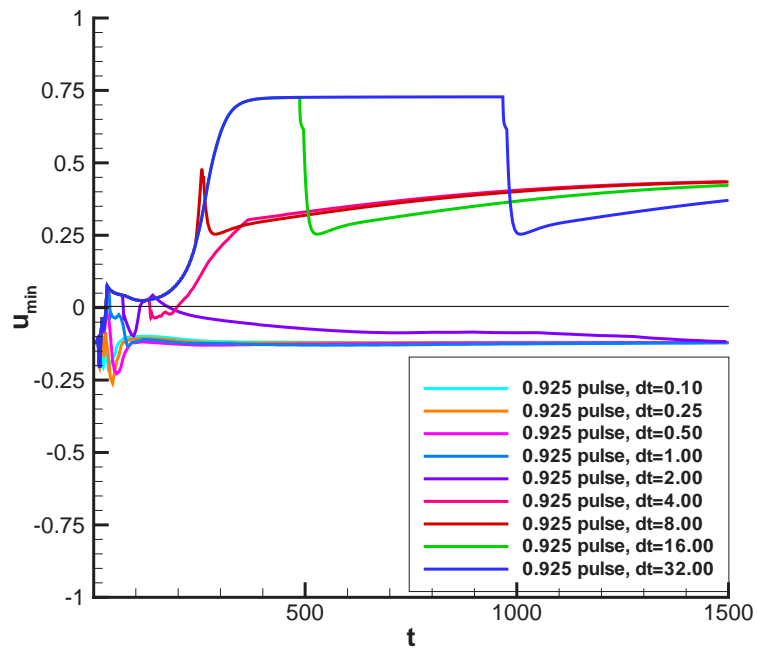


Figure 9.10: $\Omega_P = 0.925$: Minimum axial velocity vs. time for pulse durations $dt = 0.10, 0.25, 0.50, 1.00, 2.00, 4.00, 8.00, 16.00, 32.00$.

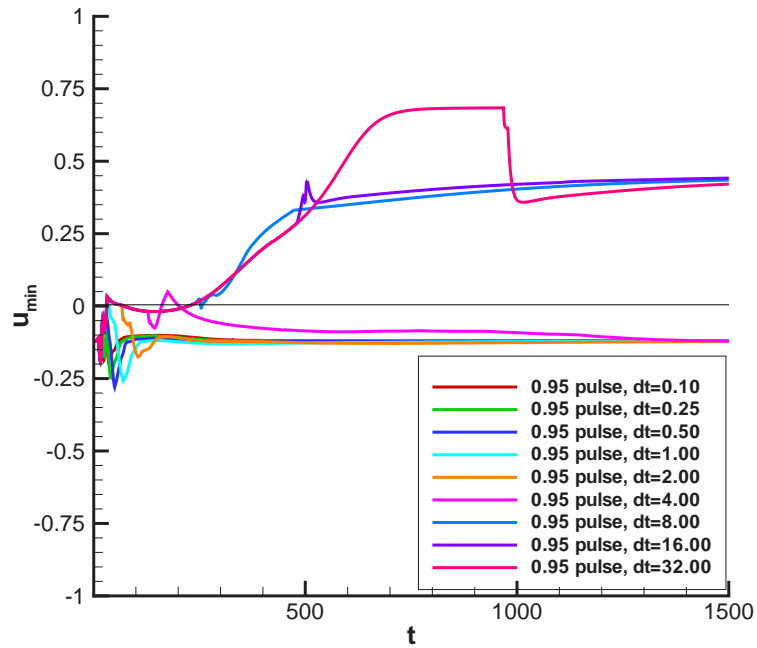


Figure 9.11: $\Omega_P = 0.95$: Minimum axial velocity vs. time for pulse durations $dt = 0.10, 0.25, 0.50, 1.00, 2.00, 4.00, 8.00, 16.00, 32.00$.

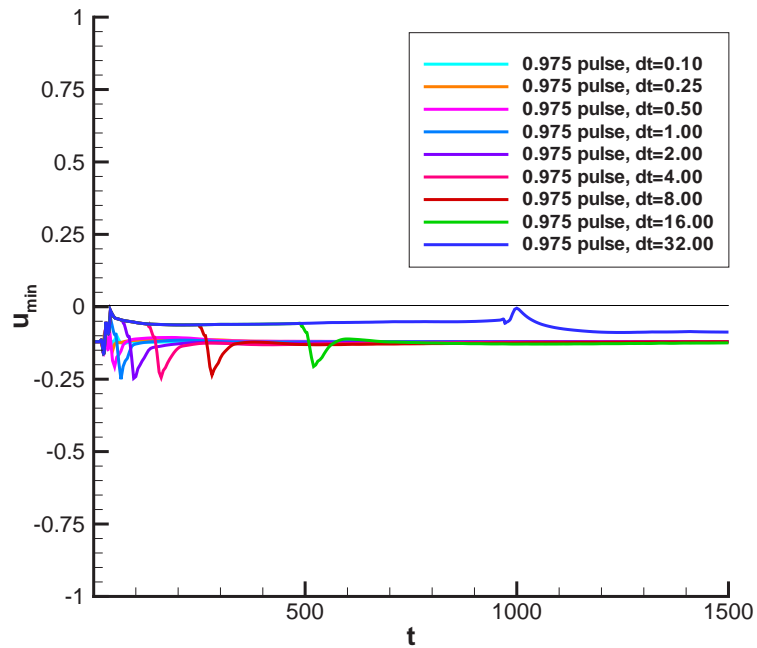


Figure 9.12: $\Omega_P = 0.975$: Minimum axial velocity vs. time for pulse durations $dt = 0.10, 0.25, 0.50, 1.00, 2.00, 4.00, 8.00, 16.00, 32.00$.

the swirl change is such that although the steady solution will not contain breakdown (as will be seen from the $dt \gg 32$ case in the next section), the slow progression of bubble evolution means there is not enough time for the bubble to disappear before the swirl is increased again to $\Omega = 1.45$. Even for the smaller Ω_P , the pulse duration dt required is much greater than that applied for the reverse transition to breakdown in chapter 8.

9.3 $dt \gg 32$

The case for $dt \gg 32$ was also tested. These results are plotted in figure 9.13, along with a summary of the preceding results. The range over which a transition to no breakdown could be effected was increased to $0.9 \leq \Omega_P \leq 0.975$, and would presumably also include all values between $\Omega_P = 0.975$ and the lower limit of the hysteresis region.

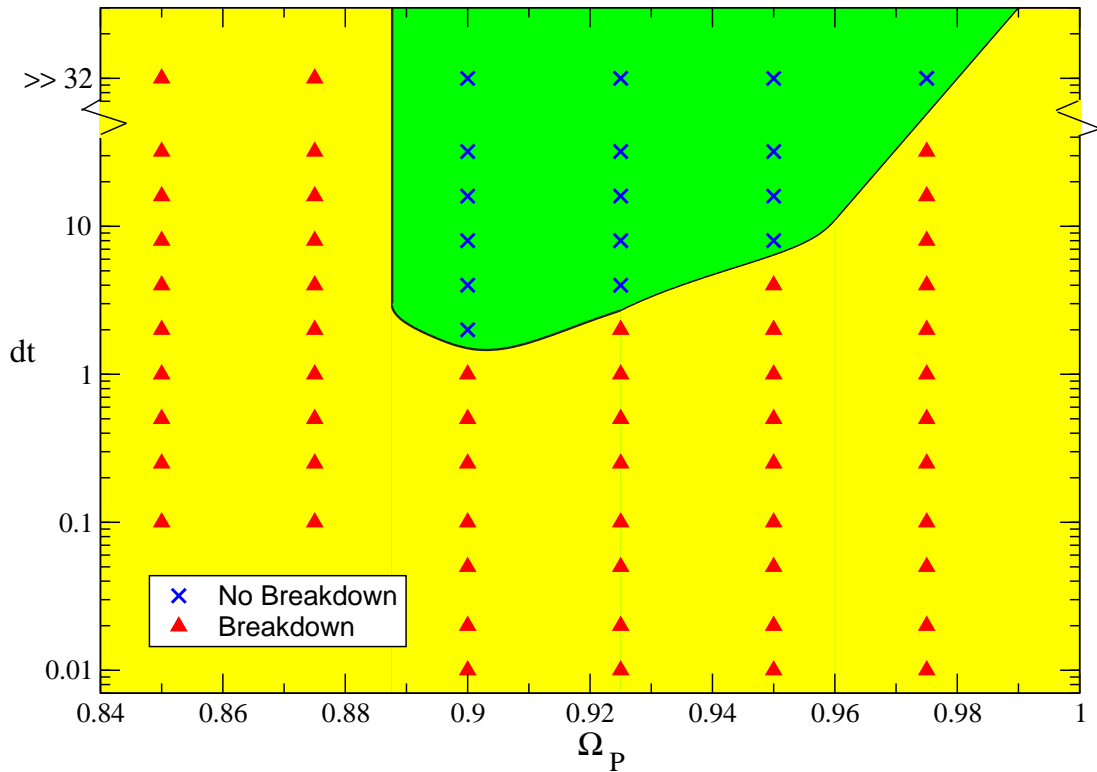


Figure 9.13: dt vs Ω_P , breakdown to no-breakdown transition.

9.4 Conclusions

The results from this chapter and chapter 8 show that it is possible to effect some control over the occurrence of breakdown by the application of a transient perturbation upstream. The control is limited to the region in Reynolds number/swirl space where vortex breakdown hysteresis is observed. Although this region is small at the Reynolds number considered, increasing Reynolds number results in an increase in the range over which hysteresis is observed, and an increase in the relevance of these results to real flows.

The transition from a flow without breakdown to one with breakdown was for the most part as expected. An increase in the amplitude Ω_P of the perturbation resulted in a greater likelihood of transition to breakdown. Likewise, an increase in the application time of the pulse also increased the likelihood of the presence of breakdown in the final solution.

There was a region of non-monotonicity for a certain range of Ω_P . This range varied with dt , but was still present for $dt \gg 32$. In this range breakdown was initially absent for small dt , appeared for larger dt , then was absent for still larger dt . It is suggested that the time in the evolution of the flow (following the initial increase in swirl) that the pulse is turned off may also have a significant effect on whether the final steady solution prefers breakdown or not.

In the present chapter, a transition from a flow with breakdown to one without breakdown was attempted. It was shown that such a transition is possible if the magnitude of the pulse is kept relatively small. Once a swirl pulse $\Omega_P < 1$ is found which is capable of tripping the transition to no-breakdown flow, increasing Ω_P (ie. decreasing the magnitude of the pulse) also allows the transition. However as Ω_P is increased the pulse duration dt required increases dramatically. It was found that the swirl where the transition could first be tripped ($\Omega_P = 0.90$) required the smallest time dt to produce a flow with breakdown.

In short, the pipe flow is dominated by the state with breakdown; increasing the swirl from zero always results in a breakdown bubble if the increase is sudden. Obtaining a solution without breakdown requires more gentle manipulation of the flow.

9.5 Relevance and further work

Since at lower Reynolds number the difference between the no-breakdown and breakdown flows is not large, it may be easier to trip the flow into the other conjugate state here than for higher Reynolds number. It was also a simple matter to introduce the swirl changes in the geometry considered here. For other geometries (eg. over wings) there are alternative methods, as have been discussed in chapter 2, for introducing swirl changes to a free vortex, such as azimuthal blowing or suction. The swirl is a ratio of azimuthal to axial velocities, so a swirl change can also be effected by manipulating the axial velocity. The application of these measures is beyond the scope of this work.

Chapter 10

Conclusions

There have been three themes to the study presented in the preceding chapters:

- *A test of the applicability of the azimuthal vorticity dynamics explanation for the onset of breakdown to the torsionally driven cylinder.*

Brown and Lopez [44], [6] identified the role of negative azimuthal vorticity generation in breakdown. Further studies, including those by Darmofal [9], [7], [8], have illustrated how this vorticity is generated in the open pipe flow. In the present study this analysis is applied to the cylinder, and it is shown that breakdown in this geometry can also be interpreted in terms of vorticity generation upstream of breakdown, resulting from tilting and stretching of extant vorticity. The rotating lid proved to be another important source of vorticity.

- *Comparison of the types of breakdown produced in the pipe and cylinder, with a proposed explanation for the differences, and justification for the labelling of the cylinder breakdown as breakdown.*

Some argue (eg. Leibovich [42], Hall [30], Goldshtik and Hussain [22]) that the inclusion of the cylinder flow in the group of phenomena termed breakdown is questionable. The arguments presented are based on differences between the breakdown forms observed in the cylinder and those observed in open pipes and over delta wings. Fundamentally, the breakdown observed in the more open geometries tends to be three-dimensional, whereas in the cylinder breakdown is generally axisymmetric (some asymmetry in the bubble forms has been noted, eg. by Spohn [64], however

this degree of asymmetry is not comparable to that of the spiral form of breakdown observed in pipes). In this report it is maintained that the reason for this discrepancy is the large difference in Reynolds number regimes. Reducing the Reynolds number in a pipe to that found in the cylinder resulted in the loss of three-dimensionality, and formation of a bubble similar to that which occurs in cylinders.

The cylinder has a simple geometry and lends itself to computational modelling as a result of the assumption of axisymmetry. It allowed early analytical and numerical studies to contribute to the understanding of a mechanism for breakdown. The present study provides more confidence in the applicability of results from these and future cylinder studies, as this apparatus does produce a phenomenon akin to that which occurs in the more open geometries.

- *A method for control of breakdown which relies on manipulating azimuthal vorticity generation in the pipe, and another which prompts transitions between conjugate states in the hysteresis region.*

Control of breakdown in a numerical simulation of an open pipe was achieved by placing a flow diverter (actually a cylindrical structure with an aerofoil cross-section) upstream of the location where breakdown is normally expected. The greatest effect was obtained by placing the aerofoil the maximum distance from the axis radially. The aerofoil suppressed breakdown from far upstream until just upstream of the location where a bubble would normally form. The aerofoil acts by reducing the radial outflow and hence suppressing generation of negative azimuthal vorticity. Other flow control measures could also affect breakdown via this mechanism.

The application of a swirl pulse showed that it was possible to transfer between breakdown and no-breakdown states within the hysteresis range in the open pipe. The flow containing breakdown appeared to be preferred, as the transition to a no-breakdown state was more difficult to implement than the transition to one with breakdown. The perturbation duration was large in this study, and would be expected to decrease for flows at higher Reynolds number.

The absence of a full theory for breakdown has not prevented the implementation of measures to influence breakdown. As mentioned in chapter 2, already various control devices and methods have been tested in experiments, and at least one used in practice.

These methods will be improved and added to with further understanding of breakdown. Fundamental research is also important for improving the understanding of these types of flows in general.

Bibliography

- [1] Yasir M. Al-Abdeli and Assaad R. Masri. Flowfield Regimes of Non-Reacting Swirling Flows. In *Proceedings of the 14th Australasian Fluid Mechanics Conference*, Adelaide, Australia, December 2001.
- [2] B. Badran, S. McCormick, and I. Gursul. Control of Leading-Edge Vortices with Suction. *J. Aircraft*, 35(1):163–165, 1997.
- [3] T. Brooke Benjamin. Theory of the Vortex Breakdown Phenomenon. *J. Fluid Mech.*, 14(4):593–629, 1962.
- [4] Philip S. Beran and Fred E.C. Culick. The role of non-uniqueness in the development of vortex breakdown in tubes. *J. Fluid Mech.*, 242:491–527, 1992.
- [5] Paul Billant, Jean-Marc Chomaz, and Patrick Huerre. Experimental study of vortex breakdown in swirling jets. *J. Fluid Mech.*, 376:183–219, 1998.
- [6] G.L. Brown and J.M.Lopez. Axisymmetric vortex breakdown Part 2. Physical mechanisms. *J. Fluid Mech.*, 221:553–576, 1990.
- [7] David L. Darmofal. The Role of Vorticity Dynamics in Vortex Breakdown. AIAA paper 93-3036, 1993.
- [8] D.L. Darmofal. *A Study of the Mechanisms of Axisymmetric Vortex Breakdown*. PhD thesis, Massachusetts Institute of Technology, November 1995.
- [9] D.L. Darmofal and E.M. Murman. On the Trapped Wave Nature of Axisymmetric Vortex Breakdown. AIAA paper 94-2318, 1994.
- [10] Jean M. Delery. Aspects of Vortex Breakdown. *Prog. Aerospace Sci.*, 30:1–59, 1994.

- [11] Q. Deng and I. Gursul. Effect of Leading-Edge Flaps on Vortices and Vortex Breakdown. *J. Aircraft*, 33(6):1079–1086, November - December 1996.
- [12] Q. Deng and I. Gursul. Vortex breakdown over a delta wing with oscillating leading edge flaps. *Experiments in Fluids*, 23:347–352, 1997.
- [13] NASA Dryden Flight Research Center.
- [14] Marcel Escudier. Vortex Breakdown: Observations and Explanations. *Prog. Aerospace Sci.*, 25:189–229, 1998.
- [15] M.P. Escudier and J.J. Keller. Vortex Breakdown: A Two-Stage Transition. *AGARD Conference Proceedings*, paper 25:183–219, 1983.
- [16] M.P. Escudier and N. Zehnder. Vortex-flow regimes. *J. Fluid Mech.*, 115:105–121, 1982.
- [17] J.H. Faler and S. Leibovich. Disrupted states of vortex flow and vortex breakdown. *Phy. Fluids*, 20(9):1385–1400, September 1977.
- [18] J.H. Faler and S. Leibovich. An experimental map of the internal structure of a vortex breakdown. *J. Fluid Mech.*, 86(2):313–335, 1978.
- [19] D. Gangulee and T. Terry Ng. Vortex Control over Sharp-Edged Slender Bodies. *J. Aircraft*, 32(4):739–745, July - August 1995.
- [20] A.K. Garg and S. Leibovich. Spectral characteristics of vortex breakdown flowfields. *Phys. Fluids*, 22(11):2053–2064, November 1979.
- [21] A.Yu. Gelfgat, P.Z. Bar-Yoseph, and A. Solan. Stability of confined swirling flow with and without vortex breakdown. *J. Fluid Mech*, 311:1–36, 1996.
- [22] M. Goldshtik and F. Hussain. Analysis of inviscid vortex breakdown in a semi-infinite pipe. *Fluid Dyn. Res.*, 23:189–234, 1998.
- [23] M. Goldshtik and F. Hussain. Analysis of inviscid vortex breakdown in a semi-infinite pipe. *Fluid Dynamics Research*, 23:189–234, 1998.
- [24] L.J.W. Graham, M.C. Jones, K. Hourigan, and M.C. Thompson. Convergence and Validation of Vortex Breakdown Predictions. (In progress).

- [25] Sheldon I. Green. Introduction to Vorticity. In *Fluid Vortices*, pages 1–34. Kluwer Academic Publishers, Netherlands, 1995.
- [26] W. Gu, O. Robinson, and D. Rockwell. Control of Vortices on a Delta Wing by Leading-Edge Injection. *AIAA Journal*, 31(7):1177–1186, July 1993.
- [27] I. Gursul, S. Srinivas, and G. Batta. Active Control of Vortex Breakdown over a Delta Wing. *AIAA Journal*, 33(9):1743–1745, 1995.
- [28] Ismet Gursul. Effect of Nonaxisymmetric Forcing on a Swirling Jet With Vortex Breakdown. *J. Fluids Engineering*, 118:316–321, June 1996.
- [29] Sheshagiri K. Habbar, Max F. Platzer, and Abdullah M. Alkhozam. Experimental Study of Vortex Flow Control on Double-Delta Wings Using Fillets. *J. Aircraft*, 33(4):743–751, July - August 1996.
- [30] M.G. Hall. Vortex Breakdown. *Ann. Rev. Fluid Mech.*, 4:195–218, 1972.
- [31] A.H. Hirs, J.M. Lopez, and R. Miraghaie. Symmetry breaking to a rotating wave in a lid-driven cylinder with a free surface: Experimental observation. *Phys. Fluids*, 285:69–94, 1995.
- [32] K. Hourigan, L.J.W. Graham, and M.C. Thompson. Spiral streaklines in pre-vortex breakdown regions of axisymmetric swirling flows. *Phys. Fluids*, 7(12):3126–3128, December 1995.
- [33] L.N. Howard and A.S. Gupta. On the Hydrodynamic and Hydromagnetic Stability of Swirling Flows. *J. Fluid Mech.*, 14:463–476, 1962.
- [34] H. Hussain, V. Stern, and F. Hussain. Control of vortex breakdown using vortex generators. AIAA paper 97-1879, 1997.
- [35] Jinhee Jeong and Fazle Hussain. On the identification of a vortex. *J. Fluid Mech.*, 285:69–94, 1995.
- [36] H. Johari and J. Moreira. Delta Wing Vortex Manipulation Using Pulsed and Steady Blowing during Ramp-Pitching. *J. Aircraft*, 33(2):304–310, March - April 1996.
- [37] H. Johari, D.J. Olinger, and K.C. Fitzpatrick. Delta Wing Vortex Control via Recessed Angled Spanwise Blowing. *J. Aircraft*, 32(4):804–810, July - August 1995.

- [38] John D. Anderson Jr. *Aircraft Performance and Design*. McGraw-Hill, 1999.
- [39] G.E. Karniadakis, M. Israeli, and S.A. Orszag. High-Order Splitting Methods for the Incompressible Navier-Stokes Equations. *J. Comput. Phys.*, 97:414–443, 1991.
- [40] G.E. Karniadakis and G.S. Triantafyllou. Three-dimensional Dynamics and Transition to Turbulence in the Wake of Bluff Objects. *J. Fluid Mech.*, 238:1–30, 1993.
- [41] B.C. Khoo, K.S. Yeo, D.F. Lim, and X. He. Vortex Breakdown in an Unconfined Vortical Flow. *Experimental Thermal and Fluid Science*, 14:131–148, 1997.
- [42] Sidney Leibovich. Vortex Stability and Breakdown: Survey and Extension. *AIAA J.*, 22(9):1192–1206, 1984.
- [43] Martin Lessen, Pawan Jit Singh, and Frederick Paillet. The stability of a trailing line vortex Part 1. Inviscid Theory. *J. Fluid Mech.*, 63(4):753–763, 1974.
- [44] J.M. Lopez. Axisymmetric vortex breakdown part 1. Confined swirling flow. *J. Fluid Mech.*, 221:533–552, 1990.
- [45] J.M. Lopez. On the bifurcation structure of axisymmetric vortex breakdown in a constricted pipe. *Phys. Fluids*, 6(11):3683–3693, November 1994.
- [46] M.V. Lowson. Some Experiments with Vortex Breakdown. *J. Royal Aero Soc.*, 8:343–346, 1964.
- [47] M.V. Lowson and A.J. Riley. Vortex Breakdown Control by Delta Wing Geometry. *J. Aircraft*, 32(4):832–838, 1995.
- [48] A. Mager. Dissipation and breakdown of a wing-tip vortex. *J. Fluid Mech.*, 55(4):609–628, 1972.
- [49] T. Maxworthy. Laboratory Modelling of Atmospheric Vortices: A Critical Review. In *Topics in Atmospheric and Oceanographic Science: Intense Atmospheric Vortices*, pages 229–246. Springer Verlag, Berlin, 1982.
- [50] S. McCormick and I. Gursul. Effect of Shear-Layer Control on Leading-Edge Vortices. *J. Aircraft*, 33(6):1087 – 1093, November - December 1996.

- [51] Anthony M. Mitchell, Didier Barberis, Pascal Molton, and Jean Delery. Oscillation of Vortex Breakdown Location and Blowing Control of Time-Averaged Location. *AIAA J.*, 38(5):793–803, May 2000.
- [52] B.R. Morton. The Generation and Decay of Vorticity. *Geophys. Astrophys. Fluid Dynamics*, 28:277–308, 1984.
- [53] S.V. Patankar and D.B. Spalding. A Calculation Procedure for Heat, Mass and Momentum Transfer in Three-dimensional Parabolic Flows. *Int. J. Heat Mass Transfer*, 15:1787, 1972.
- [54] J.D. Randall and S. Leibovich. The Critical State: a trapped wave model of vortex breakdown. *J. Fluid Mech.*, 58(3):495–515, 1973.
- [55] B.A. Robinson, R.M. Barnett, and S. Agrawal. Simple Numerical Criterion for Vortex Breakdown. *AIAA Journal*, 32(1):116–122, 1994.
- [56] M.D. Salas and G. Kuruwila. Vortex Breakdown Simulation: A Circumspect Study of the Steady, Laminar, Axisymmetric Model. *Computers and Fluids*, 17(1):247–262, 1989.
- [57] Turgut Sarpkaya. On stationary and travelling vortex breakdowns. *J. Fluid Mech.*, 45(3):545–559, 1971.
- [58] Turgut Sarpkaya. Vortex Breakdown in Swirling Conical Flows. *AIAA J.*, 9(9):1792–1799, 1971.
- [59] A. Schmücker and K. Gersten. Vortex breakdown and its control on delta wings. *Fluid Dynamics Research*, 3:268–272, 1998.
- [60] Chiang Shih and Zhong Ding. Trailing Edge Jet Control of Leading-Edge Vortices of a Delta Wing. *AIAA J.*, 34(7):1447–1457, 1996.
- [61] V. Shtern and F. Hussain. Collapse, Symmetry Breaking, and Hysteresis in Swirling Flows. *Ann. Rev. Fluid Mech.*, 31:537–566, 1999.
- [62] Jens Nørkær Sørensen and Erik Adler Christensen. Direct numerical simulation of rotating fluid flow in a closed cylinder. *Phys. Fluids*, 7(4):764–778, April 1995.

- [63] F. Sotiropoulos and Y. Ventikos. Transition from bubble-type vortex breakdown to columnar vortex in a confined swirling flow. *Int. J. Heat and Fluid Flow*, 19:446–458, 1998.
- [64] A. Spohn, M. Mory, and E.J. Hopfinger. Experiments on vortex breakdown in a confined flow generated by a rotating disc. *J. Fluid Mech.*, 370:73–99, 1998.
- [65] S. Srigrarom and M. Kurosaka. Shaping of Delta-Wing Planform to Suppress Vortex Breakdown. *AIAA Journal*, 38(1):183, January 2000.
- [66] S. Srigrarom and M. Kurosaka. Surface Shaping to Suppress Vortex Breakdown on Delta Wings. *AIAA Journal*, 38(1):185, January 2000.
- [67] J.L. Stevens, J.M. Lopez, and B.J. Cantwell. Oscillating flow states in an enclosed cylinder with a rotating endwall. *J. Fluid Mech*, 389:101–118, 1999.
- [68] D.H. Thompson. Water Tunnel Flow Visualisation of Vortex Breakdown over the F/A-18. Flight Mechanics Report 179, DSTO ARL, AR-005-607, 1990.
- [69] Tan Boon Thong. *Vortex Shedding and Interaction in Flows around Bluff Plates*. PhD thesis, Monash University, July 2000.
- [70] Lance W. Traub, Samuel F. Galls, and Othon K. Rediniotis. Reynolds Number Effects on Vortex Breakdown of a Blunt-Edged Delta. *J. Aircraft*, 33(4):835–837, March 1996.
- [71] Jeffrey C. Tromp and Philip S. Beran. Temporal Evolution of Three-Dimensional Vortex Breakdown from Steady, Axisymmetric Solutions. *AIAA Journal*, 34(3), 1995.
- [72] N. Tsitverblit and E. Kit. On the onset of unsteadiness in confined vortex flows. *Fluid Dynamics Research*, 23:125–152, 1998.
- [73] H.K. Versteeg and W. Malalasekera. *An introduction to Computational Fluid Dynamics, The Finite Volume Method*. Longman Scientific and Technical, 1995.
- [74] Peter V. Vorobieff and Donald O. Rockwell. Vortex Breakdown on Pitching Delta Wing: Control by Intermittent Trailing Edge Blowing. *AIAA J.*, 36(4):585–589, April 1998.

- [75] Wentz and Kohlman. Vortex Breakdown on Slender Sharp-Edged Wings. *J. Aircraft*, 8(3):156–161, 1970.
- [76] N.J. Wood, L. Roberts, and Z. Celik. Control of Asymmetric Vortical Flows over Delta Wings at High Angles of Attack. *J. Aircraft*, 27(5):429–435, May 1990.
- [77] J.Z. Wu and J.M. Wu. Vorticity Dynamics on Boundaries. *Advances in Applied Mechanics*, 32:119–275, 1996.